Development and Application of Differential-Equation Based Numerical Techniques to Electromagnetic Scattering and Radiation Problems

Neil R. S. Simons

A thesis presented to
the University of Manitoba
in partial fulfillment of the requirements for
the degree of Doctor of Philosophy

Winnipeg, Manitoba, 1994

Canada

Name _____ NEIL SIMONS

Dissertation Abstracts International is arranged by broad, general subject categories. Please select the one subject which most nearly describes the content of your dissertation. Enter the corresponding four-digit code in the spaces provided.

ENGINEERING, ELECTRONICS + ELECTRICAL

SUBJECT TERM

⬛0⬛5⬛4⬛4⬛ U·M·I

SUBJECT CODE

Subject Categories

THE HUMANITIES AND SOCIAL SCIENCES

COMMUNICATIONS AND THE ARTS
Architecture 0729
Art History 0377
Cinema 0900
Dance 0378
Fine Arts 0357
Information Science 0723
Journalism 0391
Library Science 0399
Mass Communications 0708
Music 0413
Speech Communication 0459
Theater 0465

EDUCATION
General 0515
Administration 0514
Adult and Continuing 0516
Agricultural 0517
Art 0273
Bilingual and Multicultural 0282
Business 0688
Community College 0275
Curriculum and Instruction 0727
Early Childhood 0518
Elementary 0524
Finance 0277
Guidance and Counseling 0519
Health 0680
Higher 0745
History of 0520
Home Economics 0278
Industrial 0521
Language and Literature 0279
Mathematics 0280
Music 0522
Philosophy of 0998
Physical 0523

Psychology 0525
Reading 0535
Religious 0527
Sciences 0714
Secondary 0533
Social Sciences 0534
Sociology of 0340
Special 0529
Teacher Training 0530
Technology 0710
Tests and Measurements 0288
Vocational 0747

LANGUAGE, LITERATURE AND LINGUISTICS
Language
  General 0679
  Ancient 0289
  Linguistics 0290
  Modern 0291
Literature
  General 0401
  Classical 0294
  Comparative 0295
  Medieval 0297
  Modern 0298
  African 0316
  American 0591
  Asian 0305
  Canadian (English) 0352
  Canadian (French) 0355
  English 0593
  Germanic 0311
  Latin American 0312
  Middle Eastern 0315
  Romance 0313
  Slavic and East European 0314

PHILOSOPHY, RELIGION AND THEOLOGY
Philosophy 0422
Religion
  General 0318
  Biblical Studies 0321
  Clergy 0319
  History of 0320
  Philosophy of 0322
Theology 0469

SOCIAL SCIENCES
American Studies 0323
Anthropology
  Archaeology 0324
  Cultural 0326
  Physical 0327
Business Administration
  General 0310
  Accounting 0272
  Banking 0770
  Management 0454
  Marketing 0338
Canadian Studies 0385
Economics
  General 0501
  Agricultural 0503
  Commerce-Business 0505
  Finance 0508
  History 0509
  Labor 0510
  Theory 0511
Folklore 0358
Geography 0366
Gerontology 0351
History
  General 0578

Ancient 0579
Medieval 0581
Modern 0582
Black 0328
African 0331
Asia, Australia and Oceania 0332
Canadian 0334
European 0335
Latin American 0336
Middle Eastern 0333
United States 0337
History of Science 0585
Law 0398
Political Science
  General 0615
  International Law and
    Relations 0616
  Public Administration 0617
Recreation 0814
Social Work 0452
Sociology
  General 0626
  Criminology and Penology ... 0627
  Demography 0938
  Ethnic and Racial Studies 0631
  Individual and Family
    Studies 0628
  Industrial and Labor
    Relations 0629
  Public and Social Welfare 0630
  Social Structure and
    Development 0700
  Theory and Methods 0344
Transportation 0709
Urban and Regional Planning 0999
Women's Studies 0453

THE SCIENCES AND ENGINEERING

BIOLOGICAL SCIENCES
Agriculture
  General 0473
  Agronomy 0285
  Animal Culture and
    Nutrition 0475
  Animal Pathology 0476
  Food Science and
    Technology 0359
  Forestry and Wildlife 0478
  Plant Culture 0479
  Plant Pathology 0480
  Plant Physiology 0817
  Range Management 0777
  Wood Technology 0746
Biology
  General 0306
  Anatomy 0287
  Biostatistics 0308
  Botany 0309
  Cell 0379
  Ecology 0329
  Entomology 0353
  Genetics 0369
  Limnology 0793
  Microbiology 0410
  Molecular 0307
  Neuroscience 0317
  Oceanography 0416
  Physiology 0433
  Radiation 0821
  Veterinary Science 0778
  Zoology 0472
Biophysics
  General 0786
  Medical 0760

EARTH SCIENCES
Biogeochemistry 0425
Geochemistry 0996

Geodesy 0370
Geology 0372
Geophysics 0373
Hydrology 0388
Mineralogy 0411
Paleobotany 0345
Paleoecology 0426
Paleontology 0418
Paleozoology 0985
Palynology 0427
Physical Geography 0368
Physical Oceanography 0415

HEALTH AND ENVIRONMENTAL SCIENCES
Environmental Sciences 0768
Health Sciences
  General 0566
  Audiology 0300
  Chemotherapy 0992
  Dentistry 0567
  Education 0350
  Hospital Management 0769
  Human Development 0758
  Immunology 0982
  Medicine and Surgery 0564
  Mental Health 0347
  Nursing 0569
  Nutrition 0570
  Obstetrics and Gynecology .. 0380
  Occupational Health and
    Therapy 0354
  Ophthalmology 0381
  Pathology 0571
  Pharmacology 0419
  Pharmacy 0572
  Physical Therapy 0382
  Public Health 0573
  Radiology 0574
  Recreation 0575

Speech Pathology 0460
Toxicology 0383
Home Economics 0386

PHYSICAL SCIENCES
Pure Sciences
Chemistry
  General 0485
  Agricultural 0749
  Analytical 0486
  Biochemistry 0487
  Inorganic 0488
  Nuclear 0738
  Organic 0490
  Pharmaceutical 0491
  Physical 0494
  Polymer 0495
  Radiation 0754
Mathematics 0405
Physics
  General 0605
  Acoustics 0986
  Astronomy and
    Astrophysics 0606
  Atmospheric Science 0608
  Atomic 0748
  Electronics and Electricity 0607
  Elementary Particles and
    High Energy 0798
  Fluid and Plasma 0759
  Molecular 0609
  Nuclear 0610
  Optics 0752
  Radiation 0756
  Solid State 0611
Statistics 0463

Applied Sciences
Applied Mechanics 0346
Computer Science 0984

Engineering
  General 0537
  Aerospace 0538
  Agricultural 0539
  Automotive 0540
  Biomedical 0541
  Chemical 0542
  Civil 0543
  Electronics and Electrical 0544
  Heat and Thermodynamics ... 0348
  Hydraulic 0545
  Industrial 0546
  Marine 0547
  Materials Science 0794
  Mechanical 0548
  Metallurgy 0743
  Mining 0551
  Nuclear 0552
  Packaging 0549
  Petroleum 0765
  Sanitary and Municipal 0554
  System Science 0790
Geotechnology 0428
Operations Research 0796
Plastics Technology 0795
Textile Technology 0994

PSYCHOLOGY
General 0621
Behavioral 0384
Clinical 0622
Developmental 0620
Experimental 0623
Industrial 0624
Personality 0625
Physiological 0989
Psychobiology 0349
Psychometrics 0632
Social 0451

♻

DEVELOPMENT AND APPLICATION OF DIFFERENTIAL-EQUATION

BASED NUMERICAL TECHNIQUES TO ELECTROMAGNETIC

SCATTERING AND RADIATION PROBLEMS

BY

NEIL R.S. SIMONS

A Thesis submitted to the Faculty of Graduate Studies of the University of Manitoba in partial fulfillment of the requirements for the degree of

DOCTOR OF PHILOSOPHY

© 1994

ABSTRACT

In this thesis the development and application of general purpose computer simulation techniques for macroscopic electromagnetic phenomena are investigated. These techniques are applicable to a wide variety of practical problems pertaining to: Electromagnetic Compatibility and Interference, Radar-Cross-Section, and the analysis and design of antennas. The goal of this research is to examine methods that are applicable to a wide variety of problems rather than specialized approaches that are only useful for specific problems. A brief review of the computational electromagnetics literature indicates two general types of methods are applicable. These are numerical approximation of integral-equation formulations and numerical approximation of differential-equation formulations. Because of their relative efficiency for inhomogeneous geometries, the direction of the thesis proceeds with numerical approximations to differential-equation based formulations.

The differential-equation based numerical methods include various finite-difference, finite-element, finite-volume, and transmission line matrix methods. A literature review and overview of these numerical methods is provided. The goal of the overview is to provide the capability for the classification of existing and future differential equation based numerical methods to identify relative advantages and disadvantages.

Extensions to the two-dimensional transmission line matrix method are presented. The extensions are intended to provide some of the flexibility traditionally associated with finite-difference and finite-element methods. Three new two-dimensional models are presented. Two of the new models utilize triangular rather than the usual rectangular spatial discretization. The third model introduces the capability of higher-order spatial accuracy. The efficiency and application of the new models are discussed.

The development of two general-purpose electromagnetic simulation programs is presented. Both are three-dimensional time-domain methods that use local absorbing boundary conditions. The first program is based on the symmetric-condensed transmission line matrix algorithm. The second program is based on the discretization of the modified vector wave equation using nodal finite-elements in space and finite-differences in time. The applications considered are: half-space problems and remote-sensing of shallow objects; radar-cross-section of finite-sized conducting, dielectric, and

composite objects; and the analysis of microstrip antennas and circuit elements. The numerical results obtained indicate the simulation programs are capable of providing acceptable accuracy for a variety of practical applications, and therefore validates the concept of a general purpose electromagnetic simulation program. Some limitations and possible improvements are discussed. Although most of the applications have been analyzed with the transmission line matrix simulation program, the finite-element simulation program is considered to be the more powerful method because of its ability to accommodate unstructured grids and therefore geometries of arbitrary shape.

In addition, the application of cellular automata to computational electromagnetics is considered. Cellular automata are fully discrete computational models which are exactly computable using digital hardware. One type of cellular automata, the lattice gas automata are suitable for the analysis of two-dimensional scalar electromagnetic field problems. The HPP lattice gas automaton is applied to the modelling of two-dimensional electromagnetic field problems. The numerical results obtained from the analysis of some simple electromagnetic wave propagation problems and the availability of high-performance special-purpose computational hardware indicate the promise of this approach as a potentially powerful tool for modelling electromagnetic field problems.

Table of Contents

Chapter 7: Application of Cellular Automata to Computational Electromagnetics

Chapter 8: Conclusions and Future Directions

Acknowledgments:

Chapter 1: Introduction

The general scope of this research involves the development of general purpose simulation techniques for the solution of electromagnetic field problems. Efficient and accurate numerical solutions to electromagnetic field problems is of practical importance to a variety of practical problems including: the characterization of Electromagnetic Interference and Electromagnetic Compatibility, Radar Cross Section analysis, and the analysis and design of microwave circuits and antennas. The goal of this research is to investigate numerical methods which can be applied to a wide variety of electromagnetic field problems and can therefore be considered as general purpose electromagnetic simulation environments.

1.1: General Electromagnetic Field Problem

Consider the geometry described in Figure 1.1. A volume V is bounded by a surface S and contains an arbitrary arrangement of conductors and material regions which are excited by a source. This geometry describes a general electromagnetic scattering and radiation problem. As mentioned above, special cases of this geometry are relevant to many practical engineering problems. At every spatial location, the field distributions satisfy Maxwell's equations, given as,

$$\nabla \times \mathbf{E} = -\frac{\partial \mathbf{B}}{\partial t} \tag{1.1a}$$

$$\nabla \times \mathbf{H} = \mathbf{J} + \frac{\partial \mathbf{D}}{\partial t} \tag{1.1b}$$

$$\nabla \cdot \mathbf{D} = 0 \tag{1.1c}$$

$$\nabla \cdot \mathbf{B} = 0 \tag{1.1d}$$

where the electric field $\mathbf{E}$, magnetic field $\mathbf{H}$, electric flux density $\mathbf{D}$, magnetic flux density $\mathbf{B}$, and the electric current density $\mathbf{J}$, are functions of space and time (i.e., $\mathbf{E}=\mathbf{E}(x,y,z,t)$). The constitutive relations are:

$$\mathbf{D} = \varepsilon\,\mathbf{E}$$
$$\mathbf{B} = \mu\,\mathbf{H} \tag{1.2}$$
$$\mathbf{J} = \sigma\,\mathbf{E}$$

where ε, μ, and σ are the permittivity, permeability and conductivity, respectively.

  Along an interface between two material regions (with material properties $\varepsilon_1,\mu_1,\sigma_1$ and $\varepsilon_2,\mu_2,\sigma_2$; field distributions $\mathbf{E}_1,\mathbf{H}_1$ and $\mathbf{E}_2,\mathbf{H}_2$; and a normal vector $\mathbf{n}$ along the interface), the following boundary conditions are satisfied,

$$\mathbf{n}\cdot\left(\left(\varepsilon_1\frac{\partial\mathbf{E}_1}{\partial t}+\sigma_1\mathbf{E}_1\right)-\left(\varepsilon_2\frac{\partial\mathbf{E}_2}{\partial t}+\sigma_2\mathbf{E}_2\right)\right)=0$$

$$\mathbf{n}\cdot\left(\mu_1\mathbf{H}_1-\mu_2\mathbf{H}_2\right)=0$$

$$\mathbf{n}\times\left(\mathbf{E}_1-\mathbf{E}_2\right)=0 \tag{1.3}$$

$$\mathbf{n}\times\left(\mathbf{H}_1-\mathbf{H}_2\right)=0$$

If the exterior surface S represents a boundary along which a homogeneous material exists, as S recedes to an infinite distance from the objects in V, the field distributions along S satisfy the Sommerfeld radiation condition,

$$\lim_{r\to\infty}(\mathbf{E})\ \alpha\ \ \frac{e^{-jkr}}{r} \tag{1.4}$$

where k is the wave number in the homogeneous material region.

  An electromagnetic field problem can be classified into three general frequency ranges. The three frequency ranges are related to the characteristic size of the problem, L and the relevant wavelength, λ. For structures having a characteristic size that is small compared to wavelengths ($L\ll\lambda$), static approximations can be applied which assume the time variation in the field quantities is negligible. In the resonance range, the

characteristic length is on the order of a wavelength ($L \approx \lambda$). For electrically large problems ($L \gg \lambda$), an optical description can be applied for which fields can be modelled as rays and their behavior governed by the diffraction theory. The problems investigated in this thesis are in the resonance range. The methods applied, however are applicable to the other two frequency ranges with sufficient computational resources.
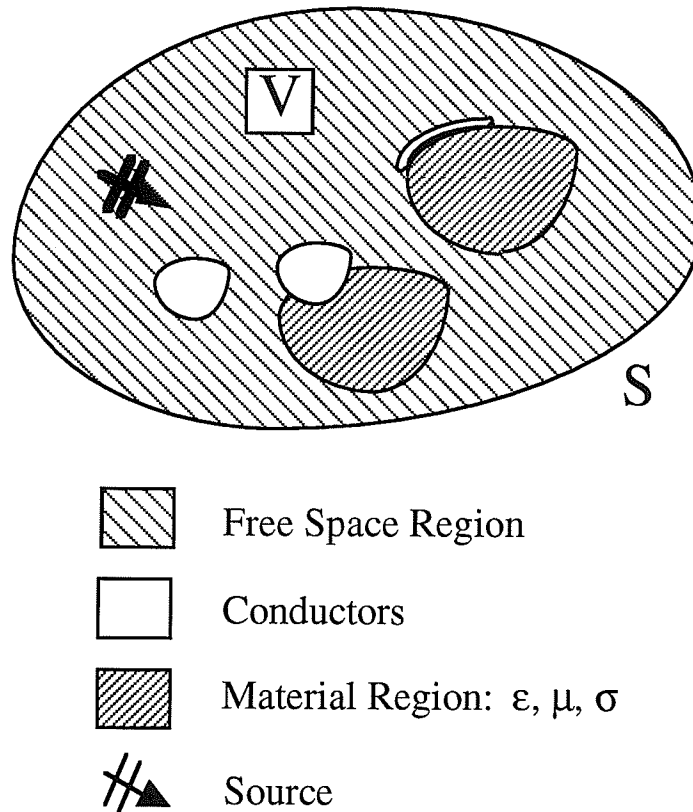
Figure 1.1: General electromagnetic scattering or radiation problem.

1.2: Purpose

The purpose of this research involves the investigation of numerical methods capable of providing accurate solutions to the general electromagnetic scattering or radiation problems described in Figure 1.1 without placing restrictions on the material or geometrical configuration of the problem. This approach can be considered as the development of a general purpose electromagnetic simulation environment. For example, the benefit of pursuing a general purpose simulation environment can be illustrated for

the computer-aided-analysis of antennas. A survey of the computational electromagnetics literature indicates that specialized techniques have been developed for a wide variety of specific antenna types. Although these codes provide optimal accuracy and efficiency (since they are well suited for the specific type of antenna considered), a disadvantage is that for each different type of antenna, a different technique is required. A general purpose electromagnetic simulation tool would be capable of analyzing a wide variety of antenna types.

1.3: Overview of Solution Techniques for General Problems

Two general techniques can be applied to the solution of electromagnetic field problems. These are analytic and numerical methods. Numerical methods can be further sub-divided into two groups. The first involves the numerical solution of integral-equation formulations (the majority of which are frequency-domain formulations), and the second involves the numerical solution of differential-equation formulations (the majority of which are time-domain formulations).

1.3.1: Analytic Methods

Analytical solutions involve the application of classical techniques (separation of variables, etc.) to a governing mathematical formulation [Stra41], [Mors53]. Since these techniques are limited to specific geometries (that conform to specific coordinate systems), it is generally not possible to obtain the exact solution to an arbitrary problem. For some problems an approximate analytic model can be obtained. As long as the approximations are not too severe, the result is an extremely efficient solution technique (as compared to numerical solutions). An example for the case of slot-coupled microstrip geometries is described in [Itti91].

Unfortunately, most real-world problems are geometrically complex, and therefore analytic solutions are not possible. The limited applicability of analytic solutions to general problems (in terms of computability) leads to the view that the traditional formulation of physical problems (in terms of differential equations) is not a computationally reasonable representation of physical phenomena and alternative representations should be pursued (for example, see [John79], [Toff84a], and [Wolf93]

and the discussion in Chapter 7). For the present investigation, analytic solutions are considered to be inadequate for providing a general approach to the solution of a wide variety of electromagnetic field problems described by Figure 1.1.

1.3.2: Numerical Solution of Integral Equation Formulations

Integral equation formulations are obtained through the use of source representations for the unknown field distributions. A detailed review of numerical methods based on integral-equation formulations of electromagnetic field problems can be found in [Mill88]. Using physical or physically-equivalent sources (corresponding to current or charge densities), and a Green's function (to take into account any analytically solvable geometrical aspects of the problem [Burk84], [Mosi90], [Poza90]), a mathematical statement can be made in the form of an integral equation. The unknown functions are usually current and charge densities, and are determined via the discretization of the mathematical formulation using the Method of Moments [Harr69].

For problems consisting of material regions, surface integral-equation formulations [Kish86], [Sark90] (the unknown functions are surface currents along material interfaces) and volume integral-equation formulations [Rich66], [Scha84], [Sark89] (the unknown functions are volume polarization currents) have been successfully applied to solve radiation and scattering problems. An expanded discussion of sections 1.3.1 and 1.3.2 can be found in [Simo91c]. The efficiency of these approaches are considered in section 1.3.4.

1.3.3: Numerical Solution of Differential Equation Formulations

Differential equation formulations involve the determination of approximate solutions by direct approximation of Maxwell's equations (or mathematically equivalent statements). A detailed review of these methods is provided in Chapter 2. The numerical solution of these equations is obtained through the application of techniques such as the finite-difference and finite-element methods. Since Maxwell's equations are satisfied throughout the entire spatial domain of the problem, the region of discretization is all space in which a non-zero field distribution exists. For open region problems, an

absorbing boundary condition is required to limit the spatial domain of the problem to a finite size and to enforce (perhaps approximately), the Sommerfeld radiation condition (1.4) on the field distributions.

1.3.4: Application to Spatially Inhomogeneous Problem

Consider the general problem of Figure 1.2, consisting of a finite-sized object, with a characteristic dimension, D (given in terms of an electrical distance). The volume of the object is D^3. The object consists of a number of material regions, separated by N interfaces. The surface area of each interface is D^2. For this problem the computational resources of the surface integral-equation formulation, volume integral-equation formulation, and a differential-equation formulation are considered. Similar theoretical investigations with the same conclusions can be found in [Tafl83] and [Mill88], and a computational investigation with the same conclusions can be found in [Pete89]. Each method is considered to be formulated in the frequency domain.

The surface integral-equation formulation requires discretization of all material interfaces. The number of unknowns is proportional to ND^2. The system matrix resulting from discretization of the mathematical formulation is full, and therefore the number of elements in the system matrix is proportional to ND^4. The volume integral-equation formulation requires discretization of the volume of the object, but is independent of the number of interfaces. The number of unknowns is proportional to D^3. The system matrix resulting from discretization of the mathematical formulation is again full, and therefore the number of elements in the system matrix is proportional to D^6. The differential-equation formulation requires discretization of the volume of the object and some of the space surrounding the object (depending on the type of absorbing boundary condition, and the manner in which it is applied). The number of unknowns is proportional to D^3. The system matrix resulting from discretization of the mathematical formulation is sparse, and therefore the number of elements in the system matrix is proportional to the number of unknowns D^3. Assuming that the number of elements in the system matrix is proportional to the computational effort required to solve the problem, this brief discussion indicates that as the complexity of the object (in terms of the number of material regions or the number of surfaces contained within a specific volume) increases, the differential-equation based formulations become more

computationally efficient than both the surface integral-equation formulation and the volume integral-equation formulation.
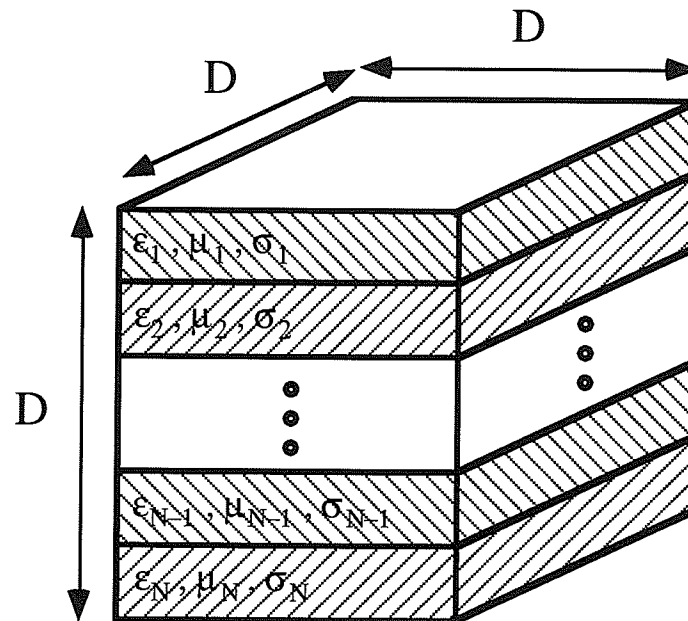
Figure 1.2: A finite-sized inhomogeneous object.

1.3.5: Conclusions of the Review

Based on the previous section, the present research will pursue numerical methods based on differential-equation formulations. A general purpose simulation environment based on the numerical solution of differential-equation formulations is capable of satisfying present and future modelling requirements (as long as Maxwell's equations are relevant and the electrical size of the structures of interest are on the order of a wavelength).

1.3.6: Outline of Thesis

In the remainder of this thesis, the development and application of differential equation based numerical techniques suitable for general purpose electromagnetic

simulation environments is investigated. In the following chapter, differential equation based numerical methods are reviewed. The transmission line matrix (TLM) method is reviewed in Chapter 3 and a general purpose electromagnetic simulation program based on the three-dimensional symmetric condensed TLM model is presented. In Chapter 4, new TLM models for the two-dimensional wave equation are introduced. These new models demonstrate that the same flexibility afforded by the finite-difference and finite-element methods (in terms of the development of new algorithms) is also applicable to the TLM method. Application of the general purpose TLM simulation program to three different classes of problem are considered in Chapter 5. These include the analysis of: half-space problems, radar-cross-section of finite-sized objects, and microstrip antennas and circuits. In Chapter 6, the development of a time-domain finite-element program based on an algorithm originally introduced by Lynch and Paulsen [Lync90] is presented. A few simple problems are considered for validation. In Chapter 7 a novel approach to computational electromagnetics is presented, based on cellular automata. Cellular automata are distinct from the traditional differential equation based description of physical phenomena. A summary of the thesis and future directions are provided in Chapter 8.

Chapter 2: Review of Differential Equation Based Numerical Methods

In this chapter, an overview of differential-equation based numerical methods is presented. The purpose of this overview is to demonstrate that the general approach used in the development of all differential-equation based numerical methods is essentially the same. The following categories are used to clasify the overall form of an arbitrary differential-equation based numerical method:

1) mathematical formulation,
2) field formulation / source description,
3) absorbing boundary condition,
4) grid structure,
5) spatial discretization,
6) organization of spatial cell, and
7) selection of time or frequency domain.

A method is obtained by selecting one possible technique from each of the above categories. Advantages and disadvantages that arise from the various selections are discussed. Throughout this chapter, several well-known differential-equation based methods will be discussed in the context of the above classification.

2.1: Mathematical Formulation

The first step in constructing a differential-equation based numerical method is the specification of the mathematical formulation. The differences are mostly notational,

although important practical considerations arise. In this section, some possible mathematical formulations are described.

2.1.1: Maxwell's Curl Equations

$$\nabla \times E = - \frac{\partial (\mu H)}{\partial t} \tag{2.1a}$$

$$\nabla \times H = \sigma E + \frac{\partial (\varepsilon E)}{\partial t} \tag{2.1b}$$

Numerical methods based on direct discretization of the two curl equations include the Yee finite-difference time-domain method [Yee66], [Tafl89]; the point-matched time-domain finite-element method [Mei84], [Cang87]; and various time-domain finite-element and finite-volume methods described in [Mads88], [Mads90] and [Holl91].

2.1.2: Double-Curl Equation

The double-curl equation is obtained by taking $\partial/\partial t$ of (2.1b), substituting (2.1a), and assuming ε and μ are constants,

$$- \nabla \times \left(\frac{1}{\mu} \nabla \times E \right) = \sigma \frac{\partial E}{\partial t} + \varepsilon \frac{\partial^2 E}{\partial t^2} \tag{2.2}$$

Numerical methods based on the discretization of (2.2) are described in [Sumb91] (a frequency-domain finite-element method for axi-symmetric geometries), and [D'Ang90], [Paul88] (frequency-domain finite-element methods).

2.1.3: Vector Wave Equation / Helmholtz Equation

Equation (2.2) can be modified by making use of the vector identity,

$$\nabla \times \nabla \times E = \nabla \left(\nabla \cdot E \right) - \nabla^2 E$$

Noting that $\nabla \cdot \mathbf{E} = 0$ from (1.1), (2.2) can be expressed as,

$$\frac{1}{\mu}\nabla^2\mathbf{E} = \sigma\frac{\partial\mathbf{E}}{\partial t} + \varepsilon\frac{\partial^2\mathbf{E}}{\partial t^2} \tag{2.3}$$

Discretization of (2.3) has been performed by Ling using finite-differences [Ling91] and Arlett *et al* using finite-elements in the frequency domain [Arle69].

2.1.4: Modified Vector Wave Equation

The modified vector wave equation is obtained by adding a divergence term to the left hand side of (2.2)

$$-\nabla\times\left(\frac{1}{\mu}\nabla\times\mathbf{E}\right) + \nabla\left(\frac{1}{\varepsilon\mu}\nabla\cdot\varepsilon\mathbf{E}\right) = \sigma\frac{\partial\mathbf{E}}{\partial t} + \varepsilon\frac{\partial^2\mathbf{E}}{\partial t^2} \tag{2.4}$$

This formulation was initially proposed in [Paul91a] for application with time-domain [Lync90], and frequency-domain finite-element methods.

2.1.5: Penalty Formulation

The modified vector wave equation described above is a special case of the penalty formulation, given by,

$$-\nabla\times\left(\frac{1}{\mu}\nabla\times\mathbf{E}\right) + p\nabla\left(\frac{1}{\varepsilon\mu}\nabla\cdot\varepsilon\mathbf{E}\right) = \sigma\frac{\partial\mathbf{E}}{\partial t} + \varepsilon\frac{\partial^2\mathbf{E}}{\partial t^2} \tag{2.5}$$

where p is referred to as the penalty factor. The modified vector wave equation corresponds to the penalty formulation with p=1. This formulation was proposed by Rahman and Davies [Rahm84]. The motivation for this formulation is discussed in section 2.1.8.

2.1.6: System of Conservation Laws

Maxwell's curl equations can be expressed as a system of conservation laws (in cartesian coordinates) as,

$$\partial_t \mathbf{u} + A_E \partial_x \mathbf{u} + A_F \partial_y \mathbf{u} + A_G \partial_z \mathbf{u} = 0 \tag{2.6}$$

where $\partial_\alpha = \partial/\partial\alpha$, and

$$A_E = \begin{bmatrix} 0 & 0 & 0 & 0 & 0 & 0 \\ 0 & 0 & 0 & 0 & 0 & e \\ 0 & 0 & 0 & 0 & -e & 0 \\ 0 & 0 & 0 & 0 & 0 & 0 \\ 0 & 0 & -m & 0 & 0 & 0 \\ 0 & m & 0 & 0 & 0 & 0 \end{bmatrix}$$

$$A_F = \begin{bmatrix} 0 & 0 & 0 & 0 & 0 & -e \\ 0 & 0 & 0 & 0 & 0 & 0 \\ 0 & 0 & 0 & e & 0 & 0 \\ 0 & 0 & m & 0 & 0 & 0 \\ 0 & 0 & 0 & 0 & 0 & 0 \\ -m & 0 & 0 & 0 & 0 & 0 \end{bmatrix}$$

$$A_G = \begin{bmatrix} 0 & 0 & 0 & 0 & e & 0 \\ 0 & 0 & 0 & -e & 0 & 0 \\ 0 & 0 & 0 & 0 & 0 & 0 \\ 0 & -m & 0 & 0 & 0 & 0 \\ m & 0 & 0 & 0 & 0 & 0 \\ 0 & 0 & 0 & 0 & 0 & 0 \end{bmatrix}$$

$e = 1/\varepsilon$, $m = 1/\mu$ and $\mathbf{u}$ is the solution vector,

$$\mathbf{u} = \begin{bmatrix} E_x \\ E_y \\ E_z \\ H_x \\ H_y \\ H_z \end{bmatrix}$$

The expression of Maxwell's curl equations as a system of conservation laws has been used in [Shan90] and [Moha91] in conjunction with a time-domain finite-volume method, and in [LoVe92] and [LoVe93] for the derivation of two- and three-dimensional symmetric-condensed transmission line matrix methods.

2.1.7: Coupling of Mathematical Formulation to Other Formulations

It can be beneficial to couple the basic mathematical formulation (2.1)-(2.6) to additional mathematical formulations to model specific geometrical features. This approach has been applied to the modelling of geometrical features that are small compared to the grid size that would be typically be applied. These features include thin wires, thin slots, and thin material layers [Cham93], [Rile93]. In all three cases, the geometrical feature to be modelled is small compared to a wavelength, and the subsequent discretization for accurate geometrical modelling would require excessive computational resources. To avoid this, the mathematical formulation applied throughout the computational domain is coupled to a mathematical formulation for the specific geometrical feature. Examples include: coupling of Ampere's law and Faraday's law to Maxwell's equations for modelling thin wires (for a numerical investigation of thin wire modelling with the Yee finite-difference time-domain see [Cham93]); and coupling of a magnetic field integral equation for modelling thin slots in conducting plates [Rile93]. The absorbing boundary conditions, reviewed in section 2.3, can also be considered within this framework. Depending on the physics of each specific case, the stability of the resulting algorithm (if a time-domain approach is applied) can be evaluated by examining its numerical reversibility [Vich84b], [Simo94e].

2.1.8: Implications of Mathematical Formulation

While the differences between the above formulations may appear to be notational, important numerical differences have been discussed in [Lync91] and [Paul91a] with respect to the problem of spurious modes. A spurious mode (also referred to as a vector parasite) is a solution that does not satisfy both the curl and divergence equations, and is therefore an unphysical artefact. The presence of these unphysical solutions contaminates the numerical results and appear as unphysical modes. In the

formulation of the general electromagnetic field problem (see Chapter 1), Maxwell's curl equations and the divergence equations are satisfied throughout the entire spatial domain of the problem. In the mathematical formulations described above, only the curl equations are applied and the divergence equations (except for the formulations described in 2.1.3-2.1.5) are ignored. Traditionally, spurious modes have been associated with the application of frequency domain finite-element methods to eigenvalue problems. Their occurrence in other schemes has been ignored or assumed to be irrelevant. The dispersive analysis contained in [Lync91] and [Paul91a] demonstrates the relevance of spurious modes to all differential-equation based numerical methods (including finite-difference, finite-element, finite-volume, and tranmission line matrix methods in both the time and frequency domain and for both driven and eigenvalue problems). Lynch and Paulsen conclude that the mathematical formulation is the cause of spurious modes and the subsequent discretization using finite-elements or finite-differences (to be discussed in following sections) is not the original cause. With properly posed boundary conditions, only the vector-wave equation/Helmholtz equation (2.1.3) and modified vector-wave equation (2.1.4) are free of spurious modes. The penalty formulation (2.1.5) was proposed to eliminate spurious modes. The penalty factor p is selected to weight the divergence term in (2.1.5) [Rahm84]. Unfortunately, the selection of p was determined to be problem specific and not a general technique for the elimination of spurious modes [Konr89]. The penalty method and modified vector wave equation are identical for p=1.

The mathematical formulations described above make no assumptions regarding the geometry of the general problem. In this thesis, numerical methods capable of modelling fully three-dimensional problems are investigated without the benefit of simplifying assumptions (such as that applied in [Mitt89a] and [Sumb91]).

A matter of numerical convenience also arises from the selection of the mathematical formulation. Maxwell's equations (2.1) contain both **E** and **H** as unknown distributions. The modified vector wave equation (2.3) contains only **E** (or alternatively only **H**). For certain applications (for instance construction of equivalent sources to calculate far fields, or evaluation of surface currents) knowledge of both field distributions **E** and **H** is desired. To calculate **H** from **E**, (2.1a) can be used (or alternatively (2.1b) to determine **E** from **H**). This requires additional programming and post-processing. Numerical implementation of the additional processing can be implemented such that the same order of accuracy is maintained in both the original field distribution, and the post-processed field distribution. As mentioned above, the formulations (2.1)-(2.6) are expressed in terms of the field distributions. Using suitable

definitions and gauges, it is also possible to express a mathematical formulation in terms of vector and scalar potential functions. This approach is discussed in [Paul92], with the motivation of simplifying the enforcement of boundary conditions at material interfaces.

All of the formulations described above are expressed in the time-domain for consistency and generality. Some of the references cited in sections 2.1.1-2.1.5 make use of these formulations expressed in the frequency-domain.

2.2: Field Formulation / Source Excitation

In our description of a general electromagnetic field problem, a source is present. It is possible to express the formulations discussed in the previous sections without source excitation, and solve for the modes supported by the structure. This class of problem is not explicitly considered in this review although all of the sections of this chapter apply with the exception of the present one.

The essential difference between a scattering and radiation problem is the location and type of source. Modelling of a source for scattering problems is not difficult because the source is distinct from the geometry (for example, a plane wave source incident upon some finite sized object). The difficulty associated with source modelling for radiation or antenna problems is that the source is usually a part of the antenna geometry and cannot be separated from it. The selection of a field formulation affects the possible source models that can be applied and therefore the fidelity of the modelling. Since input impedance characterization is usually dependent on accurate source modelling, this is an important consideration for the characterization of antenna problems. This problem is considered in section 5.1 of chapter 5.

For problems involving linear media, the total field distributions $\mathbf{E},\mathbf{H}$ can be decomposed into two components: the incident field $\mathbf{E}^i,\mathbf{H}^i$ (due to the source in the absence of any inhomogeneities or objects); and the scattered field $\mathbf{E}^s,\mathbf{H}^s$ (caused by the presence of any inhomogeneities or objects), where $\mathbf{E}=\mathbf{E}^i+\mathbf{E}^s$ and $\mathbf{H}=\mathbf{H}^i+\mathbf{H}^s$.

2.2.1: Total Field Formulation

The mathematical formulations described in section 2.1 and the boundary conditions (1.3) are applied directly for the case of modelling the total field $\mathbf{E},\mathbf{H}$. This

approach is typically applied in situations in which the source excitation is modelled in a non-rigourous manner due to its independence with respect to the solution [Hoef85].

2.2.2: Scattered Field Formulation

The mathematical formulations described in section 2.1 and the boundary conditions (1.3) require modification for the modelling of the scattered field distributions E^s, H^s. Consider the following example based on a double-curl equation formulation (*i.e.,* expression (2.2)). The total field distribution E is expressed as $E^s + E^i$, to obtain,

$$- \nabla \times \left(\frac{1}{\mu} \nabla \times \left(E^s + E^i \right) \right) = \sigma \frac{\partial \left(E^s + E^i \right)}{\partial t} + \varepsilon \frac{\partial^2 \left(E^s + E^i \right)}{\partial t^2} \qquad (2.7)$$

The incident field distribution E^i satisfies a homogeneous form of the vector wave equation,

$$- \nabla \times \left(\frac{1}{\mu_i} \nabla \times E^i \right) = \sigma_i \frac{\partial E^i}{\partial t} + \varepsilon_i \frac{\partial^2 E^i}{\partial t^2} \qquad (2.8)$$

where ε_i, μ_i, and σ_i are the permittivity, permeability, and conductivity of the medium in which the incident field exists, respectively. Subtracting (2.8) from (2.7) yields the following scattered field formulation,

$$- \nabla \times \left(\frac{1}{\mu} \nabla \times \left(E^s + E^i \right) \right) + \nabla \times \left(\frac{1}{\mu_i} \nabla \times E^i \right)$$

$$= \sigma \frac{\partial E^s}{\partial t} + \varepsilon \frac{\partial^2 E^s}{\partial t^2} + \left(\sigma - \sigma_i \right) \frac{\partial E^i}{\partial t} + \left(\varepsilon - \varepsilon_i \right) \frac{\partial^2 E^i}{\partial t^2} \qquad (2.9)$$

The boundary conditions (1.3) are also modified to separate the scattered and incident components of the field.

$$\mathbf{n} \cdot \left(\varepsilon_1 \left(E_1^i + E_1^s \right) - \varepsilon_2 \left(E_2^i + E_2^s \right) \right) = 0$$

$$\mathbf{n} \cdot \left(\mu_1 \left(H_1^i + H_1^s \right) - \mu_2 \left(H_2^i + H_2^s \right) \right) = 0$$

(2.10)

$$n \times \left(\left(E_1^i + E_1^s \right) - \left(E_2^i + E_2^s \right) \right) = 0$$

$$n \times \left(\left(H_1^i + H_1^s \right) - \left(H_2^i + H_2^s \right) \right) = 0$$

Examination of the scattered field formulation and the scattered field boundary conditions indicate the manner in which the source is introduced into the computation. The excitation is introduced along interfaces between regions with different material properties, and throughout the regions that possess material properties different from those of the incident medium. The programming requirements and complexity of the resulting code is greater for a scattered field formulation as compared to a total field formulation.

The incident field distribution E^i, H^i is known (either analytically, or calculated and stored from a previous numerical simulation). Examples of scattered field formulations for electromagnetic scattering applications are given in [Shan90], [Moha91] (applied in conjunction with a time-domain finite-volume method) and [D'Ang90] (applied in conjunction with a frequency-domain finite-element method). In Chapter 6, the application of a scattered field formulation in conjunction with a time-domain finite-element algorithm is investigated.

2.2.3: Total / Scattered Field Formulation

The total/scattered field formulation requires the spatial domain of the problem to be separated into total and scattered field regions. With this approach, the total field is modelled in a portion of the simulation space and the scattered field is modelled in the remaining spatial domain of the problem. One possible organization of the spatial domain of the problem is provided in Figure 2.1. This specific case illustrates the application of the total/scattered field formulation for the analysis of electromagnetic scattering problems. Within the separation surface (outlined by dashed lines), the total field exists and exterior to the contour only the scattered field exists. This organization of the computational domain has been applied in conjunction with the Yee time-domain finite-difference algorithm [Mere80], [Tafl89] (for scattering problems), [Wolf92] (for microstrip circuit applications); the transmission line matrix method [Simo91d],

[Simo92] (see Chapters 4 and 5); a frequency-domain finite-element method [Maye91]; and a time-domain finite-element method (see Chapter 6).
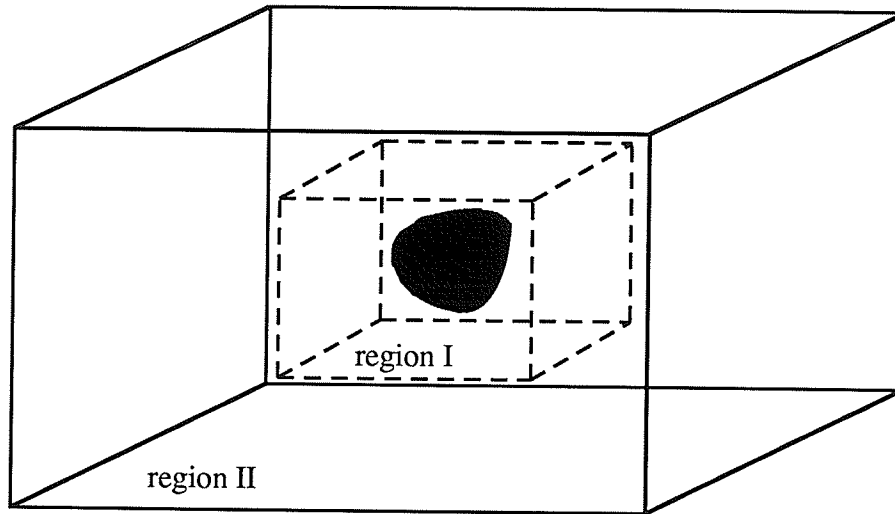
Figure 2.1: Separation of the spatial domain into scattered field and total field regions.

2.3: Absorbing Boundary Conditions

The various mathematical formulations described in section 2.1 require discretization and solution throughout the entire spatial domain of the problem. For open-region problems, the spatial domain corresponds to an infinite region. To solve a problem with a practical amount of computational resources, a boundary condition is required (applied along the outer contour in Figure 2.1) to limit the spatial domain of the problem without causing excessive errors. These special boundary conditions are referred to as absorbing boundary conditions (ABCs). Two types of ABCs are currently used, local and global ABCs. A review of both types for general problems involving wave propagation is presented in [Givo91].

2.3.1: Local ABCs

In their analytic form, local ABCs are inexact. Therefore, in the general case reflections from the outer boundary will always exist. Local ABCs can be classified as physically motivated and mathematically motivated conditions. The physically motivated conditions are realized as layers of absorbing material placed around the exterior surface of the simulation space. These layers are supposed to simulate real absorbing material. The fields are attenuated within the layers (with hopefully a small amount reflection) and after a few layers the fields are completely absorbed. This approach has been applied in conjunction with the Yee finite-difference time-domain algorithm [Rein89], the time-domain two-dimensional transmission line matrix method [Eswa90], and a frequency-domain finite-element method [Jin92a]. These boundary conditions are usually frequency dependent, and therefore not useful with time-domain simulations. In [Jin92a], the boundary conditions are tuned for optimal performance in a specific frequency band, and therefore provided excellent absorption.

Another physically motivated approach terminates the outer boundary of the mesh in the intrinsic impedance of the local medium modelled by the mesh. This method assumes that a plane wave is incident upon the outer boundary and is accurate for waves that strike the boundary with normal incidence. This boundary condition is referred to as a match termination for normal incidence and has been applied with the time-domain transmission line matrix method [Germ90b], (also see Chapter 5); and a frequency domain finite-element method for axi-symmetric geometries [Sumb91].

Mathematically motivated local ABCs can be based on series expansions or one-way wave equations. A review of these methods is given in [Moor88]. An outward propagating wave can be expressed as a convergent expansion in spherical coordinates [Pete88], [Mitt89b],

$$E = \frac{e^{-jkr}}{r} \sum_{n=0}^{\infty} \frac{A_n(\theta,\phi)}{r^n} \tag{2.11}$$

Approximate ABCs are derived by truncating the series to a few terms [Pete88]. These boundary conditions are vector analogues of the scalar ABCs presented in [Bayl80].

The one-way wave equation local ABCs are based on factorization of the wave-equation operator into *one-way* wave equations [Moor88], [Engq77]. In two-dimensions, the wave equation in lossless media expressed in cartesian coordinates is given by,

$$L\,u = 0 \tag{2.12a}$$

where,

$$L = \frac{\partial^2}{\partial x^2} + \frac{\partial^2}{\partial y^2} - \frac{\partial^2}{c\partial t^2} \tag{2.12b}$$

The operator L can be factored as,

$$L = L_x^+ L_x^- \tag{2.13}$$

where

$$L_x^{\pm} = \frac{\partial}{\partial x} \pm \frac{1}{c}\frac{\partial}{\partial t}\left(1 - \left(\frac{\frac{\partial}{\partial y}}{\frac{1}{c}\frac{\partial}{\partial t}}\right)^2\right)^{1/2} \tag{2.14}$$

The operators L_x^+ and L_x^- allow propagation in the +x and -x directions, respectively. Appropriate construction of the analytic operators yield boundary conditions that exactly absorb plane waves propagating at specific angles. Practical implementation requires the finite-difference or finite-element discretization of (2.14), which will be discussed in Chapter 6. The effects of numerical discretization of (2.14) have been investigated by [Rail92]. Numerical investigations of the accuracy of local ABCs can be found in [Blas88] and [D'Ang89].

Mathematically motivated local ABCs are the most popular and have been applied in conjunction with: the Yee time-domain finite-difference method [Moor88], [Rail92]; a frequency-domain finite-difference method for bodies of revolution [Mitt89a], frequency domain finite-element formulations [Pete88], [D'Ang89], [D'Ang90], [Maye91]; time-domain finite-volume methods [Moha91], [Holl91]; and the time-domain transmission line matrix method [Simo91d], [More92]. Local ABCs preserve the sparsity of the

system matrix (an important computational advantage), and their computational implementation is usually straightforward.

2.3.2: Global ABCs

In contrast to the local ABCs, global ABCs are exact in their analytic formulation, and are based on integral representations [McDo72] or modal expansions of the field distributions [Mei74]. The formulations based on integral representations are sometimes referred to as hybrid differential-equation/integral-equation formulations and have been used extensively with frequency-domain and static finite-element formulations [McDo72], [Paul88], [Yuan90], [Yuan91], [Deli91]. In [Ziol83] an integral representation is applied in conjunction with the Yee finite-difference time-domain algorithm. As well, in [Bark92], an integral representation is applied in conjunction with a time-domain finite-element method. A numerically derived global ABC has been applied in conjunction with the transmission line matrix method and is referred to as the Johns' matrix approach [Eswa90]. A computational disadvantage of global ABCs is that they create full submatrices within the sparse system matrix created from the discretization of the differential-equation. The creation of full-submatricies may substantially increase the computational effort required for a solution.

2.4: Type of Spatial Grid

Three types of spatial grids can be applied in the discretization of the mathematical formulations - regular structured, irregular structured, and unstructured. To illustrate the differences between these approaches, portions of two-dimensional meshes (of quadrilateral cells) near a curved boundary are provided in Figure 2.2.

The regular structured mesh does not provide a good representation of the curved surface. Numerical schemes utilizing this grid may yield errors due to the stair-stepped approximation. Numerical investigations of errors due to stair-stepped approximations in time-domain finite-difference simulations (using the Yee algorithm [Yee66]) have been performed [Cang91]. A benefit of this approach to meshing is that all mesh locations are

explicitly known, without the requirement of storing the spatial coordinates of each grid point along with connectivity information.

The irregular structured mesh provides an accurate description of a curved surface. If the geometry of the objects under investigation can be described parametrically, a mesh can be generated and described using parametric equations. This approach is able to provide accurate description of curved surfaces without explicit storage of all mesh locations. The spatial location of a mesh point is known implicitly by evaluation of a parametric function. Unfortunately, this approach can only be applied to geometries that are described parametrically. A simplified subset of the irregular structured meshing methods is the graded mesh discretization. This approach has been applied for the analysis of regular geometries with a few instances of fine geometrical detail. Examples of this approach for the analysis of microstrip circuits and antennas can be found in [Paul91b], [Cham93], [Rile93]. For this application, the thickness of the substrate can be small compared to the other dimensions of the geometry. A graded mesh scheme allows for the accurate discretization of all of the geometrical features of the model.

The unstructured mesh provides the most general approach to the discretization of arbitrary geometries. A disadvantage of this approach is that all information regarding the spatial location of grid points and their connectivity must be explicitly stored. The use of the irregular structured and unstructured mesh types imply the use of a code capable of handling such a mesh, and unfortunately not all the algorithms proposed in the computational electromagnetics literature possess this capability.

2.5: Mathematical Discretization - Spatial Domain

2.5.1: Finite-Element

Two approaches to the application of the finite-element method to electromagnetic field problems are possible. The two approaches are: the formulation of a variational principle and its discretization by the Rayleigh-Ritz method [Arle69], [Rahm84], [Davi89]; and the direct approximation of the differential-equation formulation by the method of weighted residuals [D'Ang89], [Sumb91], [Boys92]. The

second method, direct application of the method of weighted residuals, is considered to be the most general [Conn76], [Zien88]. This second approach is applied in Chapter 6.

The problems considered in this document are three-dimensional and the unknown distributions are vectors. For this type of problem two general classes of finite-elements can be applied. These are nodal-elements (scalar basis functions) and edge-elements (vector basis functions). The differences between the two element types are discussed for the case of three-dimensional tetrahedral elements.

2.5.1.1: Nodal-Elements - Scalar Bases

Consider the discretization of space using the tetrahedral nodal-element provided in Figure 2.3(a). Over each element the unknown field distribution can be represented as [Char81], [Zien88],

$$E(x,y,z) = \sum_{k=1}^{4} E_k \zeta_k \qquad (2.15)$$

where $\zeta_k = (a_k + b_k x + c_k y + d_k z)/6V$, V is the volume of the element, and

$$a_1 = \det \begin{bmatrix} x_2 & y_2 & z_2 \\ x_3 & y_3 & z_3 \\ x_4 & y_4 & z_4 \end{bmatrix} \qquad (2.16a)$$

$$b_1 = \det \begin{bmatrix} 1 & y_2 & z_2 \\ 1 & y_3 & z_3 \\ 1 & y_4 & z_4 \end{bmatrix} \qquad (2.16b)$$

$$c_1 = \det \begin{bmatrix} x_2 & 1 & z_2 \\ x_3 & 1 & z_3 \\ x_4 & 1 & z_4 \end{bmatrix} \qquad (2.16c)$$

$$d_1 = \det \begin{bmatrix} x_2 & y_2 & 1 \\ x_3 & y_3 & 1 \\ x_4 & y_4 & 1 \end{bmatrix} \qquad (2.16d)$$

and the remaining a_k, b_k, c_k and d_k are generated by revolving the above expressions.

Regular Structured Mesh:
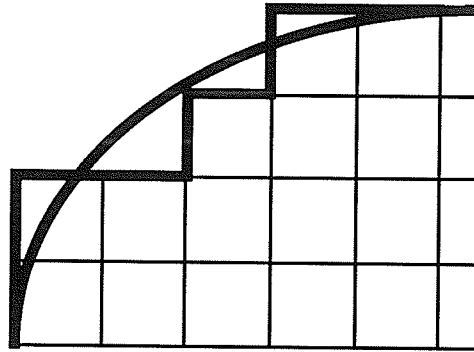
Irregular Structured Mesh:
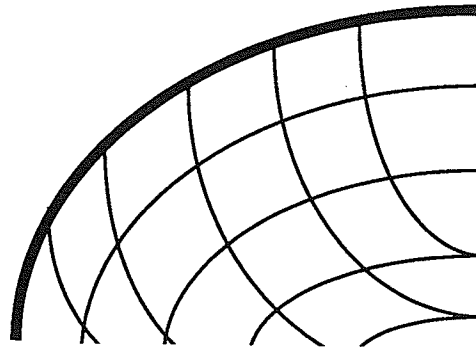
Unstructured Mesh:
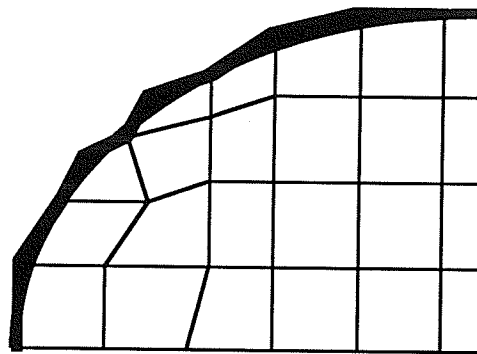
Figure 2.2: Three types of grid structures in the presence of a curved boundary: (a) regular structured, (b) irregular structured, and (c) unstructured.

The expansion functions z_k in (2.15) are scalar functions and the unknown nodal values E_k are vector quantities. All field components are continuous between inter-element boundaries (unless otherwise specified).

2.5.1.2: Edge-Elements - Vector Bases

Consider the discretization of space using the tetrahedral edge-element provided in Figure 2.3(b). Edge element were originally proposed as a cure for the problem of spurious modes. Over each element the unknown field distribution can be represented as a summation over the edges of the element [Mur85], [D'Ang90],

$$E(x,y,z) = \sum_{n=1}^{4} \sum_{m=1}^{4} E_{nm} w_{nm} \qquad (n \neq m) \qquad (2.17)$$
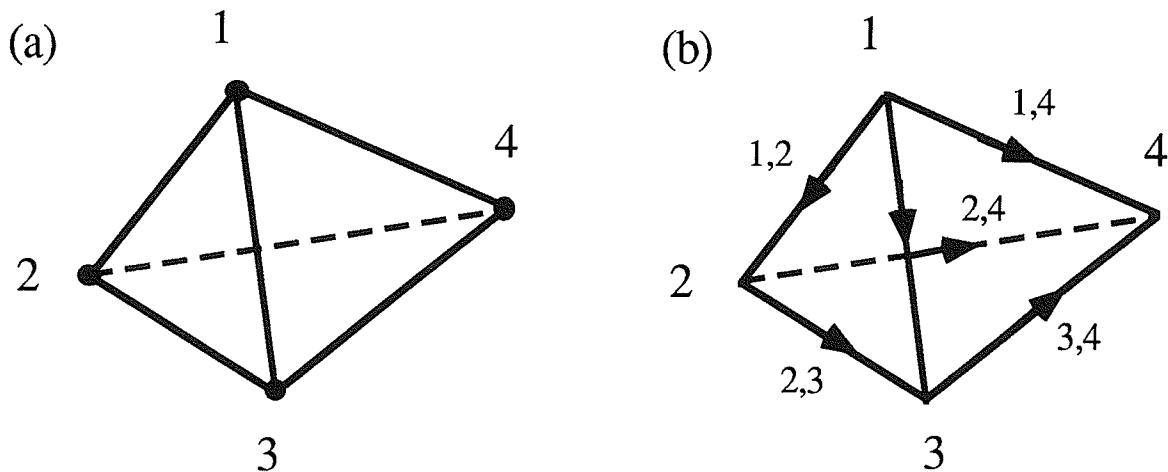
Figure 2.3: (a) Tetrahedral nodal-based finite-element, and (b) Tetrahedral edge-based finite-element.

The expansion functions w_{nm} in (2.17) are vector functions and the unknown coefficients E_{nm} are scalar quantities. The nm subscript refers to the edge connecting nodes n and m. The vector expansion functions w_{nm} are defined in terms of the scalar expansion functions ζ_k (see above) as,

$$w_{nm} = \zeta_n \nabla \zeta_m + \zeta_m \nabla \zeta_n \tag{2.18}$$

Edges are shared by adjacent elements, and therefore tangential field components are continuous across the interface between elements. If the interface between elements is a material interface, no constraints are imposed on the normal components of the fields.

2.5.1.3: Comparisons of Nodal and Edge Elements ~ Curious Contradictions ?

Various comparisons of nodal- and edge-element methods have recently appeared in the literature [Mur88], [Yuan91]. Although some of the results of these comparisons are consistent, some curious contradictions also arise. Both [Mur88] and [Yuan91] conclude that edge-elements require increased computational effort. This is due to the increase in the number of degrees of freedom. The use of edge-elements has increased the number of degrees of freedom for the tetrahedral element from 4 to 6. Boyse *et. al.* (proponents of the nodal element approach) make note of an important practical benefit of nodal elements. Most commercial mesh generation packages produce nodal based elements (because of their dominance in other disciplines) and as well, higher-order edge-elements have yet to be developed. Higher-order node elements exist and are common in some applications of computational electromagnetics (as discussed in Chapter 4, the application of higher-order approximations in conjunction with time-domain formulations is uncommon).

The most important aspect of the nodal/edge debate is the relative accuracy. Consider a comparison of the two approaches for the enforcement of interface conditions between material regions. In [Yuan91], a computational study indicates that nodal elements with the boundary conditions (1.3) (for the normal field components) explicitly enforced are more accurate than similar computations with edge elements. Mur (in [Mur88]) seems to have obtained the opposite conclusion. An important contradiction exists. Mur concludes that nodal-based elements are not appropriate for modelling inhomogeneous media because the nodal-based elements enforce continuity of all field components across an interface (*i.e.,* normal and tangential). Mur does not account for the explicit enforcement of the boundary conditions, as is the case in [Yuan91], [Lync90], and Chapter 6. Mur's conclusion regarding the use of nodal-based elements does not contradict that of Yuan *et al* if all boundary conditions at an interface are explicitly enforced.

It is possible to blend the edge and nodal element types and construct new computational cells. One possible combination is to specify only tangential components along the element boundary and all components at the centre of an element. This spatial organization of unknown field components would resemble Shankar's finite-volume method [Shan90], [Moha91] and the symmetric condensed transmission line matrix method [John87b]. The organization of field components within various computational cells is discussed in section 2.6.

2.5.2: Finite-Difference

The finite-difference approach to spatial discretization consists of discretization of the operator (and not the unknown distribution as in the finite-element method). As a simple example, consider the application of the second-order-accurate central-difference approximation to the Laplace operator,

$$\nabla^2 F(x,y) = \frac{\partial^2 F(x,y)}{\partial x^2} + \frac{\partial^2 F(x,y)}{\partial y^2} \qquad (2.19)$$

to yield

$$\nabla^2 F(x,y) = \frac{F(x+\Delta x,y) - 2F(x,y) + F(x-\Delta x,y)}{\Delta x^2}$$

$$+ \frac{F(x,y+\Delta y) - 2F(x,y) + F(x,y-\Delta y)}{\Delta x^2} \qquad (2.20)$$

The mesh of Figure 2.4 is used to implement the above spatial approximation of the Laplace operator.

A survey of the computational electromagnetics literature indicates that the use of the Yee algorithm has dominated applications of the finite-difference method to computational electromagnetics, despite the overwhelming variability of finite-difference schemes that can be developed [Lapi82]. A review of some of the references collected in the course of this research indicates that of the many journal and conference papers reviewed that involve the application of finite-differences to the numerical solution of

electromagnetic field problems, the majority involve the Yee algorithm. Notable exceptions include the review given in [LoVe91] where various classical finite-difference schemes are presented and compared for one-dimensional problems, and the dispersive analysis contained in [Shla93] in which the computational performance of several finite-difference algorithms are compared.
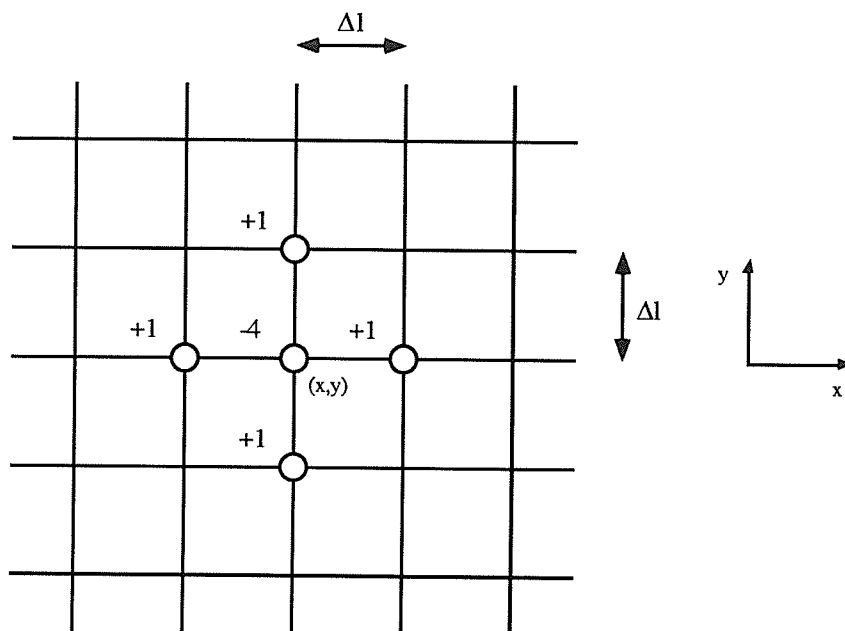
Figure 2.4: Simple example illustrating the discretization of the Laplace operator using second-order-accurate central-difference approximations.

The extension of the Yee finite-difference time-domain algorithm to handle unstructured meshes, as well as finite-volume algorithms, have been recently proposed [Mads90], [Holl91], [Lee92], [Jurg92]. As will be discussed in Chapter 6 (based on an equivalence of specific finite-difference and finite-element algorithms), these algorithms may be more conveniently derived and represented using finite-element concepts.

2.5.3: Characteristic-Based Field Decomposition (Transmission Line Matrix)

In addition to the finite-difference and finite-element approximation to the spatial-domain, the transmission line matrix method can also be applied [Hoef85], [Hoef89]. This method will be examined in detail in Chapters 3, 4 and 5. The derivation of the original two- and three-dimensional symmetric-condensed transmission line matrix algorithms by a characteristic-based field decomposition is described in [LoVe92] and [LoVe93]. The derivation of the two-dimensional algorithm is outlined in Appendix A. Traditionally, the transmission line matrix method has been considered as a physical approximation in that the spatial domain was approximated by an orthogonal grid of transmission lines [John71]. The theory presented in [LoVe92], [LoVe93] indicates the transmission line matrix approach fits within the framework described within this chapter *i.e.,* discretization of a given mathematical formulation.

2.6: Organization of Spatial Cell

In the previous section, various methods for discretization of the spatial domain were presented. For all methods, the volume of space is discretized into unit cells. In this section the manner in which field components are defined within the unit cells is discussed. The organization of the spatial cell is closely related to the method of spatial discretization. In general, it is not possible to use an arbitrary spatial cell organization with every spatial discretization technique described above. The various spatial cells that have appeared are classified in terms of two parameters: symmetry and condensation. A symmetric cell appears the same (in terms of the vector components of the fields) from each coordinate axis. A condensed cell has all field components defined at the same spatial locations. An uncondensed cell does not have any field components defined at the same spatial location, and a partially condensed cell has some field components defined at the same spatial locations. Examples of spatial discretizations are presented in Figure 2.5.

The condensation of the unit cell is relevant to the modelling of interfaces between material regions. The uncondensed cells (such as that applied with the Yee algorithm [Yee66], [Tafl89]) are unable to exactly align interfaces between dielectric and magnetic materials. As well, the boundary conditions (1.3) indicate that tangential field components are continuous and normal field components are discontinuous across

material interfaces. The continuous tangential boundary conditions are trivially satisfied. Depending on the specific layout of the spatial cell, satisfaction of the discontinuous normal boundary conditions may require additional computational effort.

2.7: Time or Frequency Domain ?

Based on the spatially discrete or semi-discrete form of the mathematical formulations, selection of the time or frequency domain for the solution is required. Solutions to the time dependent formulations described above yield transient solutions for a given excitation. For a time harmonic excitation (a single frequency, ω), the time dependence of all field quantities can be assumed *i.e.,*

$$G(r,t) = G(r)e^{j\omega t}$$

Solution of the resulting equations yields results for a single frequency for each simulation.

The choice of time or frequency domain solution depends on the specific application. For most antenna applications and radar-cross-section analysis, frequency domain results are desired. For certain EMI/EMC problems, the transient response may be required. Although time and frequency domain formulations are suited to calculation in their natural domains, numerical results in one domain can be Fourier transformed to the other. For example, a single time domain simulation (with the appropriate excitation) can be used to obtain frequency domain results over a wide bandwidth by Fourier transformation of the transient response. Therefore, if the bandwidth of interest is sufficiently wide, or if a time domain solution is desired, a time domain method is advantageous. A detailed quantitative assessment of this advantage can be found in [Mill88] and [Lync90].
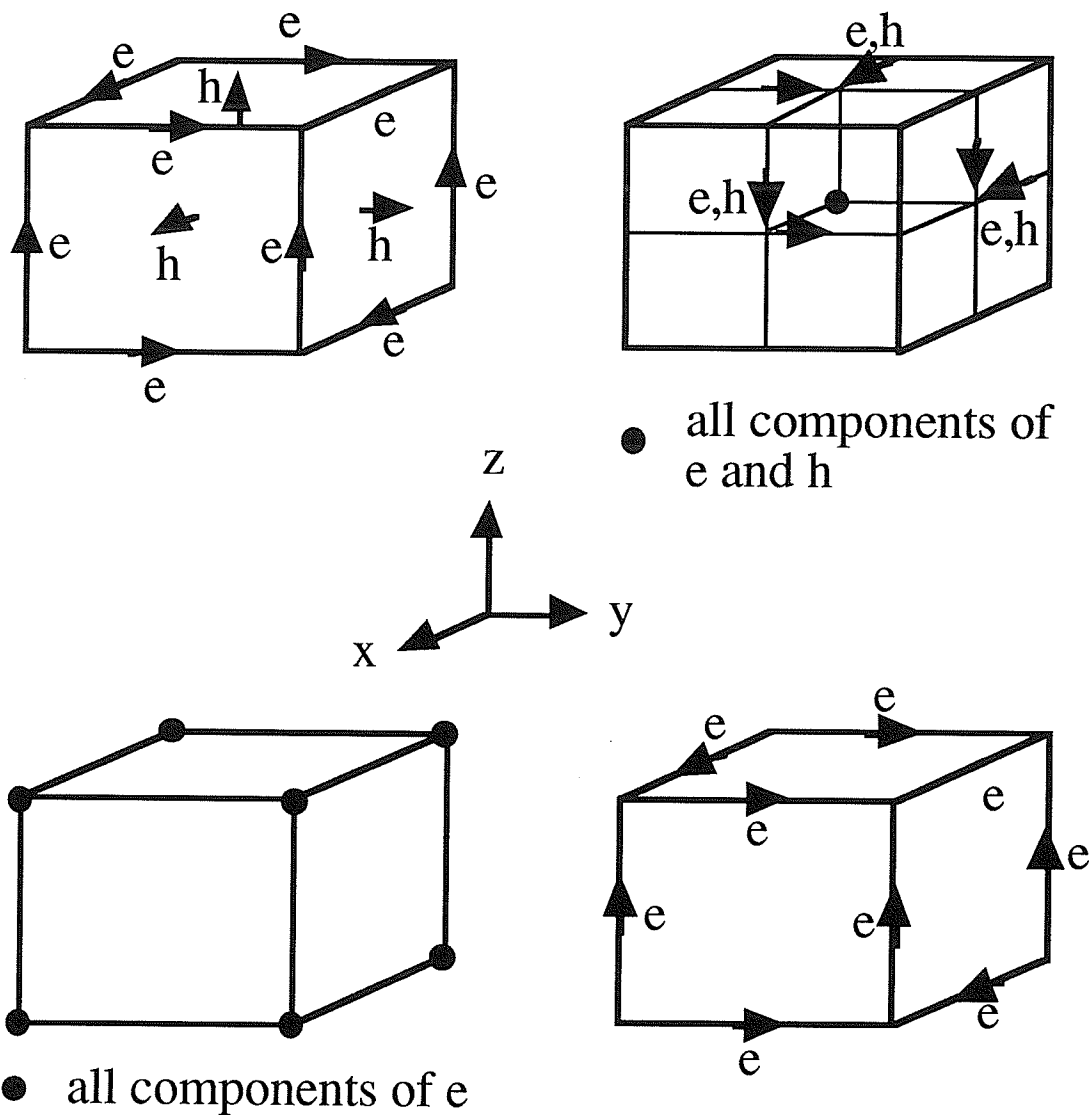
Figure 2.5: Spatial cells for various differential-equation based methods: (a) Yee finite-difference algorithm [Yee66], and the expanded node transmission line matrix model [Akht75b] (unsymmetric, uncondensed), (b) transmission line matrix algorithm [John87b] and Shankar finite-volume algorithm [Shan90] (symmetric, partially condensed), (c) nodal-based finite-element method (symmetric, condensed), (d) edge-element finite-element methods (symmetric, partially condensed).

In general, the nature of the material parameters (ε, μ, and σ) also influences the selection of the solution domain. In this document only linear materials are considered,

however, the time domain is preferred for problems that include non-linear materials [Goor92]. The frequency domain is preferred for problems with frequency dependent materials. The treatment of dispersive materials is of trivial complexity for frequency domain modelling. Investigations of modelling of linear dispersive materials in the time-domain using the Yee finite-difference time-domain algorithm are provided in [Kunz93], [Petr94].

All of the spatial discretization techniques described above are applicable to time or frequency domain analysis. The transmission line matrix method is typically formulated and applied in the time domain, although a frequency domain version has been proposed [Jin92b]. The finite-difference method is usually applied in the time-domain [Tafl89], and the finite-element method has been usually applied in conjunction with frequency domain analysis, although time domain versions have been given in [Cang87], [Lync90], [Bark92].

Discretization of the temporal domain is usually performed using finite-differences. In [Lync90] and [Bark92] finite-element spatial discretizations are applied in conjunction with finite-difference temporal discretization. The Yee algorithm applied central difference approximations in both space and time. Finite-element discretization of the time domain has been investigated in other disciplines [Pind77], [Zien83]. Application of these schemes to electromagnetics has yet to be considered.

The resulting system after discretization results in either an implicit or explicitly time stepped algorithm. An explicit time stepping scheme does not require matrix inversion, and is therefore computationally easier to implement. Some aspects of obtaining explicit time-stepping algorithms is discussed in Chapter 6. General discretization of the time-domain using finite-differences is discussed in [Bark92] and [Lee94].

2.8: Sources of Error

Two sources for error exist in the application of differential-equation based methods. The first source of error is due to the inability of the discrete algorithm to model wave propagation exactly. Discrete approximations to the various differential-equation formulations do not propagate waves ideally. The errors can be dispersive (waves at different frequencies travel at different velocities, therefore time-domain waveforms change shape as they propagate) or dissipative (waves are attenuated as they

propagate) [Tref82]. Most of the numerical schemes applied in computational electromagnetics are conservative *i.e.,* they do not dissipate energy and therefore waves do not attenuate as they propagate. However, all schemes are dispersive. A characteristic equation can be derived from the propagation model that governs wave propagation in the method, called a dispersion relation. A general discussion of dispersion relations for finite-difference and finite-element models of the wave equation can be found in [Tref82], [Vich82] and [Mull82]. Dispersive errors are also referred to as velocity error [Hoef85]. As an example, in Figure 2.6, the velocity error for the two-dimensional Yee algorithm (operated at the upper limit of stability) is presented for plane wave propagation through the numerical mesh. The velocity error is presented in the Figure as the ratio of c^*/c (where c^* is the numerical propagation velocity and c is the physical free-space propagation velocity) versus the direction of propagation for three different discretization ratios, $\Delta l/\lambda=0.1$, $\Delta l/\lambda=0.2$ and $\Delta l/\lambda=0.3$. As indicated in the figure, the velocity error increases with a reduction in discretization (*i.e.,* less Δl per wavelength, λ). As well, the anisotropy of the algorithm is also evident which also increases as the discretization is reduced. The curves are rotationally symmetric for 90° rotations due to the symmetry of the numerical mesh. Figure 2.6 also indicates that for the Yee finite-difference time-domain algorithm, the ratio of c^*/c is always less than one, and therefore the numerical mesh represents a medium in which the propagation velocity is slower than that of free space. A typical guideline for the discretization ratio applied in conjunction with the Yee finite-difference algorithm is $\Delta l/\lambda \leq 1/15$ [Tafl89]. Dispersive errors cause errors in the phase of the waves propagating through the numerical mesh. Therefore, these phase errors will accumulate with the spatial distance covered. If electrically large problems are investigated, increased discretization may be required. Higher-order-accurate numerical approximations (fourth-order-accurate finite-difference approximations and quadratic finite-elements) can be used to decrease numerical dispersion. A fourth-order accurate transmission line matrix model for the analysis of the two-dimensional wave equation is presented in Chapter 4. Investigation of dispersive errors and numerical anisotropy for two-dimensional models is considered in detail in Chapter 4.

The second source for error in the application of differential-equation based numerical methods is associated with the boundary conditions for a problem. These boundary condition errors can be separated into two unique errors. The first boundary condition error occurs only with open region problems and is due to the inexactness of the absorbing boundary conditions (for the case of local ABCs). A sufficiently large

simulation space can be modelled such that errors due to local ABCs are minimal. In addition to errors caused by inexact ABCs, if objects with sharp edges and corners are present, errors due to the inability of the method to resolve rapidly varying field distributions will also occur. Coupling of the mathematical formulation to specific formulations describing the behavior of the field distribution in the presence of geometrical details was discussed in section 2.1.7.
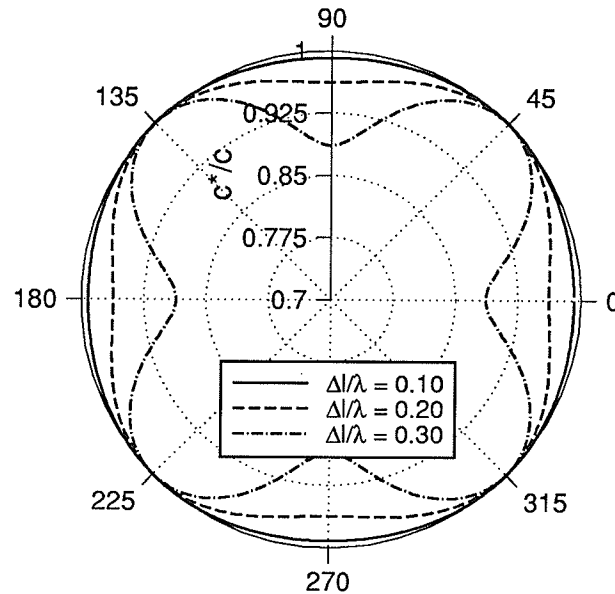
Figure 2.6: Velocity error (c*/c) for axial propagation within the two-dimensional Yee algorithm.

2.9: Classification of Various Differential Equation Based Methods

A few of the popular differential-equation based numerical methods are classified in Table 2.1. The methods classified are: the Yee finite-difference time-domain algorithm [Yee66] (as presented in [Tafl89]; the symmetric-condensed transmission line matrix algorithm (as applied in [Alle87]); Shankar's time-domain finite-volume method [Shan89], [Shan90], [Moha91]; the time-domain finite-element algorithm originally presented by Lynch and Paulsen [Lync90]; and the control region approximation [McCa89].

Table 2.1: Classification of Various Differential-Equation Based Numerical Methods

Algorithm	Math. Formulation	Field Formulation
Yee algorithm	Maxwell's Curl Eq	Total/Scattered
Symmetric condensed TLM	Conser Form Maxwell Eq	Total
Shankar Finite-Volume	Conser Form Maxwell Eq	Scattered
Lynch and Paulsen FE	Modified Vector-Wave Eq	Total
Control Region Approx.	Maxwell's Curl Eq	Total

Algorithm	Type of ABC	Grid Structure
Yee ...	Local	Structured
TLM ...	Local	Structured
Shankar FV ...	Local	Unstructured
Lynch/Paulsen ...	Global	Unstructured
Control ...	Local	Unstructured

Algorithm	Spatial Discretization	Spatial Cell	Time or Frequency ?
Yee ...	central finite-difference	Uncondensed	Time Domain fd
TLM ...	char decomposition	partial condensed	Time Domain char decomp
Shankar FV ...	fd / charac decomposition	partial condensed	Time Domain various fd
Lynch/Paulsen...	finite element Co cont.	Condensed	Time Domain fd
Control ...	generalized finite-difference	Uncondensed	Frequency Domain

2.10: Conclusions of the Review

A review of the differential equation based numerical methods, applied to computational electromagnetics, has been given. This review serves two purposes. The first purpose is to provide a literature review of the differential-equation based numerical methods, and therefore place the chapters which follow in the proper context. The second purpose is to provide a concise interpretation of the various methods that have been previously investigated. This allows comparison of different methods and a basic conceptualization of the differential-equation based methods. This review illustrates that

all of the differential-equation based numerical methods can be cast into a single unifying framework as specified by the seven categories listed on page 9.

2.11: Formulations Presented in this Thesis

Two different time-domain differential-equation based numerical methods are investigated in the remainder of this document. Recall that the purpose of this thesis is to investigate general purpose techniques for the simulation of electromagnetic phenomena. The selection of a time-domain method is based on the possible computational advantages discussed in section 2.7. In addition, applications may arise in which non-linear materials must be accounted for in the analysis. This class of problem will require time-domain analysis.

The first method is based on the symmetric condensed transmission line matrix algorithm (described in Chapter 3). A total/scattered field formulation is applied with a local absorbing boundary condition. The transmission line matrix algorithm is restricted to a regular structured grid. Stair-stepped approximations to curved surfaces are required. In Chapter 5, this algorithm is applied to the analysis of a wide variety of electromagnetic field problems to demonstrate the range of applicability of differential-equation based numerical methods and the accuracy that can be achieved.

The second method is based on the time-domain finite-element formulation originally presented by Lynch and Paulsen [Lync90] (described in chapter 6). Scattered field and total/scattered field formulations are investigated. Local absorbing boundary conditions are used to terminate the numerical mesh. The finite-element simulation program is viewed as a more advanced solution to the general purpose electromagnetic simulation environment, because of its ability to model irregular shaped objects and the ease with which higher-order elements can be applied. To fully exploit the capabilities of the finite-element simulation program, it should be interfaced to a mesh generation program.

Chapter 3: Transmission-Line Matrix Simulation Program

In this chapter an overview of the TLM method is provided. The development of new TLM models for two-dimensional electromagnetic field problems is presented in Chapter 4, and in Chapter 5 the application of a general purpose electromagnetic simulation program to various practical problems is considered. To place these topics in the proper context, a review of the TLM method is provided in this chapter. This review is not all encompassing (see [Hoef85], [Hoef89] for more complete reviews of the TLM method), however it highlights some of the unique properties and views of the TLM approach which have been discovered throughout the course of this research.

3.1: Description of TLM Algorithm

The macroscopic wave propagation characteristics of TLM algorithms are evaluated via propagation analysis. Propagation analysis is equivalent to the dispersion analysis used for the characterization of finite-difference and finite-element methods [Vich82], [Mull82]. Two methods exist for the evaluation of propagation characteristics. The first method presented by Brewitt-Taylor and Johns applies a physical approach [Brew80], where the models were analyzed as transmission-line circuits. The three-dimensional symmetric-condensed TLM model does not represent a true physical interconnection of transmission-lines and therefore, the propagation analysis typically employed in [Brew80] is not generally applicable. To overcome this difficulty, Nielson and Hoefer have developed a second method for propagation analysis that requires only the scattering and transfer events, and does not require a physical circuit representation of the TLM model [Niel91]. The disadvantage of this approach is that the determinant of an N by N matrix is required, where N is the number of branches for the node being

analyzed. For the original node (N=4) this is not a problem, but for some three-dimensional nodes N is large (N=12 for the symmetric-condensed TLM model). Evaluation of the determinant requires the use of a symbolic manipulation program such as *Maple* or *Mathematica*.

For simplicity, most of the discussions contained in this chapter involve the original two-dimensional TLM shunt node [John71]. However, all of the concepts are equally applicable to three-dimensional models. The two-dimensional model is capable of providing an approximate solution to two-dimensional electromagnetic systems (assuming independence with respect to the z coordinate), one of the independent sets of equations is expressed as,

$$\frac{\partial E_z}{\partial x} = \mu \frac{\partial H_y}{\partial t} \tag{3.1a}$$

$$\frac{\partial E_z}{\partial y} = -\mu \frac{\partial H_x}{\partial t} \tag{3.1b}$$

$$\frac{\partial H_y}{\partial x} - \frac{\partial H_x}{\partial y} = \varepsilon \frac{\partial E_z}{\partial t} \tag{3.1c}$$

The TLM method discretizes space with a uniform grid of interconnected transmission-lines (of characteristic impedance Z_1). The algorithm follows the evolution of voltage pulses on the transmission-line grid. The field components are determined as a post-processing task and is considered to be independent from the operation of the algorithm. The operation of the algorithm for a neighborhood of nodes (considered to be part of a larger mesh) for a few time steps is shown in Figure 3.1. The spatial locations of the four nodes shown in Figure 3.1 are:

node	1	(x_0, y_0)
node	2	$(x_0 + \Delta l, y_0)$
node	3	$(x_0, y_0 - \Delta l)$
node	4	$(x_0 + \Delta l, y_0 - \Delta l)$

The algorithm can be described in terms of scattering and transfer events. For the original two-dimensional shunt node [John71], the scattering event is given by,

$$
\begin{bmatrix} v_1^r \\ v_2^r \\ v_3^r \\ v_4^r \end{bmatrix}^t = \frac{1}{2} \begin{bmatrix} 1 & 1 & 1 & 1 \\ 1 & -1 & 1 & 1 \\ 1 & 1 & -1 & 1 \\ 1 & 1 & 1 & -1 \end{bmatrix} \begin{bmatrix} v_1^i \\ v_2^i \\ v_3^i \\ v_4^i \end{bmatrix}^t
\tag{3.2a}
$$

and the transfer event is,

$$
v_1^{i,t+1}(i,j) = v_3^{r,t}(i,j\text{-}1)
$$

$$
v_2^{i,t+1}(i,j) = v_4^{r,t}(i\text{-}1,j)
$$

$$
\tag{3.2b}
$$

$$
v_3^{i,t+1}(i,j) = v_1^{r,t}(i,j\text{+}1)
$$

$$
v_4^{i,t+1}(i,j) = v_2^{r,t}(i\text{+}1,j)
$$

where the i and r superscripts denote incident and reflected voltage pulses, respectively; the t superscript corresponds to the discrete time step; and the n subscript refers to the branch number (provided in Figure 3.1). Operations (3.2a) and (3.2b) are performed at every node within the mesh.

At time $(t\text{-}\Delta t/2)^+$ (Figure 3.1(a)) the voltage pulses are incident upon the branches. Note $(t)^+$ and $(t)^-$ denote times just prior to and after a time t, respectively. The voltage pulses propagate with velocity $v_l = \Delta l/\Delta t$, and therefore reach the centre of the nodes at time t. The state of the mesh at time $(t)^-$ is shown in Figure 3.1(b). The transformation from time $(t)^-$ to $(t)^+$ is accomplished through application of the scattering event (3.2a). The incident voltage pulses at time $(t)^-$ are scattered from the transmission-line junction at the centre of the node and become reflected pulses at time $(t)^+$. The state of the mesh at time $(t)^+$ is shown in Figure 3.1(c). The voltage pulses reach the midpoints between nodes at time $t+\Delta t/2$. The transformation from time $(t+\Delta t/2)^-$ to time $(t+\Delta t/2)^+$ is accomplished through application of the transfer event (3.2b). The reflected voltage pulses at time $(t+\Delta t/2)^-$ are transferred to adjacent nodes and become incident voltage pulses at time $(t+\Delta t/2)^+$. The state of the mesh at times $(t+\Delta t/2)^-$ and $(t+\Delta t/2)^+$ is shown in Figures 3.1(d) and (e), respectively.

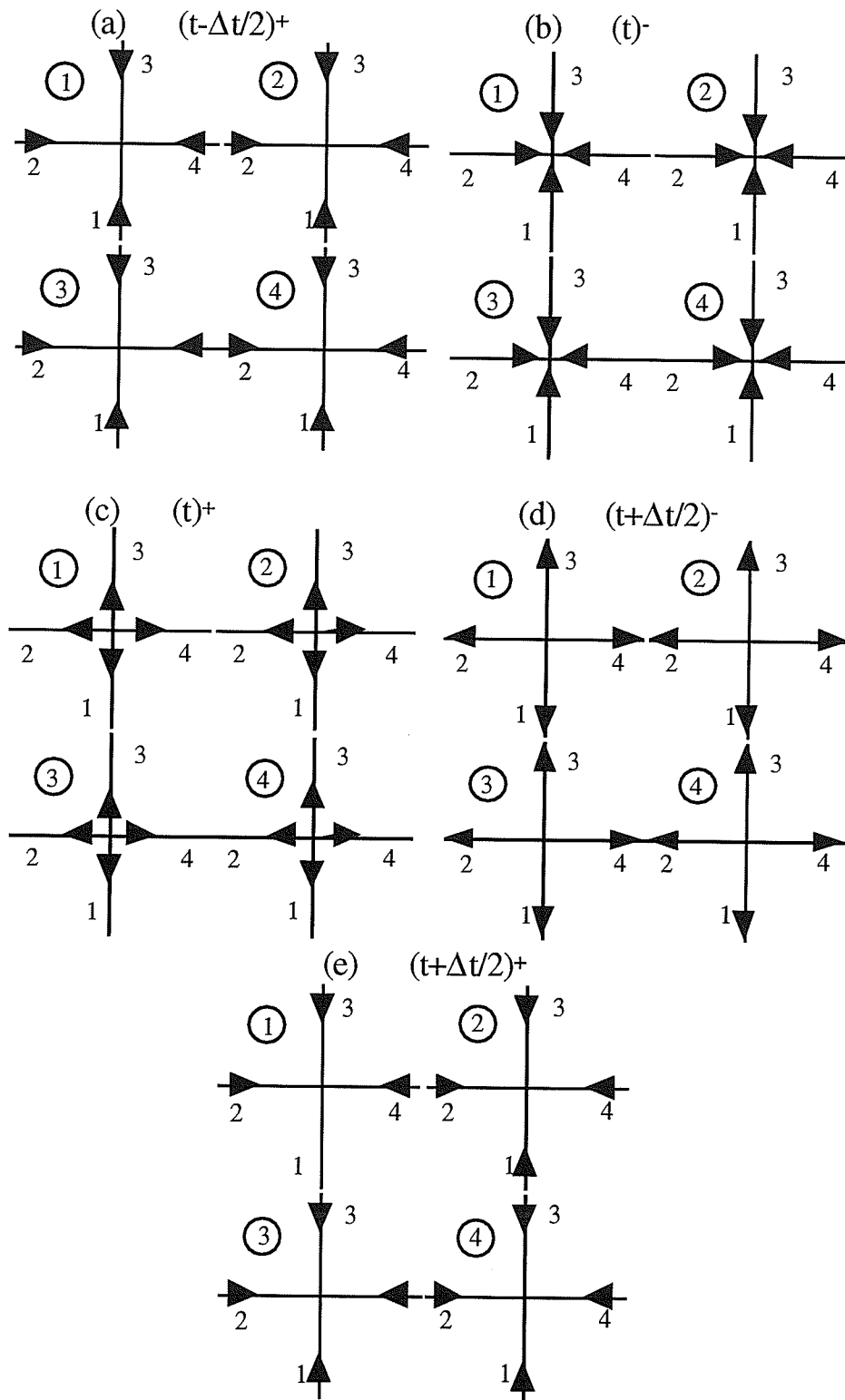**Figure 3.1:** Operation of the two-dimensional TLM algorithm [John71].

3.2: Modelling Material Regions and Boundary Conditions

The TLM method is considered as a differential-equation based numerical method (and is included in the overview presented in Chapter 2). The scattering matrix and transfer event represent an approximate model for Maxwell's equations, in an analogous way the finite-difference approximation of section 2.5 represents an approximate model for Maxwell's equations. The TLM model discussed above has the same dispersion relation as the two-dimensional Yee time-domain finite-difference algorithm [Yee66], if the Yee algorithm is operated at the upper limit of its stability range [Simo91a]. To apply any of the differential-equation based numerical methods to a specific problem, initial and boundary conditions must be specified. In this section the techniques applied in conjunction with TLM simulations of material regions and boundary conditions are reviewed.

3.2.1: Material Regions

An important requirement for the application of the TLM method to general electromagnetic field problems is the modelling of the material itself, and the satisfaction of the boundary conditions on the field distributions along the interfaces between material regions.

To model a medium of arbitrary material properties, transmission-line stubs are added to the homogeneous model [Akht75a]. In Figure 3.2, permittivity and conductivity stubs are added to the original rectangular model. The permittivity stub is an open-circuit terminated transmission-line of characteristic admittance Y_0 and length $\Delta l/2$. In terms of the operation of the algorithm, the scattering and transfer events are modified as,

$$
\begin{bmatrix} v_1^r \\ v_2^r \\ v_3^r \\ v_4^r \\ v_5^r \end{bmatrix}^{t^t} = \left\{ \frac{1}{Y} \begin{bmatrix} 1 & 1 & 1 & 1 & Y_0 \\ 1 & 1 & 1 & 1 & Y_0 \\ 1 & 1 & 1 & 1 & Y_0 \\ 1 & 1 & 1 & 1 & Y_0 \\ 1 & 1 & 1 & 1 & Y_0 \end{bmatrix} - I \right\} \begin{bmatrix} v_1^i \\ v_2^i \\ v_3^i \\ v_4^i \\ v_5^i \end{bmatrix}^{t}
\tag{3.3a}
$$

where Y=4+Y$_0$ and **I** is the unit matrix. The transfer event is,

$$v_1^{i,t+1}(i,j) = v_3^{r,t}(i,j-1)$$

$$v_2^{i,t+1}(i,j) = v_4^{r,t}(i-1,j)$$

$$v_3^{i,t+1}(i,j) = v_1^{r,t}(i,j+1) \qquad\qquad (3.3b)$$

$$v_4^{i,t+1}(i,j) = v_2^{r,t}(i+1,j)$$

$$v_5^{i,t+1}(i,j) = v_5^{r,t}(i,j)$$

At each time step, a portion of the energy incident upon the node is transmitted into the permittivity stub in the form of a transmitted voltage pulse. At the following time step, this transmitted voltage pulse is returned with the same polarity (open circuit termination). The permittivity stub has the effect of reducing the macroscopic wave propagation velocity.
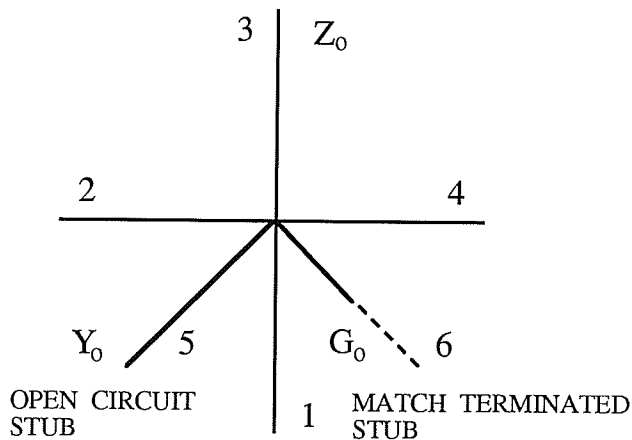

Figure 3.2: Addition of a permittivity stub and a conductivity stub to the original two-dimensional model [Akht75a].

The conductivity stub is a match terminated transmission-line of characteristic admittance G$_0$ (the length is arbitrary since it is match terminated). In terms of the operation of the algorithm, the scattering event is modified as,

$$
\begin{bmatrix} v_1^r \\ v_2^r \\ v_3^r \\ v_4^r \\ v_5^r \end{bmatrix}^{t^t} = \left[\frac{1}{Y} \begin{bmatrix} 1 & 1 & 1 & 1 & Y_o \\ 1 & 1 & 1 & 1 & Y_o \\ 1 & 1 & 1 & 1 & Y_o \\ 1 & 1 & 1 & 1 & Y_o \\ 1 & 1 & 1 & 1 & Y_o \end{bmatrix} - I \right] \begin{bmatrix} v_1^i \\ v_2^i \\ v_3^i \\ v_4^i \\ v_5^i \end{bmatrix}^t \tag{3.4}
$$

where $Y=4+Y_o+G_o$. There is no change in the transfer event. Again at each time step a portion of the energy incident upon the node is transmitted into the conductivity stub in the form of a transmitted voltage pulse. Since the conductivity stub is match terminated, this voltage pulse is not returned to the node. Conductivity stubs have the macroscopic effect of reducing the amount of energy present in the TLM mesh at each time step.

It is interesting to find that the effect of the permittivity and conductivity stubs is essentially the same as the modelling of dielectric and conducting material in the Yee time-domain finite-difference method. In [Simo91a], propagation analysis of the two-dimensional node with permittivity and conductivity stubs has been performed. The resulting dispersion relation is identical to that of the Yee algorithm for a medium with the following material parameters,

$$
\varepsilon_r = 1 + \frac{Y_o}{4} \qquad \mu_r = 1 \qquad \sigma = \frac{G_o}{\Delta l} \tag{3.5}
$$

with the Yee algorithm operated at the upper limit of stability $\Delta l/\Delta t = c_o/\sqrt{2}$.

The boundary conditions along an interface between material regions (presented in the introduction) require continuity of field components tangential to the interface and a jump in field components normal to the interface. In the traditional TLM modelling of material regions, the interface is located half-way between nodes as shown in Figure 3.3. A computational convenience results from this organization of the simulation space. From the discussion related to the maximum amount of information available in a TLM mesh (section 3.3), it is known that only the field components tangential to the interface between material regions exist along the interface between computational cells. The field components normal to the interface are not defined at these spatial locations. Since tangential field components are always continuous, no special treatment or implementation of the boundary conditions is required.

Figure 3.3 here — see image.
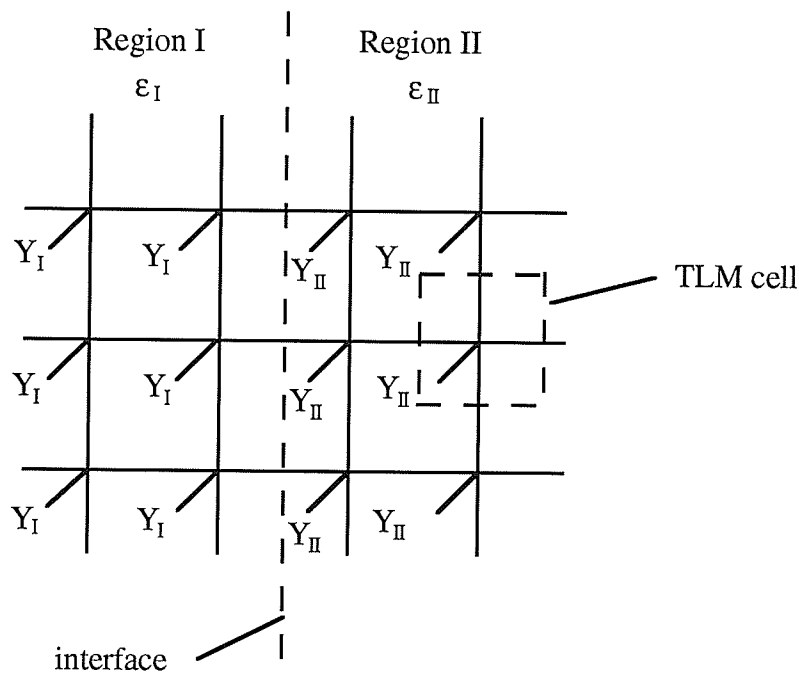
Figure 3.3: Modelling of the interface between two material regions with different permittivity.

This situation is analogous to the edge-element finite-element approach (see section 2.5), and that applied in conjunction with the Shankar time-domain finite-volume algorithm [Shan90], [Moha91]. Only tangential field components exist along the interfaces between adjacent computational cells. Although the computational convenience is noted above, a potential disadvantage to this structure may exist. In [Yuan91], a comparison of nodal-based and edge-based finite-element methods indicates that explicit enforcement of both the tangential and normal interface conditions yield the most accurate results. No theoretical or computational investigations have been performed with respect to the presence of this effect in TLM simulations. A modification of the TLM approach is suggested to place material interfaces at the centres of the nodes. At these spatial locations, all field components exist (for condensed nodes). Therefore, the boundary conditions on both the tangential and normal field components can be explicitly enforced.

3.2.2: Boundary Conditions

Boundary conditions are enforced by terminating the elemental transmission-lines with reflection coefficients at locations half-way between nodes and at the centre of nodes [Chen91a]. This requirement ensures the synchronism of voltage pulses throughout the mesh. Boundary conditions enforced via reflection coefficients include: perfect electric conductors, perfect magnetic conductors (non-physical boundary conditions applied to constrain field distributions), and local ABCs. Two equivalent methods can be used to determine the appropriate reflection coefficient to represent a specific boundary. The first is based on an intrinsic impedance of the boundary and the second utilizes the boundary condition expressed in terms of the field components tangential to the boundary. The implementation of boundary conditions at locations half-way between nodes is illustrated in Figure 3.4. A voltage pulse v^i travelling in the $+\eta$ direction is incident upon the boundary. The reflection coefficient that models the boundary Γ, results in a voltage pulse of magnitude Γv^i travelling in the $-\eta$ direction at the next time step.
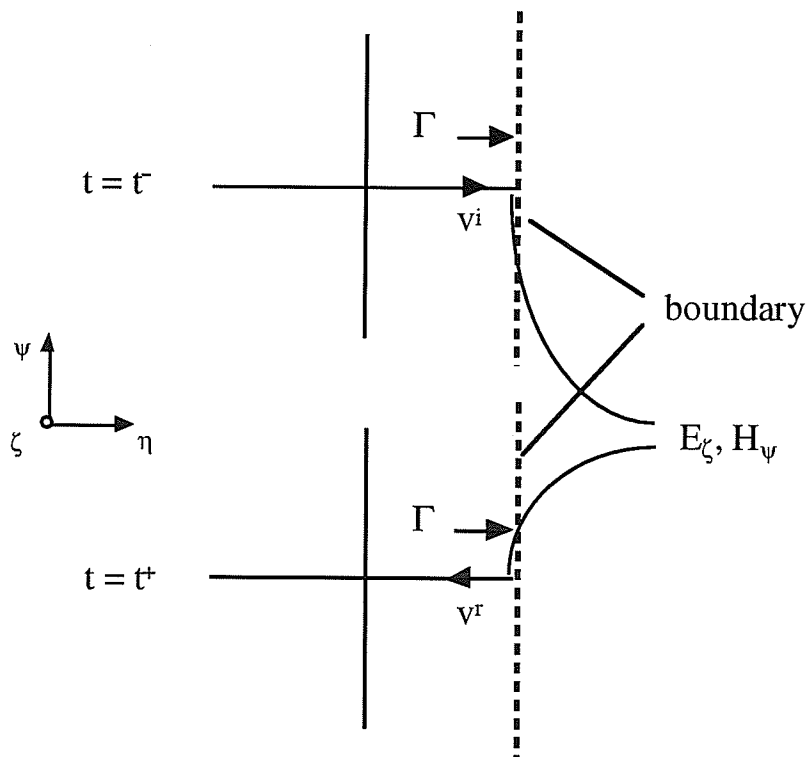

Figure 3.4: Enforcement of a boundary condition using reflection coefficients.

Consider the case of the boundary representing an arbitrary surface. In terms of an intrinsic impedance of the boundary, the reflection coefficient used to model this surface is determined from

$$\Gamma = \frac{Z_{load} - Z_l}{Z_{load} + Z_l} \tag{3.6}$$

where Z_l is the intrinsic impedance of the elemental transmission-lines of the model and Z_{load} is the effective load impedance for the boundary conditions.

For a perfect electric conductor, $Z_{load}=0$, the resulting reflection coefficient is $\Gamma = -1.0$. In terms of the field components along the boundary, the tangential electric field along a perfect electric conductor is zero. The appropriate reflection coefficient is determined to enforce this boundary condition. The incident voltage pulse v^i (travelling in the $+\eta$ direction) represents the field components E_ζ and $-H_\psi$. The reflected voltage pulse v^r (travelling in the $-\eta$ direction) represents the field components E_ζ and $+H_\psi$. Since the tangential electric field is zero along the boundary, the contributions of the electric field due to the voltage pulses v^i and v^r should cancel, and again, $\Gamma = -1.0$.

3.3: Information Available from a TLM Algorithm

In the previous sections the operation of the two-dimensional shunt node has been described. The operation of the model is described in terms of voltage pulses propagating through a grid of interconnected transmission-lines. In this section the maximum amount of information regarding field quatities from a minimum amount of post-processing is described. Traditionally field components were only defined at the centres of nodes [John71], [John87b]. In this section it is demonstrated that field components can also be defined at spatial locations corresponding to the interface between cells.

The transmission-lines within a TLM model are considered to be capable of supporting TEM waves, and therefore the fields associated with a voltage pulse v travelling in the x-y plane in a direction $\mathbf{d}$ are,

$$E_z \propto v \quad \text{and} \quad H_k \propto \frac{v}{Z_l} \tag{3.7}$$

where the direction k of the magnetic field is given by **dxz**. For the original shunt node described in Figure 3.1, the direction of propagation is limited to $\pm x$ and $\pm y$. Pulses travelling in the + and -x directions are associated with the field components,

$$E_z, -H_y \qquad \text{and} \qquad E_z, +H_y \qquad\qquad (3.8)$$

respectively. Pulses travelling in the + and -y directions are associated with the field components,

$$E_z, +H_x \qquad \text{and} \qquad E_z, -H_x \qquad\qquad (3.9)$$

respectively. Again, consider the mesh of two dimensional nodes in Figure 3.1. At half time steps $((n+1/2)\Delta t$, where n is an integer), voltage pulses are at the junctions between nodes, and at even time steps $(n\Delta t)$, voltage pulses are at the centres of nodes. A single voltage pulse is considered to be unable to represent field quantities. More than a single pulse is required to define fields. Therefore, in terms of incident voltage pulses, fields can only be defined at the centres of nodes at even time steps $(n\Delta t)^-$ as

$$E_z^{n\Delta t}(n_x\Delta l, n_y\Delta\ l) = \frac{1}{2}\,(v_1^i + v_2^i + v_3^i + v_4^i) \qquad\qquad (3.10a)$$

$$H_x^{n\Delta t}(n_x\Delta l, n_y\Delta\ l) = \frac{1}{Z_l}\,(v_1^i - v_3^i) \qquad\qquad (3.10b)$$

$$H_y^{n\Delta t}(n_x\Delta l, n_y\Delta\ l) = \frac{1}{Z_l}\,(v_4^i - v_2^i) \qquad\qquad (3.10c)$$

where the pulses v_n^i belong to the node centred at $(n_x\Delta l,\ n_y\Delta l)$, and at the junctions between nodes at half time steps $((n+1/2)\Delta t)^-$ as

$$E_z^{(n+1/2)\Delta t}((n_x+1/2)\Delta l, n_y\Delta l) = v_2^{\ i} + v_4^i \qquad\qquad (3.11a)$$

$$H_y^{(n+1/2)\Delta t}((n_x+1/2)\Delta l, n_y\Delta\ l) = \frac{1}{Z_l}\,(v_2^i - v_4^i) \qquad\qquad (3.11b)$$

where the voltage pulse v_2^i belongs to the node centred at $((n_x+1)\Delta l,\ n_y\Delta l)$ and v_4^i belongs to $(n_x\Delta l,\ n_y\Delta l)$, and

$$E_z^{(n+1/2)\Delta t}(n_x\Delta l,(n_y-1/2)\Delta l) = v_1^{\ i} + v_3^i \qquad\qquad (3.12a)$$

$$H_x^{(n+1/2)\Delta t}(n_x\Delta l,(n_y-1/2)\Delta\ l) = \frac{1}{Z_l}\,(v_3^i - v_1^i) \qquad\qquad (3.12b)$$

where the voltage pulse v_1^i belongs to the node centred at $(n_x \Delta l, n_y \Delta l)$ and v_3^i belongs to $(n_x \Delta l, (n_y+1) \Delta l)$. Similar definitions in terms of scattered voltage pulses are possible.

The definitions of field quantities in terms of voltage pulses has implications for physically unique specification of initial conditions within a TLM mesh, and for determining the equivalence with other numerical methods (to be discussed in Section 3.5.3). In terms of unique specification of initial conditions, fields can be uniquely enforced at the junctions between nodes at half time steps (*i.e.,* two field components and two voltage pulses - see equations 3.11 and 3.12). At the centres of nodes the field quatities are overconstrained in terms of voltage pulses (*i.e.,* three field components and four voltage pulses - see equations 3.10). This has been utilized in the TLM implementation of a total / scattered field formulation [Simo91d], [Simo92].

3.4: Three Dimensional Symmetric Condensed Node

The original three-dimensional TLM node was introduced by Akhtarzad and Johns [Akht75b]. This model is constructed from two-dimensional shunt and series nodes and has been demonstrated to satisfy the Yee finite-difference time-domain algorithm [John87a]. A problem with this model (along with the Yee algorithm - see discussion in section 2.6) is the misalignment of dielectric and magnetic media, and a general computational clumsiness associated with the layout of field components (see Figure 2.5).

In 1987, Johns introduced the three-dimensional symmetric-condensed node [John87b]. The purpose of this node is to overcome the difficulties associated with the original three-dimensional TLM node. Following the discussion presented in section 2.6 this node is more accurately referred to as a symmetric-*partially-condensed* node rather than a symmetric-condensed node, because tangential field components are available along the interfaces between computational cells and all field components are available at the centre of cells. A review of some three-dimensional models can be found in [Sagu89]. The three-dimensional symmetric-condensed node is shown in Figure 3.5(a), and the discretization of a general electromagnetic field problem is provided in Figure 3.5(b).
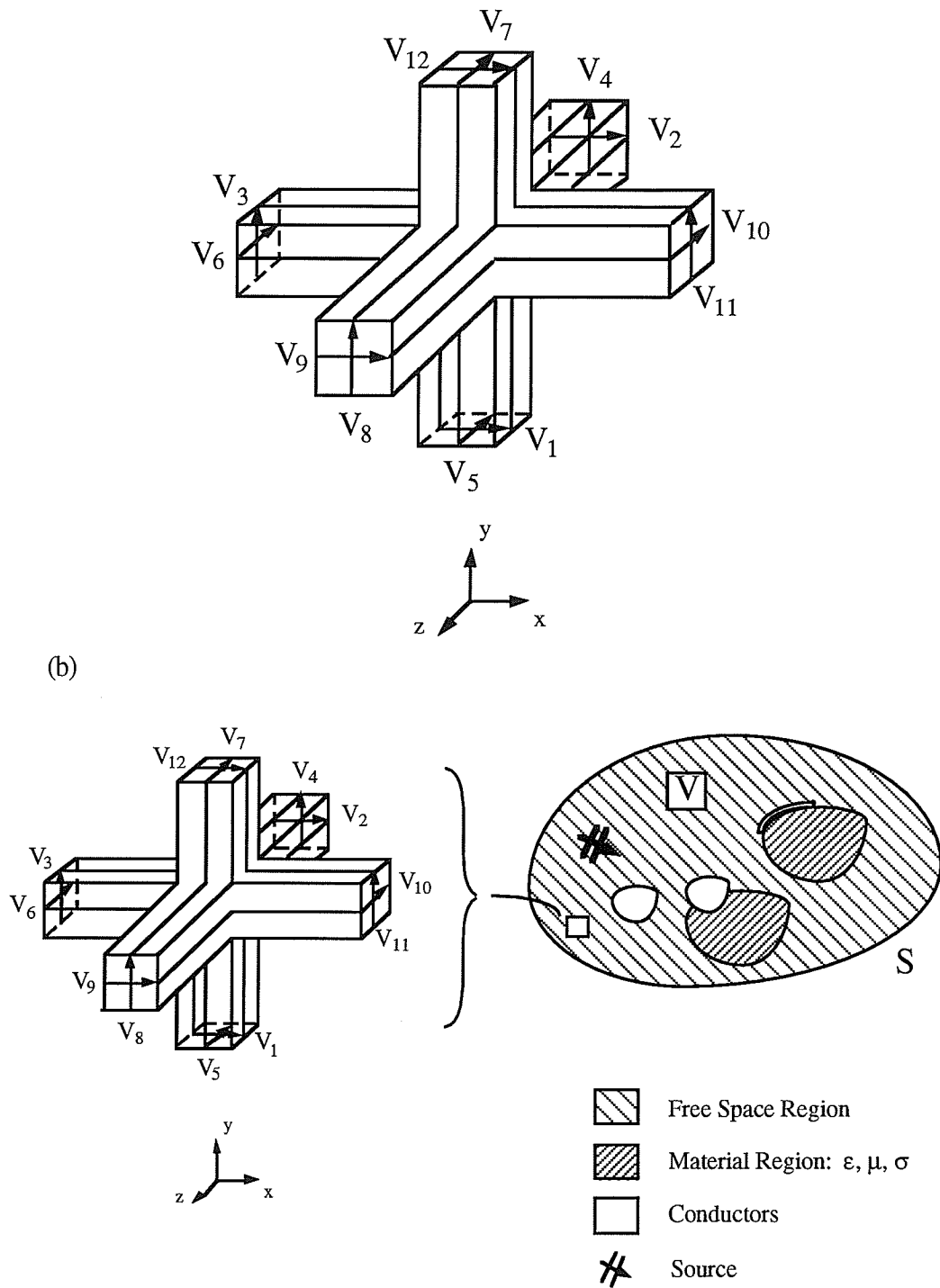
(a)

Figure 3.5: (a) Three-dimensional symmetric-condensed TLM node, and (b) discretization of the general electromagnetic field problem.

The operation of the symmetric-condensed TLM algorithm proceeds as described in section 3.1 in terms of scattering and transfer events. The scattering event is expressed as,

$$V^r = S \, V^i$$

where V^i and V^r are vectors containing incident and reflected voltage pulses, and the scattering matrix for the three-dimensional symmetric-condensed node with stubs for modelling permittivity, permeability, and electric conductivity is given by [John87b]; and in [Germ90c] for modelling magnetic conductivity. The scattering matrix as originally presented by Johns is given as [John87b], (the E and H row and column entries denote the coupling between x, y, and z field components)

			1	2	3	4	5	6	7	8	9	10	11	12	13	14	15	16	17	18
		E	x	x	y	y	z	z	z	y	x	z	y	x	x	y	z			
	E	H	z	y	z	x	x	y	x	x	y	y	z	z				x	y	z
1	x	z	a	b	d						b		-d	c	g					i
2	x	y	b	a				d			c	-d		b	g					-i	
3	y	z	d		a	b				b			c	-d	g						-i
4	y	x			b	a	d		-d	c			b					g	i		
5	z	x				d	a	b	c	-d		b					g	-i			
6	z	y		d			b	a	b		-d	c					g	i			
7	z	x				-d	c	b	a	d			b				g	i			
8	y	x				b	c	-d	d	a			b				g	-i			
9	x	y	b	c				-d			a	d		b	g			i			
10	z	y		-d			b	c	b		d	a					g	-i			
11	y	z	-d		c	b				b			a	d	g						i
12	x	z	c	b	-d						b		d	a	g						-i
13	x		e	e							e			e	h						
14	y				e	e				e			e		h						
15	z						e	e	e		e					h					
16		x				f	-f		f	-f								j			
17		y		-f				f			f	-f							j		
18		z	f		-f								f	-f							j

where,

$$a = \frac{-Y}{2(4+Y)} + \frac{Z}{2(4+Z)}$$

$$b = \frac{4}{2(4+Y)}$$

$$c = \frac{-Y}{2(4+Y)} - \frac{Z}{2(4+Z)}$$

$$d = \frac{4}{2(4+Z)}$$

$$e = b$$

$$f = Zd$$

$$g = Yb$$

$$h = \frac{Y-4}{Y+4}$$

$$i = d$$

$$j = \frac{4-Z}{4+Z}$$

and Z is the intrinsic impedance of free space, and Y=1/Z.

Fields are defined as discussed in section 3.3, all field components are defined at the centre of the node at even time steps ($n\Delta t$) and field components tangential to the faces of nodes are defined at the interface between cells at half time steps (($n+1/2$)Δt). Nielson and Hoefer have performed the propagation analysis of the symmetric-condensed TLM algorithm to determine its dispersion relation [Niel91]. Their analysis indicates that the three-dimensional symmetric-condensed TLM method is superior to the Yee finite-difference time-domain algorithm [Yee66], [Tafl89] in terms of dispersive errors.

3.5: Origins and Theoretical Justification of TLM

The TLM method was initially proposed by Johns [John71], and most of the theoretical developments (up to 1987) can be attributed to him [John86], [John87b]. Unfortunately, most researchers do not possess the insight of Johns' with respect to TLM modelling and therefore, it is important to investigate the various theoretical origins for TLM models. These investigations allow the creation of new TLM models and allow

extensions and improvements to existing methods. Some attempts have been made to interpret the TLM method within the context of various topics. In this section, some of this work is reviewed. A discussion of the advantages and disadvantages of each interpretation is provided.

3.5.1: Huygens' Principle

In 1974, Johns' discussed the relationship of the TLM method and Huygens' principle [John74b]. Johns' proposed that the TLM algorithm represents a discrete form of Huygen's principle. As discussed in [John74b] and [Hoef91], Huygens' proposed a corpuscular form of light wave propagation. The macroscopic phenomena of wave propagation is due to the interaction of particles which give rise to local wavelets. The local wavelets are spherical disturbances, each causing future disturbances as the wave propagates. From the description of the original rectangular model provided in section 3.1 it is easy to visualize the scattering and transfer events as a discrete form of Huygens' principle. Each scattering event represents the creation of an approximate spherical wavefront from each localized voltage pulse. The approximation of the model is due to the discrete nature of the spherical wavefront.

While the Huygens' principle interpretation of the TLM method is conceptually easy to comprehend, it provides few practical benefits. The first problem is that unfortunately, the equal scattering of an incident voltage pulse into equal reflected voltage pulses is not always true. The second problem is that the Huygens' principle interpretation does not suggest improvements to the model (except for the hexagonal model to be presented in Chapter 4) and the motivation for various extensions that have appeared in the literature.

3.5.2: Generalization of Lumped Element Modelling

In its original two-dimensional form [John71], the TLM method was presented in terms of the analogy between the behavior of voltages and currents on transmission-lines and electric and magnetic fields in space. Initially, this description of the method was viewed as an advantage. Since the microwave engineer is familiar with the behavior of transmission-lines, the method was conceptually easy to understand. This approach is

similar to the lumped element modelling of partial-differential-equations investigated in the 1940's.

In the 1940's, *network analyzers* were applied to the solution of electromagnetic field problems. These network analyzers consisted of lumped element models of Maxwell's equations. Consider the lumped element network shown in Figure 3.6. The network lies in the x-y plane and is oriented as indicated in the figure. Spacing between the nodes in the network is Δl and the values of inductance and capacitance are $L\Delta l$ and $2C\Delta l$, respectively. This network was proposed as a model of Maxwell's equations in two dimensions by Kron in 1943 [Kron43]. To utilize the equivalent circuit in a practical sense, *network analyzers* were built consisting of meshes of inductors and capacitors [Span49]. With the appropriate excitation and boundary conditions applied to the mesh (similar to the concepts discussed in section 3.2), a variety of electromagnetic field problems can be studied. Whinnery and Ramo used a network analyzer to study field distributions in cylindrical waveguides and the effects of discontinuities in rectangular waveguides [Whin44]. An account of the various problems associated with building a network analyzer can be found in a paper by Spangenberg, Walters, and Schott [Span49].
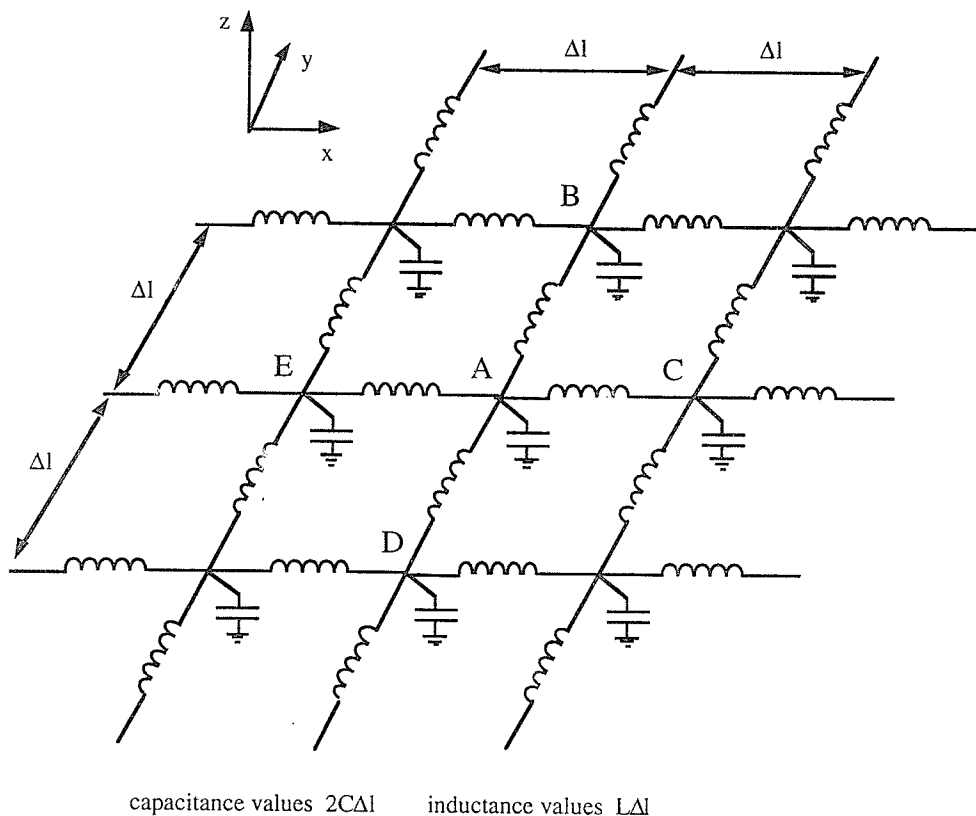

capacitance values $2C\Delta l$ inductance values $L\Delta l$

Figure 3.6: Lumped network model of Maxwell's equations in two dimensions proposed by Kron [Kron43].

Kron derived equivalent circuits to model various physical systems and established a basic theory related to the construction of circuit models of differential equations [Kron45]. Three dimensional models of Maxwell's equations were also derived, however only the two dimensional models were used in practice. The three dimensional networks contained ideal transformers and dependent voltage sources making construction of a practical network difficult [Kron44].

The analogy between Maxwell's equations and the equivalent network can be obtained by using circuit theory. In Figure 3.6, the voltage drop between nodes C and A can be expressed as

$$v_C - v_A = L\Delta l \frac{\partial i_{CA}}{\partial t} \qquad (3.13)$$

where i_{CA} is the current flowing from node C to node A (in the negative x direction), v_A is the voltage at node A, and v_C is the voltage at node C. Equation (3.13) can be written for an arbitrary voltage drop across two adjacent nodes in the x direction.

$$\frac{v(x+\Delta l) - v(x)}{\Delta l} = -L \frac{\partial i_x}{\partial t} \qquad (3.14)$$

Similarly, the following is valid for an arbitrary voltage drop across two adjacent nodes in the y direction.

$$\frac{v(y+\Delta l) - v(y)}{\Delta l} = -L \frac{\partial i_y}{\partial t} \qquad (3.15)$$

Applying Kirchoff's current law to node A yields

$$i_{EA} + i_{BA} + i_{CA} + i_{DA} = 2C\Delta l \frac{\partial v_A}{\partial t} \qquad (3.16)$$

where i_{EA} and i_{CA} represent currents flowing in the positive and negative x directions respectively; and i_{DA} and i_{BA} represent currents flowing in the positive and negative y directions respectively. If these currents are considered to be centered at locations half way between nodes, equation (3.16) can be written as,

$$i_x(x-\Delta l/2) - i_y(y+\Delta l/2) - i_x(x+\Delta l/2) + i_y(y-\Delta l/2) = 2C\Delta l\frac{\partial v_A}{\partial t} \qquad (3.17)$$

or

$$-\frac{i_x(x+\Delta l/2) - i_x(x-\Delta l/2)}{\Delta l} - \frac{i_y(y+\Delta l/2) - i_y(y-\Delta l/2)}{\Delta l} = 2C\frac{\partial v_A}{\partial t} \qquad (3.18)$$

Recognizing the left hand sides of equations (3.14), (3.15), and (3.18) as central-difference approximations to continuous derivatives, the network can be considered to be an approximation to the equations

$$\frac{\partial v}{\partial y} = -L\frac{\partial i_y}{\partial t} \qquad (3.19a)$$

$$\frac{\partial v}{\partial x} = -L\frac{\partial i_x}{\partial t} \qquad (3.19b)$$

$$-\frac{\partial i_x}{\partial t} - \frac{\partial i_y}{\partial t} = 2C\frac{\partial v}{\partial t} \qquad (3.19c)$$

Examining the set of equations (3.19) modelled by the network and the set of Maxwell's equations for two-dimensional TE propagation (3.1), the following relationships between field quantities in Maxwell's equations and circuit quantities in the lumped network of Figure 3.6 can be established;

$$E_z = v \qquad H_y = -i_x \qquad H_x = i_y$$

$$\mu = L \qquad \varepsilon = 2C \qquad (3.20)$$

The TLM method expressed in terms of transmission-lines is obtained through recognition that the lumped inductances and capacitances represent equivalent circuit models of transmission-lines. The inductors and capacitors can be replaced by ideal transmission-lines connecting adjacent nodal locations.

3.5.3: Equivalence of TLM and Finite-Difference Methods

In addition to the Huygen's principle and lumped element modelling origins of the TLM method. It is also possible to consider the relationship between TLM and finite-difference algorithms. From the review provided in this chapter it is obvious that parallels exist between the TLM and finite-difference methods. Both methods represent discrete field distributions that are defined at specific spatial locations at specific instants in time. In their natural formulations, both operate on regular grids, and as well most of the techniques required for specific problems are applicable to both methods (*i.e.*, ABCs, the various field formulations, operation in both the time and frequency domains, etc ...). During the past decade, several investigations regarding the equivalence of TLM and finite-difference methods have been performed [John87a], [Simo90], [Chen91b] and [Celu93]. Two distinct approaches to the equivalence have been adopted. They are *algorithmic* and *dispersive* equivalence.

3.5.3.1: Algorithmic Equivalence

Algorithmic equivalence attempts to demonstrate that the TLM and finite-difference methods both represent identical algorithms in terms of their time-stepping procedures. Most of the work related to establishing algorithmic equivalence has demonstrated that the TLM scattering and transfer events satisfy a given finite-difference algorithm. To rigorously demonstrate that both methods are algebraicly equivalent, one should demonstrate that both algorithms satisfy each other. To date, this has not been accomplished.

Johns has recognized the potential difficulties associated with establishing an algorithmic equivalence, " *... Great care has to be taken in comparing computer resources for the TLM method with the finite-difference method since much more information is available in the former ...* " [John87a]. To properly demonstrate that a TLM algorithm satisfies a given finite-difference algorithm, all of the information available from the TLM node (as discussed in section 3.3) should be used. In [Simo90], only a partial equivalence between the original shunt model and the two-dimensional Yee algorithm was obtained. A previous investigation demonstrated a partial equivalence between the three-dimensional expanded TLM node and the three-dimensional Yee algorithm [John87a].

Chen *et al* have presented two- and three-dimensional finite-difference algorithms and have demonstrated that the original two-dimensional node and the three-dimensional symmetric-condensed node satisfy these finite-differences algorithms [Chen91b]. Their work represents the most complete demonstration of algorithmic equivalence.

3.5.3.2: Dispersive Equivalence

The dispersion relation of a numerical method represents the fidelity of the method as a model of wave propagation. A dispersive equivalence between two methods exists if they possess identical dispersion relations. Constraints on the definitions of field quatities or operation of the algorithm are not imposed. Therefore, dispersive equivalence does not account for practical issues such as implementation of boundary conditions and availability of field components. Dispersive equivalences between TLM models and finite-difference algorithms is discussed in [Simo91a], [Simo91b], [Simo93], [Simo94a].

The dispersive equivalence between two methods only applies to the accuracy of the method for modelling wave propagation. If two methods possess identical dispersion relations, they can be considered as equivalent models for the simulation of wave propagation. The application of boundary conditions for the two methods may not be the same. Dispersive equivalence is applied in Chapter 4 to the development of new two-dimensional TLM models.

3.5.4: Derivation of a TLM Model

Of the various classifications of the TLM method discussed above, the relationship of TLM and finite-differencing is the most theoretically satisfying. Since, the TLM method is applied within the domain of computational electromagnetics a relationship in terms of a method commonly used in computational electromagnetics is beneficial. A common problem with the representations presented in 3.5.1 to 3.5.3 is underivability. None of the above representations fit within the standard method of numerical approximation of a governing mathematical formulation, and a clear derivation (in the language of computational physics) does not exist. This lack of derivability does

not represent a practical problem since the method has been demonstrated to provide accurate results for a wide variety of problems.

A first step towards the derivation of TLM methods has been presented in [LoVe92] and [LoVe93]. In Appendix A, an outline of the derivation of the original two-dimensional TLM model is presented. The derivation of the three-dimensional symmetric condensed model has been provided in [LoVe93]. Starting with Maxwell's equations written in conservation law form, the field components are decomposed into Riemman Invariant variables. These variables represent the voltage pulses described in the previous sections and are propagated along cartesian coordinate directions. Based on the continuity of field components and conservation of power considerations, the scattering and transfer events can be derived mathematically, without recourse to an equivalent circuit model, Huygens' principle, or a finite-difference algorithm.

3.6: Summary

In this chapter an overview of the TLM method has been presented. The emphasis has been placed on various unique details regarding the origin and theoretical justification of the method. As with the various other differential-equation based numerical methods, the method is applicable to the analysis of complex electromagnetic scattering and radiation problems. New TLM models for two-dimensional problems are developed in Chapter 4, and the application of a general purpose electromagnetic simulation program to various practical problems is described in Chapter 5.

Chapter 4: New TLM Models for the Two-Dimensional Wave Equation

In this chapter, three new TLM models of the two-dimensional wave equation are presented. Based on the discussions contained in Chapters 2 and 3, the TLM method is considered to be in the same class as finite-difference and finite-element methods. However, significantly more flexibility is associated with the finite-difference and finite-element methods as compared to the TLM method. The finite-difference and finite-element methods both allow flexibility in the geometrical properties of the numerical grid and the order of accuracy of the governing approximation. The finite-difference method allows various spatial arrangements of the difference approximations and different orders of accuracy. The finite-element method allows various element shapes and element expansion functions of varying order. Much of this flexibility can be attributed to the relative amount of research performed on each method. In this chapter two aspects pertaining to the numerical approximation of the two-dimensional wave equation are investigated. These are grid structure, and the accuracy of the approximation of spatial derivatives. The present study does not exhaust the two areas mentioned above as many other aspects remain to be investigated. The starting point of this chapter is the previous studies on the relationship of the TLM and finite-difference methods [Simo91a], and the questions:

> *Can models be created on something other than a rectangular grid ?*
> *Can the over all accuracy be something other than second-order-accurate ?*

4.1: The Original Rectangular Model

The original two-dimensional TLM model was introduced by Johns and Beurle [John71]. This model is based on a rectangular grid of interconnected transmission-lines.

In Figure 4.1, the geometry of the original model and a mesh of original nodes are shown. In this chapter the TLM method is considered as an approximation of the two-dimensional wave equation,

$$\frac{\partial^2 E}{\partial x^2} + \frac{\partial^2 E}{\partial y^2} = \frac{1}{c^2} \frac{\partial^2 E}{\partial t^2} \qquad (4.1)$$

where E is the z directed electric field distribution, and c is the propagation velocity. Based on the dispersive equivalence established in [Simo91a], the original TLM model can be considered as a second-order-accurate formulation based on a rectangular grid structure.
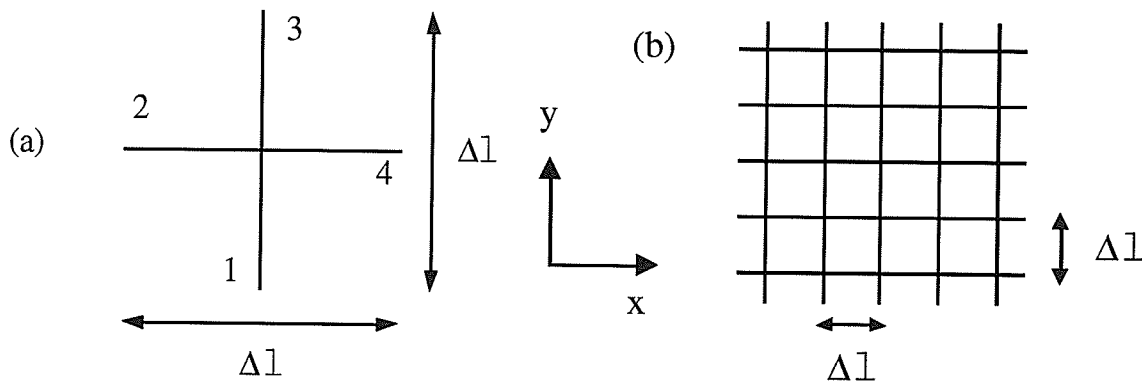

Figure 4.1: Geometry of the original rectangular TLM model introduced by Johns and Beurle [John71], and a mesh of original rectangular nodes.

4.2: Hexagonal Model

The first new TLM model introduced is the hexagonal model [Simo91b]. This model is based on an equilateral triangular grid. This development of this model represents an attempt to reduce numerical anisotropy. The geometry of the hexagonal model and a mesh of nodes is shown in Figure 4.2. The mesh of Figure 4.2 is constructed from three sets of transmission-lines, with the same characteristic impedance, oriented at 60° to one another. The scattering matrix for the hexagonal model is given as,

$$
\begin{bmatrix} v_1^r \\ v_2^r \\ v_3^r \\ v_4^r \\ v_5^r \\ v_6^r \end{bmatrix} = \frac{1}{3} \begin{bmatrix} -2 & 1 & 1 & 1 & 1 & 1 \\ 1 & -2 & 1 & 1 & 1 & 1 \\ 1 & 1 & -2 & 1 & 1 & 1 \\ 1 & 1 & 1 & -2 & 1 & 1 \\ 1 & 1 & 1 & 1 & -2 & 1 \\ 1 & 1 & 1 & 1 & 1 & -2 \end{bmatrix} \begin{bmatrix} v_1^i \\ v_2^i \\ v_3^i \\ v_4^i \\ v_5^i \\ v_6^i \end{bmatrix} \tag{4.2}
$$

and the transfer event for the hexagonal model is,

$$v_1^i(i,j) = v_4^r(i,j\text{-}1)$$

$$v_2^i(i,j) = v_5^r(i\text{-}1,j)$$

$$v_3^i(i,j) = v_6^r(i,j\text{+}1)$$

$$v_4^i(i,j) = v_1^r(i\text{+}1,j\text{+}1) \tag{4.3}$$

$$v_5^i(i,j) = v_2^r(i\text{+}1,j)$$

$$v_6^i(i,j) = v_3^r(i\text{+}1,j\text{-}1)$$

where (i,j) denote discrete (x,y) coordinates.
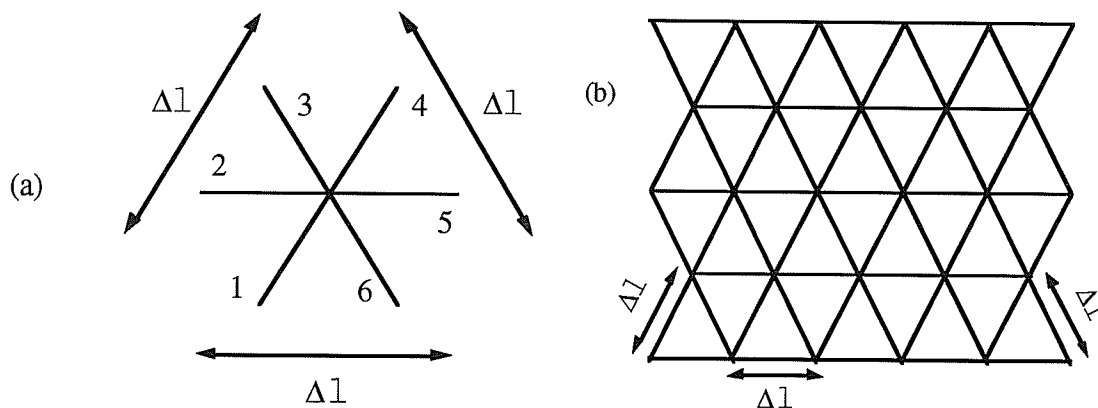

Figure 4.2: Geometry of the hexagonal TLM model, and a mesh of hexagonal nodes.

As discussed in Chapter 3, to model media with arbitrary parameters using the original node, transmission line stubs are added to the nodes [John74a], [Akht75a]. The same procedure is used with the hexagonal node. An open circuit stub of length $\Delta l/2$ is used to model permittivity and a match terminated stub is used to model conductivity. The scattering matrix for the hexagonal model with a permittivity stub is given in [Simo91b]. In section 4.2.2, the permissible values for the stub admittance, Y_0 are defined by comparison with the equivalent finite-difference stability criterion.

4.2.1: Dispersive Analysis of the Hexagonal Model

Following the procedure described in [Brew80], the dispersion relation of the hexagonal TLM model is given by,

$$\sin^2\left(\frac{\beta^*\Delta l}{2}\left(\frac{1}{2}\cos\phi+\frac{\sqrt{3}}{2}\sin\phi\right)\right) + \sin^2\left(\frac{\beta^*\Delta l\cos\phi}{2}\right) +$$

$$\sin^2\left(\frac{\beta^*\Delta l}{2}\left(\frac{1}{2}\cos\phi-\frac{\sqrt{3}}{2}\sin\phi\right)\right) = 3\left(1+\frac{Y_o}{6}\right)\sin^2\left(\frac{\omega\Delta t}{2}\right) \qquad (4.4)$$

Expression (4.4) describes the fundamental manner in which plane waves propagate through an infinite mesh of hexagonal nodes. Given the spatial and temporal discretization (Δl and Δt, respectively), frequency of excitation (ω), direction of propagation (ϕ), the numerical phase constant β^* can be obtained from (4.4). The value of β^* can be compared to the exact physical phase constant to determine the amount of velocity error.

An advantage of the hexagonal model as compared to the original rectangular model is the increase in numerical isotropy (i.e., the numerical phase velocity is approximately constant with respect to the direction of propagation). In Figure 4.3(a) and 4.3(b), contours of the ratio of numerical phase velocity to physical phase velocity are provided for the original and hexagonal models, respectively. Dispersive effects are present for both models (i.e., the phase velocity varies with frequency). However, the dispersive errors present in the hexagonal model are approximately constant with respect to the direction of propagation.
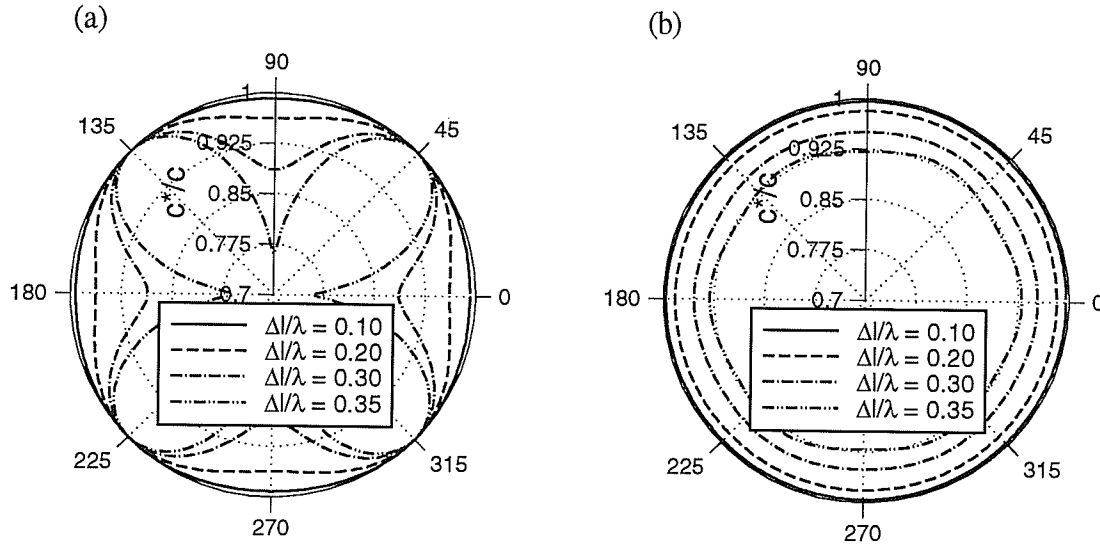
(a)   (b)

Figure 4.3: Contours of the ratio of numerical phase velocity to physical phase velocity for (a) the original model [John71], and (b) the hexagonal model.

4.2.2: Equivalent Finite-Difference Algorithm

Consider the following analytic modification to the two-dimensional wave equation (4.1). The y derivative can be re-written in terms of derivatives in the u and v directions (see Figure 4.4). The operators $\partial/\partial u$ and $\partial/\partial v$ can be written as,

$$\frac{\partial}{\partial u} = \cos\phi_o \frac{\partial}{\partial y} - \sin\phi_o \frac{\partial}{\partial x} \qquad (4.5a)$$

and

$$\frac{\partial}{\partial v} = \cos\phi_o \frac{\partial}{\partial y} + \sin\phi_o \frac{\partial}{\partial x} \qquad (4.5b)$$

respectively. The operators $\partial^2/\partial u^2$ and $\partial^2/\partial v^2$ can be expressed as,

$$\frac{\partial^2}{\partial u^2} = \cos^2\phi_o \frac{\partial^2}{\partial y^2} + \sin^2\phi_o \frac{\partial^2}{\partial x^2} - 2\sin\phi_o\cos\phi_o \frac{\partial}{\partial y}\frac{\partial}{\partial x} \qquad (4.6a)$$

and

$$\frac{\partial^2}{\partial v^2} = \cos^2\phi_0 \frac{\partial^2}{\partial y^2} + \sin^2\phi_0 \frac{\partial^2}{\partial x^2} + 2\sin\phi_0\cos\phi_0 \frac{\partial}{\partial y}\frac{\partial}{\partial x} \qquad (4.6b)$$

Adding (4.6a) and (4.6b) with $\phi_0 = 30^\circ$ yields,

$$\frac{\partial^2}{\partial u^2} + \frac{\partial^2}{\partial v^2} = \frac{3}{2}\frac{\partial^2}{\partial y^2} + \frac{1}{2}\frac{\partial^2}{\partial x^2}$$

and therefore (4.1) can be re-written as

$$\frac{\partial^2 E_z}{\partial u^2} + \frac{\partial^2 E_z}{\partial v^2} + \frac{\partial^2 E_z}{\partial x^2} = \frac{3}{2}\frac{1}{c^2}\frac{\partial E_z}{\partial t^2}^2 \qquad (4.7)$$

Expressing the wave equation in terms of x, u, and v derivatives is mathematically redundant. However, application of finite differences to (4.7) yields the numerical advantage illustrated in Figure 4.3(b). Applying second-order-accurate central difference approximations to (4.7) with equal spatial steps ($\Delta x = \Delta u = \Delta v = \Delta l$) yields,

$$\frac{E_z^t(x+\Delta l, u, v) - 2E_z^t(x, u, v) + E_z^t(x-\Delta l, u, v)}{\Delta l^2}$$

$$+ \frac{E_z^t(x, u+\Delta l, v) - 2E_z^t(x, u, v) + E_z^t(x, u-\Delta l, v)}{\Delta l^2}$$

$$+ \frac{E_z^t(x, u, v+\Delta l) - 2E_z^t(x, u, v) + E_z^t(x, u, v-\Delta l)}{\Delta l^2}$$

$$= \frac{3}{2}\frac{1}{c^2}\frac{E_z^{t+\Delta t}(x, u, v) - 2E_z^t(x, u, v) + E_z^{t-\Delta t}(x, u, v)}{\Delta t^2} \qquad (4.8)$$

The above expression can be re-written to obtain an explicit finite difference algorithm for solving the two dimensional wave equation. The computational grid used to implement this algorithm is shown in Figure 4.4.
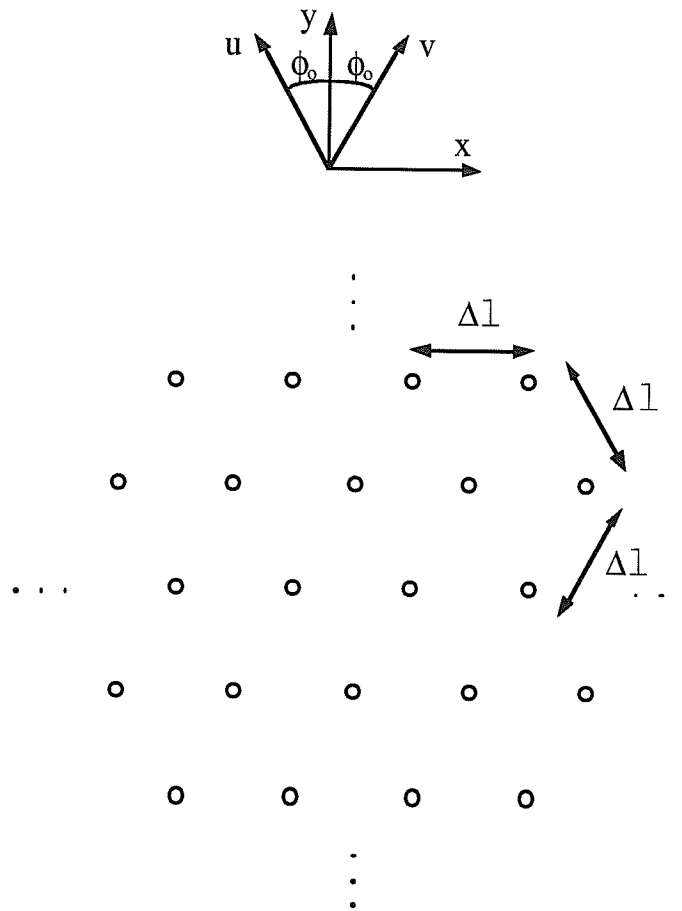
Figure 4.4: Spatial orientation of the numerical grid used for the hexagonal finite-difference algorithm.

Expression 4.8 can be written more conveniently in terms of x and y coordinates as,

$$\frac{E_z^t(x+\Delta l,y) - 2E_z^t(x,y) + E_z^t(x-\Delta l,y)}{\Delta l^2}$$

$$+ \frac{E_z^t(x-\frac{\Delta l}{2},y+\frac{\sqrt{3}\Delta l}{2}) - 2E_z^t(x,y) + E_z^t(x+\frac{\Delta l}{2},y-\frac{\sqrt{3}\Delta l}{2})}{\Delta l^2}$$

$$+ \frac{E_z^t(x+\frac{\Delta l}{2},y+\frac{\sqrt{3}\Delta l}{2}) - 2E_z^t(x,y) + E_z^t(x-\frac{\Delta l}{2},y-\frac{\sqrt{3}\Delta l}{2})}{\Delta l^2}$$

$$= \frac{3}{2}\frac{1}{c^2}\frac{E_z^{t+\Delta t}(x,y) - 2E_z^t(x,y) + E_z^{t-\Delta t}(x,y)}{\Delta t^2} \qquad (4.9)$$

The dispersion relation of hexagonal finite-difference algorithm is given as,

$$\sin^2\left(\frac{\beta^*\Delta l}{2}\left(\frac{1}{2}\cos\phi+\frac{\sqrt{3}}{2}\sin\phi\right)\right) + \sin^2\left(\frac{\beta^*\Delta l\cos\phi}{2}\right) +$$

$$\sin^2\left(\frac{\beta^*\Delta l}{2}\left(\frac{1}{2}\cos\phi-\frac{\sqrt{3}}{2}\sin\phi\right)\right) = \frac{3\Delta l^2}{2\Delta t^2}\frac{1}{c^2}\sin^2\left(\frac{\omega\Delta t}{2}\right) \qquad (4.10)$$

Expression 4.10 describes the fundamental manner in which plane waves propagate through an infinite hexagonal finite-difference mesh. Given the spatial and temporal discretization (Δl and Δt, respectively), frequency of excitation (ω), direction of propagation (ϕ), the numerical phase constant β^* can be obtained from (4.10). The value of β^* can be compared to the exact physical phase constant to determine the amount of velocity error.

The stability criterion for the hexagonal finite-difference algorithm obtained using the Von Neumann method [O'Bri50], is

$$\Delta t \le \sqrt{\frac{2}{3}}\frac{\Delta l}{c} \qquad (4.11)$$

The hexagonal TLM and finite difference algorithms have identical dispersion characteristics when Δl and Δt are selected to yield,

$$\Delta t = \frac{1}{\sqrt{\varepsilon_r\mu_r}}\frac{1}{\sqrt{2}}\frac{\Delta l}{c} \qquad (4.12)$$

where

$$\varepsilon_r \mu_r = 1 + \frac{Y_o}{6} \qquad (4.13)$$

Therefore, from the finite-difference stability criterion (4.11) and the equivalence conditions (4.12)-(4.13) the permissible values of Y_o (for stable operation of the hexagonal TLM method) are,

$$Y_o \geq -\frac{3}{2} \qquad (4.14)$$

Expression 4.14 can be considered as the stability criteria for the hexagonal TLM model and has been validated by free space propagation tests.

4.2.3: Correction for Dispersive Errors

A typical application of the two-dimensional algorithms has been the prediction of cut-off frequencies of waveguide. The most significant source of error for these calculations is caused by numerical dispersion. The numerical result for the cut-off frequency is shifted by an amount proportional to c^*/c. In a general simulation involving a waveguide with an arbitrary cross-section, waves propagate in a variety of different directions. If the simulation utilized a mesh of original rectangular nodes, at a specific frequency the amount of dispersion present is unknown (although the upper and lower bounds are known). However, if the simulation utilized a mesh of hexagonal nodes, the amount of dispersion present is *almost* independent of the direction of propagation and therefore, the amount of dispersion present can be determined from (4.4). The numerically determined cut-off frequency can be corrected to eliminate the effects of numerical dispersion for homogeneous problems.

This technique has been investigated in more detail in [Simo91b]. To evaluate the performance of the hexagonal TLM model and the above error-correction technique, the method has been applied to the calculation of cut-off frequencies in a square waveguide (13.0Δl by 13.0Δl). Table 4.1 contains a comparison of the analytical solution, hexagonal TLM solution, and error-corrected hexagonal TLM solution. The results contained in Table 4.1 and the additional results provided in [Simo91b] indicate the hexagonal model performs as expected, and the error-correction scheme provides the expected increase in accuracy.

Table 4.1: Comparison of analytic and numerical cut-off frequencies for rectangular waveguide.

Mode	Cut-off Frequency ($\Delta l/\lambda$)			% difference from analytic	
	Analytic	Hexagonal	Error-Corrected	Hexagonal	Error-Corrected
(1,1)	0.05439	0.0544	0.0544	0.08	0.01
(1,2)	0.08600	0.0858	0.0860	0.26	0.00
(2,2)	0.10879	0.1083	0.1088	0.45	0.01
(1,3)	0.12163	0.1209	0.1217	0.60	0.06
(2,3)	0.13868	0.1376	0.1387	0.77	0.02
(1,4)	0.15858	0.1569	0.1587	1.03	0.07
(3,3)	0.16318	0.1615	0.1634	1.00	0.13

4.3: Spatially-Weighted Model

The second TLM model introduced is the spatially-weighted model [Simo93]. This model is based on an isoceles triangular grid. The development of this model also represents an attempt to reduce numerical anisotropy. The spatially-weighted TLM model is synthesized from the following spatially-weighted finite-difference approximation of the two-dimensional wave equation,

$$
(1\text{-}k)\left\{ \frac{E_z(x+\Delta l,y) - 2E_z(x,y) + E_z(x-\Delta l,y)}{\Delta l^2} + \right.
$$

$$
\left. \frac{E_z(x,y+\Delta l) - 2E_z(x,y) + E_z(x,y-\Delta l)}{\Delta l^2} \right\}
$$

$$
k\left\{ \frac{E_z(x+\Delta l,y+\Delta l) - 2E_z(x,y) + E_z(x-\Delta l,y-\Delta l)}{(\sqrt{2}\Delta l)^2} + \right.
$$

$$
\left. \frac{E_z(x+\Delta l,y-\Delta l) - 2E_z(x,y) + E_z(x-\Delta l,y+\Delta l)}{(\sqrt{2}\Delta l)^2} \right\}
$$

$$
= \varepsilon\mu \frac{E_z^{t+\Delta t}(x,y) - 2E_z^{t}(x,y) + E_z^{t-\Delta t}(x,y)}{\Delta t^2} \tag{4.15}
$$

where Δl is a uniform x and y coordinate grid spacing, k is a weighting factor restricted between zero and one, and Δt is the time step. The spatial discretization applied in the above finite-difference algorithm was proposed by Vichnevetsky and Bowles [Vich82]. The purpose of the weighting factor k is to yield isotropic propagation characteristics (i.e., to obtain a numerical approximation of the wave equation with propagation characteristics similar to those of the hexagonal models). Vichnevetsky and Bowles have investigated the effects of only the spatial discretization in (4.15) (i.e., the time-derivative is not discretized as above) [Vich82]. Trefethen has investigated the fully discretized form (4.15) [Tref82]. The spatial discretization applied in (4.15) is obtained from the weighted combination of two standard five point stencils, as illustrated in Figure 4.5.
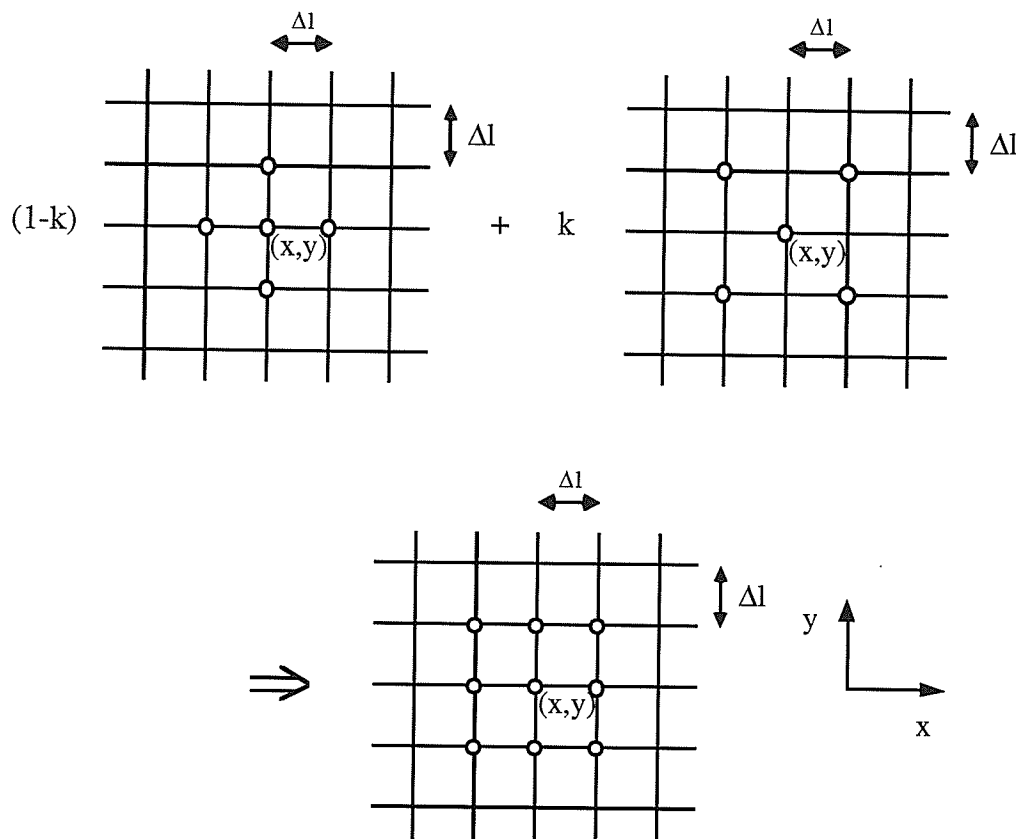
Figure 4.5: Weighted combination of two five-point stencils.

The dispersion relation for the spatially-weighted finite-difference algorithm is given by,

$$\frac{k}{2}\left\{ \sin^2\frac{\beta^*\Delta l(\cos\phi + \sin\phi)}{2} + \sin^2\frac{\beta^*\Delta l(\cos\phi - \sin\phi)}{2}\right\}$$

$$+ (1-k)\left\{ \sin^2\frac{\beta^*\Delta l\cos\phi}{2} + \sin^2\frac{\beta^*\Delta l\sin\phi}{2}\right\} = \frac{\Delta l^2}{c^2\Delta t^2}\sin^2\frac{\omega\Delta t}{2} \qquad (4.16)$$

Expression (4.16) describes the fundamental manner in which plane waves propagate through an infinite spatially-weighted finite-difference mesh. Given the spatial and temporal discretization (Δl and Δt, respectively), frequency of excitation (ω), direction of propagation (ϕ), the numerical phase constant β^* can be obtained from (4.16). The value of β^* can be compared to the exact physical phase constant to determine the amount of velocity error.

The stability criterion for the spatially-weighted finite-difference method obtained using the Von Neumann method described in [O'Bri50], is

$$\Delta t \le \frac{1}{\sqrt{2-k}} \frac{\Delta l}{c} \tag{4.17}$$

4.3.1: Synthesis of the Spatially-Weighted TLM Model

The finite-difference algorithm presented in the previous section is constructed from the weighted combination of two second-order-accurate central-difference stencils. One oriented as usual (arms of the stencil located along the x and y axis), the other rotated by 45° with its arms extended by a factor of √2. The spatially-weighted TLM model is synthesized by utilyzing the relationship between the original rectangular TLM model and the two-dimensional Yee algorithm [Simo91a]. The geometry of the spatially-weighted TLM model and a mesh of nodes are provided in Figure 4.6. The new model consists of the weighted combination of two original rectangular models. One oriented as usual (with elemental transmission-lines oriented along the x and y axis), the other rotated by 45° with its arms extended by a factor of √2. An electrical connection between diagonal and axial transmission-lines exists only at the centres of nodes, located at even multiples of Δl in both the x and y directions (denoted by the black dots in Figure 4.6(b)). To complete the model, the electrical characteristics of the elemental transmission-lines require specification.
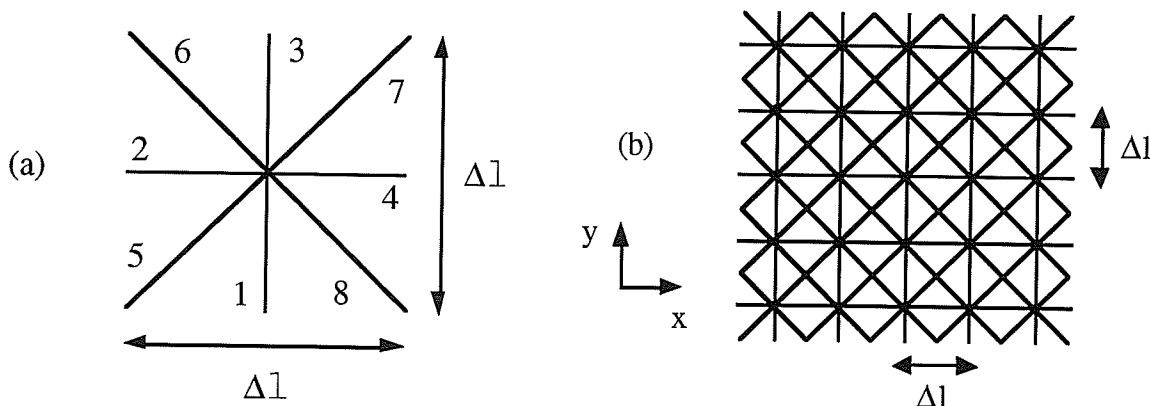

Figure 4.6: (a) Geometry of the spatially-weighted TLM model and, (b) a mesh of nodes.

The analogue of a weighting factor in an electric circuit is a variable impedance. To implement the ability to weight the two inter-connected original TLM models, the diagonal and axial elemental transmission-lines are permitted to have different characteristic impedances. The intrinsic impedance of the axial elemental transmission-lines (i.e., associated with the original model along the x and y axis) is Z_1, and the intrinsic impedance of the diagonal transmission-lines (i.e., associated with the rotated model) is mZ_1, where m is a weighting factor ($0 \leq m < \infty$).

In the operation of the finite-difference algorithm (4.15), the communication of information between axially adjacent and diagonally adjacent nodes occurs with the same speed. Therefore, to maintain the *preservation of information transfer* the propagation velocity of the diagonal elemental transmission-lines should be $\sqrt{2}$ times that of the propagation velocity of the axial elemental transmission-lines, or

$$v_1^j = \sqrt{2}\, v_1^i \tag{4.18}$$

where v_1^n refers to the propagation velocity along the nth elemental transmission-line, j=1-8, and i=1-4. A beneficial consequence of (4.18) is that the synchronism of voltage pulses is preserved in the spatially-weighted model.

As previously mentioned a medium of arbitrary permittivity and conductivity can be modelled by adding stubs. In Figure 4.7, the spatially-weighted model is shown with permittivity stubs. The spatially-weighted model is constructed from the combination of two original rectangular models, and therefore to maintain consistency, two open circuit stubs are added. One of length $\Delta l/2$ and admittance Y_0/Z_1 (associated with the shunt node with elemental transmission-lines along the x and y axis), the other of length $\Delta l/\sqrt{2}$ and admittance Y_0/mZ_1 (associated with the rotated node).

The scattering matrix for the spatially-weighted TLM model is given as,

$$
\begin{bmatrix} v_1^r \\ v_2^r \\ v_3^r \\ v_4^r \\ v_5^r \\ v_6^r \\ v_7^r \\ v_8^r \\ v_9^r \\ v_{10}^r \end{bmatrix}
=
\begin{bmatrix}
a & b & b & b & d & d & d & d & f & h \\
b & a & b & b & d & d & d & d & f & h \\
b & b & a & b & d & d & d & d & f & h \\
b & b & b & a & d & d & d & d & f & h \\
b & b & b & b & c & d & d & d & f & h \\
b & b & b & b & d & c & d & d & f & h \\
b & b & b & b & d & d & c & d & f & h \\
b & b & b & b & d & d & d & c & f & h \\
b & b & b & b & d & d & d & d & e & h \\
b & b & b & b & d & d & d & d & f & g
\end{bmatrix}
\begin{bmatrix} v_1^i \\ v_2^i \\ v_3^i \\ v_4^i \\ v_5^i \\ v_6^i \\ v_7^i \\ v_8^i \\ v_9^i \\ v_{10}^i \end{bmatrix}
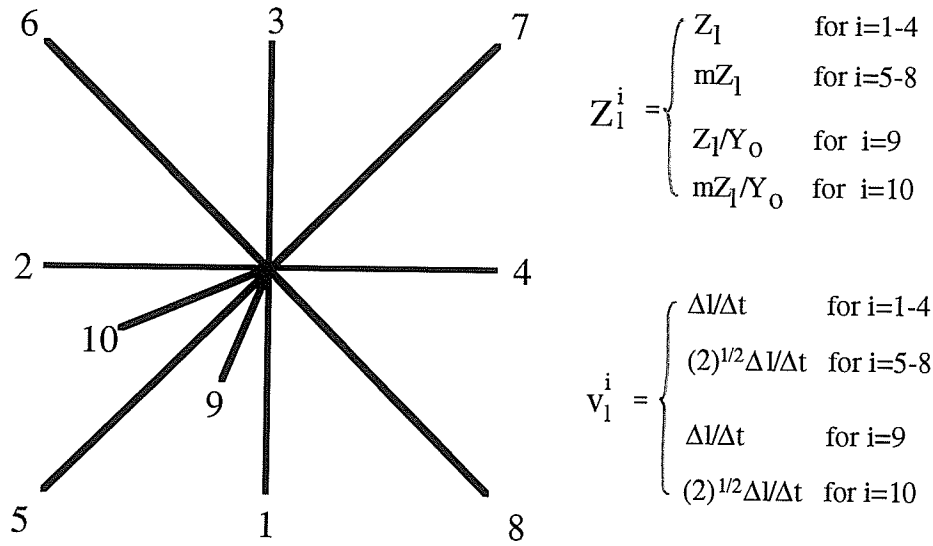\tag{4.19a}
$$

$$Z_1^i = \begin{cases} Z_1 & \text{for } i=1\text{-}4 \\ mZ_1 & \text{for } i=5\text{-}8 \\ Z_1/Y_0 & \text{for } i=9 \\ mZ_1/Y_0 & \text{for } i=10 \end{cases}$$

$$v_1^i = \begin{cases} \Delta l/\Delta t & \text{for } i=1\text{-}4 \\ (2)^{1/2}\Delta l/\Delta t & \text{for } i=5\text{-}8 \\ \Delta l/\Delta t & \text{for } i=9 \\ (2)^{1/2}\Delta l/\Delta t & \text{for } i=10 \end{cases}$$

Figure 4.7: Spatially-weighted TLM model with permittivity stubs.

where,

$$a = \frac{-2m - 4 - Y_0(m+1)}{4 + 4m + Y_0(m+1)}$$

$$b = \frac{2m}{4 + 4m + Y_0(m+1)}$$

$$c = \frac{-2 - 4m - Y_0(m+1)}{4 + 4m + Y_0(m+1)}$$

$$d = \frac{2}{4 + 4m + Y_0(m+1)}$$

$$e = \frac{-4 - 4m - Y_0(1-m)}{4 + 4m + Y_0(m+1)}$$

$$f = \frac{2mY_0}{4 + 4m + Y_0(m+1)}$$

$$g = \frac{-4 - 4m - Y_0(m-1)}{4 + 4m + Y_0(m+1)}$$

$$h = \frac{2Y_0}{4 + 4m + Y_0(m+1)}$$

The transfer event for the spatially-weighted model is,

$$v_1^i(i,j) = v_3^r(i,j-1)$$

$$v_2^i(i,j) = v_4^r(i-1,j)$$

$$v_3^i(i,j) = v_1^r(i,j+1)$$

$$v_4^i(i,j) = v_2^r(i+1,j)$$

$$v_5^i(i,j) = v_7^r(i-1,j-1) \qquad (4.19b)$$

$$v_6^i(i,j) = v_8^r(i-1,j+1)$$

$$v_7^i(i,j) = v_5^r(i+1,j+1)$$

$$v_8^i(i,j) = v_6^r(i+1,j-1)$$

$$v_9^i(i,j) = v_9^r(i,j)$$

$$v_{10}^i(i,j) = v_{10}^r(i,j)$$

where (i,j) denote discrete (x,y) coordinates.

The spatially-weighted TLM model has been implemented in the form of (4.19) and has been applied to the calculation of cut-off frequencies of rectangular waveguide. Numerical results are presented in [Simo93].

4.3.2: Dispersion Relation of the Spatially-Weighted TLM Model

Again, following the procedure described in [Brew80] the dispersion relation of the spatially-weighted TLM model is given by,

$$\sin^2\frac{\beta^*\Delta l(\cos\phi + \sin\phi)}{2} + \sin^2\frac{\beta^*\Delta l(\cos\phi - \sin\phi)}{2}$$

$$+ m\left\{ \sin^2\frac{\beta^*\Delta l\cos\phi}{2} + \sin^2\frac{\beta^*\Delta l\sin\phi}{2} \right\} = \frac{m+1}{2}(4+Y_o)\sin^2\frac{\beta_l\Delta l}{2} \qquad (4.20)$$

Expression (4.20) describes the fundamental manner in which plane waves propagate through an infinite mesh of spatially-weighted nodes. Given the spatial and temporal discretization (Δl and Δt, respectively), frequency of excitation (ω), direction of

propagation (ϕ), the numerical phase constant $\beta*$ can be obtained from (4.20). The value of $\beta*$ can be compared to the exact physical phase constant to determine the amount of velocity error.

4.3.3: Equivalence of Spatially-Weighted TLM and FD Methods

The dispersive equivalence of the spatially-weighted TLM and finite-difference methods is determined by finding the conditions that equate (4.16) and (4.20). The following relationship between the TLM impedance weighting factor m and the finite-difference weighting factor k is established,

$$m = \frac{2(1-k)}{k} \quad \text{or} \quad k = \frac{2}{m+2} \tag{4.21}$$

As well, if the finite-difference algorithm is operated such that,

$$c = \sqrt{\frac{2(m+2)}{(m+1)(4+Y_o)}} \frac{\Delta l}{\Delta t} \tag{4.22}$$

the spatially-weighted finite-difference and TLM methods possess identical propagation characteristics. From the finite-difference stability criterion (4.17), the permissible range of values for the stub admittance Y_o (the TLM stability criterion for the spatially-weighted model) is,

$$Y_o \geq 0 \tag{4.23}$$

This stability range is the same as that for the original TLM model [John71].

4.3.4: Conditions for Numerical Isotropy

The spatially-weighted finite-difference algorithm was investigated by Vichnevetsky and Bowles [Vich82], and Trefethen [Tref82] to provide an improvement in numerical isotropy. In Figure 4.8 contours of $c*/c$ for the spatially-weighted TLM model are provided for various values of the impedance weighting factor m. Inspection of these contours indicates the optimal value of m for approximate numerical isotropy is between 3.0 and 4.0.
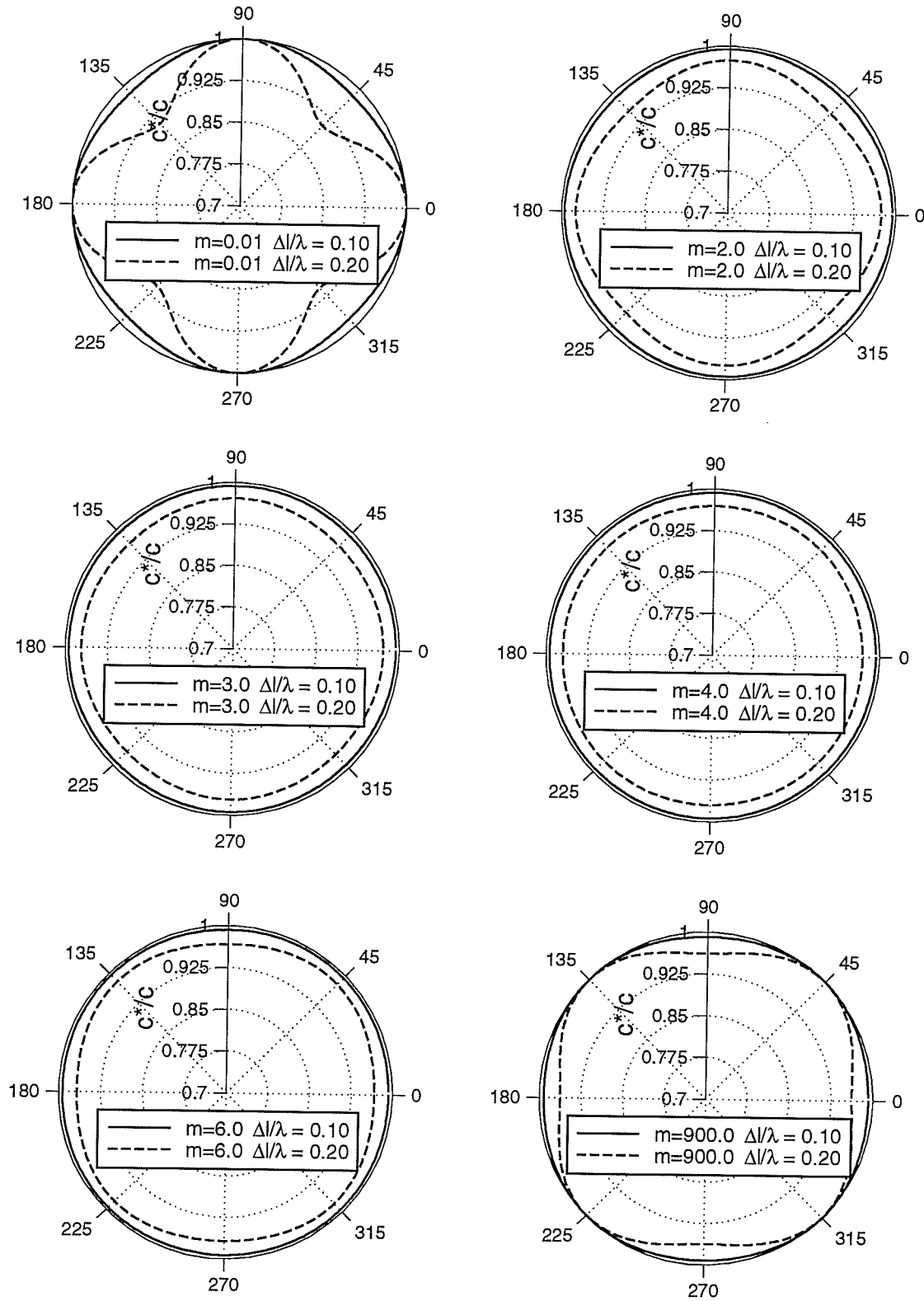
Figure 4.8: Contours of c*/c for various values of m. In each curve, c*/c is presented for discretization ratios of $\Delta l/\lambda=0.05$ and 0.1.

4.4: Spatially Fourth-Order-Accurate Rectangular Model

In the two previous sections, TLM models have been presented for two types of triangular grids: an equilateral triangular grid (hexagonal model), and an isosceles triangular grid (spatially-weighted model). Both the hexagonal and spatially-weighted models indicate the ability of the TLM approach to make use of numerical grids that are different from the traditional rectangular approach. These new TLM models possess the numerical benefit of reduced anisotropy. The fundamental accuracy of the method has not increased since second-order central difference approximations are applied. The number, spatial orientation, and relative weighting of the difference approximations has been altered. In this section, the extension of the original rectangular second-order TLM model to achieve fourth-order spatial accuracy is presented. The previously developed models demonstrated improvements to the anisotropy of the numerical model, the extension of the original second-order algorithm to achieve fourth-order spatial accuracy investigates possible improvements to the frequency dependence of the numerical model.

With the exception of the initial studies presented by Fang and Mei [Fang89], and Deveze *et al* [Deve92], the development and application of higher-order approximations to time-domain differential-equation based numerical methods (either finite-difference or finite-element) has received limited attention.

4.4.1: Fourth-Order Finite-Difference Algorithm

Consider the discretization of (4.1) using fourth-order central-difference approximations in space and a second-order central-difference approximation in time, to yield

$$\frac{- E^t(x+2\Delta l,y) + 16E^t(x+\Delta l,y) - 30E^t(x,y) + 16E^t(x-\Delta l,y) - E^t(x-2\Delta l,y)}{12(\Delta l)^2}$$

$$+ \frac{- E^t(x,y+2\Delta l) + 16E^t(x,y+\Delta l) - 30E^t(x,y) + 16E^t(x,y-\Delta l) - E^t(x,y-2\Delta l)}{12(\Delta l)^2}$$

$$= \frac{1}{v^2} \frac{E^{t+\Delta t}(x,y) - 2E^{t}(x,y) + E^{t-\Delta t}(x,y)}{(\Delta t)^2} \tag{4.24}$$

where Δl is the grid size in the x and y directions, and Δt is the time step. The computational molecule for this algorithm is provided in Figure 4.9.
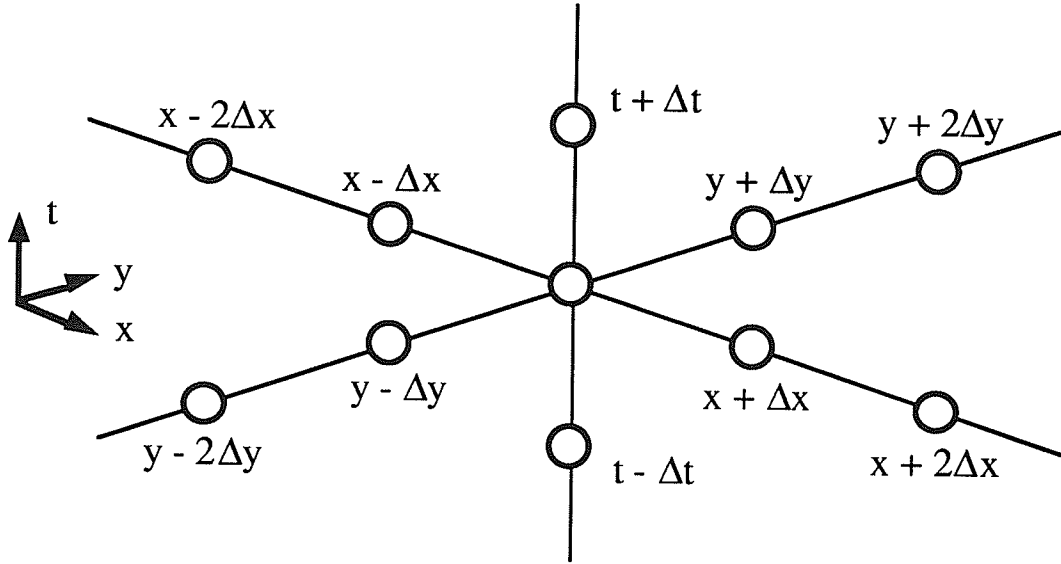

Figure 4.9: Computational molecule for the fourth-order in space and second-order in time finite-difference algorithm.

Following [Vich82], the dispersion relation of the finite-difference algorithm (4.24) is,

$$- \sin^2\left(\beta^* \Delta l \cos\phi\right) - \sin^2\left(\beta^* \Delta l \sin\phi\right)$$

$$+ 16\sin^2\left(\frac{\beta^* \Delta l \cos\phi}{2}\right) + 16\sin^2\left(\frac{\beta^* \Delta l \sin\phi}{2}\right) = \frac{12\Delta l^2}{v^2 \Delta t^2}\sin^2\left(\frac{\omega\Delta t}{2}\right) \tag{4.25}$$

Equation (4.25) describes the fundamental manner in which plane waves propagate through a finite-difference mesh of infinite extent. Given the spatial Δl and temporal discretization Δt, respectively, frequency of excitation ω, direction of propagation ϕ, the numerical phase constant β^* can be obtained from (4.25). The value of β^* can be compared to the exact physical phase constant β to determine the amount of velocity error.

The stability criterion for the spatially fourth-order finite-difference algorithm determined using the Von Neumann method [O'Bri50] is

$$\Delta t \leq \sqrt{\frac{3}{8}} \frac{\Delta l}{v} \tag{4.26}$$

The maximum allowable Courant number is $\sqrt{3/8}$.

The Yee finite-difference time-domain algorithm [Yee66], [Tafl89] is obtained from discretization of Maxwell's curl equations (2.1) using second-order central-difference approximations in both space and time. The Yee algorithm can be expressed in terms of only the electric field values at even space and time steps. In two dimensions the equivalent algorithm in terms of only electric field values is expressed as,

$$\frac{E^t(x+\Delta l,y) - 2E^t(x,y) + E^t(x-\Delta l,y)}{(\Delta l)^2} + \frac{E^t(x,y+\Delta l) - 2E^t(x,y) + E^t(x,y-\Delta l)}{(\Delta l)^2}$$

$$= \frac{1}{v^2} \frac{E^{t+\Delta t}(x,y) - 2E^t(x,y) + E^{t-\Delta t}(x,y)}{(\Delta t)^2} \tag{4.27}$$

The memory storage requirements of the fourth-order in space and second-order in time algorithm (4.24) and the second-order in both space and time algorithm (4.27) are identical. However, the fourth-order in space and second-order in time algorithm (4.24) requires more computation per time step than the second-order algorithm (4.27).

4.4.2: Synthesis of Fourth-Order TLM Model

The spatially fourth-order TLM model is synthesized directly from the finite difference algorithm (4.24). The synthesis closely follows that of the spatially-weighted TLM model [Simo93] presented in the previous section. The propagation velocities of the elemental transmission-lines are selected to mimic the *propagation of information* within the finite-difference algorithm, and the intrinsic impedances of the elemental transmission-lines are selected to provide appropriate weighting between the analogous finite-difference operators.

The fourth-order central-difference operator can be expressed in terms of two second-order operators,

$$\frac{\partial^2 f}{\partial \eta^2} \approx \frac{4}{3} D_{\Delta l} f - \frac{1}{3} D_{2\Delta l} f \tag{4.28}$$

where,

$$D_h f = \frac{f(\eta + h) - 2f(\eta) + f(\eta - h)}{h^2}$$

One operator has a weight 4/3 and operates on a $1\Delta l$ grid, the other has a weight -1/3 and operates on a $2\Delta l$ grid. The spatially fourth-order TLM model is constructed from the interconnection of two original models, one with a mesh spacing of Δl, the other with a mesh spacing of $2\Delta l$. An individual node is provided in Figure 4.10(a), and a mesh of fourth-order TLM nodes is provided in Figure 4.10(b). The required weighting is accomplished by the different intrinsic impedances (Z_1 for elemental transmission-lines 1 to 4 and $-16Z_1$ for elemental transmission-lines 5 to 8), and preservation of the speed of information transfer is accommodated using different propagation velocities (v_1 for elemental transmission-lines 1 to 4 and $2v_1$ for elemental transmission-lines 5 to 8). At all nodal locations, eight elemental transmission-lines intersect. These lines connect a node $(n\Delta l, m\Delta l)$ to nodes $((n\pm1)\Delta l, m\Delta l)$, $((n\pm2)\Delta l, m\Delta l)$, $(n\Delta l, (m\pm1)\Delta l)$, and $(n\Delta l, (m\pm2)\Delta l)$, where n and m are integers describing an arbitrary spatial location in the mesh. Essentially, nodes separated by a distance Δl (in the x and y directions) are directly connected by an elemental transmission-line of intrinsic impedance Z_1 and propagation velocity v_1. Nodes separated by a distance $2\Delta l$ (in the x and y directions) are directly connected by an elemental transmission-line of intrinsic impedance $-16Z_1$ and propagation velocity $2v_1$. Following the development of the spatially-weighted model, two permittivity stubs are used. One is of length $\Delta l/2$, with propagation velocity v_1, and admittance Y_0/Z_1 ; the other of length Δl, with propagation velocity $2v_1$, and admittance $-Y_0/16Z_1$. The complete fourth-order TLM node, with a description of the electrical properties of the elemental transmission-lines, is provided in Figure 4.11.
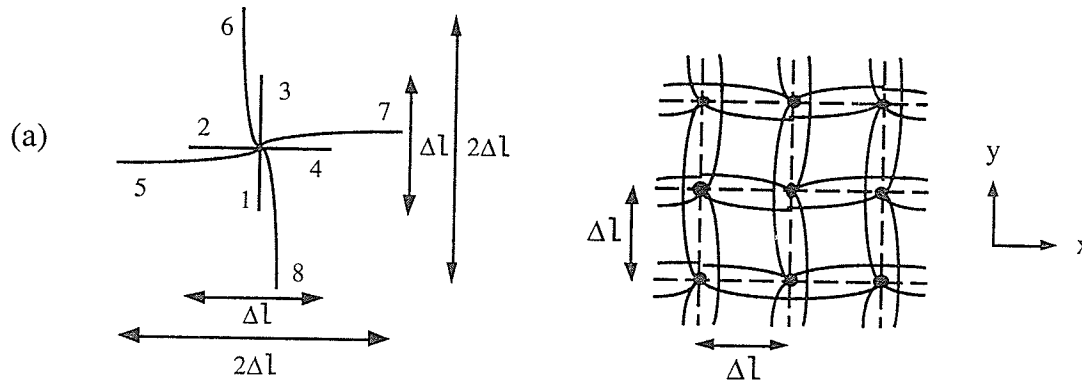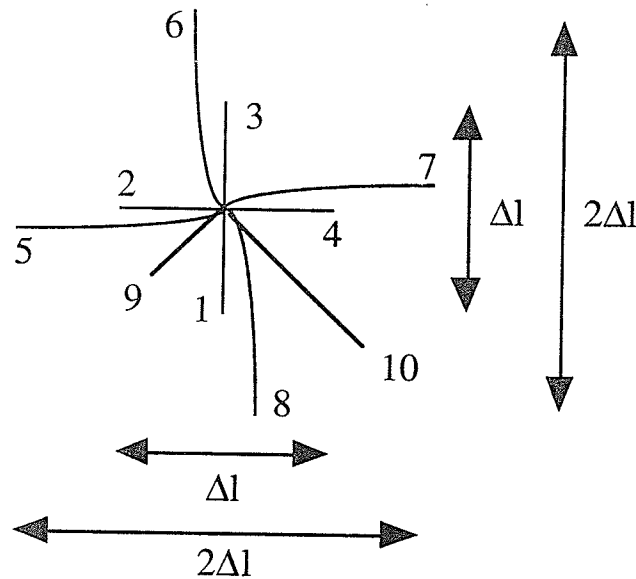
Figure 4.10: Geometry of the spatially fourth-order-accurate TLM model, and a mesh of nodes.

$$V_{1-4} = V_9 = V_1 \qquad Z_{1-4} = Z_1 \;, Z_9 = Z_1/Y_o$$
$$V_{5-8} = V_{10} = 2v \qquad Z_{5-8} = -16Z_1 \;, Z_{10} = -16Z_1/Y_o$$

Figure 4.11: An individual fourth-order TLM node with permittivity stubs for modelling an arbitrary dielectric material.

Following the procedure described in [Brew80] the dispersion relation of the fourth-order TLM model is given by,

$$- \sin^2\left(\beta^* \Delta l \cos\phi\right) - \sin^2\left(\beta^* \Delta l \sin\phi\right)$$

$$+ 16\sin^2\left(\frac{\beta^*\Delta l\cos\phi}{2}\right) + 16\sin^2\left(\frac{\beta^*\Delta l\sin\phi}{2}\right) = \left(30+\frac{15}{2}Y_o\right)\sin^2\left(\frac{\omega\Delta t}{2}\right) \qquad (4.29)$$

Expression 4.29 describes the fundamental manner in which plane waves propagate through an infinite mesh of fourth-order TLM nodes.

Consider a mesh of fourth-order TLM models with a specific value for the stub admittance Y_0. If the finite-difference algorithm (4.24) is operated such that Δl and Δt satisfy,

$$v = \sqrt{\frac{24}{60+15Y_o}}\,\frac{\Delta l}{\Delta t} \qquad (4.30)$$

expressions (4.25) and (4.29) are identical, and therefore the fourth-order finite-difference algorithm and TLM model possess identical dispersion relations. From the finite-difference stability criterion (4.26), the permissible range of values for the stub admittance Y_0 (the stability criterion for the fourth-order TLM model) is given by,

$$Y_o \geq \frac{4}{15} \qquad (4.31)$$

Selecting $Y_0=4/15$ to represent a free-space medium, the relationship between the stub admittance value and the relative dielectric constant of the medium modelled by a mesh of fourth-order nodes is,

$$\varepsilon_r = \frac{60 + 15Y_o}{64} \qquad (4.32)$$

For certain positive stub values (i.e., $0 \leq Y_0 < 4/15$) the fourth-order model is unstable. This instability for a range of positive Y_0 is unique to the fourth-order model. All previously investigated second-order algorithms [Simo91b], [Simo93], [John71] are stable for positive Y_0.

4.4.3: Evaluation of Propagation Characteristics

In Figure 4.12 the propagation characteristics of the original TLM model [John71] and the spatially fourth-order model are compared for propagation along a coordinate

direction. The two curves are provided at the upper limit of stability (i.e., $Y_0=0$ for the original algorithm and $Y_0=4/15$ for the fourth-order algorithm). Two benefits of the fourth-order model are evident. The first benefit is the improved accuracy of the fourth-order model. The second benefit is the increase in cut-off frequency provided by the fourth-order model.

The propagation characteristics of the fourth-order model display different behavior than the second-order models. The second-order models [Simo91b], [Simo93], [John71] simulate a medium in which the propagation velocity is too slow, $v^*/v \leq 1.0$. At the limit of stability and for fine spatial discretization, the fourth-order model simulates a medium in which the propagation velocity is too fast, $v^*/v \geq 1.0$, and for frequencies near cut-off, the fourth-order model simulates a medium in which the propagation velocity is too slow. For propagation along a mesh axis, the accuracy of the fourth-order model is always superior to the original model.
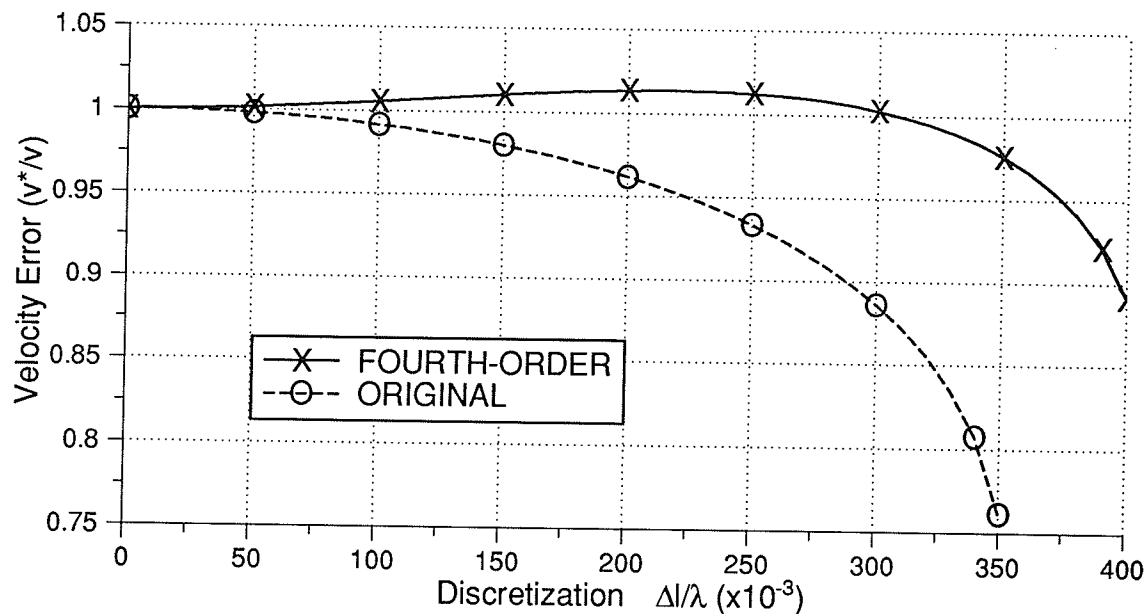

Figure 4.12: Velocity error v^*/v versus $\Delta l/\lambda$ for the original model [John71] and the spatially fourth-order model for propagation along a coordinate direction (both algorithms operated at their respective stability limits).

To gain more insight into the relative performance of the original and fourth-order algorithms, consider the following measure of error for characterizing the various algorithms:

$$E_d\left(\frac{\Delta l}{\lambda}\right) = \frac{1}{360} \sum_{\phi=0^o}^{360^o} \left|\left(\frac{v^*}{v}\right)_{\frac{\Delta l}{\lambda}} - 1\right|$$ (4.33)

The value of $E_d(\Delta l/\lambda)$ will provide a measure of the dispersive errors at a given discretization $(\Delta l/\lambda)$ averaged over all directions of propagation. Therefore, E_d does not provide information regarding the anisotropy of the model. This measure is perhaps more relevant for general problems (in which wave propagation takes place in a variety of different directions) rather than investigating the propagation characteristics for specific directions of propagation. Also, note the normalization factor and the upper limit of the summation can be reduced from 360° to 90° due to the rotational symmetry of the models considered in this section.

In Figure 4.13, the values of E_d are provided for the original and fourth-order models versus $\Delta l/\lambda$. This figure indicates that for $\Delta l/\lambda \le 0.1875$ the original algorithm possesses a slightly lower value of E_d than the fourth-order algorithm. This unexpected result is due to the perfect propagation which occurs in the original algorithm for propagation diagonally through the mesh.
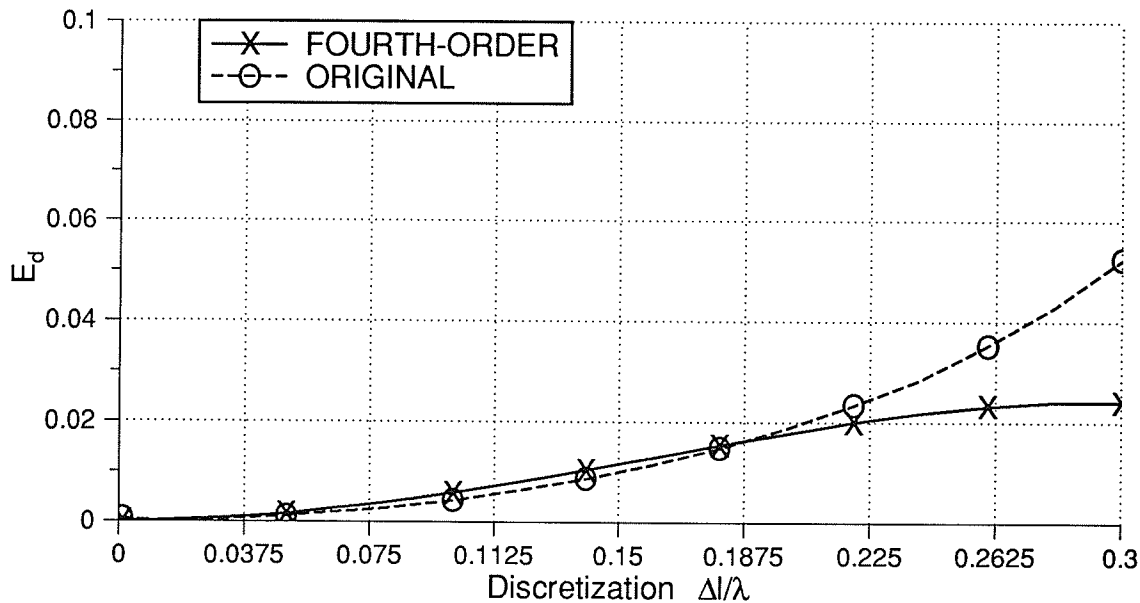

Figure 4.13: Error E_d versus $\Delta l/\lambda$ for the original and fourth-order TLM models (both algorithms operated at their respective stability limits).

In Figure 4.14, the values of E_d for the original and fourth-order algorithms are compared for the case of modelling a dielectric material with $\epsilon_r=4$. These results indicate

superior performance of the fourth-order algorithm. In fact, for increasing values of ε_r, the dispersive errors of the fourth-order algorithm decrease (for small values of $\Delta l/\lambda$). In Figure 4.15, E_d is provided versus $\Delta l/\lambda_d$ for $\varepsilon_r=1$, 2, 10, and 25. The results of this figure indicate that for typical practical discretizations $\Delta l/\lambda<0.10$ the value of E_d decreases with increasing ε_r. This aspect of the behavior of the fourth-order model is distinct from the second-order models. In the equivalent finite-difference algorithms, the effect of increasing ε_r is equivalent to decreasing the Courant number. For the second-order algorithms, it is usually desirable to run simulations at (or very close to) the Courant number, where the optimal propagation characteristics are obtained. This is not the case for the fourth-order algorithm presented in this section. For this reason it may be desirable to renormalize the algorithm for a value of $Y_0>4/15$ to represent a free-space medium such that the optimal propagation characteristics of the fourth-order algorithm can be exploited.
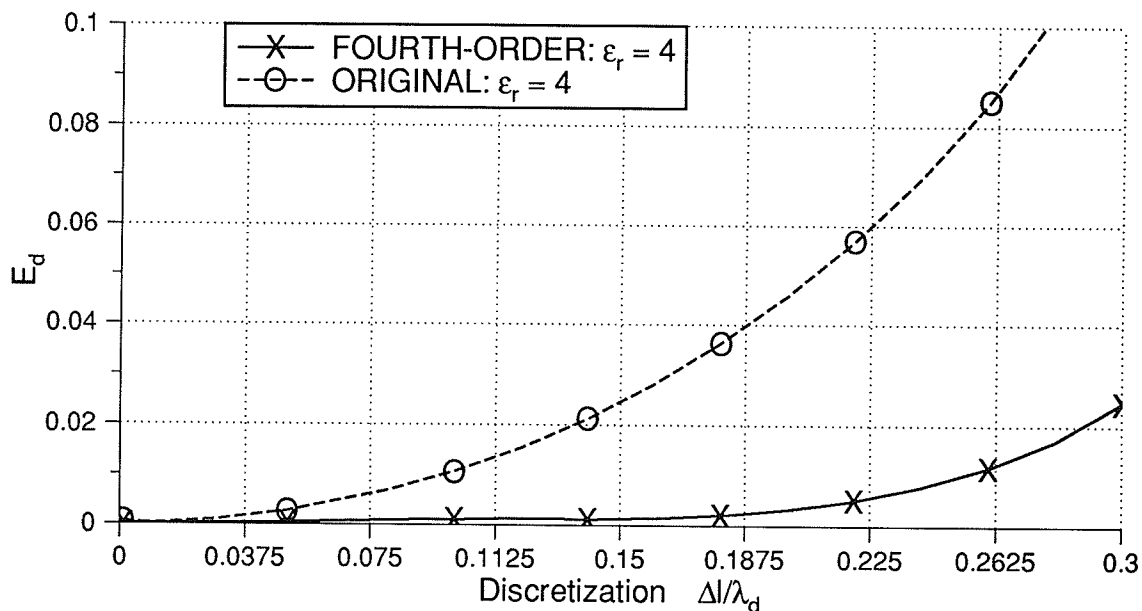

Figure 4.14: Error E_d versus $\Delta l/\lambda$ for the original and fourth-order TLM models for the case of modelling a dielectric material with $\varepsilon_r=4$.
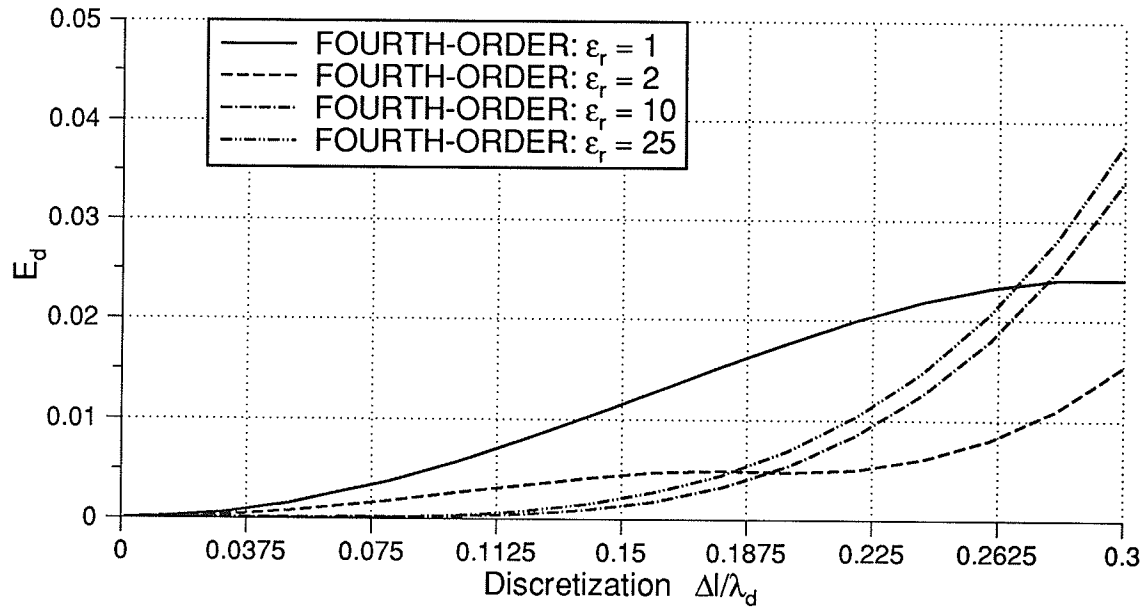
Figure 4.15: Error E_d versus $\Delta l/\lambda$ for the fourth-order TLM model for modelling a dielectric material of ε_r=1, 2, 10, and 25.

4.4.4: Implementation - Scattering and Transfer Events

The nodal scattering matrix for the spatially fourth-order TLM model is assembled by examining the reflection and transmission coefficients of a voltage pulse on each of the ten elemental transmission-lines. For example, a voltage pulse approaching the transmission-line junction on branch 1 (a Z_1 transmission-line) sees a parallel connection of three Z_1 lines, four $-16Z_1$ lines, one Z_1/Y_o line and one $-16Z_1/Y_o$ line. The corresponding reflection coefficient (describing the magnitude of the voltage pulse reflected from the transmission-line junction back onto line 1) is,

$$\Gamma = \frac{\left(\dfrac{3}{Z_1} - \dfrac{4}{16Z_1} + \dfrac{Y_o}{Z_1} - \dfrac{Y_o}{16Z_1}\right)^{-1} - Z_1}{\left(\dfrac{3}{Z_1} - \dfrac{4}{16Z_1} + \dfrac{Y_o}{Z_1} - \dfrac{Y_o}{16Z_1}\right)^{-1} + Z_1}$$

$$= \frac{\dfrac{16}{44 + 15Y_o} - 1}{\dfrac{16}{44 + 15Y_o} + 1} = \frac{-28 - 15Y_o}{60 + 15Y_o}$$

The corresponding transfer coefficient (describing the magnitude of the voltage pulse transmitted to the other nine transmission-line branches) is,

$$T = 1 + \Gamma = \frac{32}{60 + 15Y_o}$$

Following the above procedure, the complete nodal scattering matrix can be assembled:

$$
\begin{bmatrix} v_1^r \\ v_2^r \\ v_3^r \\ v_4^r \\ v_5^r \\ v_6^r \\ v_7^r \\ v_8^r \\ v_9^r \\ v_{10}^r \end{bmatrix} =
\begin{bmatrix}
a & b & b & b & d & d & d & d & f & h \\
b & a & b & b & d & d & d & d & f & h \\
b & b & a & b & d & d & d & d & f & h \\
b & b & b & a & d & d & d & d & f & h \\
b & b & b & b & c & d & d & d & f & h \\
b & b & b & b & d & c & d & d & f & h \\
b & b & b & b & d & d & c & d & f & h \\
b & b & b & b & d & d & d & c & f & h \\
b & b & b & b & d & d & d & d & e & h \\
b & b & b & b & d & d & d & d & f & g
\end{bmatrix}
\begin{bmatrix} v_1^i \\ v_2^i \\ v_3^i \\ v_4^i \\ v_5^i \\ v_6^i \\ v_7^i \\ v_8^i \\ v_9^i \\ v_{10}^i \end{bmatrix}
\qquad (4.34a)
$$

where

$$a = -\frac{28 + 15Y_o}{60 + 15Y_o}$$

$$b = \frac{32}{60 + 15Y_o}$$

$$c = -\frac{62 + 15Y_o}{60 + 15Y_o}$$

$$d = -\frac{2}{60 + 15Y_o}$$

$$e = \frac{17Y_o - 60}{60 + 15Y_o}$$

$$f = \frac{32Y_o}{60 + 15Y_o}$$

$$g = -\frac{60 + 17Y_o}{60 + 15Y_o}$$

$$h = -\frac{2Y_o}{60 + 15Y_o}$$

The transfer event for the fourth-order model is:

$$v_1^i(i,j) = v_3^r(i,j-1)$$

$$v_2^i(i,j) = v_4^r(i-1,j)$$

$$v_3^i(i,j) = v_1^r(i,j+1)$$

$$v_4^i(i,j) = v_2^r(i+1,j)$$

$$v_5^i(i,j) = v_7^r(i,j-2) \qquad\qquad (4.34b)$$

$$v_6^i(i,j) = v_8^r(i-2,j)$$

$$v_7^i(i,j) = v_5^r(i,j+2)$$

$$v_8^i(i,j) = v_6^r(i+2,j)$$

$$v_9^i(i,j) = v_9^r(i,j)$$

$$v_{10}^i(i,j) = v_{10}^r(i,j)$$

where (i,j) denote discrete (x,y) coordinates.

In section 4.4.1 it was noted that increasing the spatial accuracy from second to fourth-order did not require an increase in memory storage requirements for the finite-difference algorithm. This is not true for the TLM model. The fourth-order TLM model requires twice the memory storage of the second-order TLM model. For both the fourth-order TLM and finite-difference algorithms, increasing the spatial accuracy from second to fourth-order requires more computation per time step.

The performance and stability of the spatially fourth-order model has been verified for various wave propagation problems. In Figure 4.16, the improved propagation characteristics of the spatially fourth-order model are demonstrated. The fourth-order model and the original TLM model [John71] are applied to the simulation of a Gaussian-pulsed plane wave. An effective one-dimensional simulation in the x direction is created by applying magnetic walls along the minimum and maximum y boundaries. The fourth-order model preserves the shape of the pulse more accurately than the original model. As well, the fundamental difference in the propagation characteristics provided in Figure 4.12 is evident. The Gaussian pulse contains

significant energy from $\Delta l/\lambda=0$ to approximately 0.250. The dispersion caused by the original model is evident in the trailing edge of the pulse (i.e., certain components of the wave propagate too slow). The dispersion caused by the fourth-order model is evident in the leading edge of the pulse (i.e., some frequency components of the pulse propagate too fast).
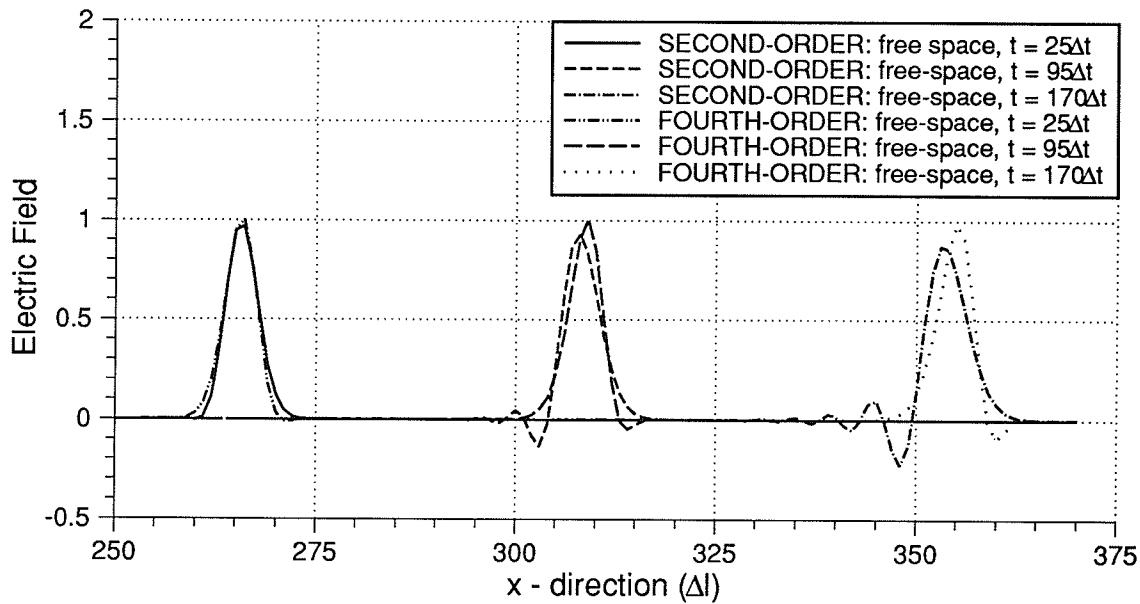

Figure 4.16: Simulation of a Gaussian-pulsed plane wave by a mesh of original nodes [John71], and a mesh of spatially fourth-order nodes.

4.4.5: Computational Efficiency

The dispersive analysis presented in section 4.4.3, and the one-dimensional propagation examples provided in the previous section indicate the superior accuracy of the new fourth-order model. These examples do not, however, demonstrate the computational advantage of the new model in terms of cpu time or memory storage. In [Simo94a], the improved computational performance of the fourth-order model is demonstrated by considering specific examples. The analysis indicates that application of the fourth-order model can result in an increase in computational efficiency, in terms of both cpu time and memory storage.

4.4.6: Potential Benefits of Fourth-Order Models

In this section a spatially fourth-order version of the original two-dimensional TLM algorithm has been presented. The fundamental accuracy of the spatial approximation has been increased from second to fourth-order. The same improvement is possible for the hexagonal [Simo91b] and spatially-weighted TLM models [Simo93] to obtain spatially fourth-order versions. The accuracy of the temporal discretization remains second-order. The concept of a stability criteria has been introduced to the TLM method and is based on the permissible values for the stub admittance Y_o.

As discussed in section 4.4.2, the fourth-order TLM model is constructed with elemental transmission-lines with negative characteristic impedances. Although physically unrealistic, these negative impedance transmission-lines are required to obtain the appropriate weighting present in the equivalent finite-difference algorithm. The negative impedance transmission-lines could have been avoided through the use of bi-directional impedance inverters (which would require infinite bandwidth) to interface lines 1-4 and 9 with lines 5-8 and 10, however, the bi-directional impedance inverters are also physically unrealistic. These aspects of the fourth-order model should not be a cause for concern since TLM models are used as a simulation tool and their physical realizability is not an issue.

Some unique properties of the fourth-order model have emerged. For the modelling of dielectric material, the dispersive errors associated with the algorithm decrease for moderate ε_r (also true for the equivalent finite-difference algorithm). The improved dispersive properties of the fourth-order models make them attractive candidates for the analysis of electrically large (and inhomogeneous) problems.

4.5: General Discussion of the New TLM Models

In this chapter three new TLM models for the two-dimensional wave equation have been presented. These new models demonstrate that some of the flexibility of the finite-difference and finite-element methods are also applicable to the TLM method. This flexibility in grid structure and accuracy has been achieved at the expense of a considerable increase in complexity.

The concept of a stability criteria has been introduced to the TLM method and is based on the permissible values for the stub admittance. One interesting aspect of this

concept is that the hexagonal model permits negative stub admittance values, and the rectangular spatially fourth-order-accurate model is unstable for some positive stub admittance values.

Chapter 5: Applications of the TLM Simulation Program

In this chapter a general purpose electromagnetic simulation program, based on the symmetric-condensed TLM algorithm, is applied to three classes of electromagnetic field problems which include: half-space/remote-sensing of shallow objects; radar-cross section analysis of conducting, dielectric, and composite objects; and the analysis of microstrip antennas and circuit elements.

5.1: Half-Space / Remote-Sensing

In this section, the TLM simulation program is applied to the solution of half-space problems [Simo94b]. Applications involve the evaluation of a remote-sensing systems for the detection of shallow buried objects such as utility pipes/cables, mines, or mineral deposits. In the present analysis, only an idealized electromagnetic system is considered, practical considerations required for a complete remote sensing environment such as the presence of noise and the need for signal processing are neglected. The geometry of the general problem is shown in Figure 5.1. A plane interface separates two regions (I and II). Region I is considered as free space ($\varepsilon_r=1$, $\mu_r=1$, $\sigma=0$). Region II is considered to represent a lossy ground ($\varepsilon_r \neq 1$, $\mu_r=1$, $\sigma \neq 0$). Sources and objects can be located within either region.

Traditionally, integral equation techniques have been applied to the solution of scattering and radiation from objects in the presence of a material half-space [Parh80], [Burk81], [Burk84], [Hela90]. In this approach, an integral equation is formulated to model the presence of any objects and a Sommerfeld type Green's function is used to model the material half space. A limited amount of work however has been performed on the application of differential-equation based numerical methods to the solution of half-space problems. Breakall *et al* presented a preliminary study for the detection of a buried perfectly conducting bar [Brea86]. Results provided by the Yee finite-difference time-

domain algorithm were compared to those calculated by NEC (Numerical Electromagnetics Code - a frequency-domain electric field integral-equation formulation) with the results indicating a reasonable agreement between the two methods. In [Take92a] a similar study is provided that also employs the Yee finite-difference time-domain algorithm. Liu and Shen have applied an axially symmetric two-dimensional TLM algorithm for the analysis of an electromagnetic-pulse logging sonde [Liu91a] and a subsurface radar [Liu91b].
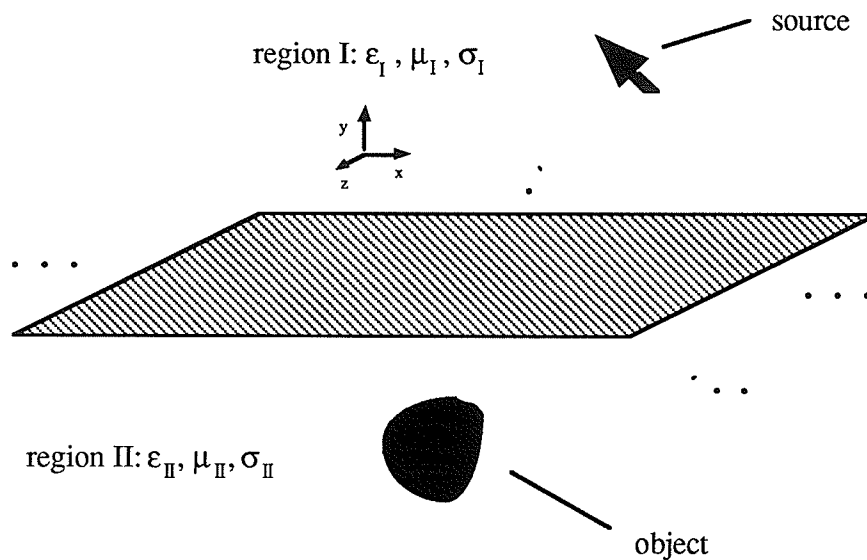
Figure 5.1: Geometry of the general half-space problem.

As shown in Figure 5.2, the TLM mesh used to analyze the half-space problem simulates a cubic region of space which contains the source, scattering objects, as well as portions of each material region. To terminate the exterior boundary of the mesh, a match termination for normal incidence boundary condition is applied where the exterior boundary of the mesh is terminated with the intrinsic impedance of the local medium (see Chapter 3 for details). For simplicity and to maintain a frequency independent boundary condition, the boundary condition is calculated accounting for the permittivity, but not the conductivity of the lossy ground.
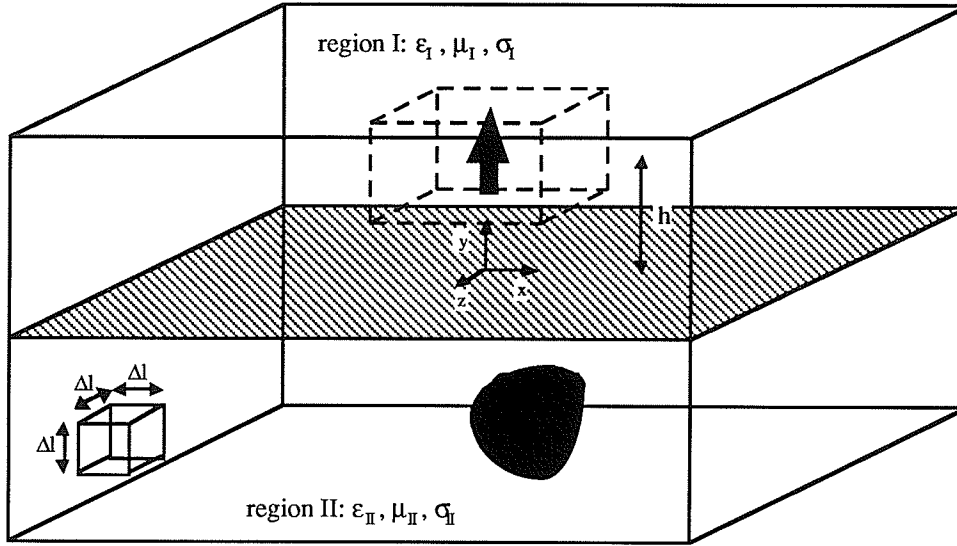
Figure 5.2: Configuration of the TLM mesh applied to the general half-space problem.

The source used in this study is an electrically short electric dipole which can be oriented in x, y, or z directions. To apply the fields produced by this source, the total/scattered field formulation (as described in Chapter 2) is used. Here, the field produced by the electric dipole and that diffracted from the half-space/buried-object are considered to be the incident and scattered fields, respectively. The dashed lines shown in Figure 5.2 define the contour which separates the mesh into total and scattered field regions. The total field exists exterior to the contour and only the scattered field exists within the contour. A similar analysis can be used for magnetic dipole sources to simulate the loop antennas commonly used in detectors for subsurface objects. An analytical form for the source fields is required to apply the total/scattered field formulation. The time-domain fields produced by a z directed electrically short dipole located at the origin of a Cartesian coordinate system are given as [Ziol83],

$$H_x\,(x,y,z,t) = -\frac{y}{4\pi r^3}\left[I(t\text{-}\tau) + \tau\frac{\partial I(t\text{-}\tau)}{\partial t} \right]$$

$$H_y\,(x,y,z,t) = -\frac{x}{y}\,H_x(x,y,z,t)$$

$$H_z(x,y,z,t) = 0$$

<div align="right">(5.1)</div>

$$E_x\,(x,y,z,t) = \frac{xz}{4\pi\varepsilon r^5}\left[3\left(\int I(t\text{-}\tau)\,dt + \tau I(t\text{-}\tau)\right) + \tau^2\frac{\partial I(t\text{-}\tau)}{\partial t}\right]$$

$$E_y\,(x,y,z,t) = \frac{y}{x}\,E_x(x,y,z,t)$$

$$E_z\,(x,y,z,t) = \frac{1}{4\pi\varepsilon r^5}\left[\left(2z^2-\left(x^2+y^2\right)\right)\left(\int I(t\text{-}\tau)\,dt + \tau I(t\text{-}\tau)\right) - \left(x^2+y^2\right)\tau^2\frac{\partial I(t\text{-}\tau)}{\partial t}\right]$$

where $t=r/c$, $r=\sqrt{(x^2+y^2+z^2)}$, and $I(t)$ is the time-domain variation of the current distribution on the dipole, and can be expressed in terms of the dipole moment $p(t)$,

$$I(t) = \frac{dp(t)}{dt} \tag{5.2}$$

In our analysis the time-domain variation of the dipole moment is selected as a Gaussian distribution,

$$p(t) = e^{-(t-t_o)^2/w^2} \tag{5.3}$$

where t_o represents a time delay and w determines the pulse width. The time-domain variation of the current is therefore the derivative of a Gaussian distribution. This selection is made to ensure a zero DC component of the dipole current and thus, a zero DC component of the magnetic field surrounding the source. As noted by Furse *et al* [Furs90], a DC component is slow to evolve and therefore reduces the accuracy and speed of convergence of the discrete Fourier transform. Since the problems considered in this section are not of a highly resonant nature, rapid convergence of the discrete Fourier transform is achieved. The duration of the time-domain simulation required for convergence of the discrete Fourier transform is approximately two to three periods of the lowest desired frequency component. The pulse width of the Gaussian is selected to provide sufficient frequency content over the desired bandwidth.

5.1.1: Numerical Results - Near Fields

The TLM method provides a solution for the electric and magnetic fields at any spatial location within the mesh. In this section numerical results are provided and compared to a spectral domain analytic solution. The time harmonic solution for an electrically short electric harmonic oscillator located above a lossy ground can be obtained by solving the Helmholtz equation in each half-space region. A solution was obtained by Sommerfeld [Somm64] employing the Hankel Transform and is usually presented in an infinite integral form (see [Bano66], [Wait69], [Fels69]). For example, the electric field in the region I (E^I) due to a vertical electric dipole source Idly located at $(0, h, 0)$ is,

$$E^I(x,y,z) = \nabla\nabla\cdot\overline{\Pi}^I + k_I{}^2\overline{\Pi}^I \tag{5.4a}$$

$$\overline{\Pi}^I = \frac{Idly}{-j2\pi\omega\varepsilon_I}\int_0^\infty\left[\frac{e^{-u_I|y-h|}}{2u_I} + \frac{n^2u_I-u_{II}}{n^2u_I+u_{II}}\frac{e^{-u_I(y+h)}}{2u_I}\right]J_0\left(\lambda\sqrt{x^2+y^2}\right)\lambda\,d\lambda \tag{5.4b}$$

$$u_I = \sqrt{\lambda^2+k_I^2} \qquad u_{II} = \sqrt{\lambda^2+n^2k_I^2} \tag{5.4c}$$

where $k_I=\omega\sqrt{(\mu_I\varepsilon_I)}$ and $n^2=(\varepsilon_{II}+j\sigma_{II}/\omega)/\varepsilon_I$. In the following figures, the results referred to as *analytic frequency-domain results* have been obtained by a direct real axis integration of these integrals. The results referred to as *analytic time-domain results* have been obtained by applying the discrete Fourier transform to the analytic frequency-domain data with the appropriate source excitation $I(\omega)$ [Brid93].

The time-domain and frequency-domain fields for two typical simulations are provided in Figures 5.3-5.5. The results shown in Figure 5.3 are for a y directed electrically short electric dipole (VED) located h=0.055m above the interface. The specific time-domain form of the dipole moment is given in (5.3) with t_0=70Δt and w=15Δt. The two regions (I and II) are characterized by $\varepsilon_I=\varepsilon_0$, $\mu_I=\mu_0$, $\sigma_I=0$, $\varepsilon_{II}=4.0\varepsilon_0$, $\mu_{II}=\mu_0$, and $\sigma_{II}=0.1$S/m. The observation location for Figure 5.3 is located at (0.0m, 0.005m, 0.07m) (i.e., in region I, 0.005m above the interface). A comparison of the analytic and TLM time-domain E_y and E_z field components are provided in Figure 5.3. The E_x component will be zero at this location. The magnitude of the E_y and E_z components in the frequency domain (at the same observation locations) are provided in Figure 5.4.

The frequency domain results of a similar case with h=0.0275m and $\varepsilon_I=\varepsilon_o$, $\mu_I=\mu_o$, $\sigma_I=0$, $\varepsilon_{II}=4.0\varepsilon_o$, $\mu_{II}=\mu_o$, and $\sigma_{II}=0.01S/m$ are provided in Figure 5.5. The magnitude of the E_y and E_z components of the total electric field at an observation point just below the interface (0.0m, -0.0025m, 0.035m) are provided over a bandwidth of 0.2 to 3.0GHz.

The results for both cases show the agreement between the spectral domain analytic and numerical TLM techniques is within a few percent. The mesh used for the TLM calculations of Figures 5.3-5.5 is of size $40\Delta l$ by $40\Delta l$ by $40\Delta l$, where Δl=0.01m and 0.005m, respectively. The above results demonstrate the accuracy of the TLM technique for this class of problem. The electrical size of a problem that can be accurately characterized using the TLM technique is related to the computational capabilities of the user. The algorithm can provide accurate results over a wide frequency band from a single simulation. The lower limit of the frequency band is determined by the electrical distance from the source to the outer mesh boundary (where the absorbing boundary condition is applied). The upper limit of the frequency band is determined by the spatial discretization ratio $\Delta l/\lambda$. The CPU time required for the analysis of the problems considered in this section is on the order of one hour on a SUN Sparcstation 10.
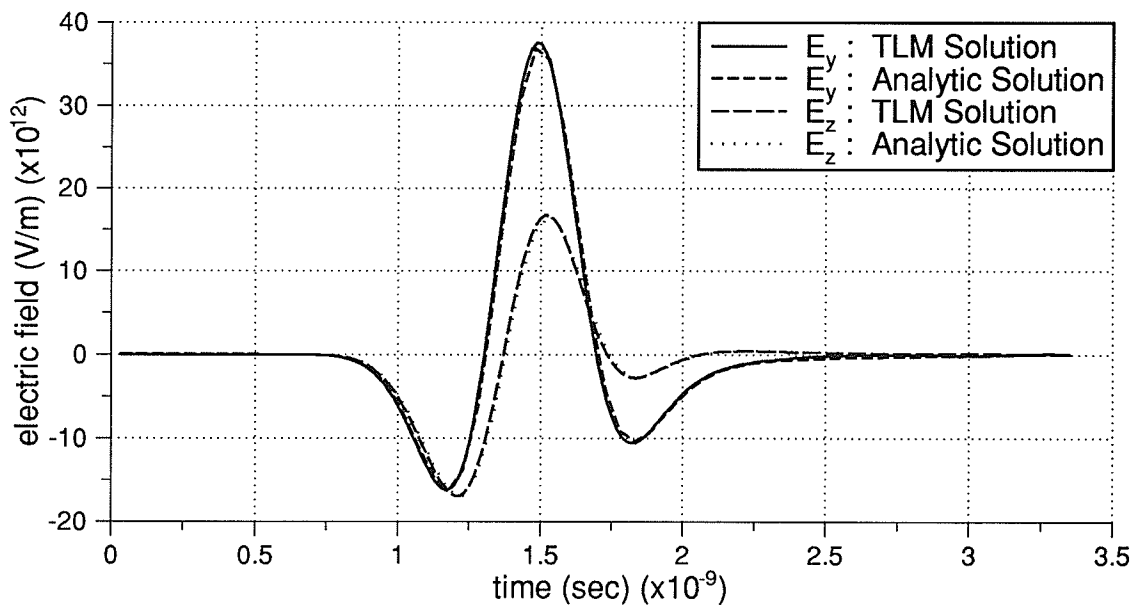

Figure 5.3: Comparison of TLM and analytic time-domain solutions for the y and z components of the electric field for the h=0.055m problem.
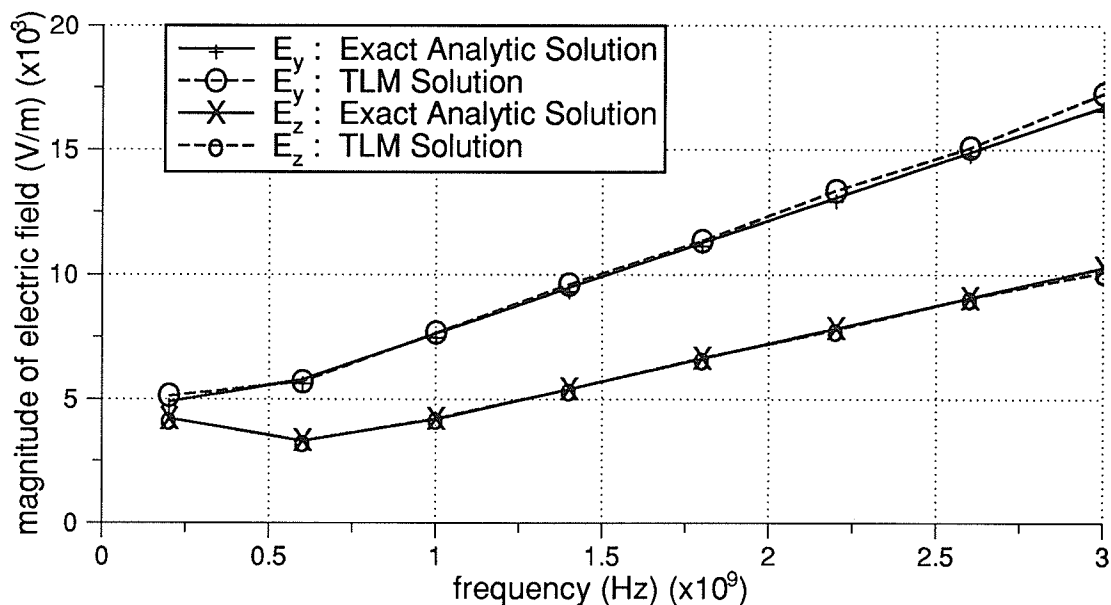
Figure 5.4: Comparison of TLM and analytic frequency-domain solutions for the y and z components of the electric field for the h=0.055m problem.
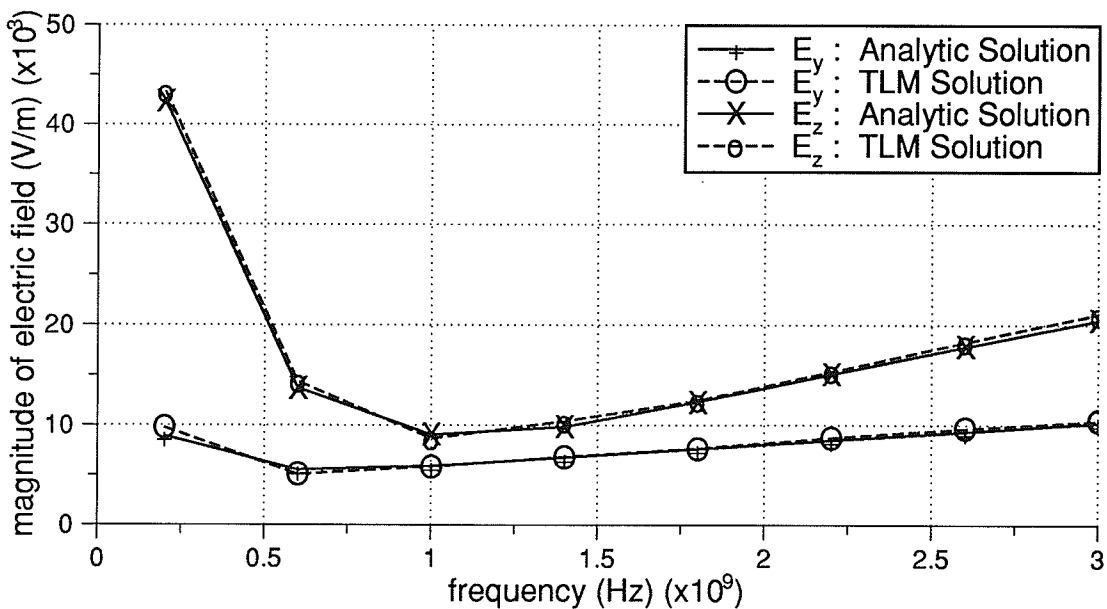

Figure 5.5: Comparison of TLM and analytic frequency-domain solutions for the y and z components of the electric field for the h=0.0275m problem.

5.1.2: Evaluation of Change in Source Input Impedance

The input impedance of an antenna is affected by obstacles located in its near field. Therefore, sensing the variation in the input impedance of an antenna can yield information about its surrounding environment. The change in the input impedance of an electric dipole source can be obtained via the *induced emf method* [Bala89], where knowledge of the scattered field is required. In our analysis, the dipole is assumed to be electrically short and carry a uniform current I along its length dl. The scattered field at the source location, E^s, is then used to determine the voltage induced on the electric dipole due to the half-space and any other scattering objects as,

$$\Delta V = E^s \cdot dl \qquad\qquad (5.5)$$

The change in the input impedance, ΔZ due to the presence of the half-space and underground object is $\Delta Z = \Delta V/I$. As noted in the previous sections, the TLM simulation provides an approximate solution for the electric and magnetic fields at any spatial location within the mesh, this including a solution for the scattered field at the source location using the total/scattered field formulation. The use of the total/scattered field formulation allows for only first-order interaction of the source and scatterer, with the subsequent re-radiation and higher-order couplings being ignored. The same assumption is made in the formulation of an analytic solution [Wait69].

The TLM scheme has been used to determine the change in the input impedance of the electric dipole caused by the presence of the material half-space. The results presented are normalized to the radiation resistance of the dipole in free space $(R_o=80(\pi dl/\lambda)^2)$. Table 5.1 provides a comparison of TLM results and image theory [Alan84] for $\Delta Z/R_0$ of a y directed (vertical) electric dipole located at a height of h=0.0275m above the interface. The material properties of region I are characterized by $\varepsilon_I=\varepsilon_0$, $\mu_I=\mu_0$, and $\sigma_I=0.0$. The material properties of region II are provided in Table 5.1 in a complex permittivity form ($\mu_{II}=\mu_0$ for all cases). The excitation frequency is 1.091GHz for all cases, corresponding to h=0.1λ.

Table 5.1: $\Delta Z/R_0$ of a VED in the Presence of a Lossy Half Space

ε_{II}	TLM	Exact Image Theory	% difference
2.0 - j 0.2	0.45 + j 0.65	0.53 + j 0.64	15.0 + j 1.5
2.0 - j 2.0	1.29 + j 0.70	1.32 + j 0.69	2.3 + j 1.4
2.0 - j 20.0	1.37 + j 2.01	1.43 + j 2.00	4.2 + j 0.5
9.0 - j 0.9	0.99 + j 1.50	1.05 + j 1.57	5.7 + j 4.4
9.0 - j 9.0	1.29 + j 1.68	1.32 + j 1.70	2.3 + j 1.2
9.0 - j 90.0	1.07 + j 2.20	1.13 + j 2.18	5.3 + j 0.9
40.0 - j 4.0	1.00 + j 1.90	1.05 + j 1.93	4.8 + j 1.5
40.0 - j 40.0	1.07 + j 2.04	1.12 + j 2.04	4.5 + j 0.0
40.0 - j 400.0	0.92 + j 2.27	0.98 + j 2.23	6.1 + j 1.8

all cases h=0.0275m, f=1.091GHz (h=0.1λ)

In Figure 5.6, the input impedance change $\Delta Z/R_0$ for a VED as calculated using the spectral domain analytic solution (5.4) is compared to results obtained from a single TLM simulation. The problem geometry is specified as: h=0.055 m, $\varepsilon_I=\varepsilon_0$, $\mu_I=\mu_0$, $\sigma_I=0$, $\varepsilon_{II}=9.0$, $\mu_{II}=\mu_0$, and $\sigma_{II}=0.0$, 0.1 and 1.0S/m. The results are provided over the frequency range 0.5 to 3.0GHz and indicate reasonable agreement between the analytic and numerical results.

In Figure 5.7, the spectral domain analytic solution is compared to results obtained from a TLM simulation for the case of a z directed (*i.e.,* horizontal) electric dipole (HED) with the following parameters: h=0.055m, $\varepsilon_I=\varepsilon_0$, $\mu_I=\mu_0$, $\sigma_I=0$, $\varepsilon_{II}=9.0$, $\mu_{II}=\mu_0$, and $\sigma_{II}=0.1$S/m. The results are provided over a frequency range 0.5 to 3.0GHz and indicate reasonable agreement between the two methods. The simulation space used for this example is a cube of size 49Δl, with a spatial step Δl=6.47mm.
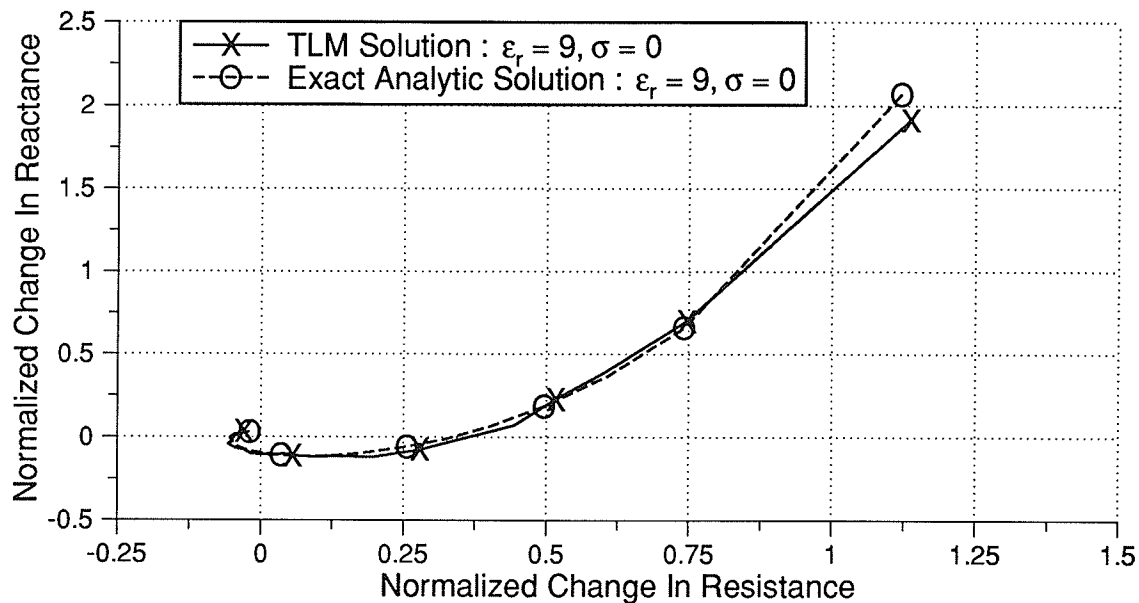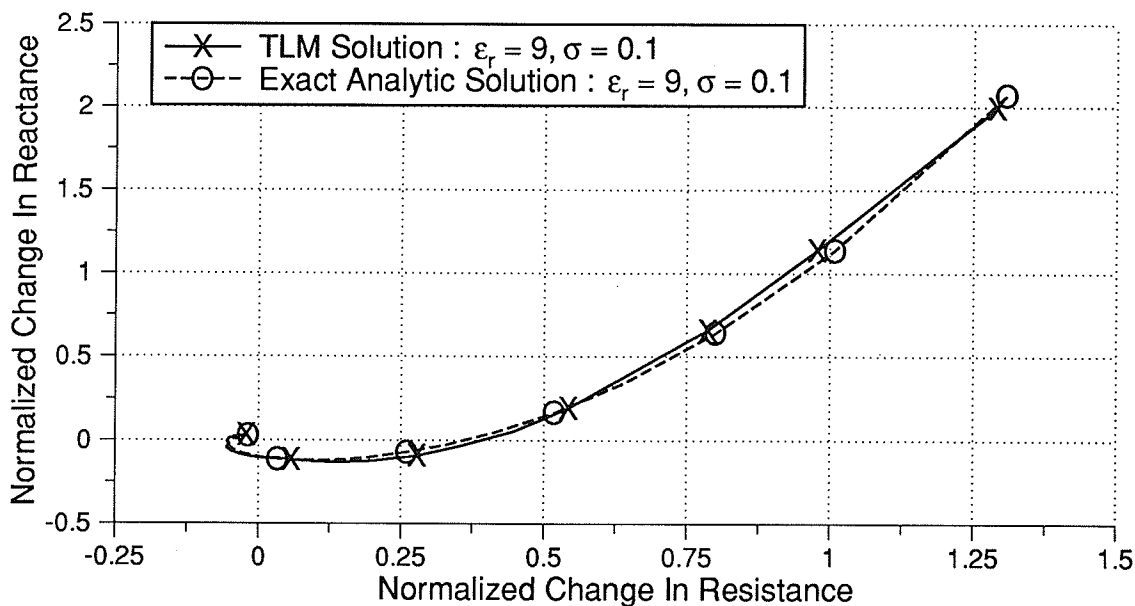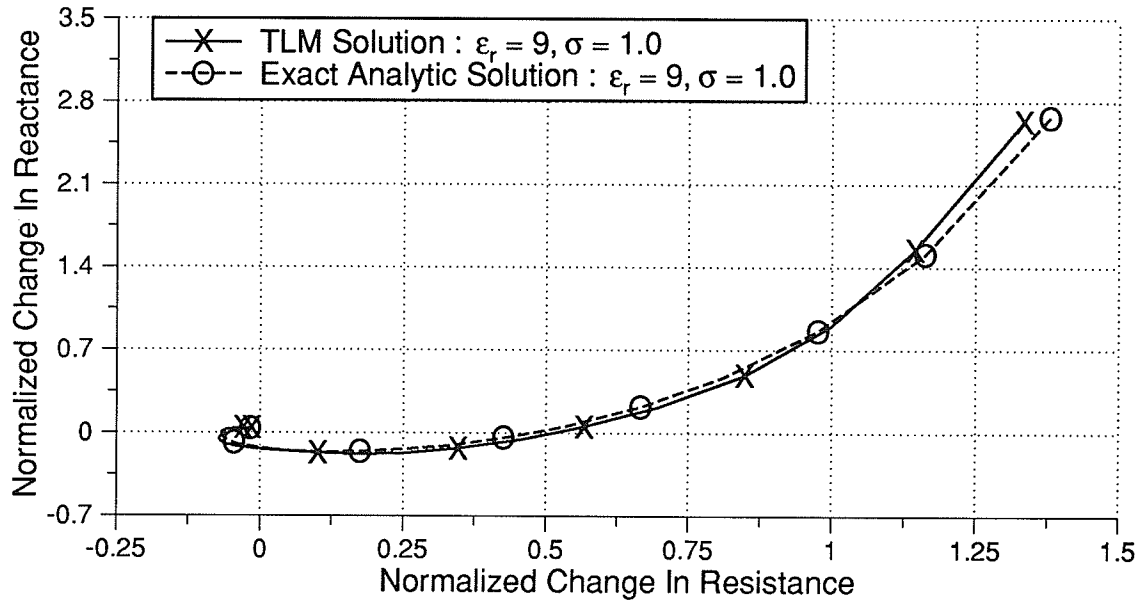
Figure 5.6(a): Comparison of TLM and analytic frequency-domain solutions for $\Delta Z/R_0$ for a **y** directed dipole (VED) with h=0.055m, $\varepsilon_I=\varepsilon_0$, $\mu_I=\mu_0$, $\sigma_I=0$, $\varepsilon_{II}=9.0$, $\mu_{II}=\mu_0$, and $\sigma_{II}=0.0$S/m.
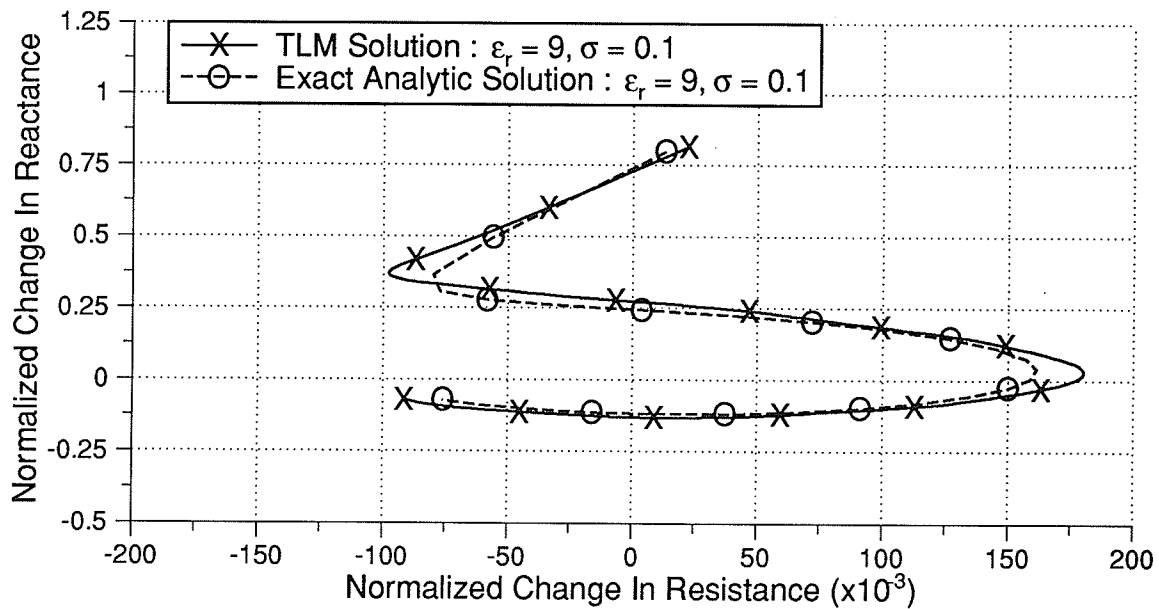

Figure 5.6(b): Comparison of TLM and analytic frequency-domain solutions for $\Delta Z/R_0$ for a **y** directed dipole (VED) with h=0.055m, $\varepsilon_I=\varepsilon_0$, $\mu_I=\mu_0$, $\sigma_I=0$, $\varepsilon_{II}=9.0$, $\mu_{II}=\mu_0$, and $\sigma_{II}=0.1$S/m.

Figure 5.6(c): Comparison of TLM and analytic frequency-domain solutions for $\Delta Z/R_0$ for a **y** directed dipole (VED) with h=0.055m, $\varepsilon_I=\varepsilon_0$, $\mu_I=\mu_0$, $\sigma_I=0$, $\varepsilon_{II}=9.0$, $\mu_{II}=\mu_0$, and $\sigma_{II}=1.0$S/m.

Figure 5.7: Comparison of TLM and analytic frequency-domain solutions for $\Delta Z/R_0$ for a **z** directed dipole (HED) with h=0.055m, $\varepsilon_I=\varepsilon_0$, $\mu_I=\mu_0$, $\sigma_I=0$, $\varepsilon_{II}=9.0$, $\mu_{II}=\mu_0$, and$\sigma_{II}=0.1$S/m.

5.1.3: Sensing an Underground Object

In the previous section the change in source input impedance caused by the presence of a lossy half space was examined. As discussed in [Wait69], the system shown in Figure 5.8 can be applied to determine properties of the environment. Consider the problem of detecting shallow underground objects by monitoring the change in input impedance of a dipole antenna probe. To detect the object, sufficient perturbation in the input impedance must occur as a result of the object when compared to the perturbation due to the half space. In Figures 5.8-5.10, results examining the detection of a perfectly conducting square plate are presented. The results in the Figures are provided over the frequency range 0.5 to 3.0GHz. In Figure 5.8, the dependence of $\Delta Z/R_0$ on plate size is examined. As expected, as the plate size is increased, the effect on $\Delta Z/R_0$ increases. The $\Delta Z/R_0$ curve obtained from a simulation without the plate is provided for comparison. The effect of the plate depth on the input impedance is demonstrated in Figure 5.9. As the depth of the plate is increased, the effect on $\Delta Z/R_0$ decreases. Figure 5.10 contains results which demonstrate the effect of the ground conductivity. As the conductivity of the ground is increased, the effect on $\Delta Z/R_0$ decreases. The simulation space used to analyze this problem is of size $40\Delta l$ by $40\Delta l$ by $40\Delta l$, where $\Delta l = 0.01$m.
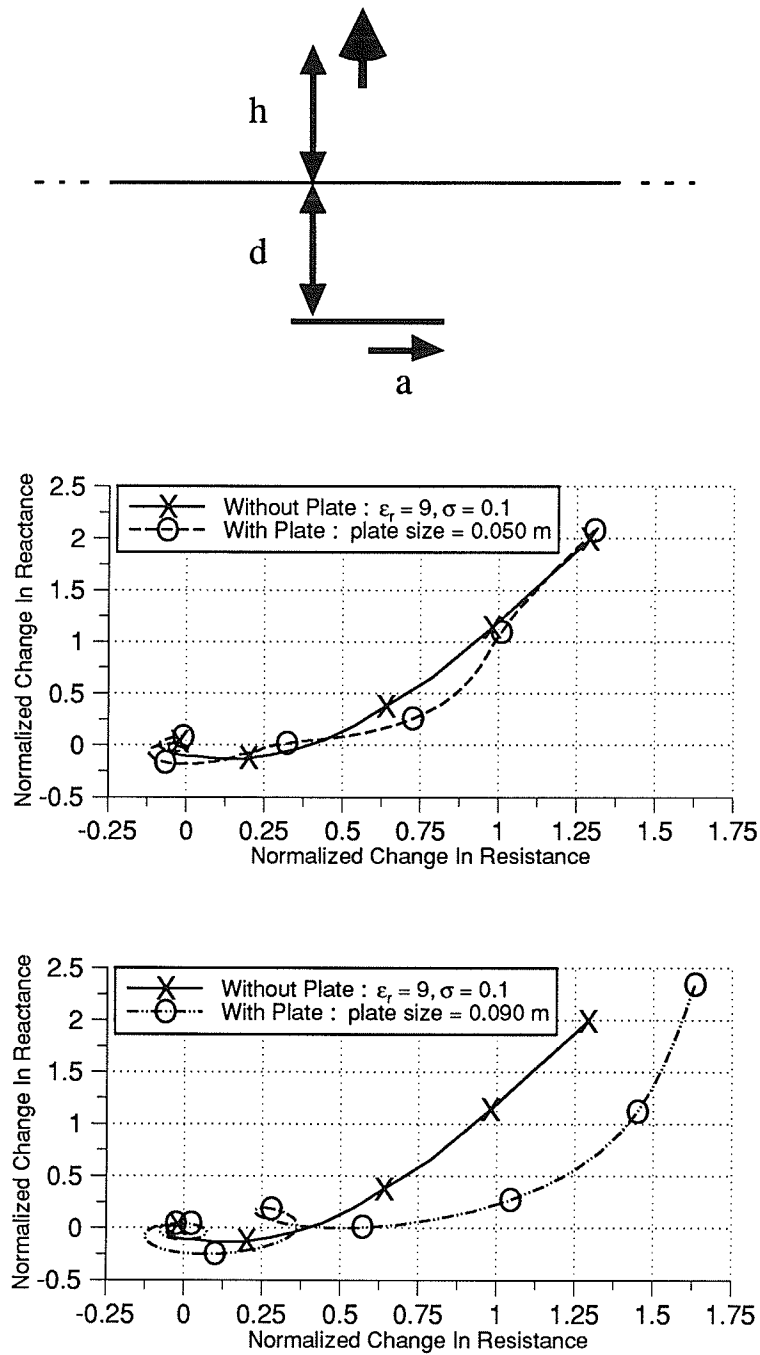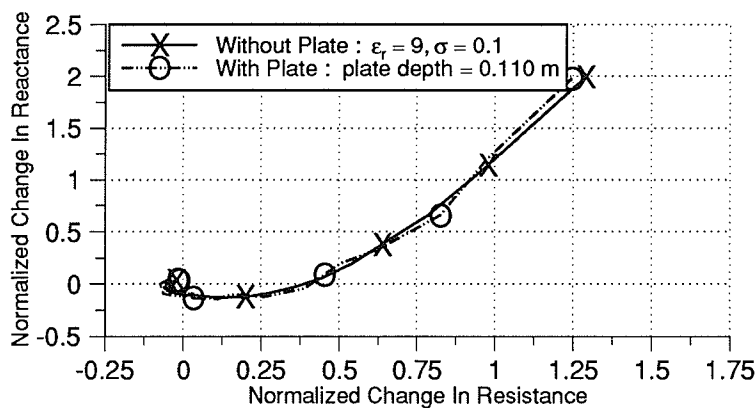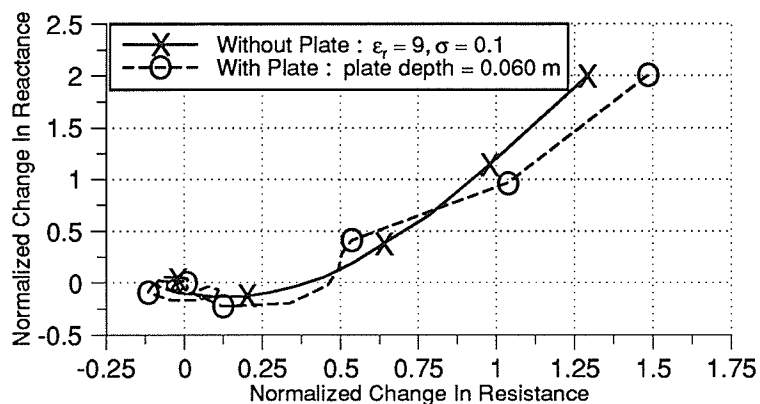
Figure 5.8: Variation of $\Delta Z/R_0$ with respect to plate size for sensing a perfectly conducting square plate. Dipole height h=0.055 m, plate depth d=0.045m, $\varepsilon_I=\varepsilon_0$, $\mu_I=\mu_0$, $\sigma_I=0$, $\varepsilon_{II}=9.0$, $\mu_{II}=\mu_0$, and $\sigma_{II}=0.1$S/m. Plate radii considered are (a) a=0.050m , and (b) a=0.090m

Figure 5.9: Variation of $\Delta Z/R_0$ with respect to plate size for sensing a perfectly conducting square plate. Dipole height h=0.055 m, plate size = 0.070m, $\varepsilon_I=\varepsilon_o$, $\mu_I=\mu_o$, $\sigma_I=0$, $\varepsilon_{II}=9.0$, $\mu_{II}=\mu_o$, and $\sigma_{II}=0.1$. Plate depths considered are (a) 0.06m, and (b) 0.11m.
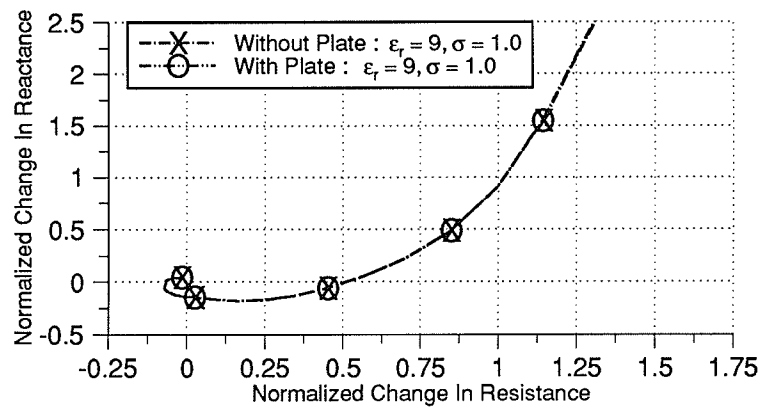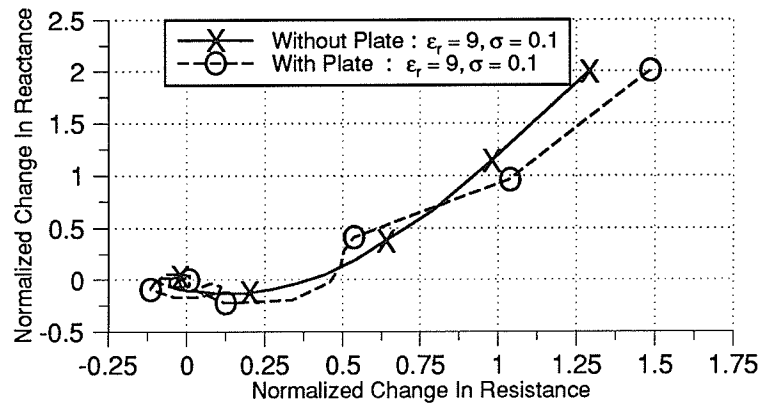
Figure 5.10: Variation of $\Delta Z/R_0$ with respect to plate size for sensing a perfectly conducting square plate. Dipole height h=0.055 m, plate size=0.070 m, plate depth=0.060 m, $\varepsilon_I=\varepsilon_0$, $\mu_I=\mu_0$, $\sigma_I=0$, $\varepsilon_{II}=9.0$, $\mu_{II}=m_0$. Ground conductivities considered are (a) $\sigma_{II}=0.1$, and (b) $\sigma_{II}=1.0$S/m.

5.2: Radar-Cross-Section Analysis

In this section the three-dimensional symmetric-condensed transmission line matrix (TLM) model is applied to the analysis of electromagnetic scattering from finite sized conducting and dielectric objects. The specific structures analyzed include conducting cubes, conducting plates and dielectric cubes. Based on this investigation, various guidelines for the successful application of the TLM method to this class of problem are provided. These objects have been selected for validation purposes (since some measured data and numerical results exist for these objects). These objects do not demonstrate the utility of the differential-equation based approach *i.e.*, the analysis of inhomogeneous objects.

A wide variety of the numerical methods that can be applied to the analysis of radar cross section are presented in [Ston89]. The numerical techniques employed involve the numerical approximation of integral-equation [Mill92], or differential-equation based formulations. With respect to differential-equation based formulations: the Yee finite-difference time-domain method has been extensively applied [Umas82], [Tafl89], [Brit89], [Furs90]; various finite-element formulations have been presented [Cang87], [Maye91], [Jin92a], [Yuan90]; as well as time-domain finite-volume algorithms [Shan90]; and some initial investigations involving the transmission-line matrix method [Germ90a].

The simulation space used to analyze the electromagnetic scattering problem is provided in Figure 5.11. The simulation space models the object and a region of space surrounding it. The conducting and material regions of the objects are modelled using the techniques described in Chapter 3. An outline of the total/scattered field contour, along which the source is applied, is shown as a dashed line in Figure 5.11. The source can be either a plane-wave (with arbitrary angle of incidence and polarization) or an electrically short electric dipole that can be oriented in the x, y, or z directions. In the previous section, the dipole source has been applied in the analysis of radiation and scattering in the presence of a material half-space. To terminate the exterior boundary of the mesh, the match termination for normal incidence boundary condition is applied (see discussion in Chapter 3).
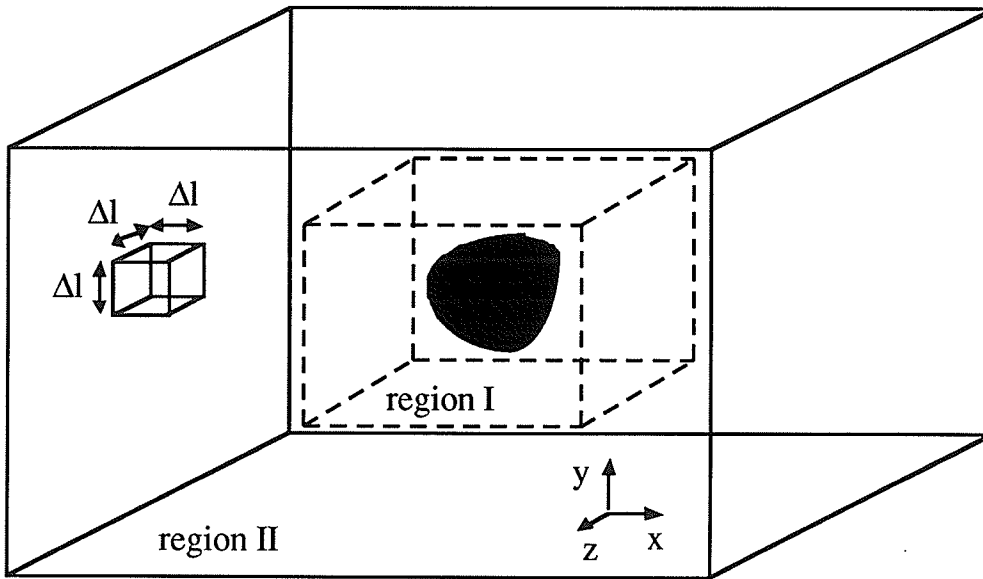
Figure 5.11: Simulation space used for the analysis of an RCS problem. The dashed line outlines the total/scattered field contour. A gaussian-pulsed plane wave of arbitrary angle of incidence is specified as the excitation.

Equivalent currents surrounding the geometry are used as sources to determine the scattered far field patterns (following [Harr61]). The equivalent surface currents are calculated along a contour located outside of the total/scattered field contour. The near-field to far-field transformation is performed in the frequency domain. The frequency domain equivalent currents are obtained via discrete Fourier transformation of the time domain equivalent currents. The discrete Fourier transformation is performed incrementally during the computation and therefore the entire time domain response at each spatial location on the transformation contour is not explicitly stored. The equivalent currents are obtained from tangential electric and magnetic fields along the contour by,

$$\mathbf{M_e} = -\,\mathbf{n} \times \mathbf{E} \qquad \mathbf{J_e} = \mathbf{n} \times \mathbf{H} \qquad\qquad (5.6)$$

where $\mathbf{M_e}$ and $\mathbf{J_e}$ are the equivalent magnetic and electric surface currents, respectively, and $\mathbf{n}$ is a unit normal vector to the surface. These surface currents are transformed to the far-field using the free-space Green's function by,

$$E_\theta = -jk\eta \left(A_\theta + \frac{F_\phi}{\eta} \right) \qquad\qquad (5.7a)$$

$$E_\phi = -jk\eta \left(A_\phi + \frac{F_\theta}{\eta} \right) \qquad (5.7b)$$

where

$$A_\theta = A_x \cos\theta \cos\phi + A_y \cos\theta \sin\phi - A_z \sin\theta$$

$$F_\theta = F_x \cos\theta \cos\phi + F_y \cos\theta \sin\phi - F_z \sin\theta$$

$$A_\phi = -A_x \sin\phi + A_y \cos\phi$$

$$F_\phi = -F_x \sin\phi + F_y \cos\phi$$

and

$$A(r) = \frac{e^{-jkr}}{4\pi r} \int_S J(r') e^{-jkr' \cos\zeta} dS$$

$$F(r) = \frac{e^{-jkr}}{4\pi r} \int_S M(r') e^{-jkr' \cos\zeta} dS$$

and $r' \cos\zeta = (x' \cos\phi + y' \sin\phi)\sin\theta + z' \cos\theta$, and the primed coordinates denote a spatial location on the contour and the non-primed coordinates indicate an observation point.

5.2.1: Perfectly Conducting Objects

5.2.1.1: Perfectly Conducting Thin Plate

The first geometry considered is a perfectly-conducting infinitely-thin square plate illuminated by a **y** polarized plane wave incident from $\theta_i = 0^\circ$ (see Figure 5.12). For the TLM analysis, a simulation space of size $41\Delta l$ by $41\Delta l$ by $41\Delta l$ is used, within which the plate is of size $20\Delta l$ by $20\Delta l$ and is centered within the mesh. For this example 350 time steps were required for convergence of frequency domain results. The TLM results for the θ and ϕ components of the bistatic radar cross section are compared to results

from Mahadevan *et al* [Maha92] in Figures 5.13(a) and 5.13(b), respectively. The results are provided for a square plate with an electrical size of 1.0λ and 2.0λ. The patterns are symmetric about $\theta = 90°$ and therefore the portion of the curve from $\theta = 90°$ to $180°$ is not provided. Reasonable agreement between the TLM results and the results from [Maha92] is obtained. In addition to the results contained in Figures 5.13, additional numerical results have been obtained for plate sizes of 0.5λ and 1.5λ [Simo94c].
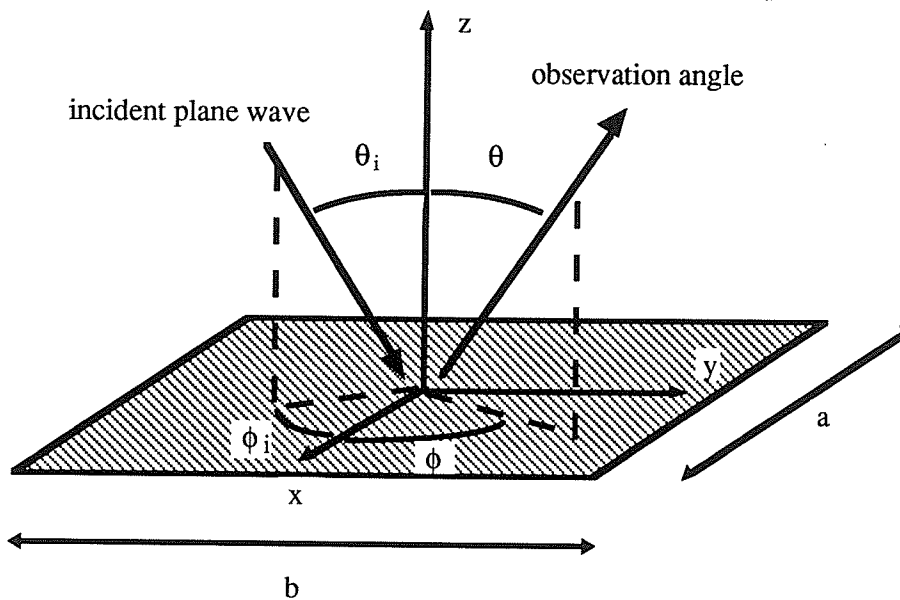

Figure 5.12: Perfectly conducting, infinitely thin, rectangular plate (size a by b). Plane wave incident from θ_i, ϕ_i.

As previously mentioned, the plate is discretized using $20\Delta l$ for each side length. The 1.0 and 2.0λ square plates correspond to discretizations of $\Delta l/\lambda = 20.0$ and $\Delta l/\lambda = 10.0$, respectively, which are within the typical guidelines for acceptable accuracy [Tafl89]. The distance from the plate to the absorbing boundary condition is $20.5\Delta l$ in the forward and back scattering directions and $10\Delta l$ in the plane of the plate. For the 1.0λ square plate this corresponds to an electrical distance of 1.0λ in the forward and back scattering direction and 0.5λ in the plane of the plate. For the 2.0λ square plate this corresponds to an electrical distance of 2.0λ in the forward and back scattering directions and 1.0λ in the plane of the plate. The contour used to perform the near to far field transformation is the surface of a cube with equal side lengths of $32\Delta l$. The total/scattered field contour used to apply the plane wave excitation is the surface of a cube with equal side lengths of $25\Delta l$.
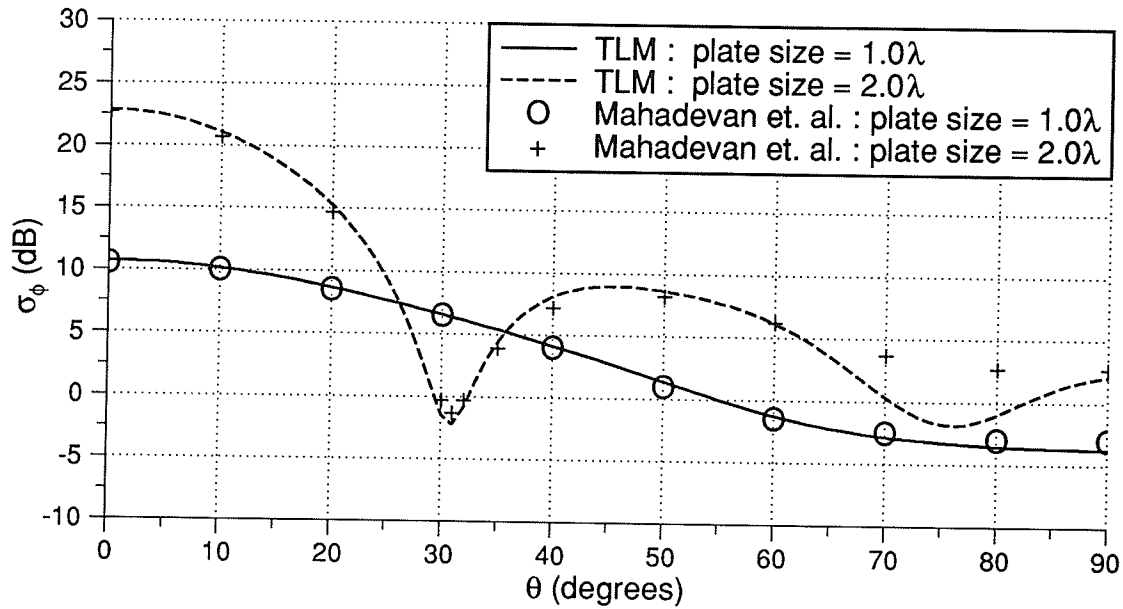
Figure 5.13(a): Comparison of results calculated by the TLM simulation program and results from [Maha92] for a 1.0λ and 2.0λ square plate in the φ=90°plane.
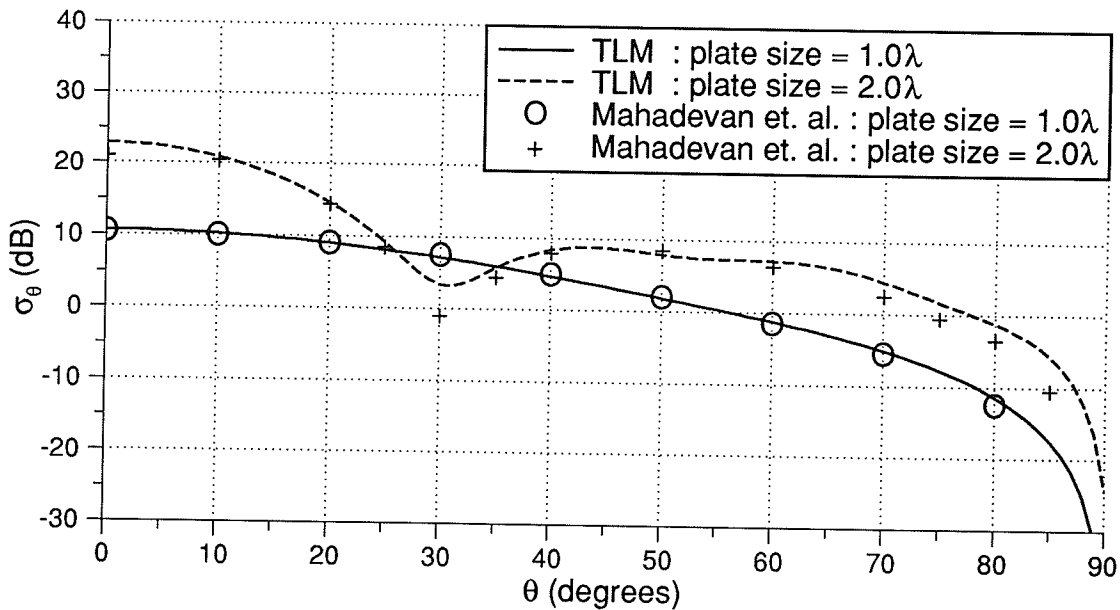

Figure 5.13(b): Comparison of results calculated by the TLM simulation program and results from [Maha92] for a 1.0λ and 2.0λ square plate in the φ=0°plane.

To demonstrate the ability of the program to provide accurate results over a wide bandwidth, the back scattering cross section of the thin conducting plate has been calculated for an electrical size of plate (in terms of the side length) ranging from 0.2 to 1.0λ. The TLM results are compared in Figure 5.14, to those from [Rao82] obtained using a method-of-moments solution to a frequency-domain electric-field integral-equation formulation. Good agreement between the TLM results and those from [Rao82] is obtained.
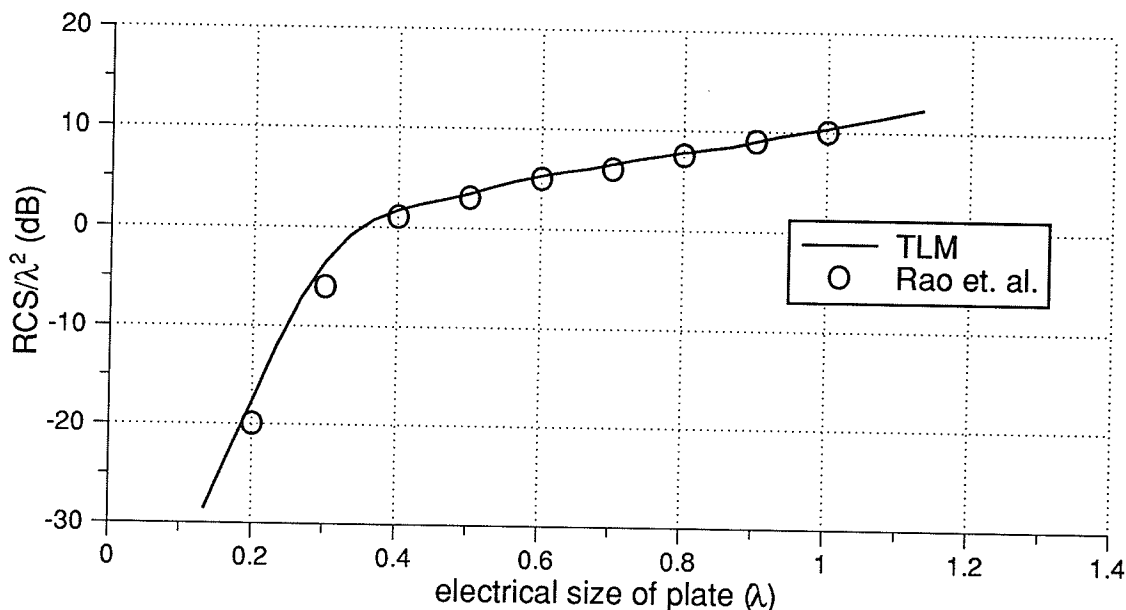

Figure 5.14: Comparison of results calculated by the TLM simulation program and results from [Rao82] for the back-scattering cross-section of a square conducting plate versus the electrical side length of the plate.

5.2.1.2: Perfectly Conducting Cube

The second object analyzed is a conducting cube, shown in Figure 5.15. The numerical results for the bistatic radar-cross-section of a conducting cube of side length 1.5λ determined by the TLM simulation program are presented in Figure 5.16. The (a), (b), and (c) parts of Figure 5.16 correspond to the bistatic patterns in the E-, H-, and 45º-planes, respectively. The results are compared to measured data and numerical results from a frequency-domain augmented-magnetic-field-integral-equation (AMFIE) formulation provided in [Cote88]. Good agreement between the TLM, measured and AMFIE results is obtained.

Results for the back scattering cross-section versus the electrical size of the cube are provided in Figure 5.17. The TLM results are compared to measured data from [Cote88]. Good agreement is observed over the entire frequency range provided in Figure 5.17. These results again demonstrates the ability of the program to provide accurate results over a wide bandwidth. The back scattering cross section of the conducting cube has been calculated for an electrical size (in terms of the side length of the cube) ranging from 0.2 to 3.2λ. The cube is modelled using $20\Delta l$ per side in a $57\Delta l$ by $57\Delta l$ by $57\Delta l$ cubic simulation space. The range in the electrical size of the cube for the results provided in Figure 5.17 corresponds to discretizations from $\Delta l=\lambda/100$ to $\Delta l=\lambda/6.2$. The upper limit of the discretization range ($\Delta l=\lambda/6.2$) is beyond the expected range for accuracy [Tafl89], however, accurate results are still obtained. This general trend has been noticed for a variety of different objects i.e., accurate back-scattered values are obtained for discretizations that in general are insufficient for accurate characterization of the entire bistatic pattern. For accurate characterization of results in the low frequency range of Figure 5.17 (especially near the minima which appears for an electrical size of 0.375λ), the $57\Delta l$ sized cubic simulation space was the minimum acceptable size (maintaining the same discretization for the cube *i.e.*, $20\Delta l$ per side). Accurate determination of the results at the high frequency range of Figure 5.17 is possible with a smaller simulation space. The essential observation is that a sufficient electrical distance from the object to the outer boundary condition is required for simulations that employ the match termination for normal incidence absorbing boundary condition.
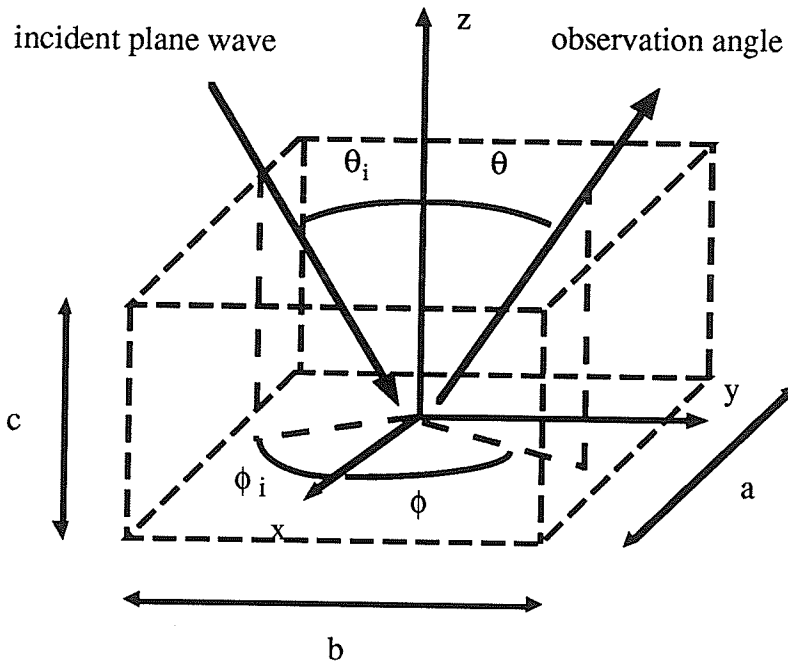
Figure 5.15: Perfectly conducting cube. Plane wave incident from θ_i , ϕ_i.

Figure 5.16(a): Comparison of E-Plane results calculated by the TLM simulation program and results from [Cote88] for a cube with equal side lengths of 1.50λ.
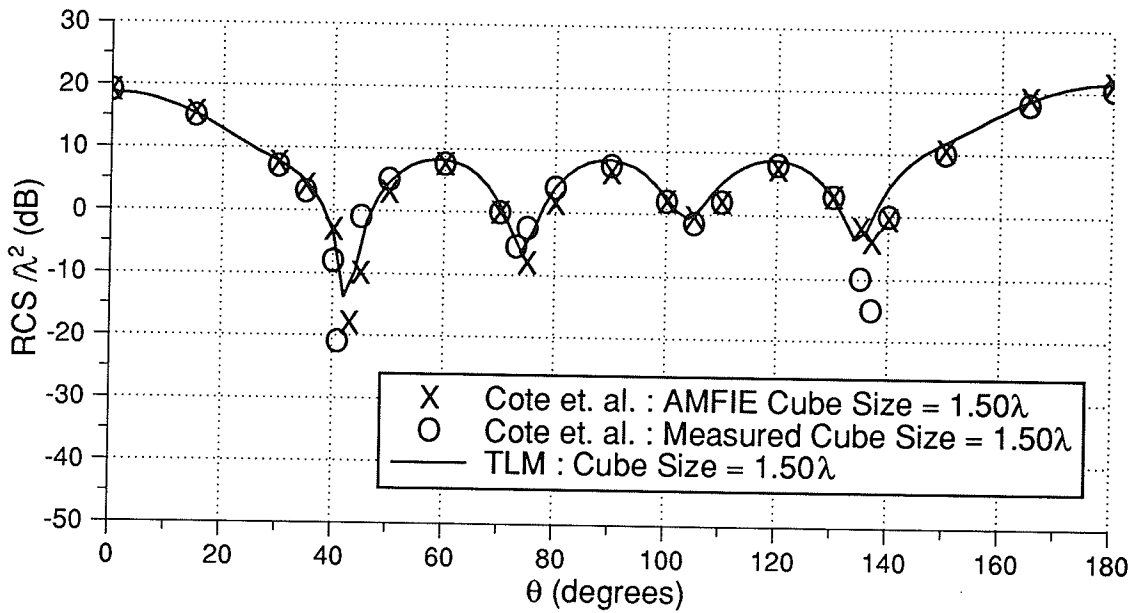
Figure 5.16(b): Comparison of H-Plane results calculated by the TLM simulation program and results from [Cote88] for a cube with equal side lengths of 1.50λ.

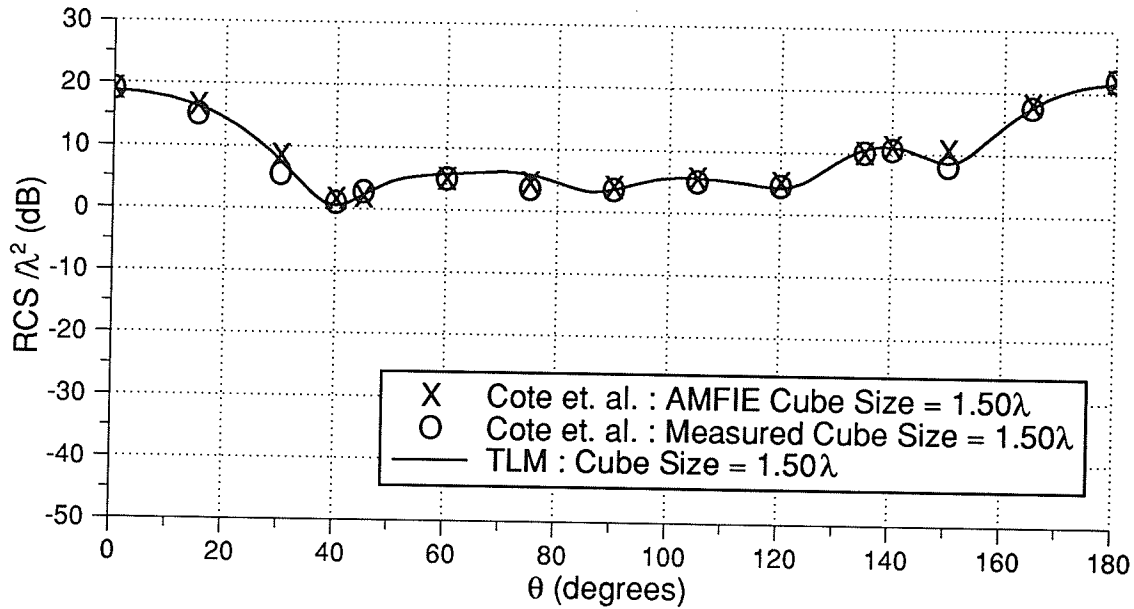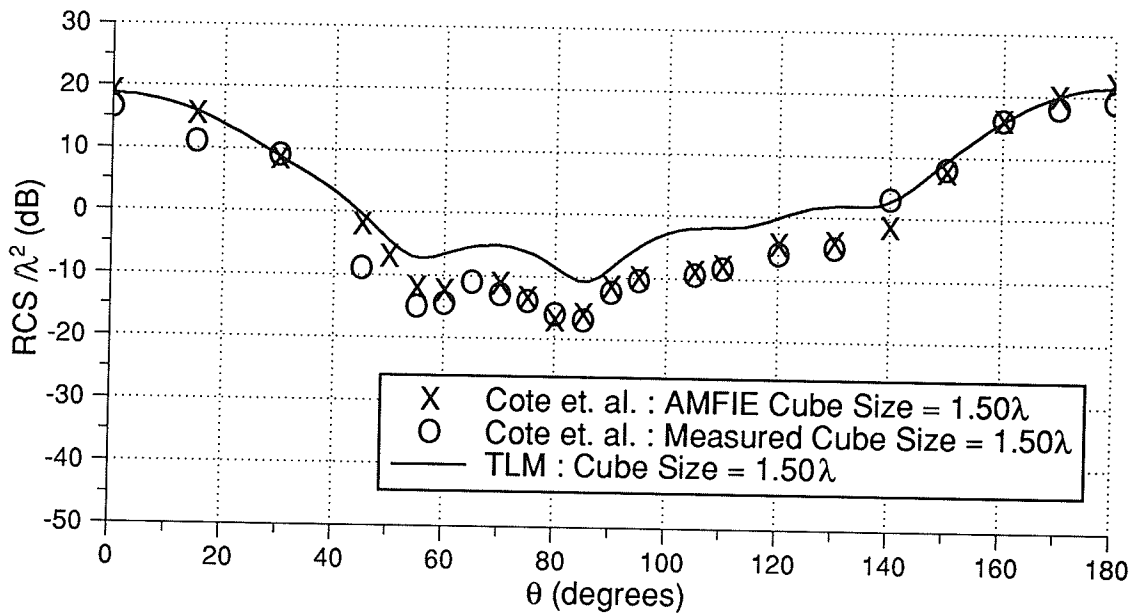**Figure 5.16(c):** Comparison of 45°-Plane results calculated by the TLM simulation program and results from [Cote88] for a cube with equal side lengths of 1.5λ.
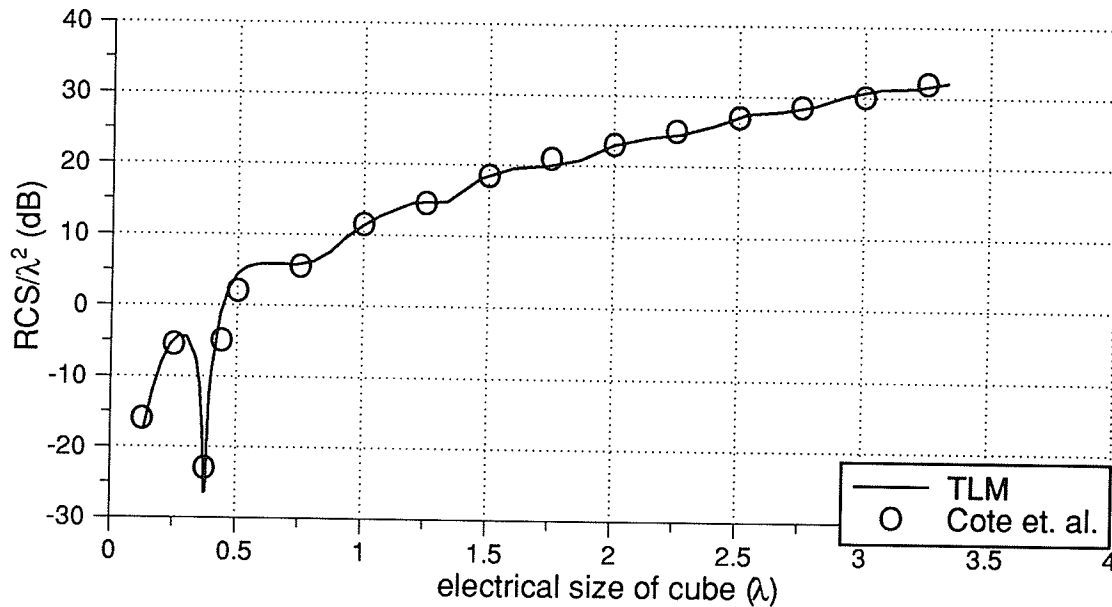
Figure 5.17: Comparison of results calculated by the TLM simulation program and measured results from [Cote88] for the back-scattering cross-section of a conducting cube versus the electrical size of the cube.

5.2.2: Dielectric Objects

The third object considered is a homogeneous dielectric cube illuminated by an x polarized plane wave incident from $\theta_i=180^\circ$. In Figure 5.18, TLM results are compared to those obtained from frequency-domain volume and surface integral-equation formulations [Sark89]. The cube has equal side lengths of 0.2λ and relative permittivity $\varepsilon_r=4.0$. A cubic simulation space of size $58\Delta l$ is used in which the dielectric cube is modelled as a $19\Delta l$ cube. Reasonable agreement of the TLM results with those from a volume integral equation formulation and a surface integral equation formulation is observed.

Figure 5.18(a): Comparison of the magnitude of E_ϕ in the $\phi=90^\circ$ plane calculated by the TLM simulation program and results from [Sark89] (volume integral-equation formulation and a surface integral-equation formulation) for a dielectric cube ($\varepsilon_r=4.0$) with equal side lengths of 0.20λ.
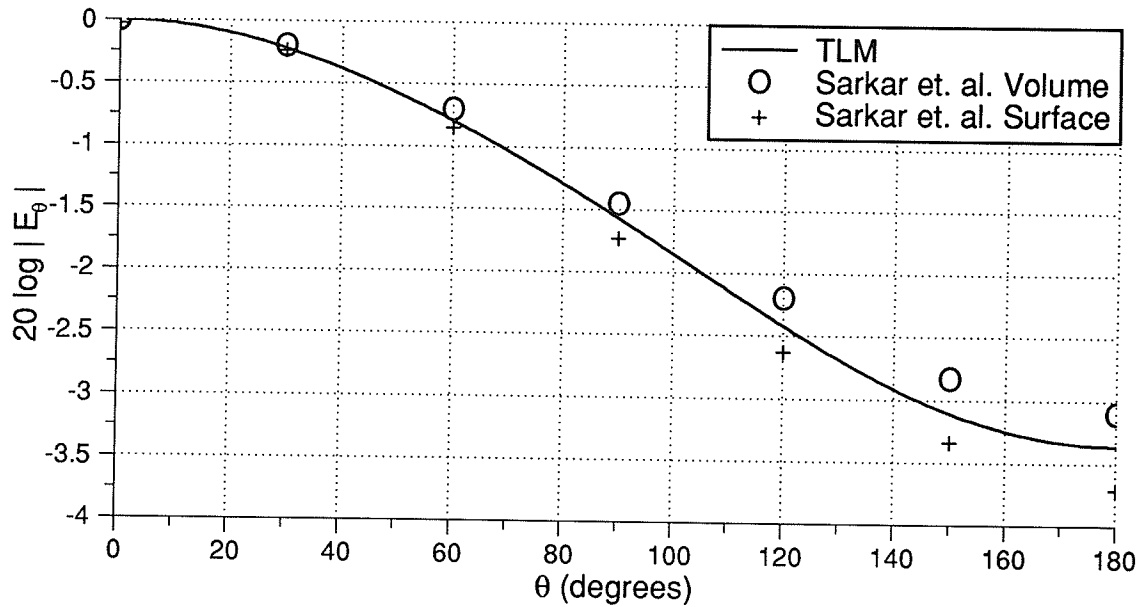

Figure 5.18(b): Comparison of the magnitude of E_θ in the $\phi=0^\circ$ plane calculated by the TLM simulation program and results from [Sark89] (volume integral-equation formulation and a surface integral-equation formulation) for a dielectric cube ($\varepsilon_r=4.0$) with equal side lengths of 0.20λ.
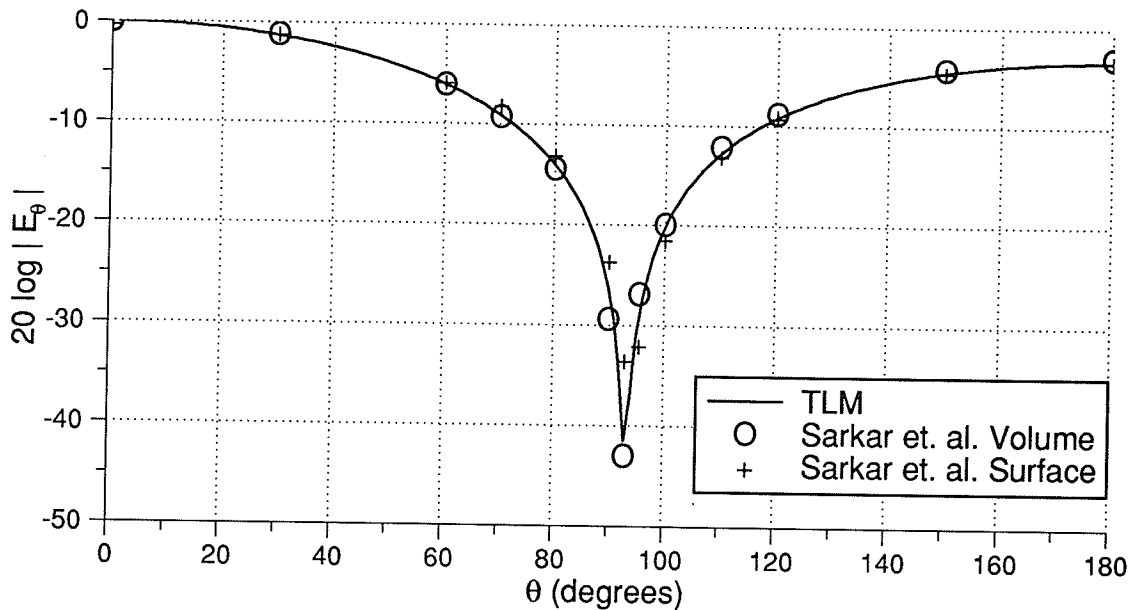
5.2.3: Conducting/Material Objects

Consider the combination of a dielectric block and conducting plate shown in Figure 5.19. An x polarized plane wave is incident from the negative z direction. This object has been analyzed by Arvas *et al* [Arva91] using two frequency-domain integral-equation formulations (referred to in [Arva91] as a surface / surface formulation and a volume / surface formulation). The dielectric block (ε_r=2) is of size L_x=L_y=0.4λ and L_z=0.2λ. The distance between the dielectric block and the conducting plate is 0.15λ. The dielectric block is centered over the perfectly conducting square plate which is of size 0.75λ by 0.75λ. Due to the restrictions imposed by the requirement of equal spatial steps in the TLM model, the exact dimensions of the block are not modelled. A spatial discretization of Δl=λ/26.7 was used in the TLM analysis. The square plate is modelled using 20Δl per side length. The block is modelled with L_x=L_y=10Δl and L_z=5Δl, corresponding to L_x=L_y=0.375λ and L_z=0.188λ. Various simulations indicate that the results are not significantly affected by small changes in the size of the dielectric block. The simulation space used to analyze this object is of size 43Δl by 43Δl by 43Δl. The distance from the object to the absorbing boundary conditions is slightly less than 0.5λ. Approximately 6 periods (or 350 time steps) were required for convergence of the frequency-domain results. In Figure 5.19, the normalized value of E_θ versus θ in the ϕ=0° plane are compared to results provided by Arvas *et al* [Arva91]. The TLM results are in better agreement with the surface/surface formulation results than the volume/surface formulation results. Also included are the TLM results for the case of the dielectric block is touching the plate.

The final object considered (see Figure 5.20) is similar to the object provided in Figure 5.19, however an aperture is present in the conducting plate. The aperture is centered within the plate and of the same size as the dielectric block. The plate is square with a side length of 0.75λ. The dielectric block has an electrical length of 0.3λ in the x and y directions and 0.15λ in the z direction. The object is modelled within a 49Δl by 49Δl by 49Δl simulation space using a discretization ratio of 26.67$\Delta l/\lambda$. The object is illuminated with an x polarized plane wave incident from the positive z direction. The bistatic radar cross section in the ϕ=0° plane for θ=0° to 180° is provided in Figure 5.20 for various values of h, the separation distance between the dielectric block and the conducting plate. Also provided are results obtained without the dielectric block. To

achieve convergence of the frequency domain results, 400 time steps were required. The electrical distance from the object to the absorbing boundary conditions is 0.75λ in the forward and back scattering directions and 0.56λ in the plane of the plate. The results contained in Figure 5.20 indicate that as the dielectric block is moved closer to the plate, the back-scattering cross section ($\theta=0^{\circ}$) decreases. Additional simulations have been performed that indicate that as the distance h from the dielectric block to the plate is increased, the scattered field pattern approaches that of the plate with aperture alone (i.e., without the dielectric block).
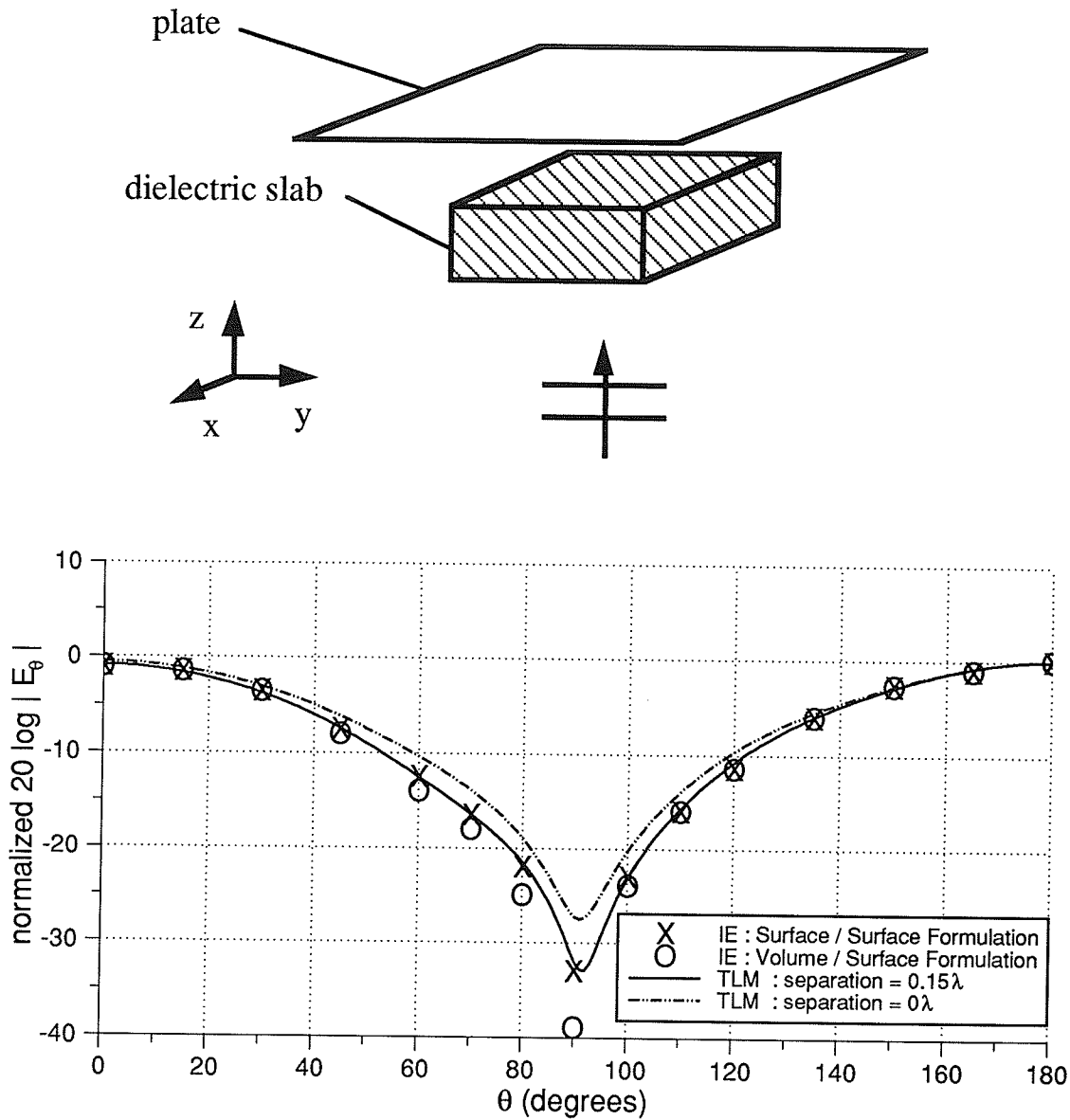
Figure 5.19: Comparison of the magnitude of E$_\theta$ in the ϕ=0° plane for the combination of conducting plate and dielectric block. The TLM results for a separation distance of 0.15λ (between the dielectric block and the plate) are compared to the surface/surface intergal formulation and the volume/surface formulation of [Arva91]. TLM results for the case of no separation between the block and plate are also provided.
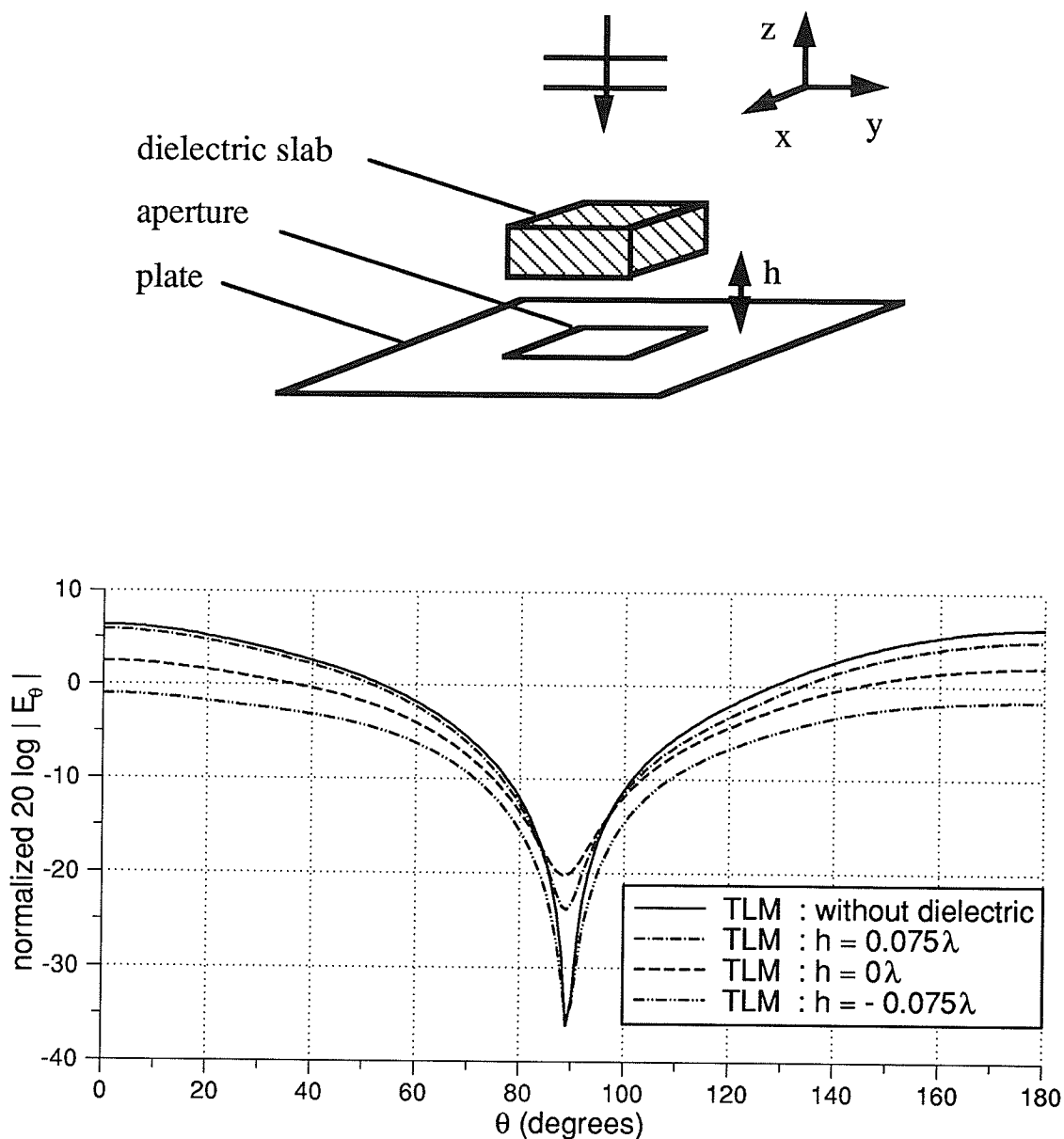
Figure 5.20: Magnitude of E_θ in the $\phi=0^\circ$ plane for the combination of conducting plate (with an aperture) and dielectric block shown in the Figure. TLM results are provided for h=0.075λ, 0λ and -0.075λ. Results for only the plate and aperture (i.e., without the dielectric block) are provided for comparison.

5.3: Analysis of Microstrip Circuits/Antennas

In this section the TLM simulation program is applied to the analysis of microstrip antenna and circuit elements. The analysis of microstrip geometries using differential equation based methods has been previously reported. Examples of the application of the Yee finite-difference time-domain algorithm can be found in [Zhan88a], [Zhan88b], [Shee90], [Paul91b], and [Wolf92]. Mariki and Yeh have analyzed microstrip lines on anisotropic substrates using the expanded node TLM method [Mari85], and German *et al* have analyzed microstrip structures using the symmetric-condensed TLM method [Germ90b] for the purpose of characterizing interconnections used in VLSI technology, and Dubard *et al* have attempted to characterize slot-coupled microstrip patch antennas using the TLM method with the Prony-Pisarenko algorithm to extract the frequency domain results [Duba90]

This section is divided into four parts. In the first part, the basic approach is described and applied to simple geometries for validation and to determine the accuracy of the basic apporach. The initial examples considered include a match-terminated microstrip line (on high and low permittivity substrate) and an open-end discontinuity. In the second part, the method is applied to the analysis of microstrip circuit components. These include a three section side-coupled microstrip filter, and a T-juntion. In the third part slot-coupled microstrip geometries are investigated: slot-coupled microstrip lines and slot-coupled microstrip patch antennas. In the fourth part the determination of the radiation patterns of microstrip geometries on both finite and infinite substrate/ground planes are considered.

5.3.1: Basic Approach / Initial Examples

5.3.1.1: Mesh Configuration and Discretization

The application of the TLM simulation program to the analysis of a microstrip structure requires discretization of the entire spatial domain of interest. The method is capable of analyzing microstrip structures on both finite and infinite substrate/ground planes. The discretization of a microstrip patch antenna is provided in Figure 5.21 for

both an infinite substrate/ground plane and a finite substrate/ground plane. The conducting surfaces are considered to be perfectly-conducting and infinitely thin. The substrates are modelled by specifying appropriate stub values to model permittivity, permeability, and/or conductivity. The match termination for normal incidence boundary condition is applied to terminate the exterior mesh boundaries. The boundary condition is applied such that the permittivity value immediately adjacent to the boundary is used in the determination of the appropriate reflection coefficient.
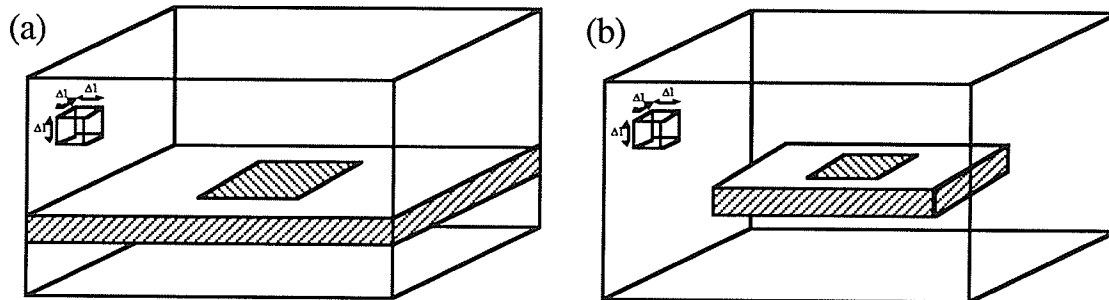

Figure 5.21: TLM Discretization of a microstrip patch antenna on (a) an infinite substrate and ground plane and, (b) a finite substrate/ground plane.

5.3.1.2: Excitation and Calculation of Scattering Parameters

Excitation is provided by a Gaussian-pulsed TEM voltage source. As illustrated in Figure 5.22, the source is applied by imposing a z-directed electric field (which is normal to the ground plane and strip conductor) along the $y=y_{min}$ plane of the simulation space. For the analysis of microwave circuit/antenna applications the scattering parameters of the element are usually desired. To illustrate the determination of scattering parameters from the TLM analysis, consider the general N-port microstrip discontinuity provided in Figure 5.23. The scattering matrix of the N-port microstrip discontinuity is given as,

$$S = \begin{bmatrix} S_{11} & S_{1j} & S_{1N} \\ S_{21} & S_{2j} & S_{2N} \\ \cdot & \cdot & \cdot \\ \cdot \,\cdots & \cdot \,\cdots & \cdot \\ \cdot & \cdot & \cdot \\ S_{N1} & S_{Nj} & S_{NN} \end{bmatrix}$$

In general, the characterization of the complete scattering matrix, S requires N TLM simulations. If the structure possesses symmetry, the number of simulations can be reduced. For each of the N simulations, a different port is excited. Essentially, a single column of S is determined from each simulation for the entire frequency spectrum contained in the incident Gaussian-pulsed TEM source. The scattering parameters of the discontinuity are determined from the voltage response at each port. For example, consider a simulation in which the jth port of the circuit is excited. At port i the voltage response $v_i(t)$ is determined from,

$$v_i(t) = \int_{l_i} E(r,t) \cdot l_i \, dl_i$$

where l_i is a linear contour from the ground plane to the microstrip line at the geometrical location of port i, and $E(r,t)$ is the time-domain electric field distribution. The frequency domain voltage response at port i, $v_i(f)$ is obtained by discrete Fourier transform of $v_i(t)$. To obtain the scattering parameters, $v_i(f)$ is normalized to $v_I(f)$, the frequency domain incident voltage distribution. This incident voltage distribution is obtained from the voltage response on the jth port. The location of the input port is placed a sufficient distance from the discontinuity such that the Gaussian-pulsed incident wave can be separated from the reflections caused by the discontinuity. A time $t=t_0$ is selected in order to separate the incident voltage response from the reflected voltage response. For $t<t_0$, the transient response at port j contributes to the incident voltage wave, $v_I(t)$ and for time $t>t_0$ the transient response contributes to $v_j(t)$. The scattering parameters S_{ij} (for i=1 , ... , N) are determined from,

$$S_{ij}(f) = \frac{v_i(f)}{v_I(f)}$$

Because the input signal is *gated-out* of the simulation, the observation ports are located a non-zero distance from the discontinuity. As well, placing the observation locations a distance from the discontinuity allows the higher-order modes to die-out. Therefore, only the propagating quasi-TEM mode of the microstrip contributes to the scattering parameter characterization. The scattering parameters at an arbitrary point on the line can be obtained through transformation of S_{ij} along the transmission line with knowledge of the electrical characteristics of the transmission line.
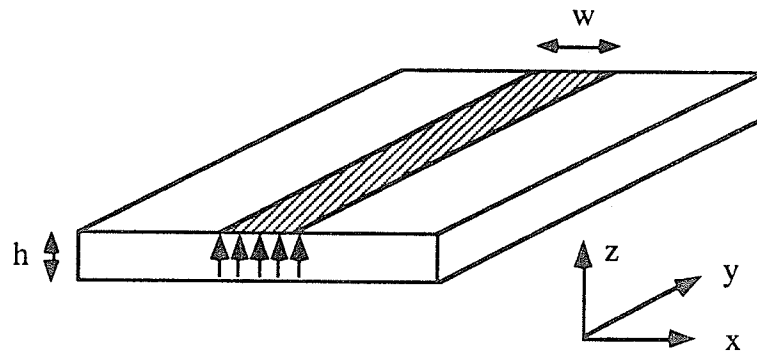
Figure 5.22: TEM excitation of a microstrip line.
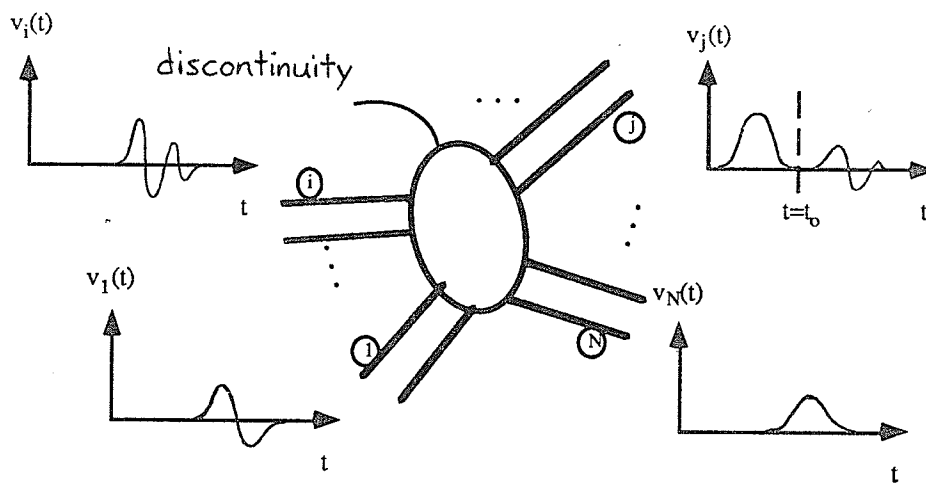
Figure 5.23: General N-port microstrip discontinuity.

5.3.1.3: Match Terminated Microstrip Line

The first geometry analyzed is a match terminated microstrip transmission line. This simple geometry is selected to demonstrate the program and obtain an estimate of the *computational dynamic range* of the TLM method for this class of problem. Consider a match terminated microstrip transmission line with the following parameters: substrate permittivity ε_r=2.22, substrate thickness h=0.762mm, and line width w=2.54mm ($Z_0 \approx 50\Omega$). The mesh used for this application is of size N_x=120Δl, N_y=60Δl, N_z=20Δl, where Δl=0.381mm. The transient response at three spatial locations separated by 15.24mm (along the length of the line) is provided in Figure 5.24. These results provide

the z component of the electric field (i.e., the component normal to the ground plane) at a spatial location centered under the line between the ground plane and conducting strip. The x and y components of the field are negligible in comparison to the z component (at least three orders of magnitude less). The pulse propagates with a minimal change in shape indicating low dispersion for this particular set of parameters (and frequency content of the TEM source).
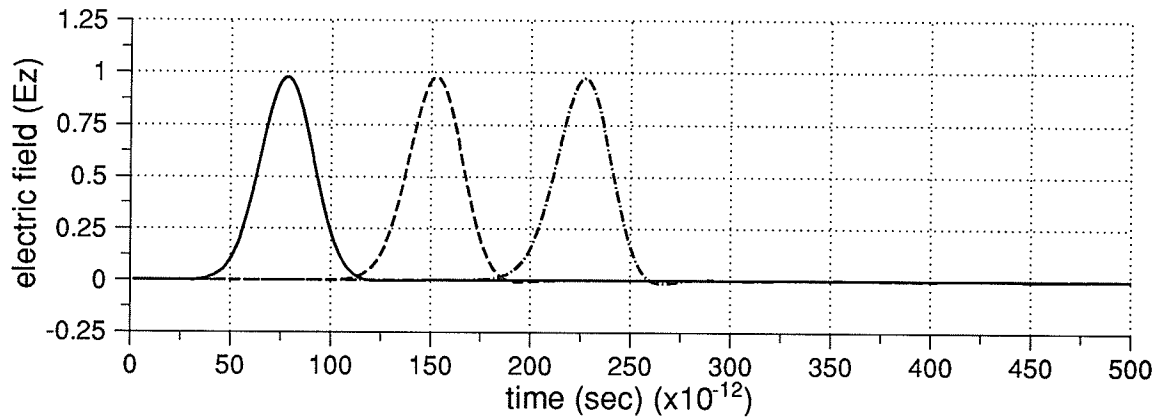
Figure 5.24: Transient response at spatial locations separated by 15.24mm, substrate permittivity ε_r=2.22.
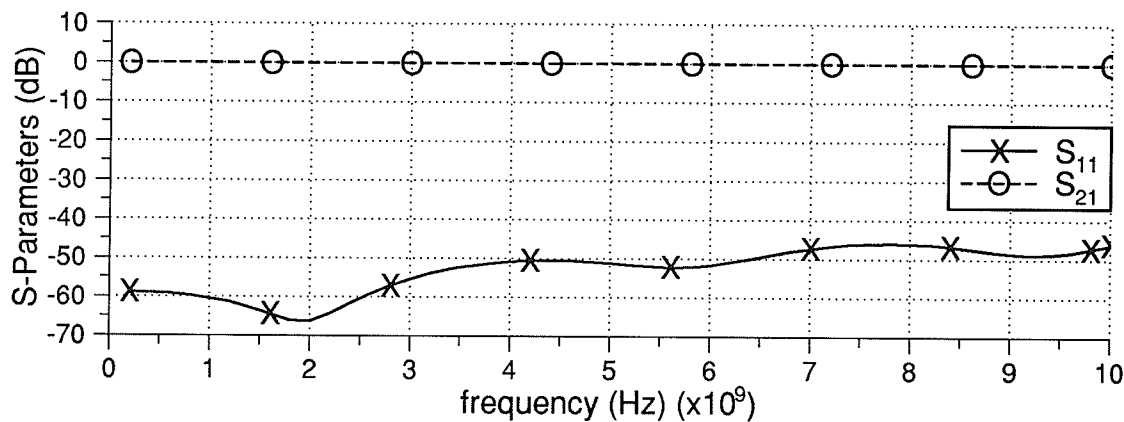
Figure 5.25: S_{11} and S_{21} of a match terminated microstrip line, substrate permittivity ε_r=2.22.

The return and insertion loss S_{11} and S_{21}, respectively, for this example are provided in Figure 5.25. The value of S_{11} is less than 45dB and value of S_{21} varies between 0 and

-0.05dB over the frequency range 0 to 10 GHz. These results indicate the computational dynamic range that is available from the TLM simulation program for the analysis of microstrip structures with low dielectric constant substrates. The value of a scattering parameter close to 0dB should be given an artificial uncertainty of ±0.05dB and any scattering parameter with a value less than -45dB should be considered as beyond the expected range of accuracy.

As an additional example consider the following line parameters: ε_r=10.2, h=0.635mm, and w=0.635mm ($Z_0 \approx 50\Omega$ line). The mesh used for this application is of size N_x=120Δl, N_y=60Δl, N_z=20Δl, where Δl=0.127mm. The transient response at three spatial locations separated by 5.08mm (along the length of the line) are provided in Figure 5.26. For this particular set of parameters (and frequency content of the pulse) the dispersive effects of the line are noticeable.
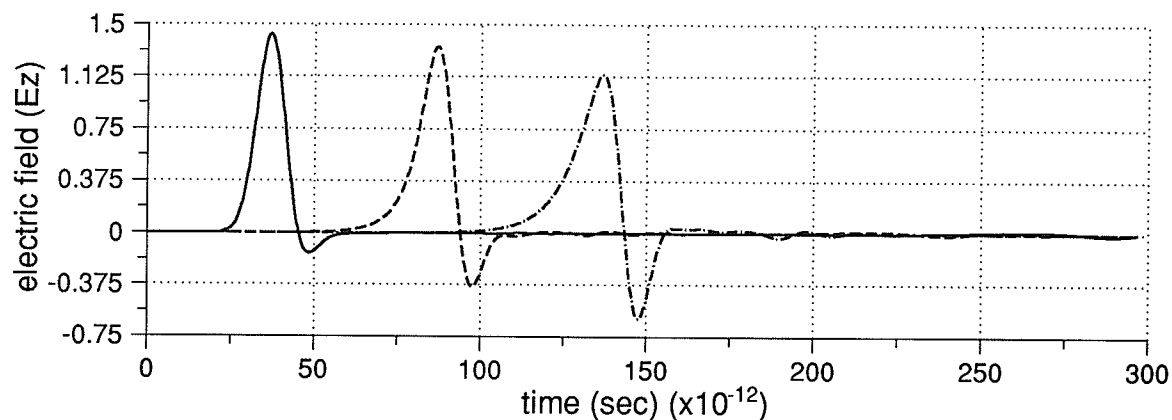

Figure 5.26: Transient response at spatial locations separated by 5.08mm, substrate permittivity ε_r=10.2.

The numerical results for S_{11} and S_{21} are provided in Figure 5.27 and indicate the value of S_{11} is less than -30dB and the value of S_{21} is between ±0.25dB over the frequency range 0 to 20GHz. These results are similar to those obtained for other simulations of microstrip transmission-lines on high permittivity substrates (ε_r=8.0 to 12.0) and indicate the computational dynamic range of the TLM simulation program for the analysis of microstrip geometries on high permittivity substrates is not as large as that for the analysis of geometries on low permittivity substrate. It is unlikely that the decreased performance is due to the increase in numerical dispersion associated with the increase in the permittivity value. At 30GHz, the discretization ratio for the problem analyzed above

($\lambda \geq 20\Delta l$) is within the expected range for accurate results. The decrease in accuracy with an increase in the substrate permittivity is likely due to the absorbing boundary conditions used to truncate the simulation space. A recent investigation has compared the performance of various absorbing boundary conditions for the analysis of microstrip geometries [Rail92], [Rail93], [Litv93]. Numerical results provided in [Rail93] and [Litv93] indicate that first-order absorbing boundary conditions are only capable of providing an S_{11} of less than -20dB for high permittivity substrates (ε_r=8.0 to 12.0). Second-order absorbing boundary conditions are capable of providing an S_{11} of less than -50dB for high permittivity substrates. Our numerical results indicate that the match termination for normal incidence absorbing boundary condition provides accuracy somewhere between first and second-order accuracy and is considered to be adequate for the present investigation.
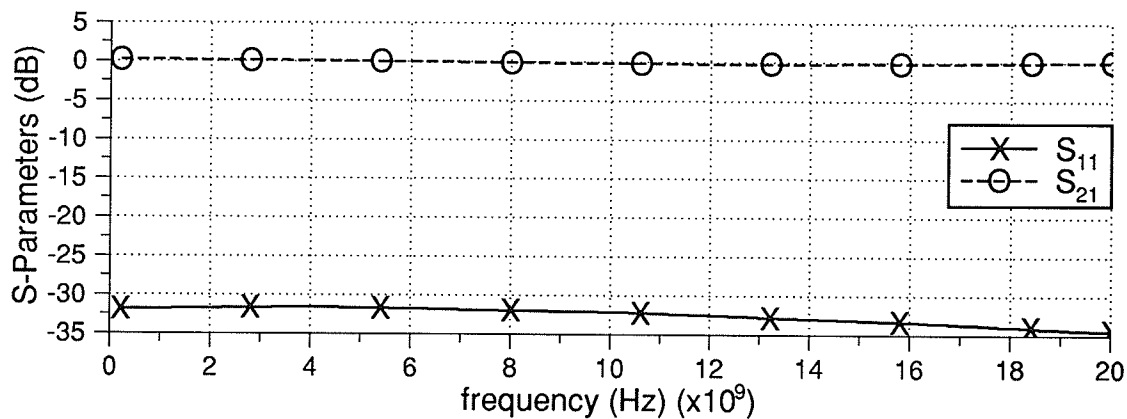
Figure 5.27: S_{11} and S_{21} of a match terminated microstrip line, substrate permittivity ε_r=10.2.

5.3.2: Analysis of Microstrip Circuit Elements

5.3.2.1: Microstrip T-Junction

In this section, the TLM simulation program is applied to the analysis of two microstrip circuit elements. The first example considered is a T-junction. The geometry of a microstrip T-junction is provided in Figure 5.28, with w_1=w_2=0.610mm, a substrate height h=0.635mm, and substrate relative permittivity ε_r=9.9. The TLM mesh used for the analysis of this structure is of size N_x=104Δl, N_y=57Δl, N_z=19Δl, with Δl=0.0907mm. The difference between substrate height and microstrip width is ignored in the TLM analysis. The duration of the simulation was 1500Δt. This example has been previously

analyzed in [Wu90] where measured data and results from a frequency-domain integral equation formulation are provided. Figure 5.29 contains a comparison of TLM results with numerical results from [Wu90] for S_{11}, S_{21}, and S_{31}. Good agreement of the TLM and the frequency-domain integral equation data is observed.

Figure 5.28: Geometry of a microstrip T-junction.

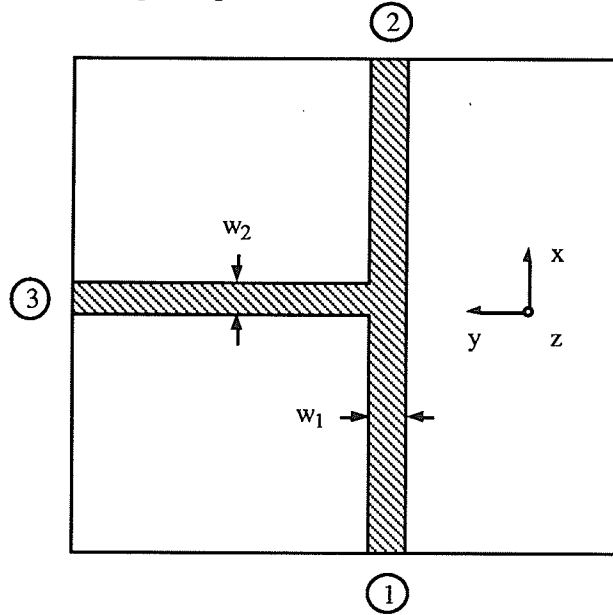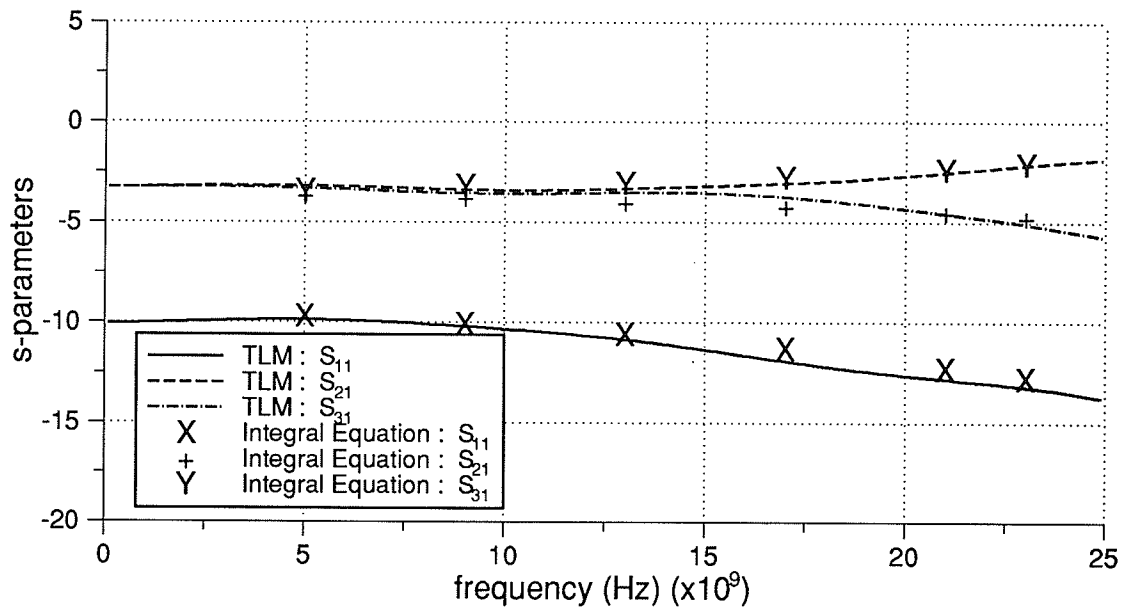**Figure 5.29:** S_{11}, S_{21} and S_{21} for the microstrip T-junction shown in Figure 5.28. Results obtained from the TLM simulation program are compared to numerical results from [Wu90].

5.3.2.2: Three-Section Side-Coupled Microstrip Band-Pass Filter

The next example considered is a three section side-coupled microstrip band-pass filter. The geometry is provided in Figure 5.30, with $w_1=w_2=w_3=1.272mm$, $s_1=s_2=1.272mm$, $L_1=L_2=L_3=12.72mm$, and a substrate height $h=1.272mm$. This geometry has been previously analyzed using the Spatial Network Method [Shib88] and the Yee finite-difference time-domain algorithm [Rail93]. The simulation space used to analyze this structure is of size $N_x=108\Delta l$, $N_y=60\Delta l$, $N_z=20\Delta l$, with $\Delta l=0.2544mm$

The transient response at the input and output port of this structure is provided in Figure 5.31. The duration of the simulation used to characterize this geometry is $25,000\Delta t$ - orders of magnitude more time steps than that usually required in the analysis of non-resonant geometries. The highly resonant nature of the side-coupled filter is noticeable by the ringing observed in Figure 5.31. Computational aspects of modelling resonant structures is discussed further in Section 5.3.3.2, where the analysis of slot-coupled microstrip antennas is investigated. The scattering parameters (S_{11} and S_{21}) determined from the TLM analysis are compared to measured data from [Shib88] in Figure 5.32. Reasonable agreement between the TLM results and the measured data is observed. The pass-band frequencies are predicted reasonably well by the TLM analysis, however, the magnitude of S_{11} at these pass-band frequencies is not as low as that observed in the measurements. The same discrepancy is evident in the Spatial Network results [Shib88] and finite-difference time-domain results [Rail93].
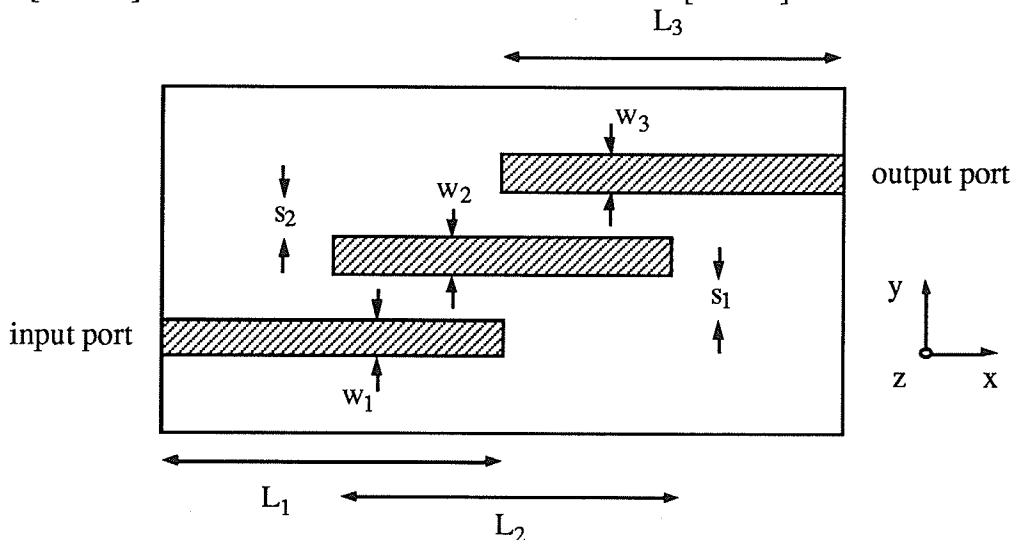

Figure 5.30: Geometry of a three-section side-coupled microstrip filter.
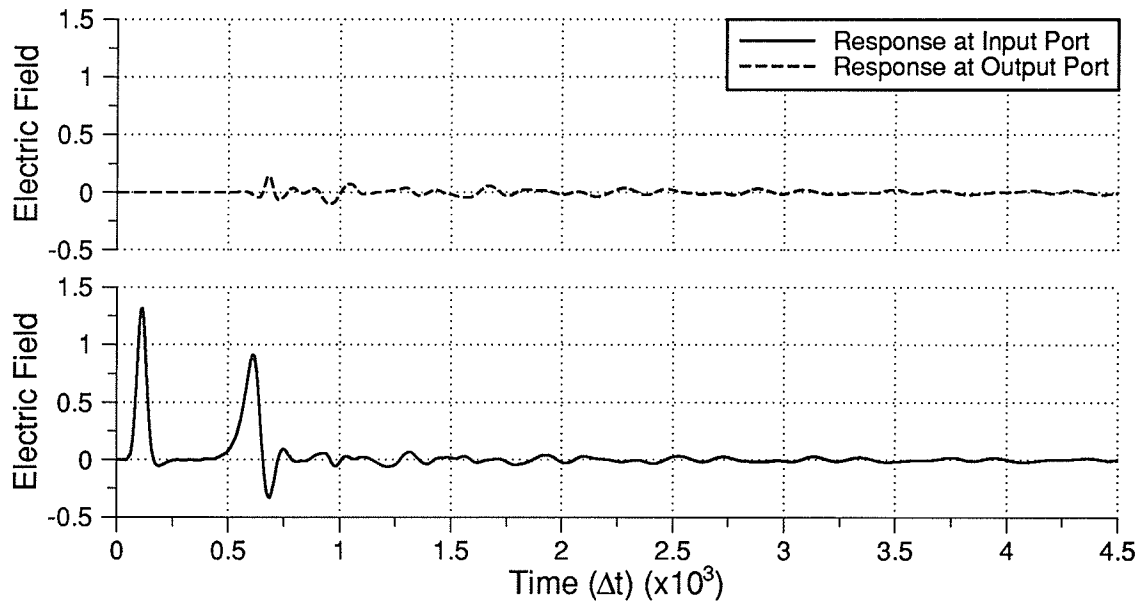
Figure 5.31: Transient repsonse at the input and output ports of the side-coupled filter.
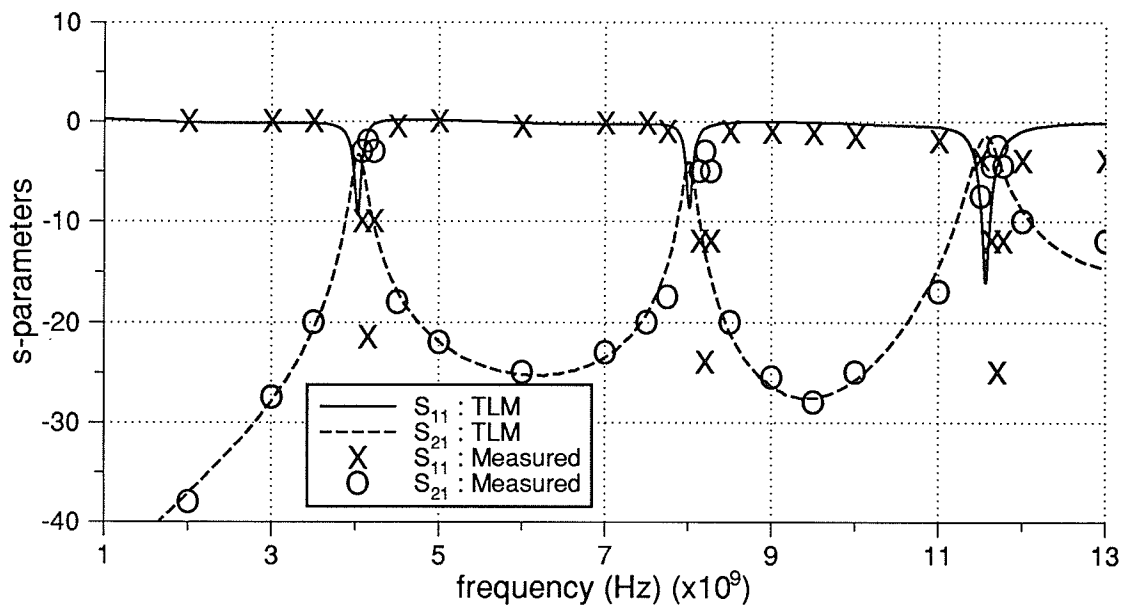
Figure 5.32: Comparison of measured data (from [Shib88]) with TLM results for S_{11} and S_{21} of the side-coupled microstrip filter.

5.3.3: Analysis of Slot-Coupled Microstrip Structures

5.3.3.1: Slot-Coupled Microstrip Lines

Consider the slot coupled microstrip lines shown in Figure 5.33. Port labels are also provided in the figure. The specific example is selected from [Hers91]. The geometry is defined by: ε_r=2.22 (both substrates), t_1=t_2=0.762mm, w_1=w_2=2.667mm (both lines), w_a=1.143mm, L_a=14.86mm. The mesh used for this application is of size N_x=120Δl, N_y=60Δl, N_z=40Δl, where Δl=0.381mm. In Figure 5.34, the TLM results for the magnitude of S_{21} and S_{31} are compared to those obtained by an integral equation based approach given in [Hers91]. Reasonable agreement is achieved over the entire bandwidth.

Additional results for an example on a high permittivity substrate ε_r=10.2 are presented in Figure 5.35 [Ittip93]. The geometry of this example is defined by: ε_r=10.2 (both substrates), t_1=t_2=0.635mm, w_1=w_2=0.635mm (both lines), w_a=0.635mm, L_a=2.16mm. The mesh used to analyze this problem is of the same size as above, but with Δl=0.127mm. The TLM results are compared to measured data as well as results calculated from a modal analysis method described in [Itti91]. Again, reasonable agreement is achieved over the entire bandwidth.
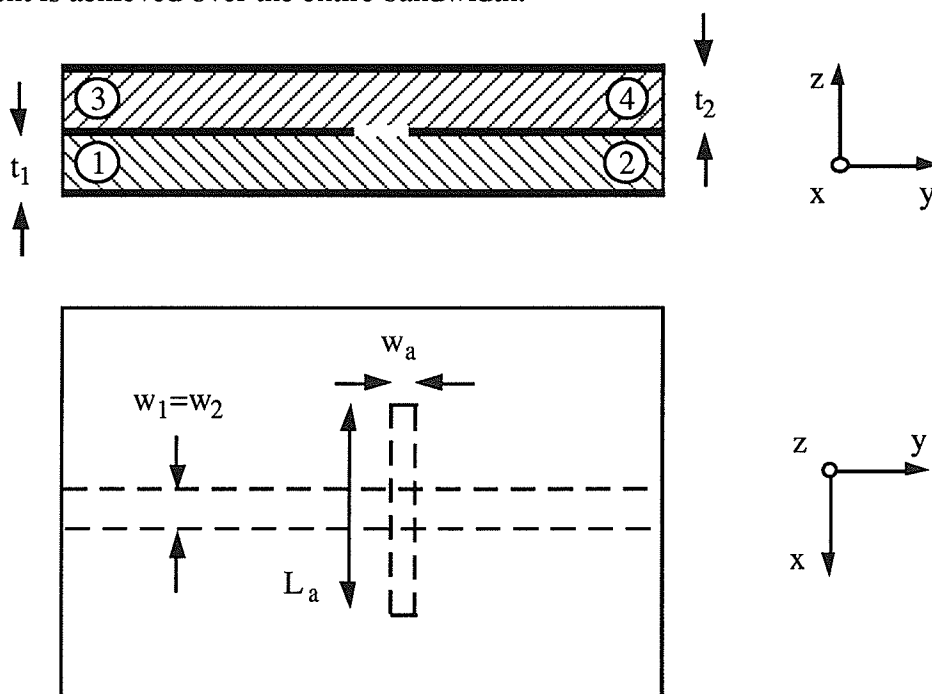
Figure 5.33: Slot-coupled microstrip lines.
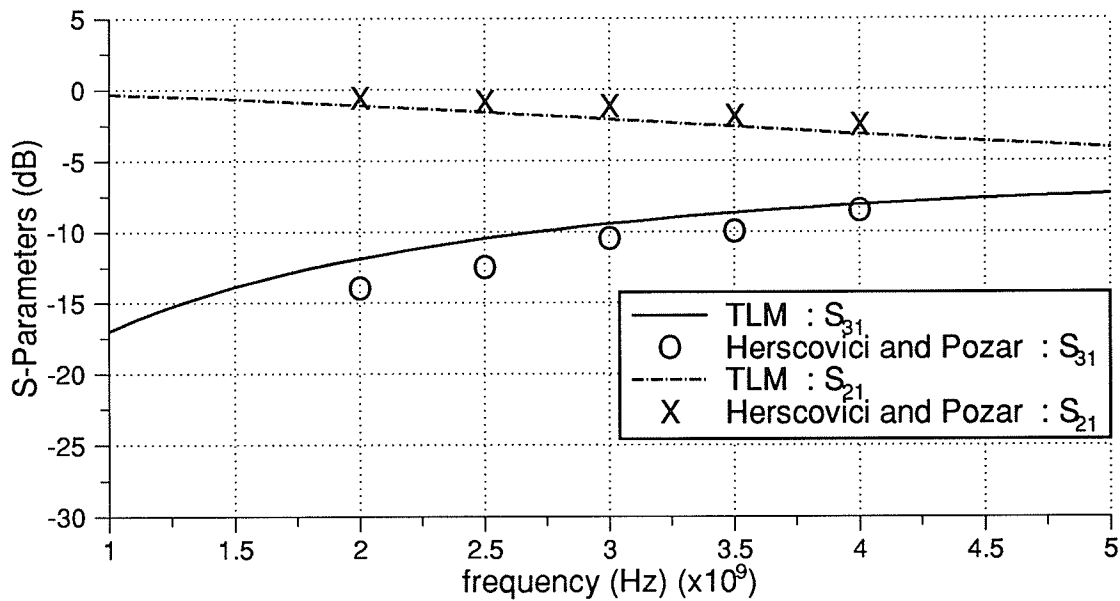
Figure 5.34: Comparison of TLM results for the magnitude of S_{21} and S_{31} for the analysis of slot-coupled microstrip lines (ε_r=2.22) and results from [Hers91].
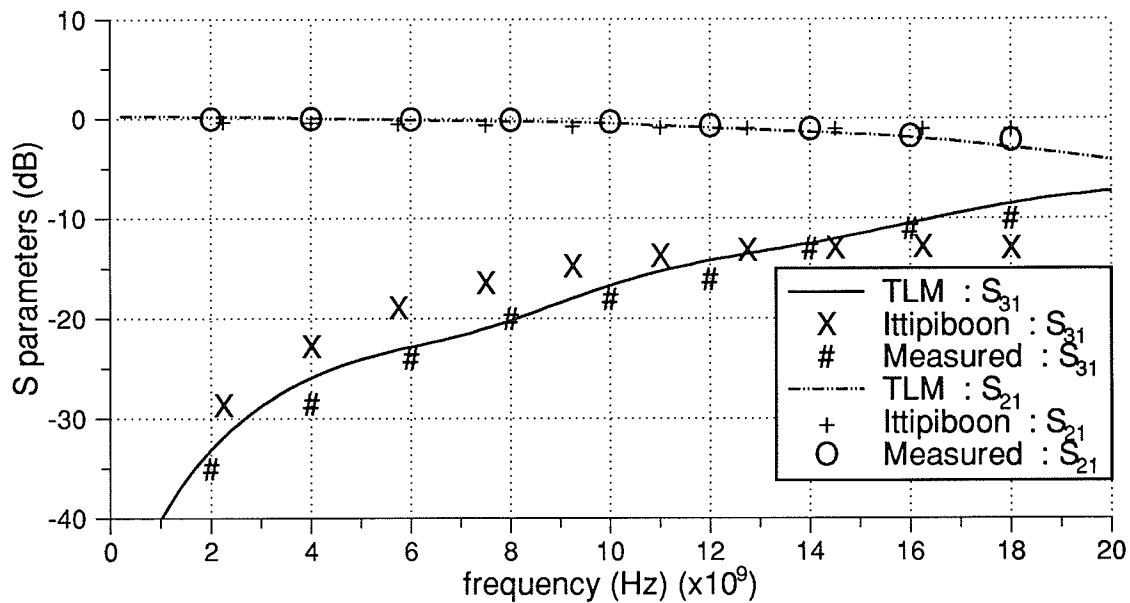
Figure 5.35: TLM results for the magnitude of S_{21} and S_{31} for the analysis of slot-coupled microstrip lines (on an ε_r=10.2) [Itti93]. TLM results are compared to measured data as well as results determined by modal-analysis method [Itti91].
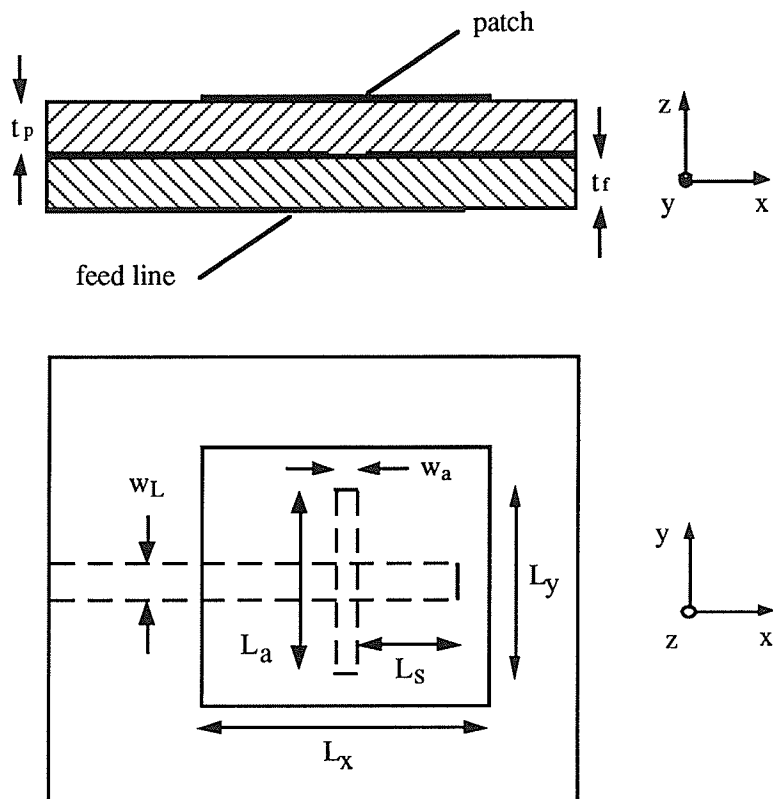
Figure 5.36: Slot-coupled microstrip antenna.

5.3.3.2: Slot-Coupled Microstrip Patch Antenna

Consider the general geometry of a slot-coupled microstrip patch antenna shown in Figure 5.36. The specific example is selected from [Himd89]. The geometry is defined by: ε_r=2.54 (both substrates), t_f=t_p=1.60mm, w_L=4.80mm, w_a=1.60mm, L_a=11.2mm, Ls=20.4mm, L_x=30.4mm, L_y=40.0mm. The mesh used in the analysis of this example is of size N_x=120Δl, N_y=60Δl, N_z=40Δl, where Δl=0.800mm.

In Figure 5.37, the transient response at an observation point on the microstrip feed line (located 35.6mm from the slot discontinuity) is provided. Reflection from the slot, open-circuit termination, and the resonances due to the patch are distinguishable.
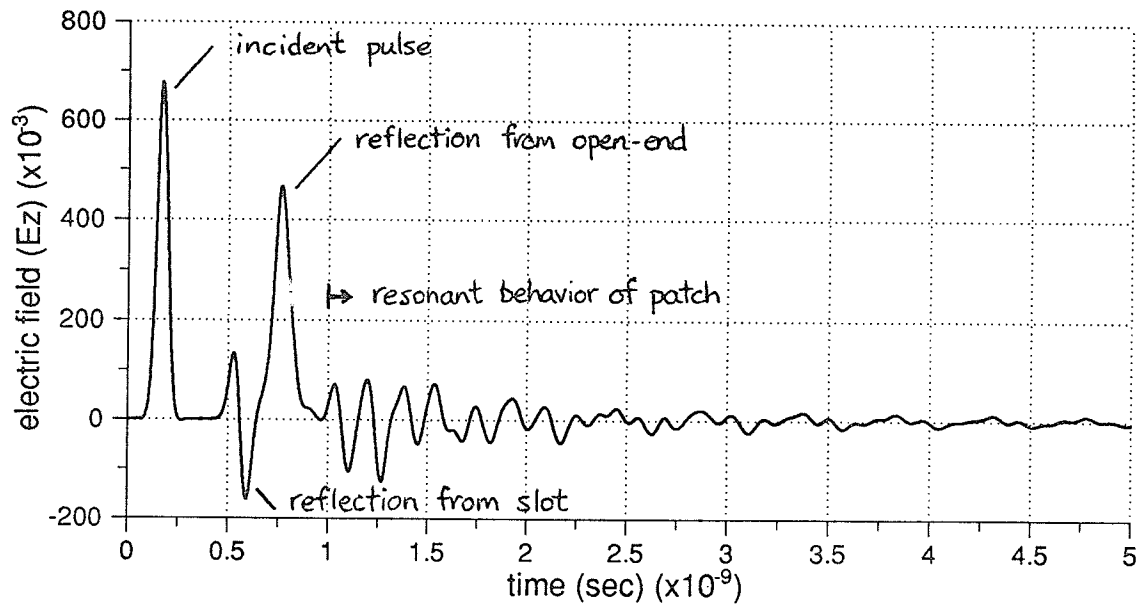
Figure 5.37: Transient response of a slot-coupled microstrip antenna.

Examining the response provided in Figure 5.37, it appears that this antenna is not matched (because of the large amount of energy that is reflected back to the input port). However, calculation of S_{11} indicates a return loss of around -15dB at the specified design frequency. Because this antenna has a narrow bandwidth, only a small portion of the energy contained in the gaussian pulse is coupled to the patch and radiated. Therefore, a broadband mismatch is apparent although a narrow band match is realized. Due to the thin antenna substrate, this particular antenna has a large Q-factor and therefore a small bandwidth. This highly resonant example also demonstrates a disadvantage of the traditional discrete Fourier transform applied to calculate the frequency domain results from the time domain response provided in Figure 5.37. In Figure 5.38, S_{11} is provided after 2000, 4000, and 8000 time steps. As was the case for the three-section side-coupled filter considered in a previous section, the number of time steps required to characterize the geometry represents almost an order of magnitude more computation than that required by the analysis of non-resonant geometries. The discrete Fourier transform requires 8000 time steps before a sharp S_{11} is obtained. The use of an alternative method for predicting the frequency domain response - such as Prony's method [Marp87] may significantly reduce computation time required to obtain an accurate frequency response for S_{11}.
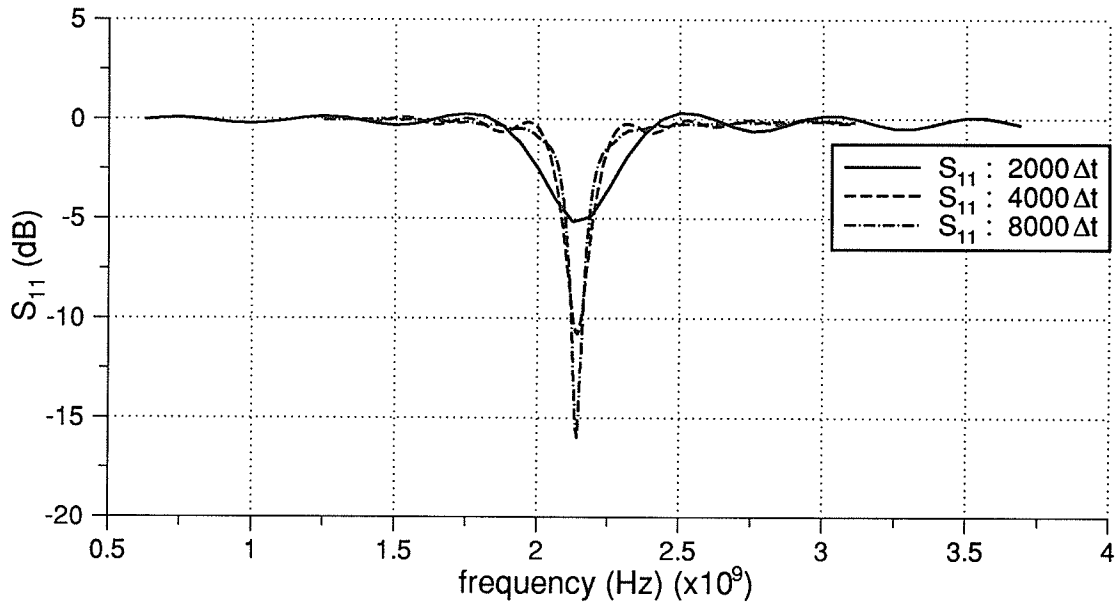
Figure 5.38: S_{11} for a slot-coupled microstrip antenna. The three curves correspond to results calculated after 2000, 4000, and 8000 time steps.
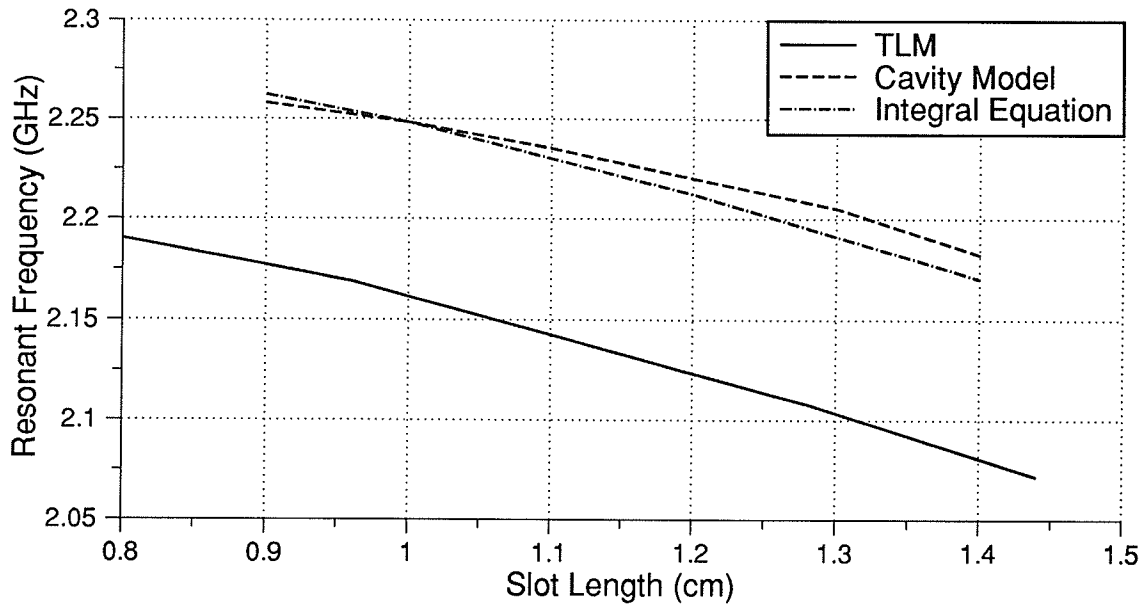
Figure 5.39: S_{11} versus slot-length. Comparison of TLM results with results from [Himd89] and [Sull86].

In Figure 5.38, the resonant frequency predicted by the TLM code is within 3% of that given in [Himd89]. Simulations have been performed to determine the effect of the slot length on resonant frequency. In Figure 5.39, the predicted resonant frequency

versus slot length is provided. The results indicate the expected behavior, as the length of the slot increases, the resonant frequency decreases. Also provided in Figure 5.39 are results from [Himd89] and [Sull86]. The difference between the cavity model results [Himd86] and integral equation results [Sull86] as compared to the TLM results is around 3% for the range of slot-lengths considered.

In addition to the above example, the TLM simulation program has been applied to the analysis of several slot-coupled microstrip antennas provided in [Take92b]. Takeuchi *et al* examine slot-coupled microstrip antennas with different feed substrates. For each example, the same patch geometry and substrate is assumed: length of the rectangular patch L_x=5.2mm, patch substrate thickness t_p=0.8mm and patch substrate relative permittivity ε_r=2.7. A value for the patch width was not provided in [Take92b]. In the present analysis a patch width of L_y=4.2mm is assumed. Three different feed geometries for this patch are provided in Table 5.2. For each geometry the characteristic impedance of the feed microstrip line is 50.0Ω and the feed is designed for a resonant frequency of 14.2GHz. The TLM simulation space applied to the analysis of this problem is of size N_x=60Δl, N_y=60Δl, and N_z=40Δl, with a spatial discretization Δl=0.20mm. In Figure 5.40, S_{11} of the above antenna geometries determined from the TLM analysis is provided. The resonant frequencies predicted by the TLM analysis are provided in Table 5.3. At the TLM-predicted resonant frequency a match of -23dB (for Geometry 1), -14dB (for Geometry 2), and -20dB (for Geometry 3) is determined (the resonant frequency is assumed to be at the minimum value of S_{11}). This example indicates the ability of the TLM simulation program to analyze slot-coupled microstrip geometries having different feed and antenna substrates.

Table 5.2: Different Feed Geometries for a Slot-Coupled Microstrip Patch Antenna

Geometry	ε_r (feed)	t_f (mm)	w_f (mm)	L_s (mm)
1	2.7	0.8	1.90	3.50
2	5.0	0.8	1.50	2.63
3	10.0	0.8	0.65	1.90

Table 5.3: Resonant Frequencies (GHz) for the Antennas Provided in Table 5.2

Geometry	f_{res} (design)	f_{res} (TLM)	% diff
1	14.20	14.55	+2.4
2	14.20	14.75	+3.7
3	14.20	14.85	+4.3
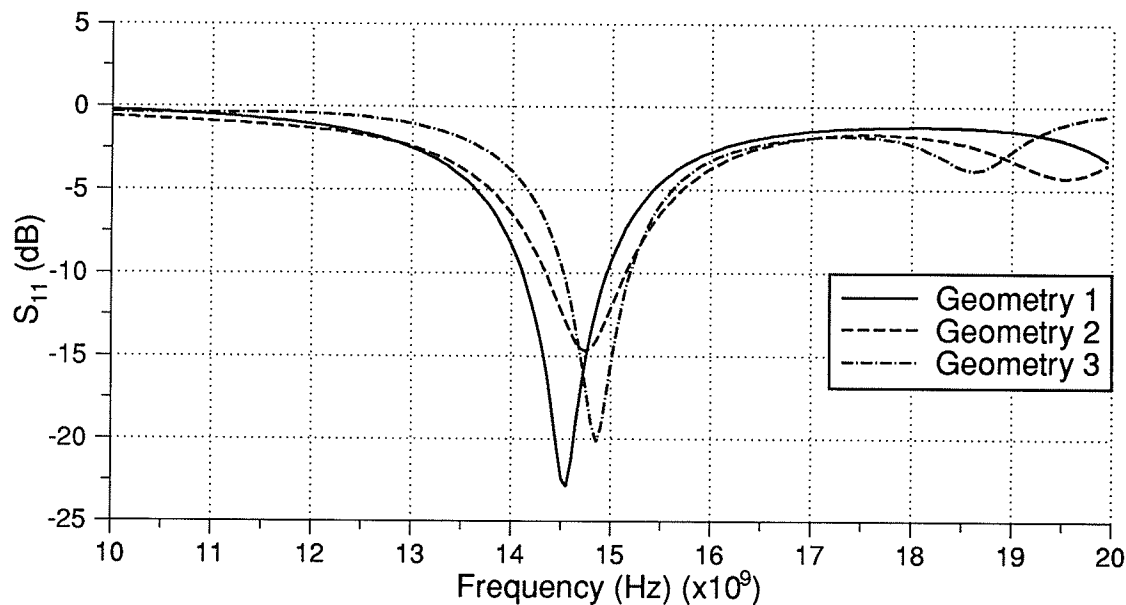
Figure 5.40: S_{11} of the slot-coupled microstrip antennas described in Table 5.2.

In addition to the results presented in this section, animations of the field distribution along the feed line and also of the field distribution under the patch have been performed. The animations qualitatively demonstrate the operation of the slot-coupled microstrip antenna for dominant mode excitation. The animations were performed using the *PV-WAVE* visualization package at the Communications Research Centre, Ottawa. Qualitative results of this nature are useful for educational purposes.

5.3.4: Calculation of Radiation Patterns

In this section, the calculation of the radiation pattern of microstrip antennas analyzed using the TLM simulation program are considered. The simulation space is

terminated at an electrically small distance from the antenna. Therefore, the far-field distributions are not directly available. To calculate the radiation patterns equivalent sources are defined (from field values directly available from the simulation) and then transformed to the far-field using a geometrically suitable Green's function.

5.3.4.1: Antennas on an Infinite Substrate/Ground Plane

Consider the calculation of the radiation patterns of arbitrary microstrip elements on an *infinite* single layer substrate/ground-plane, following the theory presented by Mosig and Gardiol [Mosi85]. Essentially, the Sommerfeld theory (pertaining to the radiation of sources in the presence of an infinite layered medium) is applied to yield the appropriate Green's function to account for the presence of the substrate and ground-plane. Therefore, the electric surface current on the patch is sufficient to determine the radiation patterns of the antenna. In Figure 5.21(a) the TLM simulation space used for the analysis of a microstrip antenna on an infinite-substrate/ground-plane is provided. Absorbing boundary conditions are applied along the substrate and free-space boundaries to simulate an infinite substrate/ground-plane. The TLM simulation yields a discrete representation of the electric surface current on the patch.

Given the surface current distribution on the patch, the theory provided in [Mosi85] can be applied to determine the radiation patterns. The electric field distribution, in the far field, is given as,

$$E_\alpha = G_{\alpha,x}^E (r) \sum_{i=1}^{M} a I_{xi} e^{jk_o e_r \cdot \rho_i{}'} + G_{\alpha,y}^E (r) \sum_{j=1}^{M} b I_{yi} e^{jk_o e_r \cdot \rho_j{}'} \qquad (5.8)$$

where $\alpha = \theta, \phi$; I_{xk} and I_{yk} are the x and y components of the electric surface current on the kth portion of the patch; a and b are the x and y dimensions of each elemental segment of the patch (for the present problem, $a = b = \Delta l$); k_o is the free space wave number; e_r is a unit vector in the r direction (i.e., to the observation location θ, ϕ); and $\rho_{k'}$ is the spatial position of the kth elemental segment. The components of the Green's functions are defined as,

$$G_{\theta,x}^E (r) = -j \frac{Z_o}{\lambda_o} \cos(\phi) \, g_\theta(\theta) \frac{e^{-jk_o r}}{r} \qquad (5.9a)$$

$$G_{\phi,x}^{E}(\mathbf{r}) = -j\frac{Z_o}{\lambda_o}\sin(\phi)\, g_\phi(\theta)\, \frac{e^{-jk_o r}}{r} \tag{5.9b}$$

where $Z_o = \sqrt{(\mu_o/\varepsilon_o)}$, $\lambda_o = 2\pi/k_o$, and $g_\theta(\theta)$ and $g_\phi(\theta)$ are defined as,

$$g_\theta = \frac{T\cos(\theta)}{T - j\varepsilon_r\cos(\theta)\cot(k_o hT)}$$

$$g_\phi = \frac{\cos(\theta)}{\cos(\theta) - jT\cot an(k_o hT)}$$

and

$$T = \sqrt{\varepsilon_r - \sin^2(\theta)}$$

The values of $G_{\theta,x}^{E}(\mathbf{r})$ and $G_{\phi,x}^{E}(\mathbf{r})$ are determined by a 90° rotation of ϕ in (5.9) (*i.e.*, ϕ is replaced by ϕ-90°). The Green's function (5.9) is determined from asymptotic approximation (*i.e.*, r->∞) of the exact Green's function of an electric surface current element on an infinite substrate/ground-plane.

Consider the slot-coupled microstrip patch antenna previously analyzed in section 5.3.3.2. The specific example was selected from [Himd89]. In Figures 5.41 and 5.42, the magnitude of the x and y components of the surface current distribution on the patch are provided. In Figures 5.43 and 5.44, the phase of the x and y components of the surface current distribution on the patch are provided. Note that the noisy nature of the J_y phase distribution occurs near the zero-magnitude locations. At these locations the phase is meaningless (because of the negligible magnitude) and the noisy data can be ignored. The phase distributions indicate an in-phase co-polarized current distribution and a 180° out-of-phase (organized by the four quadrants of the patch) cross-polarized current distribution. The magnitude and phase distributions are provided at the computed resonant frequency (f=2.15GHz).
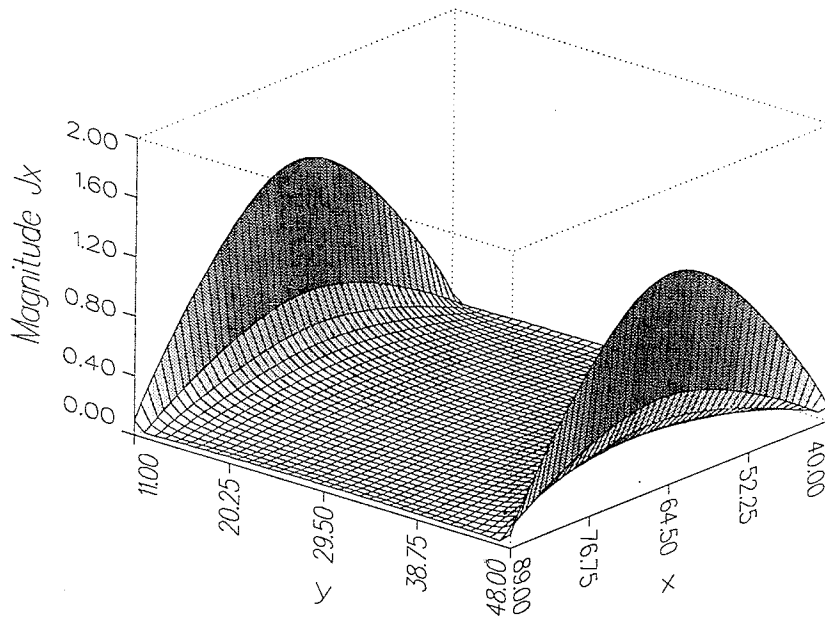
Figure 5.41: Magnitude of J_x on the surface of the patch.
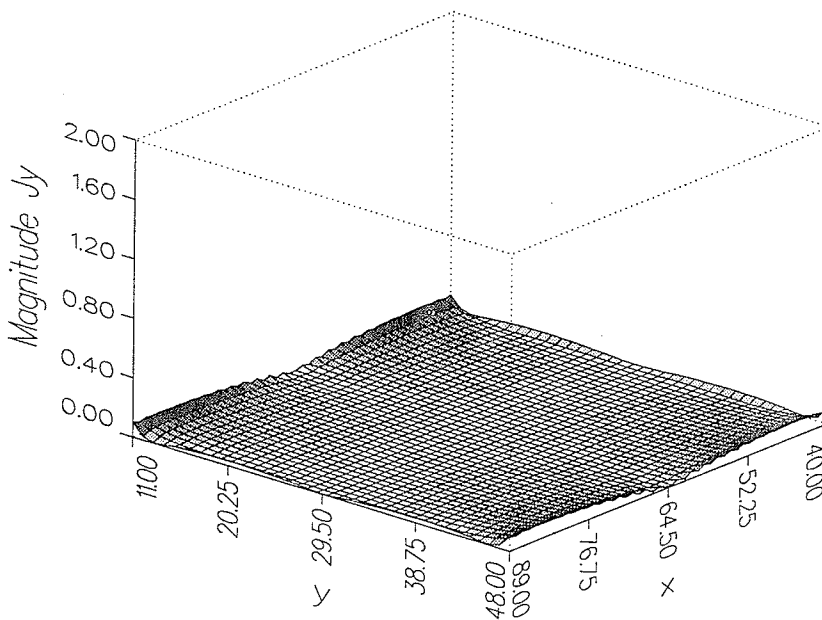
Figure 5.42: Magnitude of J_y on the surface of the patch.
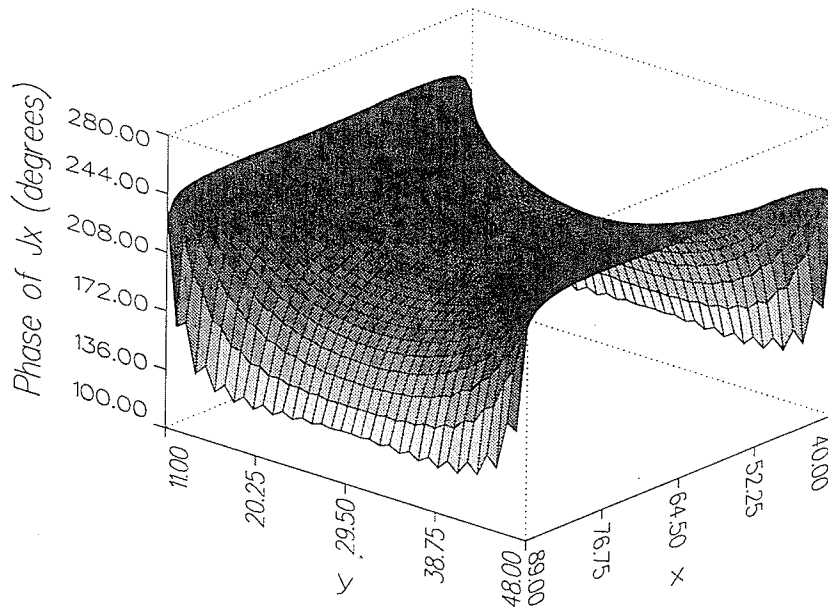
Figure 5.43: Phase of J$_x$ on the surface of the patch.
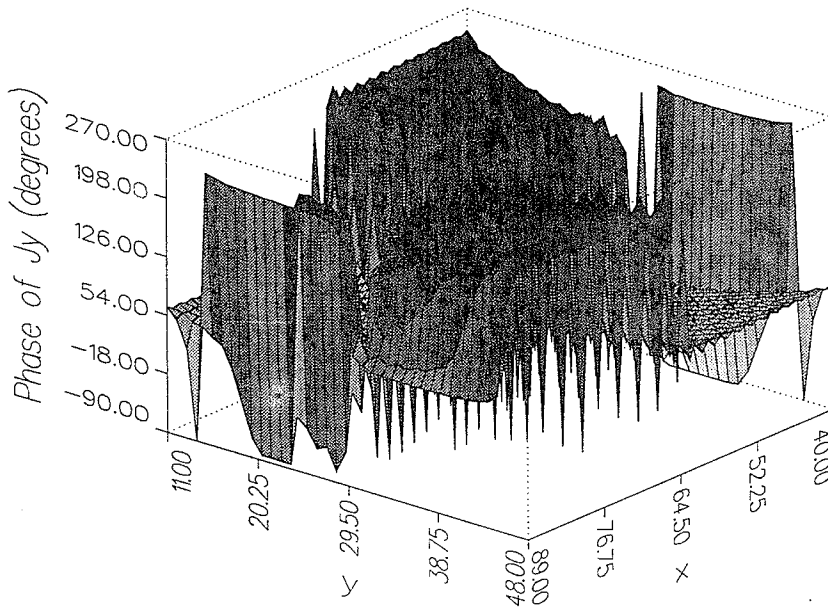
Figure 5.44: Phase of J$_y$ on the surface of the patch.

E- and H-plane radiation patterns are provided in Figures 5.45 for the slot-coupled microstrip antenna. The patterns qualitatively agree with typical results reported in the literature. Cross polarization levels are essentially zero (around - 100dB below the co-polarized levels). This low cross-polarization level is due to the slot-coupled feed. Although the magnitude of the J_y component of the surface current is not 100dB below that of the J_x component, the low cross-polarization levels are due to the phase distribution of the surface currents (see Figure 5.44). In the E- and H-planes, minimal (zero) cross-polarization levels are expected.
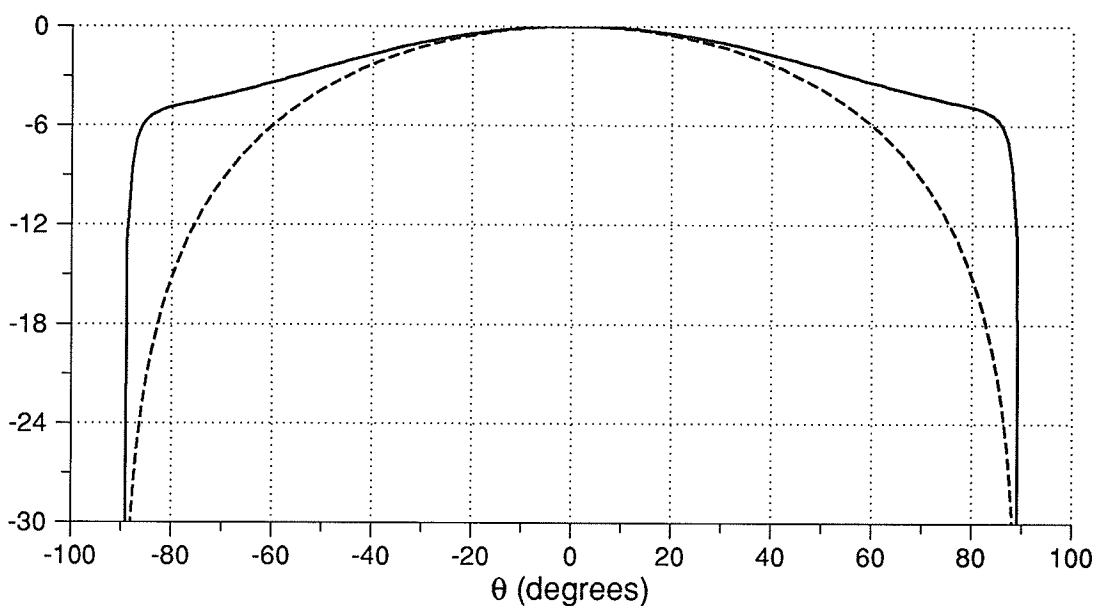
Figure 5.45: E- and H-plane radiation pattern for a slot-coupled microstrip antenna.

5.3.4.2: Antennas on a Finite Substrate/Ground Plane

In this section the theory required for the calculation of the radiation pattern of a microstrip antenna on a *finite* substrate/ground-plane is presented. Shafai and Kishk have analyzed circular microstrip antennas on a finite substrate/ground-plane using a frequency-domain integral-equation formulation for bodies of revolution [Shaf90]. In Figure 5.21(b), the TLM simulation space for the analysis of a microstrip antenna on a finite substrate/ground-plane is provided. Note that the interface between free-space and

the edge of the substrate is directly modelled as well as the finite-sized ground-plane. Free-space absorbing boundary conditions are applied to terminate the free-space region which surrounds the entire antenna.

Because the antenna does not possess an infinite substrate/ground-plane, the Sommerfeld Green's function is no longer applicable and the electric surface current on the patch antenna is not a sufficient source for determining the radiation patterns. In section 5.2, a near to far field transformation for determining scattered field distributions in the far field was presented. The same approach is applied here. Equivalent magnetic and electric surface currents on a surface surrounding the antenna are used to determine the radiation patterns.

Due to the requirement of modelling the antenna and the free-space region surrounding the antenna, the size of the simulation space required for analyzing microstrip antennas on a finite-sized substrate/ground-plane is usually prohibitively large. For most examples found in the literature, the simulation space required for accurate analysis would exceed the memory capacity of the available computational facilities.

5.4: Summary of Applications

In this section, the TLM simulation program has been applied to the analysis of microstrip circuit and antenna elements. Reasonable accuracy has been obtained for the geometries considered in this section. Again, as was the case in the previous two sections, the examples considered tend to be more homogeneous than inhomogeneous (*i.e.,* only a couple of different materials exist, with a relatively low geometrical complexity). The efficiency of the TLM simulation program (as with all differential-equation based numerical methods) is not optimal for homogeneous geometries. In terms of present day engineering computing environments, the differential-equation based numerical methods are capable of analyzing a wide variety of microstrip circuit/antenna elements, however due to the large amount of computation required for analysis, these methods are beyond the realm of an efficient design tool.

The analysis of the microstrip geometries considered in this section also indicate possible improvements which can be made to the TLM simulation program. The microstrip geometries tend to have dimensions which have much different relative sizes. For example, considering the slot-coupled microstrip antenna, the width of the slot and

thickness of substrate tend to be much smaller than the length of the slot, or length of the patch. These disparities cause excessive discretization for methods based on regular grids. An algorithm capable of making use of a variable grid would be usefull for the analysis of microstrip geometries. The density of the mesh could be increased in the vicinity of the slot and other areas where accurate modelling of the field distributions is critical to the accurate characterization of the geometry. As well, as previously discussed, for resonant structures such as the three-section side-coupled filter and the slot-coupled microstrip antenna, the use of an efficient algorithm to predict the frequency domain response (other than the discrete Fourier transform) can be applied to significantly reduce the cpu time.

The numerical results presented in section 5.1 indicate the accuracy of the TLM method for the analysis of half-space problems. In the analysis of an electrically short electric dipole in the presence of a material half-space, reasonable agreement with analytic results has been achieved for both the transient and frequency domain field distributions, as well as for the change in source input impedance due to the presence of the half-space. As with other differential-equation based methods, the efficiency of the TLM method for this class of problem is expected to be optimal for problems containing inhomogeneous objects, and multi-layer ground models.

Originally, the numerical implementation of the induced-emf method (described in section 5.1) was intended for the analysis of probe-fed microstrip antennas. However, problems arise if the size of the total/scattered contour becomes electrically small, and the source fields are not sufficiently resolved by the numerical grid. For antennas of an electrically moderate size, such as a waveguide aperture antenna, this approach should provide reasonable results. However, the model is inappropriate for most microstrip antenna applications due to the electrically thin substrate. The total/scattered contour would have to be placed between the ground plane and patch (an electrically small region in terms of the substrate thickness), and insufficient resolution of the fields produced by the dipole would occur. For the application considered in section 5.1, this impedance model has provided reasonable accuracy. The numerical implementation of the induced-emf method is applicable to any differential equation based numerical method that employs a total/scattered or a pure-scattered field formulation.

In section 5.2 the TLM simulation program has been applied to the radar-cross-section analysis of finite-sized conducting and dielectric objects. Reasonable agreement between the TLM results and a variety of published data has been obtained. To obtain accurate results, the spatial discretization of the problem domain should meet two criteria.

The first requires appropriate discretization of the object in terms of the number of spatial cells Δl per λ, where λ is the wavelength of the highest frequency at which accurate results are desired. Taflove and Umashankar suggest a spatial resolution of 10 to $20\Delta l$ per λ in conjunction with the Yee finite-difference time-domain algorithm [Tafl89]. The analysis presented in [Niel91] suggests that the symmetric condensed TLM model is more accurate than the Yee finite-difference time-domain algorithm (in terms of dispersive errors). However, the numerical experiments which we have performed do not indicate that the symmetric-condensed TLM algorithm possesses a significant advantage, and that the range of discretizations suggested by Taflove and Umashankar is also a good rule of thumb for simulations involving the symmetric-condensed TLM model. Discretizations with fewer than $10\Delta l$ per λ should be considered with caution. The second criterion that must be met to ensure accurate characterization is a sufficient distance from the scattering object to the exterior mesh boundary. In general, the required distance will depend on the object considered, its electrical size, and the specific absorbing boundary condition employed. The results presented in this section indicate that the minimum distance from the object to the exterior mesh boundary varies from 0.25 to 0.5λ. To ensure the absorbing boundary conditions do not affect the results, for each new object considered, various simulations are performed to ensure insensitivity to the location of the mesh boundary. The specific absorbing boundary condition applied is the match termination for normal incidence. If a more accurate boundary condition is applied, the 0.25 to 0.5λ requirement can be relaxed. In [Simo91d], [Simo92] an increase in accuracy is achieved from the application of alternative absorbing boundary conditions for the TLM analysis of two-dimensional scattering problems. In three dimensions, the successful application of absorbing boundary conditions other than the match termination for normal incidence boundary condition has yet to be reported. For each new object considered, various computational studies were conducted to minimize the number of time steps and the size of simulation space required. In each case, the size of the simulation space was increased until the changes in the far field patterns were reduced to a fraction of a dB. Smaller simulation spaces can be used (which require less computation time) if lower levels of accuracy are acceptable. The cpu time for most of the problems considered in section 5.2 is on the order of one hour (on a SUN SPARCstation 10). As well, these objects have been selected because of the availability of previously published results. Although the results demonstrate the accuracy of the TLM approach, the objects do not exploit the capabilities of the method. Again, as with other differential-equation based methods (such as finite-difference, finite-element, and

finite-volume methods), the efficiency of the TLM method is expected to be optimal for the analysis of inhomogeneous objects. For the analysis of objects with fine geometrical detail such as material layers, slots, and wires (whose dimensions are small relative to the mesh discretization Δl), special computational capabilities are required [Duff93], [Rile93].

The numerical results obtained in section 5.2 were insensitive to changes in the locations of the total/scattered field contour and the near-to-far field transformation contour. In a typical simulation, the total/scattered field contour is placed around $5\Delta l$ from the edge of the object and the near-to-far field transformation contour is placed approximately $3\Delta l$ outside of the total/scattered field contour. The electrical size of the objects considered in this section range from a side length of 0.2λ to a few λ. To analyze objects that are either electrically smaller or larger one only requires more computation time. To examine electrically smaller objects, the distance from the object to the exterior boundary of the mesh (in terms of Δl) should be increased to accommodate the 0.25 to 0.5λ requirement. To analyze electrically large objects, the number of spatial cells required must be increased to accommodate the minimum $10\Delta l/\lambda$ discretization ratio.

The results obtained in this chapter validate the accuracy of the TLM simulation program, and supports the concept of a general purpose electromagnetic simulation environment.

Chapter 6: Time-Domain Finite-Element Method and Applications

In this chapter a time-domain finite-element algorithm is investigated which is based on a formulation originally introduced by Lynch and Paulsen [Lync90]. In chapter 2, this algorithm has been classified in terms of the general overview of differential-equation based numerical methods. This algorithm can also be considered as a general purpose electromagnetic field simulation program. In the first part of this chapter, the time-domain finite-element algorithm is introduced with emphasis placed on aspects of the algorithm which differ from that presented in [Lync90]. Numerical examples are provided to validate the program. In the second part of this chapter, the equivalence of the finite-element formulation (if applied on a regular mesh) and a finite-difference formulation is demonstrated.

6.1: Finite-Element Formulation

6.1.1: Mathematical Formulation

The general problem considered is provided in Figure 6.1 and consists of a volume of space V bounded by an exterior surface S_1 and several interior surfaces $S_2, \ldots ,$ S_N. This problem is equivalent to the general electromagnetic field problem described in Figure 1.1. The modified vector wave equation (discussed in section 2.1) is given by,

$$\varepsilon \frac{\partial^2 E}{\partial t^2} + \sigma \frac{\partial E}{\partial t} = -\frac{1}{\mu} \nabla \times \nabla \times E + \nabla \left(\frac{1}{\mu\varepsilon} \nabla \cdot \varepsilon E \right) \qquad (6.1)$$

148

which describes the behavior of the total electric field throughout V. Boundary conditions for **E** on S_1, S_2, ... , S_N are specified to complete the description of the problem. The region V is assumed to consist of linear, isotropic, but arbitrarily inhomogeneous media.
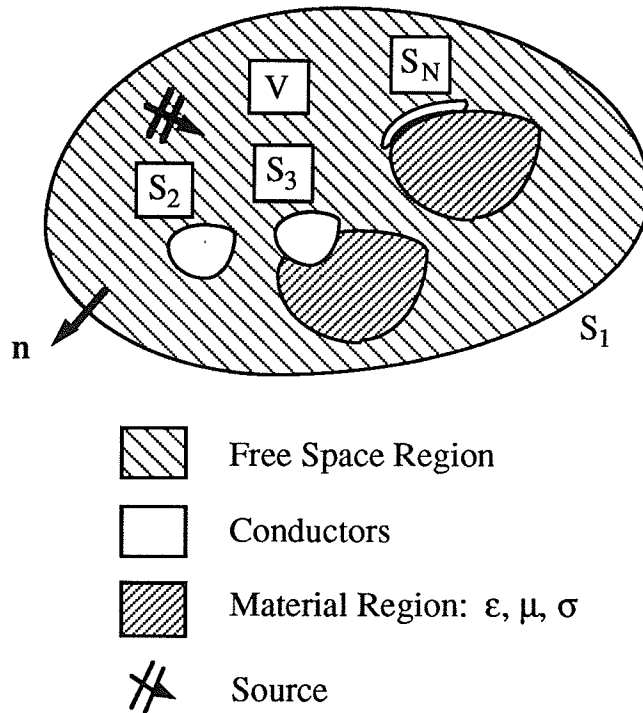
Figure 6.1: General configuration: A volume V bounded by an exterior surface S_1, and N-1 interior surfaces S_2 , ... , S_N.

The surface S_1 is a truncated free space boundary (i.e., ideally it should extend to infinity). To terminate this outer boundary, local absorbing boundary conditions are applied. The first order Engquist-Majda absorbing boundary condition [Engq77] is applied along S_1. This condition is expressed as,

$$\frac{\partial E}{\partial t} - \frac{1}{c}\frac{\partial E}{\partial n} = 0 \tag{6.2}$$

where **E** is the electric field distribution and n is the direction normal to the exterior boundary. The interior surfaces S_2, ... , S_N represent the perfectly conducting surfaces of the geometry. Along these surfaces the boundary condition $n \times (E^s + E^i) = 0$ is applied.

6.1.2: Scattered Field Formulation

A scattered field formulation is applied (see discussion in section 2.2). The total electric field distribution E is expressed as, $E = E^s + E^i$, where E^i is the incident field distribution, and E^s is the scattered electric field distribution. The incident field distribution satisfies,

$$\varepsilon_o \frac{\partial^2 E^i}{\partial t^2} + \sigma_o \frac{\partial E^i}{\partial t} = - \nabla \times \left(\frac{1}{\mu_o} \nabla \times E^i \right) + \nabla \left(\frac{1}{\mu_o \varepsilon_o} \nabla \cdot \varepsilon_o E^i \right) \tag{6.3}$$

where ε_o, μ_o, and σ_o represent the material properties of the medium in which the incident field exists. Subtracting (6.3) from (6.1) yields the scattered field formulation of the modified vector wave equation,

$$\varepsilon \frac{\partial^2 E^s}{\partial t^2} + (\varepsilon - \varepsilon_o) \frac{\partial^2 E^i}{\partial t^2} + \sigma \frac{\partial E^s}{\partial t} + (\sigma - \sigma_o) \frac{\partial E^i}{\partial t}$$

$$= - \nabla \times \left(\frac{1}{\mu} \nabla \times E^s \right) - \nabla \times \left(\left(\frac{1}{\mu} - \frac{1}{\mu_o} \right) \nabla \times E^i \right) + \nabla \left(\frac{1}{\mu} \nabla \cdot E^s \right) + \nabla \left(\left(\frac{1}{\mu} - \frac{1}{\mu_o} \right) \nabla \cdot E^i \right) \tag{6.4}$$

Along the exterior boundary, S_1, the absorbing boundary condition (6.2) can be applied to the scattered field distribution and does not require modification. Along the conducting boundaries, S_2 to S_N, the boundary condition $E^s = -E^i$ is applied.

6.1.3: Discretization of Space and Time

Consider the application of the method of weighted residuals to approximate the spatial domain of (6.4). The desired weak form of the problem is obtained by multiplying (6.4) by a set of time-independent weighting functions w_i, where $i = 1, \ldots N$, and integrating over the computational domain V, to obtain,

$$\int_v w_i \, \epsilon \frac{\partial^2 \mathbf{E}^s}{\partial t^2} \, dV + \int_v w_i \, (\epsilon - \epsilon_o) \frac{\partial^2 \mathbf{E}^i}{\partial t^2} \, dV + \int_v w_i \, \sigma \frac{\partial \mathbf{E}^s}{\partial t} \, dV + \int_v w_i \, (\sigma - \sigma_o) \frac{\partial \mathbf{E}^i}{\partial t} \, dV$$

$$= - \int_v w_i \, \nabla \times \left(\frac{1}{\mu} \nabla \times \mathbf{E}^s \right) dV - \int_v w_i \, \nabla \times \left(\left(\frac{1}{\mu} - \frac{1}{\mu_o} \right) \nabla \times \mathbf{E}^i \right) dV$$

$$+ \int_v w_i \, \nabla \left(\frac{1}{\mu} \nabla \cdot \mathbf{E}^s \right) dV + \int_v w_i \, \nabla \left(\left(\frac{1}{\mu} - \frac{1}{\mu_o} \right) \nabla \cdot \mathbf{E}^i \right) dV \qquad (6.5)$$

To reduce the dimensionality of the second-order spatial derivatives in (6.5), the terms on the right hand side of (6.5) are modified using the following identities,

$$\phi \nabla \times \mathbf{A} - \mathbf{A} \times \nabla \phi = \nabla \times (\phi \mathbf{A}) \qquad \int_v \nabla \times \mathbf{A} \, dV = - \int_s \mathbf{A} \times \hat{n} \, dS$$

and

$$\nabla (\phi \psi) = \phi \nabla \psi + \psi \nabla \phi \qquad \int_v \nabla \times \phi \, dV = - \int_s \phi \hat{n} \, dS$$

to yield,

$$\int_v w_i \, \epsilon \frac{\partial^2 \mathbf{E}^s}{\partial t^2} \, dV + \int_v w_i \, (\epsilon - \epsilon_o) \frac{\partial^2 \mathbf{E}^i}{\partial t^2} \, dV + \int_v w_i \, \sigma \frac{\partial \mathbf{E}^s}{\partial t} \, dV + \int_v w_i \, (\sigma - \sigma_o) \frac{\partial \mathbf{E}^i}{\partial t} \, dV$$

$$= \int_v \nabla w_i \times \left(\frac{1}{\mu} \nabla \times \mathbf{E}^s \right) dV + \int_v \nabla w_i \times \left(\left(\frac{1}{\mu} - \frac{1}{\mu_o} \right) \nabla \times \mathbf{E}^i \right) dV$$

$$- \int_v \left(\frac{1}{\epsilon \mu} \nabla \cdot \epsilon \mathbf{E}^s \right) \nabla w_i \, dV - \int_v \left(\frac{1}{\epsilon \mu} \nabla \cdot \epsilon \mathbf{E}^i - \frac{1}{\epsilon_o \mu_o} \nabla \cdot \epsilon_o \mathbf{E}^i \right) \nabla w_i \, dV$$

$$- \int_s n \times \left(\frac{1}{\mu} \nabla \times \mathbf{E}^s \right) w_i \, dS - \int_s n \times \left(\left(\frac{1}{\mu} - \frac{1}{\mu_o} \right) \nabla \times \mathbf{E}^i \right) w_i \, dS$$

151

$$+ \int_S \left(w_i \frac{1}{\varepsilon\mu} \nabla \cdot \varepsilon \mathbf{E}^s \right) \mathbf{n} \, dS + \int_S w_i \left(\frac{1}{\varepsilon\mu} \nabla \cdot \varepsilon \mathbf{E}^i - \frac{1}{\varepsilon_0\mu_0} \nabla \cdot \varepsilon_0 \mathbf{E}^i \right) \mathbf{n} \, dS \qquad (6.6)$$

Examination of (6.6) indicates the manner in which the incident field is introduced. Throughout regions which possess material properties that are different from the incident field medium (ε_0, μ_0, σ_0), the terms containing $\mathbf{E}^i$ represent surface and volume sources for the incident field. The unknown scattered field distribution $\mathbf{E}^s$ is expanded as,

$$\mathbf{E}^s(\mathbf{r},t) = \sum_{j=1}^{N} \mathbf{E}_j^s(t) \, \phi_j(\mathbf{r}) \qquad (6.7)$$

where $\mathbf{E}_j^s(t)$ are *time-dependent* and *spatially-independent* vector nodal values, and $\phi_j(\mathbf{r})$ are *spatially-dependent* and *time-independent* scalar expansion functions. Substituting (6.7) into (6.6), and for simplicity examining only the volume integrals from (6.6) containing the unknown $\mathbf{E}^s$, yields,

$$\sum_{j=1}^{N} \int_V \varepsilon w_i \phi_j \, dV \frac{\partial^2 \mathbf{E}_j^s(t)}{\partial t^2} + \sum_{j=1}^{N} \int_V \sigma w_i \phi_j \, dV \frac{\partial \mathbf{E}_j^s(t)}{\partial t}$$

$$= \sum_{j=1}^{N} \int_V \frac{1}{\mu} \nabla w_i \times \left(\nabla \phi_j \times \mathbf{E}_j^s \right) dV - \sum_{j=1}^{N} \mathbf{E}_j^s \cdot \int_V \left(\frac{1}{\mu\varepsilon} \nabla \varepsilon \phi_j \right) \nabla w_i \, dV + \text{ST} + \text{IFT} \qquad (6.8)$$

where ST denotes the surface integrals, and IFT denotes the terms containing $\mathbf{E}^i$ in (6.6). The semi-discrete system (6.8), can be expressed in traditional finite-element notation [Zien91] as,

$$\mathbf{M}\ddot{\mathbf{e}}^s + \mathbf{C}\dot{\mathbf{e}}^s + \mathbf{K}\mathbf{e}^s = \mathbf{f} \qquad (6.9)$$

where $\mathbf{M}$ is the mass matrix, $\mathbf{C}$ is the damping matrix (the elements of $\mathbf{C}$ are non-zero only if $\sigma \neq 0$), $\mathbf{K}$ is the stiffness matrix, $\mathbf{e}^s$ is a vector of nodal values representing the unknown scattered field distribution, $\dot{\mathbf{e}}^s$ is the first derivative of $\mathbf{e}^s$ with respect to time, $\ddot{\mathbf{e}}^s$ is the second derivative of $\mathbf{e}^s$ with respect to time, and $\mathbf{f}$ is a vector containing the incident

field terms [Zien83], [Mull82]. The following second-order central-difference formulas are applied to discretize the temporal derivatives in (6.8),

$$\frac{\partial f(t)}{\partial t} = \frac{f(t+\Delta t) - f(t-\Delta t)}{2\Delta t} \qquad \text{and} \qquad \frac{\partial^2 f(t)}{\partial t^2} = \frac{f(t+\Delta t) - 2f(t) + f(t-\Delta t)}{\Delta t^2}$$

The resulting system is given by,

$$\left(\frac{1}{\Delta t^2} \sum_{j=1}^{N} \int_V \varepsilon w_i \phi_j \, dV + \frac{1}{2\Delta t} \sum_{j=1}^{N} \int_V \sigma w_i \phi_j \, dV \right) E_j^{s,t+\Delta t}$$

$$= \sum_{j=1}^{N} \int_V \frac{1}{\mu} \nabla w_i \times \left(\nabla \phi_j \times E_j^{s,t} \right) dV - \sum_{j=1}^{N} E_j^{s,t} \cdot \int_V \left(\frac{1}{\mu\varepsilon} \nabla\varepsilon\phi_j \right) \nabla w_j \, dV + \frac{2}{\Delta t} \sum_{j=1}^{N} \int_V \sigma w_i \phi_j \, dV \, E_j^{s,t}$$

$$\left(\frac{1}{\Delta t} \sum_{j=1}^{N} \int_V \sigma w_i \phi_j \, dV + \frac{1}{2\Delta t} \sum_{j=1}^{N} \int_V \sigma w_i \phi_j \, dV \right) E_j^{s,t-\Delta t} + ST + IFT \qquad (6.10)$$

where Δt is the time step, and $E_j^{s,t}$ is the value of E_j^s at time t. To complete the specification of (6.10), we specify $\phi_j = w_j$ (i.e., Galerkin's method) and select a suitable C_o continuous three-dimensional element with linear expansion functions [Zien91]. Presently, only cubic elements are applied, shown in Figure 6.2. The expansion functions for this element are expressed as,

$$N_i = \frac{1}{8} \left(1+\xi_o \right) \left(1+\eta_o \right) \left(1+\zeta_o \right)$$

where $\xi_o = \xi\xi_i$, $\eta_o = \eta\eta_i$, $\zeta_o = \zeta\zeta_i$, and

$$\xi_1, \eta_1, \zeta_1 = -1,-1,-1; \quad \xi_2, \eta_2, \zeta_2 = +1,-1,-1; \quad \xi_3, \eta_3, \zeta_3 = +1,+1,-1;$$

$$\xi_4, \eta_4, \zeta_4 = -1,+1,-1; \quad \xi_5, \eta_5, \zeta_5 = -1,-1,+1; \quad \xi_6, \eta_6, \zeta_6 = +1,-1,+1;$$

$$\xi_7, \eta_7, \zeta_7 = +1,+1,+1; \quad \xi_8, \eta_8, \zeta_8 = -1,+1,+1$$
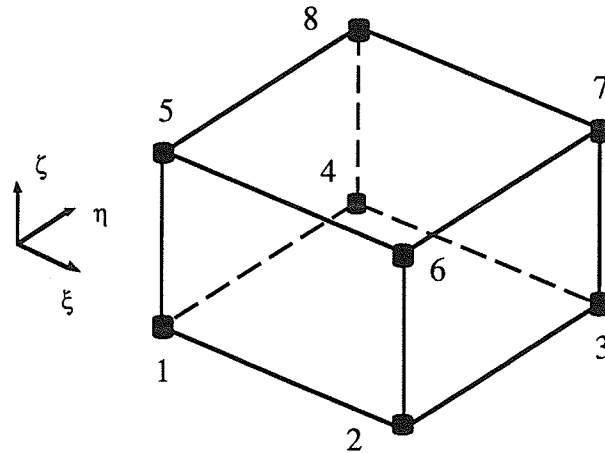
Figure 6.2: Cubic element used for spatial discretization.

Expression (6.10) represents a system of linear algebraic equations, that can be expressed as,

$$[A][E]^{t+1} = [B][E]^t + [C][E]^{t-1} \tag{6.11}$$

where $[E]^t$ represents a vector containing the nodal values which represent the electric field distribution at time t. Equation (6.11) represents an explicitly time stepped algorithm if $[A]$ is a diagonal matrix, since calculation of $[A]^{-1}$ would not require formal matrix inversion. The coefficients a_{ij} of the matrix A are proportional to

$$\int_V w_i \phi_j \, dV \tag{6.12}$$

The possible techniques for evaluating the element integrals (such as (6.12)) are limited by the convergence criterion for the finite-element method [Zien91]. The convergence criterion states that the integration algorithm should be exact to order 2(p-m), where p is the degree of the complete polynomial in the element expansion functions, and m is the order of differentials occurring in the mathematical formulation. For the present application p=1 and m=1, and therefore, any integration scheme capable of integrating zeroth order functions is acceptable to yield no loss in convergence. A comparison of the numerical algorithms obtained from exact and approximate numerical integration is provided in section 6.2. In [Care84], various nodal quadrature integration schemes are

154

presented. Any numerical scheme for the integration of a function f(x) over an interval L can be expressed as,

$$\int_L f(x)\,dx = \sum_{n=1}^{N} w_n f(x_n)$$

where w_n are the weighting coefficients and x_n are the evaluation points. The evaluation points for nodal quadrature formulas are the node locations. Because of the nature of the expansion functions,

$$\phi_i(x_j) = 0 \qquad j \neq i \qquad\qquad (6.13)$$

the integral (6.12) is equal to zero for $i \neq j$. Therefore the matrix $[A]$ is diagonal and an explicitly time-stepped algorithm is obtained without loss of accuracy.

6.1.4: Discretization of Absorbing Boundary Conditions

The discretization of the absorbing boundary condition (6.2) can also be accomplished using the same numerical strategy applied to the modified vector wave equation as described above. Three implementations of (6.2) have been considered, all of which can be considered as analogues of finite-difference approximations of (6.2). The details of obtaining the appropriate finite-difference analogue require knowledge of the equivalence between the integral lumped time-domain finite-element algorithm with central finite-difference approximations, which is presented in section 6.2. The implementation of the absorbing boundary conditions is considered with respect to a portion of the exterior boundary illustrated in Figure 6.3.

The weak-form of the absorbing boundary condition (6.2) is given by,

$$\int_v w_i \left(\frac{\partial}{\partial n} + \frac{1}{c}\frac{\partial}{\partial t} \right) E\,dV = 0 \qquad\qquad (6.14)$$

where, w_i are the same sub-domain basis functions applied in conjunction with the discretization of the modified vector wave equation. Expanding E in terms of *time-*

dependent and *spatially-independent* vector nodal values, and *spatially-dependent* and *time-independent* scalar expansion functions, yields,

$$\sum_j \int_V w_i \left(\frac{\partial \phi_j}{\partial n} E_j + \frac{1}{c} \phi_j \frac{\partial E_j}{\partial t} \right) dV = 0 \tag{6.15}$$

Various approaches to the organization of the approximations to the partial derivatives in (6.15) are now investigated.

In the first implementation of (6.15) the time derivative is centred around the temporal location at which the spatial derivative is evaluated as,

$$\sum_j \int_V w_i \left(\frac{\partial \phi_j}{\partial n} E_j^k + \frac{1}{c} \phi_j \frac{E_j^{k+1} - E_j^{k-1}}{2\Delta t} \right) dV = 0 \tag{6.16}$$

Following the same discretization procedure applied to the modified vector wave equation over a regular mesh, (6.15) results in a finite-difference expression of the form,

$$\frac{1}{\Delta n} \left(E_j^k - E_{j'}^k \right) + \frac{1}{2c\Delta t} \left(E_j^{k+1} - E_j^{k-1} \right) = 0 \tag{6.17}$$

where Δn is the distance from node j to node j' (see Figure 6.3) in the **n** direction. The numerical form of (6.17) is exactly reversible [Vich84b]. The physical situation corresponding to the excitation of a source within the computational volume, and the subsequent propagation of electromagnetic waves out of the simulation space can be considered as an attractor *i.e.,* given an initial disturbance in the general electromagnetic field problem desribed in Figure 6.1, the field distribution will always approach zero as t->∞. Therefore, application of the numerically reversible absorbing boundary condition (6.17) in the presence of this attractor, yields instability [Vich84b]. Numerical investigation of these concepts with respect to computational electromagnetics is considered in [Simo94e]. Numerical experimentation verifies the instability of the implementation (6.17).

In the second implementation of (6.15), a backward difference formula is applied to the discretization of the temporal derivative to yield,

$$\sum_j \int_v w_i \left(\frac{\partial \phi_j}{\partial n} E_j^{k+1} + \frac{1}{c} \phi_j \frac{E_j^{k+1} - E_j^k}{\Delta t} \right) dV = 0 \qquad (6.18)$$

Again, following the same discretization procedure as outlined above over a regular mesh, (6.18) results in a finite-difference expression of the form,

$$\frac{1}{\Delta n} \left(E_j^{k+1} - E_{j'}^{k+1} \right) + \frac{1}{c \Delta t} \left(E_j^{k+1} - E_j^k \right) = 0 \qquad (6.19)$$

In the third implementation of (6.15), the spatial derivatives are averaged in time, and the temporal derivatives are weighted in space as,

$$\sum_j \int_v w_i \left(\frac{\partial \phi_j}{\partial n} \left(E_j^{k+1} + E_j^k \right) + \frac{1}{c} \phi_j \left(\frac{\partial E_j}{\partial t} + \frac{\partial E_{j'}}{\partial t} \right) \right) dV = 0$$

to yield,

$$\sum_j \int_v w_i \left(\frac{\partial \phi_j}{\partial n} \left(E_j^{k+1} + E_j^k \right) + \frac{1}{c} \phi_j \left(\frac{E_j^{k+1} - E_j^k}{\Delta t} + \frac{E_{j'}^{k+1} - E_{j'}^k}{\Delta t} \right) \right) dV = 0 \qquad (6.20)$$

Again, following the same discretization procedure as outlined above, over a regular mesh (6.20) results in a finite-difference expression of the form,

$$\frac{1}{\Delta n} \left(\left(E_j^{k+1} - E_{j'}^{k+1} \right) + \left(E_j^k - E_{j'}^k \right) \right) + \frac{1}{c \Delta t} \left(\left(E_j^{k+1} - E_j^k \right) + \left(E_{j'}^{k+1} - E_{j'}^k \right) \right) = 0 \qquad (6.21)$$

The numerical approximations (6.19) and (6.21) correspond to the *first-order* and *box* schemes of Engquist and Majda [Engq77], respectively.
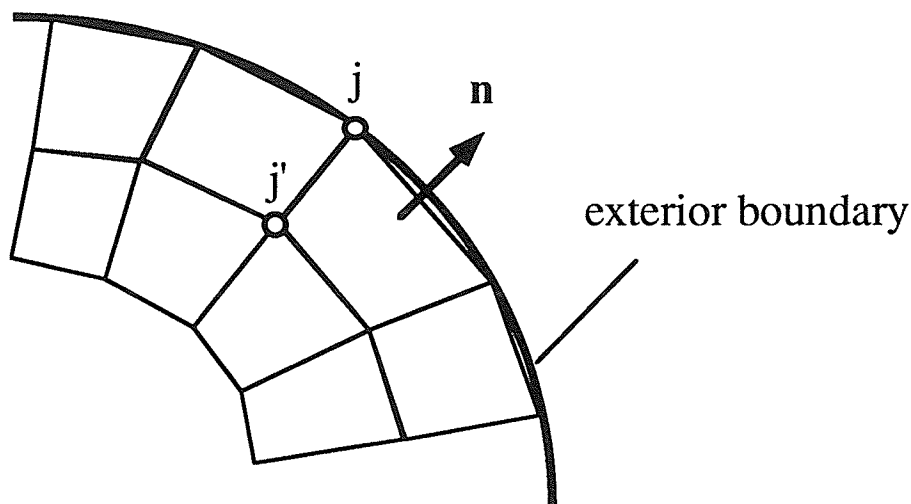
Figure 6.3: Two dimensional slice of a finite-element mesh to illustrate the application of absorbing boundary conditions along on exterior mesh boundary.

6.1.5: Boundary Conditions Along Material Interfaces

Consider the enforcement of boundary condtions between two material regions 1 and 2, shown in Figure 6.4. The procedure presented in [Lync90] is applied with modifications to account for the scattered field formulation. The boundary conditions (1.3) for the electric field distribution are applied. Because the normal field components are discontinuous, along the interface, the nodes are split such that two nodes exist at the same spatial location, but are allowed to possess different field values. The total electric field distribution at the two nodes in Figure 6.4 satisfy,

$$\hat{n} \cdot \left(\varepsilon_1 \frac{\partial^2 \mathbf{E}_1}{\partial t^2} + \sigma_1 \frac{\partial \mathbf{E}_1}{\partial t} \right) = \hat{n} \cdot \left(\varepsilon_2 \frac{\partial^2 \mathbf{E}_2}{\partial t^2} + \sigma_2 \frac{\partial \mathbf{E}_2}{\partial t} \right)$$

and
$$\hat{n} \times \frac{\partial \mathbf{E}_1}{\partial t} = \hat{n} \times \frac{\partial \mathbf{E}_2}{\partial t} \tag{6.22}$$

The nodal values $\mathbf{E}_1$ and $\mathbf{E}_2$ can be expressed in terms of their normal and tangential components as,

$$E_1 = E_{n1}\widehat{n} + E_{t1}\widehat{t} + E_{g1}\widehat{g} \quad \text{and} \quad E_2 = E_{n2}\widehat{n} + E_{t2}\widehat{t} + E_{g2}\widehat{g} \qquad (6.23)$$

The normal and tangential unit vectors at each nodal location are calculated in the same manner as in [Enge82]. Substituting (6.23) into (6.22) yields,

$$\varepsilon_1 \frac{\partial^2 E_{n1}}{\partial t^2} + \sigma_1 \frac{\partial E_{n1}}{\partial t} = \varepsilon_2 \frac{\partial^2 E_{n2}}{\partial t^2} + \sigma_2 \frac{\partial E_{n2}}{\partial t} \qquad (6.24)$$

$$\frac{\partial E_{t1}}{\partial t} = \frac{\partial E_{t2}}{\partial t} \quad \text{and} \quad \frac{\partial E_{g1}}{\partial t} = \frac{\partial E_{g2}}{\partial t} \qquad (6.25)$$

The nodal values E_1 and E_2 are represented in terms of their total and scattered field components as, $E_{u1} = E_{u1}^i + E_{u1}^s$ and $E_{u2} = E_{u2}^i + E_{u2}^s$ where u=n, g, or t (see Figure 6.4). The incident field distribution, E^i is the same at nodes 1 and 2, and is therefore denoted as E_u^i (where u=n, g, or t). The normal field boundary condition (6.24), is expressed as,

$$\varepsilon_1 \frac{\partial^2 E_{n1}^s}{\partial t^2} + \sigma_1 \frac{\partial E_{n1}^s}{\partial t} = \varepsilon_2 \frac{\partial^2 E_{n2}^s}{\partial t^2} + \sigma_2 \frac{\partial E_{n2}^s}{\partial t} + (\varepsilon_2 \text{-}\varepsilon_1) \frac{\partial^2 E_n^i}{\partial t^2} + (\sigma_2 \text{-}\sigma_1) \frac{\partial E_n^i}{\partial t} \qquad (6.26)$$

Applying the second-order contral difference approximations used in section 6.1.3 for the discretization of the mathematical formulation to the temporal derivatives yields,

$$\left(\varepsilon_2 + \frac{\sigma_2 \Delta t}{2}\right) E_{n2}^{s,k+1} = \left(\varepsilon_1 + \frac{\sigma_1 \Delta t}{2}\right) E_{n1}^{s,k+1} - 2\varepsilon_1 E_{n1}^{s,k} + \left(\varepsilon_1 + \frac{\sigma_1 \Delta t}{2}\right) E_{n1}^{s,k-1}$$

$$+ 2\varepsilon_2 E_{n2}^{s,k} - \left(\varepsilon_2 + \frac{\sigma_2 \Delta t}{2}\right) E_{n2}^{s,k-1}$$

$$+ \left((\varepsilon_1 \text{-} \varepsilon_2) + (\sigma_1 \text{-} \sigma_2)\frac{\Delta t}{2}\right) E_n^{i,k+1} - 2(\varepsilon_1 \text{-} \varepsilon_2)E_n^{s,k} + \left((\varepsilon_1 \text{-} \varepsilon_2) + (\sigma_1 \text{-} \sigma_2)\frac{\Delta t}{2}\right) E_n^{s,k-1} \qquad (6.27)$$

where k denotes the time step *(i.e., the difference between times k and k+1 is Δt)*. The boundary conditions for the tangential components are given as,

$$E_{t1}^{s,k+1} = \left(E_{t2}^{s,k+1} - E_{t2}^{s,k-1}\right) + E_{t1}^{s,k-1} \quad \text{and} \quad E_{g1}^{s,k+1} = \left(E_{g2}^{s,k+1} - E_{g2}^{s,k-1}\right) + E_{g1}^{s,k-1} \qquad (6.28)$$

These conditions are much simpler than those for the normal field component (6.27) because the tangential field component is continuous across the interface. The above approach to the modelling of the interface between material regions rigourously enforces the boundary conditions on both the tangential and normal components of the electric field distribution.

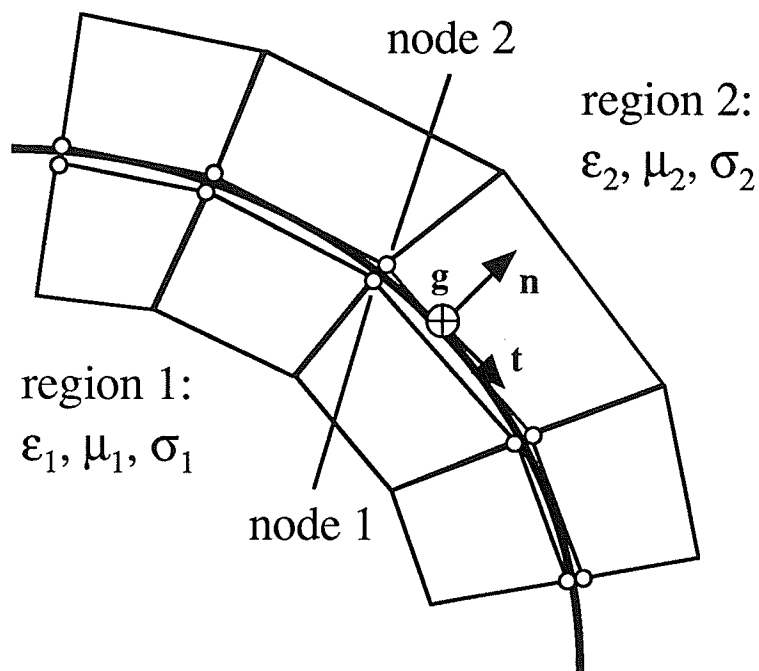**Figure 6.4:** Two dimensional slice of a finite-element mesh to illustrate the application of boundary conditions along the interface between two material regions.

6.1.6: Excitation

Two types of sources have been applied in conjunction with the above algorithm. These are a plane wave (arbitrary polarization and arbitrary angle of incidence) and an infinitesimal electric dipole (described in section 5.1).

6.1.7: Calculation of Magnetic Field Distribution

The mathematical formulation applied in this chapter is expressed in terms of the electric field distribution. In general, calculations of far field patterns or input impedance require knowledge of both the electric and magnetic field distributions. The electric and magnetic field distributions are related through Maxwell's curl equations (2.1), the second of which is given by,

$$\frac{\partial H}{\partial t} = -\frac{1}{\mu} \nabla \times E$$

In the mathematical discretization procedure described above, the electric field distribution $E(r,t)$ is represented in terms of scalar time-independent and vector spatially-dependent expansion functions ϕ_j, and time-dependent and spatially-independent expansion coefficients E_j, as $\Sigma(E_j \phi_j)$, substitution into the curl equation above yields,

$$\frac{\partial H}{\partial t} = -\frac{1}{\mu} \nabla \times \sum_j E_j \phi_j = \frac{1}{\mu} \sum_j E_j \times \nabla \phi_j \qquad (6.29)$$

The right hand side of (6.29) can be evaluated numerically, to yield the derivative of the magnetic field distribution with respect to time. To determine the magnetic field distribution, a temporal second-order finite-difference approximation is assumed (consistent with the numerical discretization procedure described above),

$$\frac{\partial H(t)}{\partial t} = \frac{H(t+\Delta t/2) - H(t-\Delta t/2)}{\Delta t} \quad \text{to yield,} \quad H(t+\Delta t/2) = \Delta t \frac{\partial H(t)}{\partial t} + H(t-\Delta t/2)$$

In the above expression $\partial H/\partial t$ is available from the numerical evaluation of (6.29) and therefore starting from an initial field distribution $H(t=0)$, the magnetic field at a time t, is determined by incrementally summing the following expression,

$$H(t+\Delta t/2) = \frac{\Delta t}{\mu} \sum_j \left(E_j \times \nabla \phi_j \right) + H(t-\Delta t/2) \qquad (6.30)$$

The method described above for determining **H** from **E** is computationally consitent with the numerical discretization procedure. The numerical evaluation of (6.30) is performed

using an 8 by 2 matrix. The dimension of 8 arises for linear cubic elements with eight nodes, and the dimension of 2 arises because the curl operation couples two components of the electric field to one component of the magnetic field. Because sub-domain basis functions are applied, the summation in (6.30) is only performed over the element which contains the observation point. Therefore, before the time-stepping begins, a preliminary search is required to determine in which element the observation point is located.

6.1.8: Numerical Results

To validate the basic capabilities of the method, some problems involving conducting plates and dielectric bodies have been considered. Results produced by two other numerical methods (an integral-equation-based conformal-mapping/method of moments code [Mohe90], [Mohe91] and the TLM simulation program described in previous chapters) are used for validation.

The first problem considered is shown in Figure 6.5(a), and consists of a short probe radiating in the presence of finite-sized, conducting ground plane. In Figure 6.5(b)-(d) the transient response at various observation points around the plate as calculated by the finite-element algorithm are compared to results generated by the TLM code. Excellent agreement is obtained at all three observation locations. The same approch discussed in Chapter 5 (section 5.2) is applied to determine the far field patterns. In Figure 6.5(e), the radiation pattern of the system calculated by the finite-element method is compared to both TLM and integral-equation results. Excellent agreement is obtained in the region in front of the plate. Explanation of the poor agreement in the region behind the plate is due to the first-order absorbing boundary condition (6.2), and possibly the use of a scattered field rather than a total/scattered field formulation.
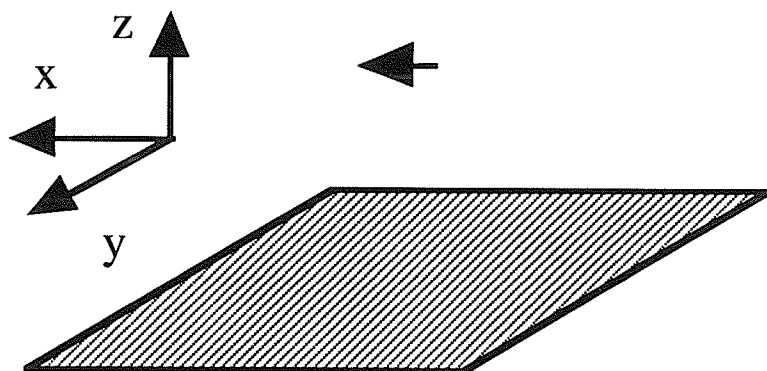
Figure 6.5(a): Electric current element illuminating a thin conducting plate.
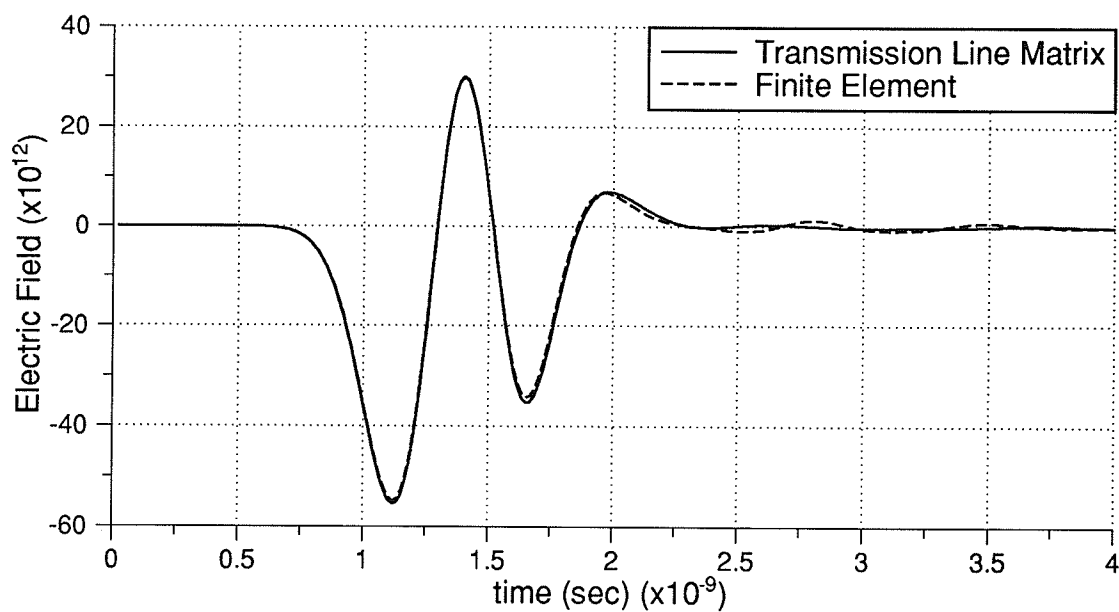
Figure 6.5(b): Transient response of the conducting plate at an observation point above the plate, centred under the current element.
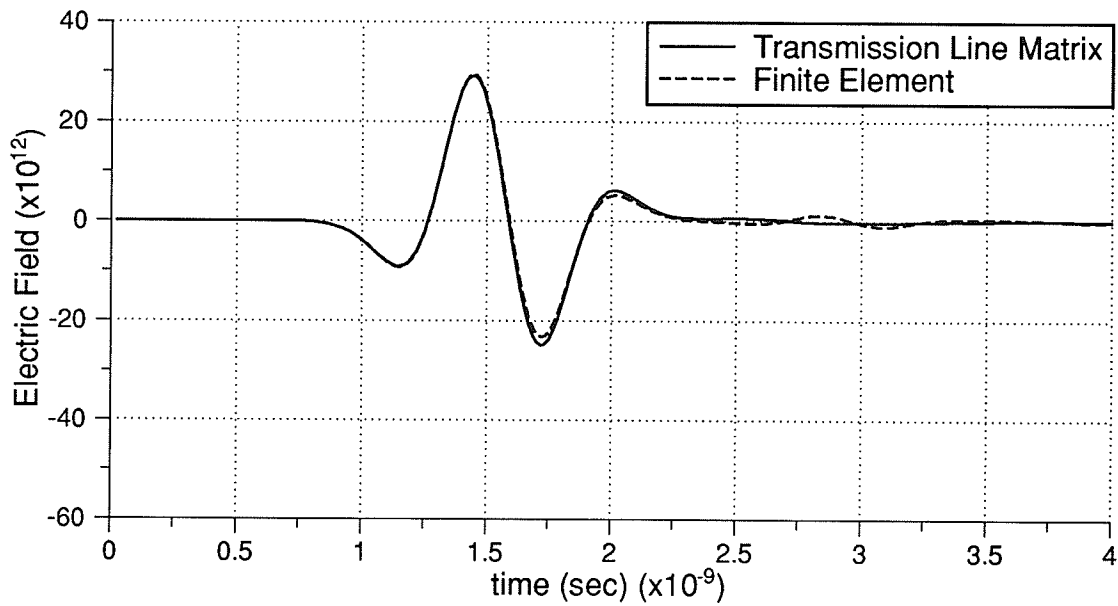
Figure 6.5(c): Transient response of the conducting plate at an observation point offset from the centre of the the plate (x-component of the electric field).
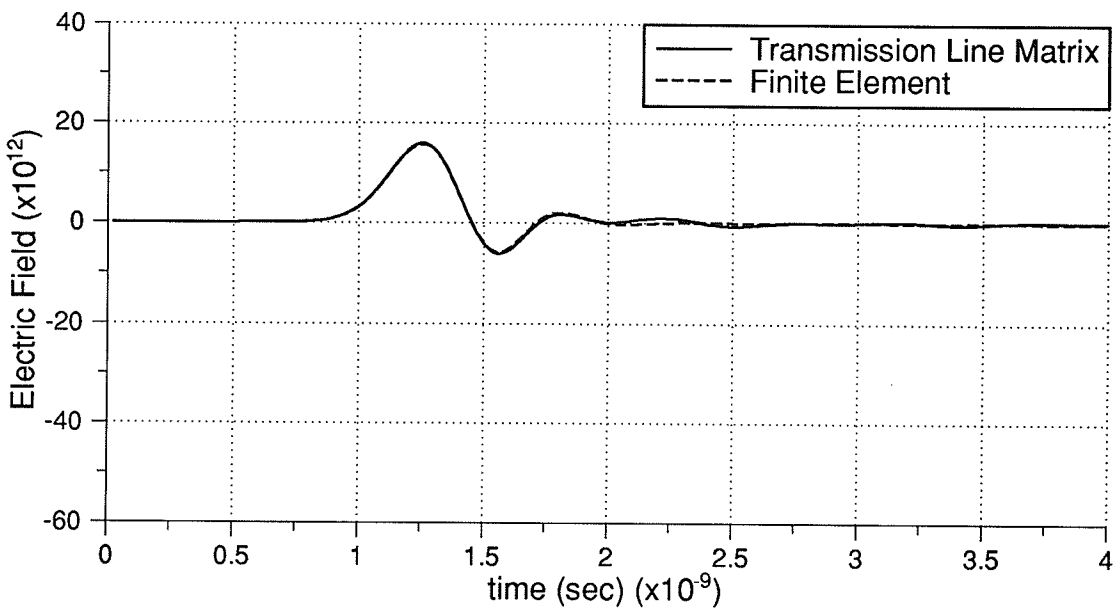
Figure 6.5(d): Transient response of the conducting plate at an observation point offset from the centre of the the plate (y-component of the electric field).
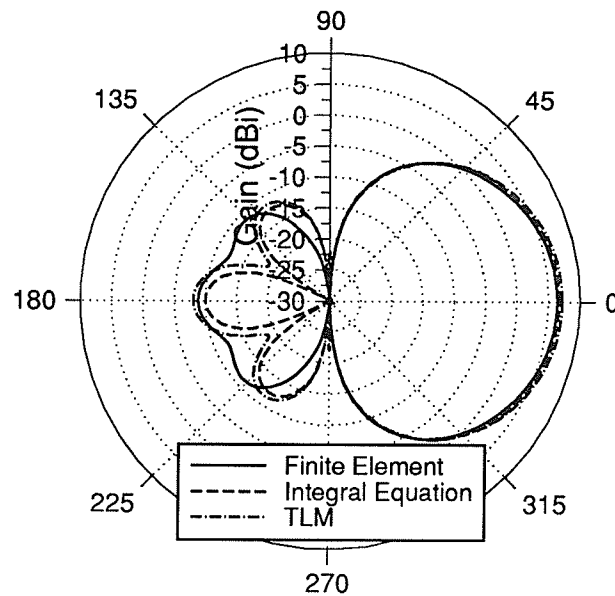
Figure 6.5(e): Radiation pattern of the current element and plate configuration of Figure 6.5(a).

The second problem considered involves the validation of the modelling of material regions within the finite-element simulation program. Consider the problem illustrated in Figure 6.6(a), in which a plane wave (polarized in the -x direction) is incident upon a dielectric block. The finite-element mesh used for the analysis of this problem is of size $N_x=30$, $N_y=30$, and $N_z=45$ with $\Delta l=0.01m$. The dielectric block is of size $L_x=0.20$, $L_y=0.20$, $L_z=0.05m$ and is centred within the mesh. Three observation locations are shown in Figure 6.6(a), observation locations 1 and 3 are located a distance of 0.025m above and below the slab, and observation location 2 is centred within the slab. The time variation of the incident plane wave has the form of a Gaussian pulse (pulse width w=0.25nsec). The maximum permissible time step is applied (*i.e.*, $\Delta t=\Delta l/\sqrt{3}$). In Figure 6.6(b), (c), and (d), results obtained from the finite-element simulation program are compared to results obtained from an equivalent TLM simulation for material blocks with $\varepsilon_r=4.0$, $\mu_r=1.0$, and $\sigma=0$, 0.1, and 0.5S/m, respectively. The results of Figure 6.6 indicate a reasonable agreement. Since both sets of results were obtained from numerical methods, it is difficult to discuss quantitative differences. However, the results do illustrate a difference in the scattered field and total field formulations. Note that the transient response at output locations 2 and 3 determined by

the finite-element method is non-zero before the plane wave physically reaches these output locations (at times between 0.75 and 1.0nsec). The small non-zero fields are due to numerical dispersion within the finite-element mesh. A portion of the scattered field distribution (the distribution modelled within the finite-element mesh) propagates at a speed $c_0=1/\sqrt{(\epsilon_0\mu_0)}$, regardless of the material properties of the physical medium. This portion of the scattered field distribution cancels the incident field distribution (which also propagates at $c_0=1/\sqrt{(\epsilon_0\mu_0)}$), before the total field arrives. The numerical dispersion of the finite-element mesh causes slight distortion in the scattered field distribution and therefore, exact cancellation of the scattered and incident field distributions does not occur.
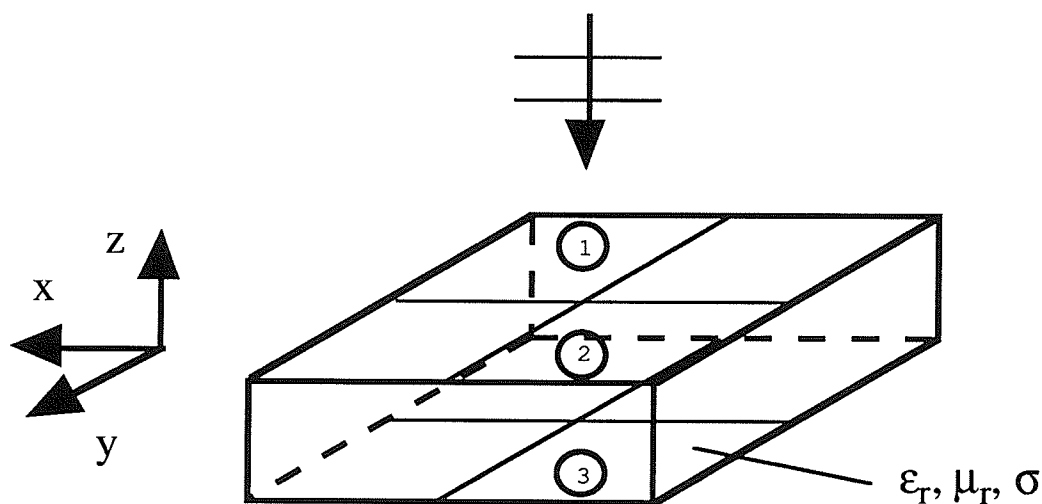
Figure 6.6(a): Problem geometry describing a plane wave incident upon a material slab.
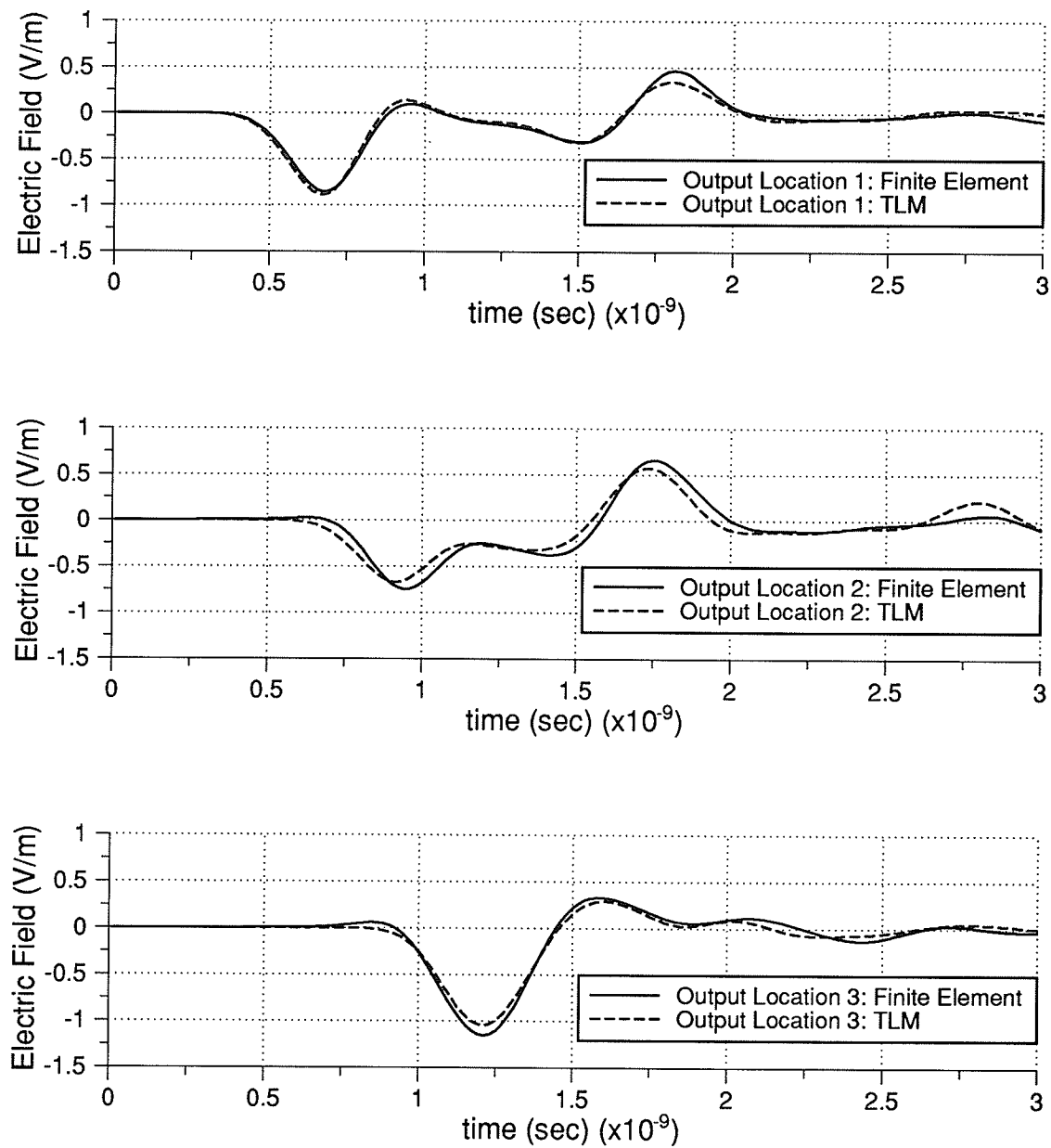
Figure 6.6(b): Transient response of a material block (ε_r=4.0, μ_r=1.0, σ=0). Comparison of time-domain finite-element and TLM results at three observation locations.
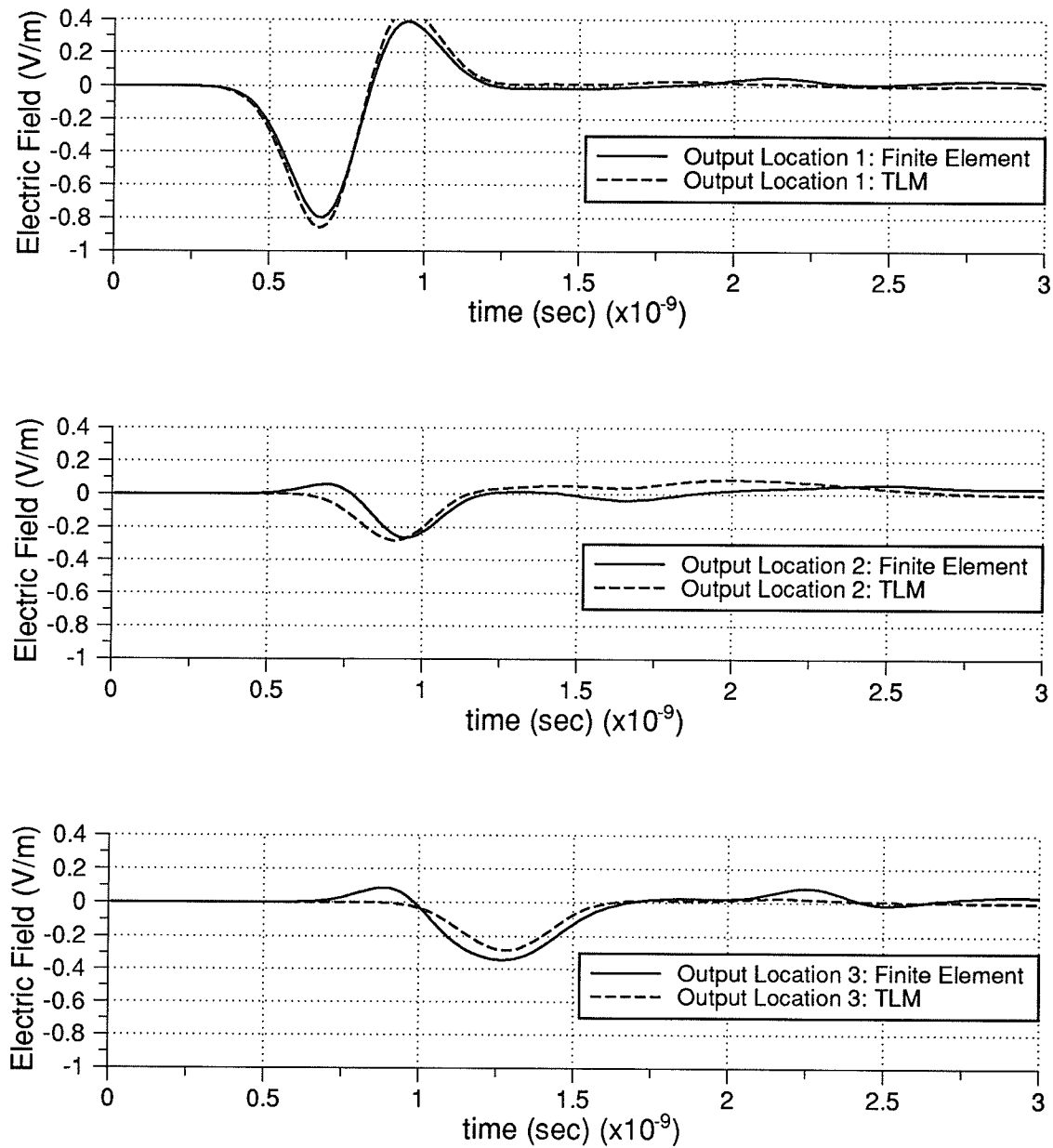
Figure 6.6(c): Transient response of a material block (ε_r=4.0, μ_r=1.0, σ=0.1S/m). Comparison of time-domain finite-element and TLM results at three observation locations.
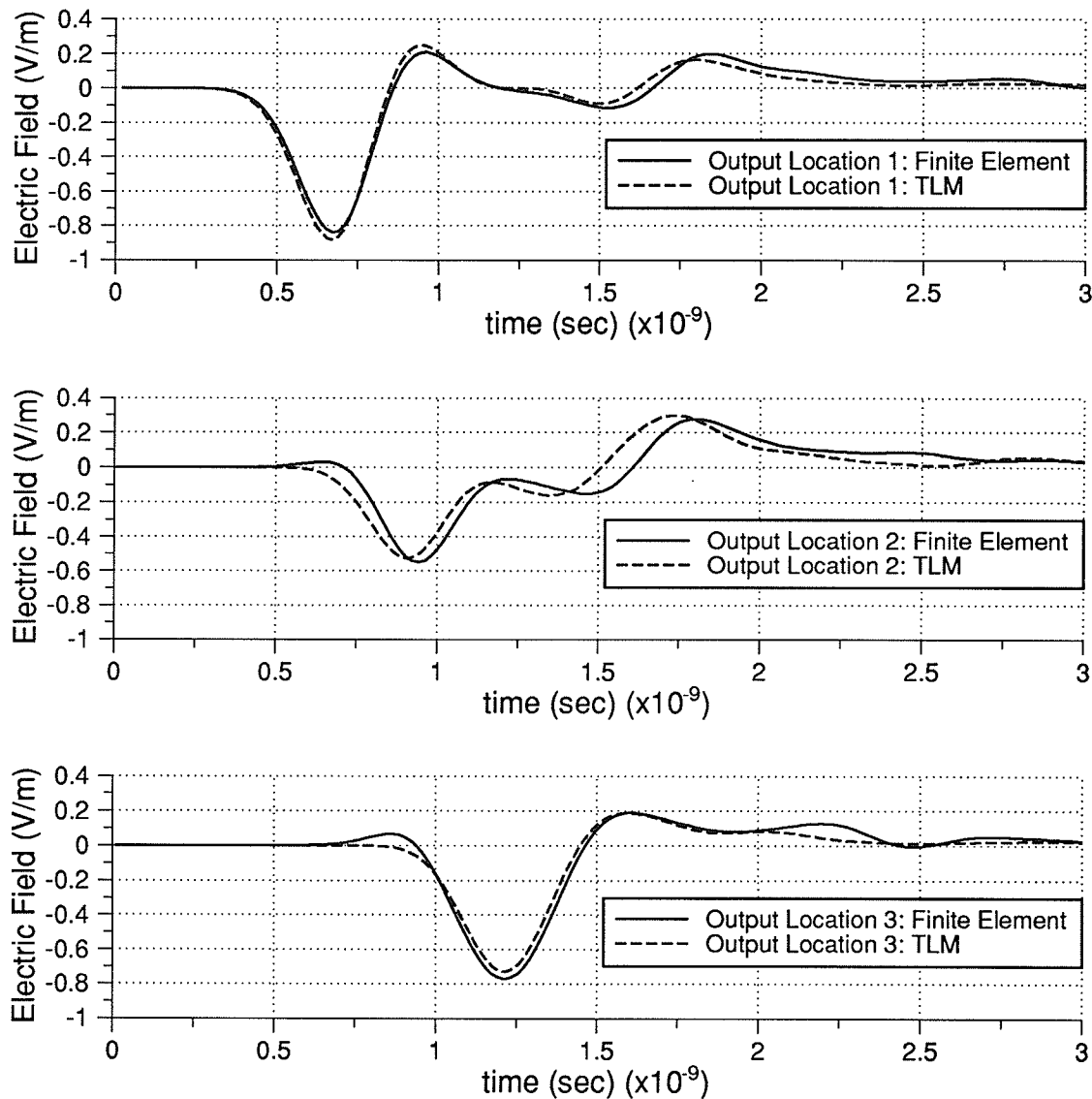
Figure 6.6(d): Transient response of a material block (ε_r=4.0, μ_r=1.0, σ=0.5S/m). Comparison of time-domain finite-element and TLM results at three observation locations.

Another example investigated to validate the modelling of dielectric media is the calculation of the radar-cross-section of a dielectric cube. The finite-element mesh applied to this problem is of size N_x=30, N_y=30, and N_z=30 with Δl=0.01m. The dielectric cube is centred within the mesh and is of size 0.10m. In Figure 6.6(e), a comparison of bistatic scattering patterns at a frequency of 0.6 GHz is provided. A

reasonable agreement between the results obtained from the finite-element, TLM, and integral-equation methods is obtained.
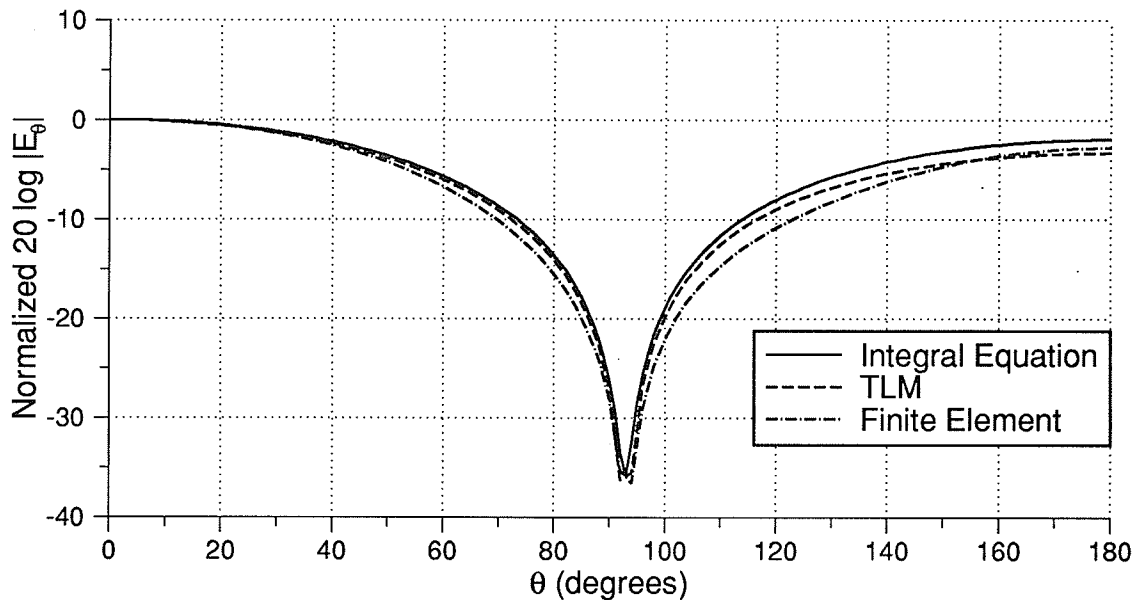
Figure 6.6(e): Bistatic radar cross section of a 0.10m dielectric cube (ε_r=4.0) at 0.6 GHz. Comparion of time-domain finite-element results with integral-equation results from [Mohe91] and TLM results obtained using the simulation program described in Chapter 5.

6.1.9: Total/Scattered Field Formulation

In addition to the algorithm described above, based on the scattered field formulation of the modified vector wave equation, a total/scattered field formulation has also been investigated. The implementation of a total/scattered field formulation in conjunction with a frequency-domain finite-element algorithm has been previously described [Maye91]. Separation of the finite-element mesh into a total field region (the volume V_t) and a scattered field region (the volume V_s) is shown in Figure 6.7(a). A few elements along the contour separating the total and scattered field regions is provided in Figure 6.7(b). In the separation of the simulation space provided in Figure 6.7(a), it is assumed that the source exists external to the mesh. Other organizations of the simulation space are possible, such as that applied in section 5.1. The boundary conditions applied to model the object are implemented as described in [Lync90] for the

total fields. This formulation has been tested with respect to the application of plane wave and electrically short dipole sources.

(a)
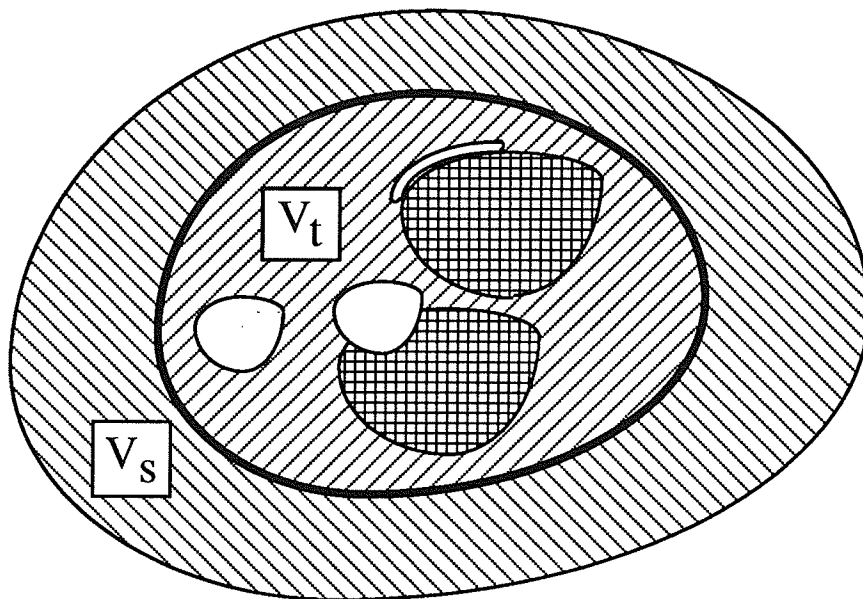
(b)
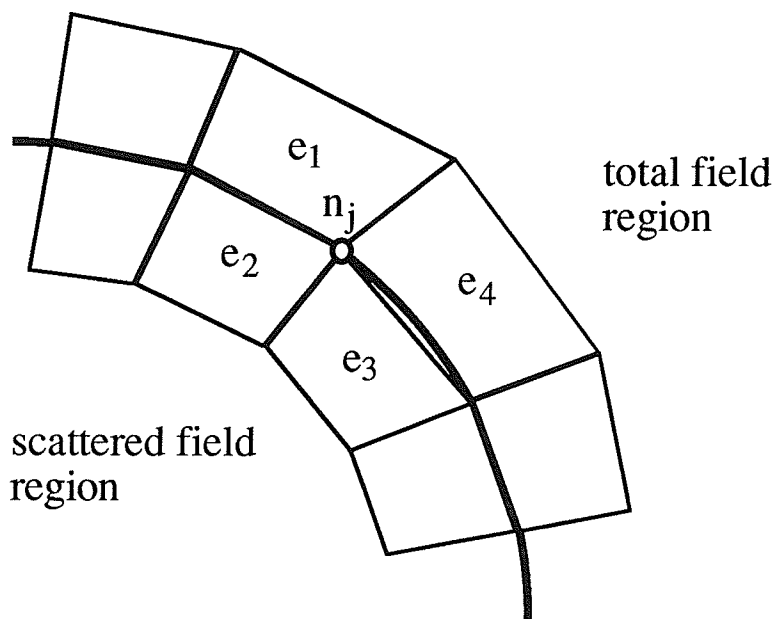
Figure 6.7: Total/scattered field formulation for the time-domain finite-element algorithm: (a) mesh configuration, and (b) a two-dimensional cross-section displaying the elements along the contour separating the total and scattered field regions.

6.2: Relationship of Finite-Element and Finite-Difference Methods

In this section, it is demonstrated that on a regular computational grid, the time-domain finite-element algorithm described in the previous section reduces to a second-order central-difference algorithm, and the accuracy of the general three-dimensional algorithm (in terms of dispersive errors) is identical to that of the Yee finite-difference time-domain algorithm [Yee66], [Tafl89].

Gray and Pinder have investigated the relationship of finite-element and finite-difference approximations of the convective-diffusion equation [Gray76]. The general conclusion of their work is that the system produced by Galerkin finite-element discretization (with exact integration) resembles a spatially averaged finite-difference approximation. The same conclusion is found in the present investigation. The effect of the element integration scheme (exact versus nodal quadrature) is investigated.

6.2.1: One-Dimensional Finite-Element Algorithm

In the previous section, the general form of the three-dimensional time-domain finite-element algorithm was presented. For the purpose of this investigation, the algorithm is considered with respect to a simplified one-dimensional system. The notation of Lynch and Paulsen is followed [Lync90]. For elements not connected to boundaries, the general algorithm (6.10) reduces to,

$$\sum_{j=1}^{N} S_{ij}\Delta E_j = \sum_{j=1}^{N} P_{ij}\left(E_j^t - E_j^{t-1}\right) + \Delta t^2 \sum_{j=1}^{N} Q_{ij}E_j^t \qquad (6.31)$$

where,

$$S_{ij} = \int_V \left(\varepsilon + \frac{\sigma\Delta t}{2}\right)\phi_i\phi_j dV \qquad (6.32a)$$

$$P_{ij} = \int_V 2\varepsilon\phi_i\phi_j dV \tag{6.32b}$$

$$Q_{ij} = -\int_V \frac{1}{\mu}\frac{\partial\phi_i}{\partial x}\frac{\partial\phi_j}{\partial x} dV \tag{6.32c}$$

and,

$$\Delta E_j = E_j^{t+1} - E_j^{t-1} \tag{6.32d}$$

The expansion functions for a one-dimensional linear element are provided below.
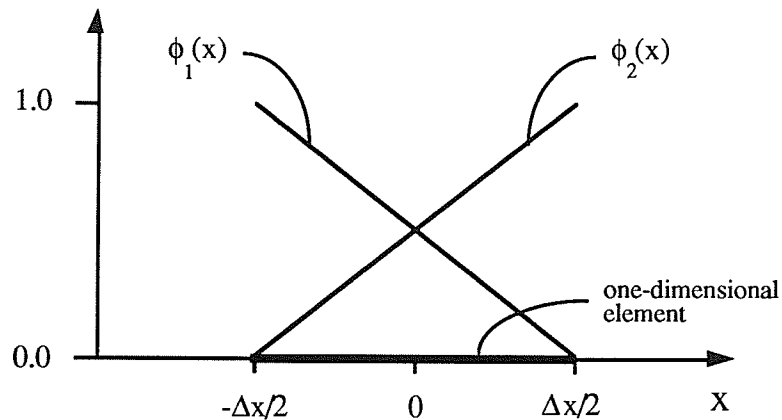
$$\phi_1 = \frac{1}{\Delta x}\left(\frac{\Delta x}{2} - x\right) \qquad \frac{\partial\phi_1}{\partial x} = -\frac{1}{\Delta x}$$

$$\phi_2 = \frac{1}{\Delta x}\left(\frac{\Delta x}{2} + x\right) \qquad \frac{\partial\phi_2}{\partial x} = \frac{1}{\Delta x}$$

Consider the application of the above finite-element algorithm to a uniform one-dimensional computational grid (see Figure 6.8). The remaining portion of the algorithm that requires specification is the method for evaluating the element integrals (6.32a-c). In the following sections, two methods are applied to evaluate (6.32a-c) and a comparison of the resulting algorithms is provided.
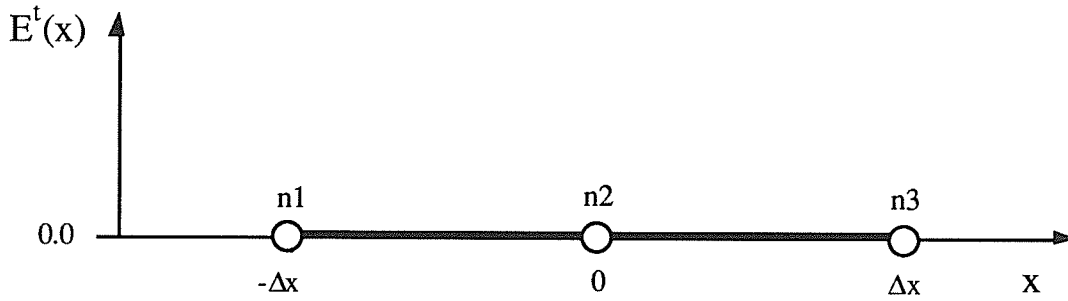
Figure 6.8: Uniform one-dimensional computation grid.

6.2.1.1: Evaluation of Element Integrals Using Exact Integration

Evaluating the integrals in (6.32) exactly yields the following algorithm,

$$\left\{ \frac{E_{n_1}^{t+1}}{6} + \frac{2E_{n_2}^{t+1}}{3} + \frac{E_{n_3}^{t+1}}{6} \right\}$$

$$= \left\{ \left(\frac{1}{3} + k^2 \right) E_{n_1}^{t} + \left(\frac{4}{3} - 2k^2 \right) E_{n_2}^{t} + \left(\frac{1}{3} + k^2 \right) E_{n_3}^{t} \right\}$$

$$- \left\{ \frac{E_{n_1}^{t-1}}{6} + \frac{2E_{n_2}^{t-1}}{3} + \frac{E_{n_3}^{t-1}}{6} \right\} \qquad (6.33)$$

where, $k=c\Delta t/\Delta x$. Equation (6.33) represents an implicitly time stepped algorithm. The future values of a particular field value $E_{n_2}^{t+1}$ are dependent on future values of other field values in the vicinity of node n_2, (i.e. , $E_{n_1}^{t+1}$ and $E_{n_3}^{t+1}$). Applying the Von Neumann method of stability analysis [O'Bri50], the stability criterion of (6.33) is,

$$\Delta t \le \frac{1}{\sqrt{2}} \frac{\Delta x}{c} \qquad (6.34)$$

A dispersion analysis of (6.33) has also been performed (the mathematical details are not included here). From this analysis, the algorithm has been determined to be non-dissipative. The dispersion relation is given by,

$$\cos\left(2\pi\frac{\Delta x}{\lambda}\right) = \frac{2 - 3k^2 + (1 + 3k^2)\cos\left(2\pi\frac{\Delta x}{\lambda*}\right)}{2 + \cos\left(2\pi\frac{\Delta x}{\lambda*}\right)} \tag{6.35}$$

where, λ and $\lambda*$ denote the exact and numerical wavelengths, respectively.

6.2.1.2: Evaluation of Element Integrals Using Nodal-Quadrature

In the practical implementation of a finite-element algorithm, the element integrals are not evaluated exactly. Usually a numerical integration scheme is used. The benefit of a numerical integration scheme is realized for isoparametric implementations in higher dimensions (i.e., two and three dimensional implementations for curved and arbitrary shaped geometries). Applying a first-order-accurate nodal-quadrature formula [Care84] to (6.32), yields the following algorithm.

$$E_{n_2}^{t+1} = \left\{ k^2 E_{n_1}^t + (2 - 2k^2) E_{n_2}^t + k^2 E_{n_3}^t \right\} - E_{n_2}^{t-1} \tag{6.36}$$

Due to nature of the shape functions, nodal-quadrature eliminates non-diagonal terms of S_{ij} and P_{ij}.

Applying the Von Neumann method of stability analysis [O'Bri50], the stability criterion of the nodal-quadrature based algorithm is,

$$\Delta t \leq \frac{\Delta x}{c} \tag{6.37}$$

A dispersion analysis of (6.36) has also been performed (the mathematical details are not included here). The nodal-quadrature algorithm is also non-dissipative. The dispersion relation is given by,

$$\sin\left(\pi\frac{\Delta x}{\lambda}\right) = k \sin\left(\pi\frac{\Delta x}{\lambda*}\right) \tag{6.38}$$

6.2.1.3: Comparison of Integration Schemes

Three advantages of using a nodal quadrature formula arise from the analysis contained in the previous two sections. First, the stability range of the nodal-quadrature algorithm (6.37) is greater than that of the exactly integrated algorithm (6.34). This permits the use of a larger time step and therefore less cpu time for a given problem. Second, the nodal-quadrature algorithm is explicit, while the exactly integrated algorithm is implicit. An implicit algorithm requires inversion of a system matrix (an added computational expense), while the explicit algorithm does not. Third, the dispersive errors associated with the nodal-quadrature algorithm are less than those of the exactly integrated algorithm. Intuitively, one would expect optimal accuracy with the use of exact integration and degradation in accuracy with the use of an approximate quadrature formula. However, the opposite is true. Close examination of Figures 6.9 and 6.10 indicate the dispersive errors of the nodal-quadrature algorithm are less than those of the exactly integrated algorithm. The surprising result of increased accuracy through the use of approximate integration schemes is supported by Strang and Fix [Stra73], ``... *We regret to inform that these inexact numerical integrations have even been shown in some cases to improve the quality of the solution. This is one instance in which computational experiments yield results which are frustrating to the mathematical analyst but nevertheless numerically valid and important ...*''.

An additional difference in the character of the dispersion relations exists (see Figures 6.9 and 6.10). For the exactly integrated algorithm the ratio c^*/c is always greater than 1. The exact integrated algorithm models a medium with a phase velocity greater than that of free space velocity. The ratio c^*/c is always less than 1 for the nodal-quadrature algorithm. Thus, the nodal-quadrature algorithm models a medium with a phase velocity less that that of free space.
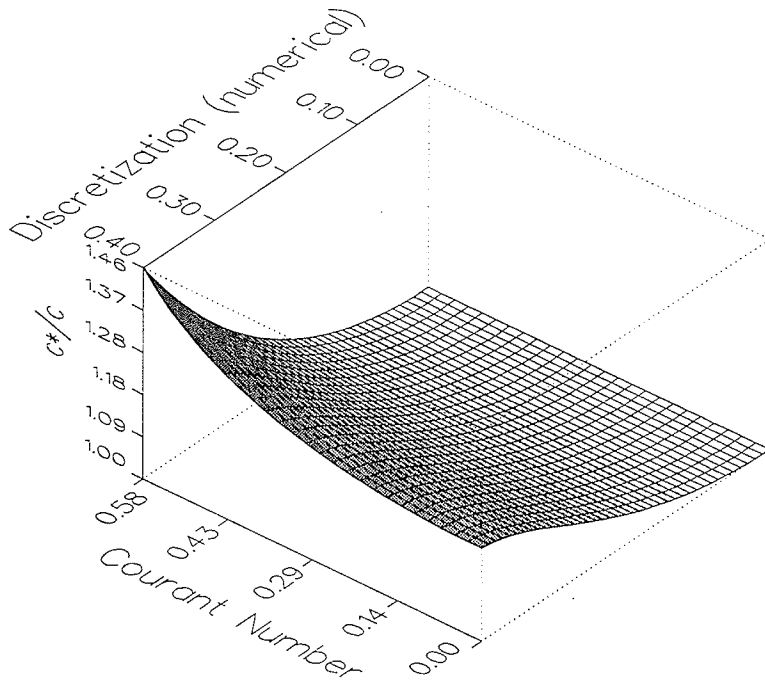
Figure 6.9: c*/c as a function of the Courant number k and the numerical discretization ratio Δl/λ* (Exact Integration Algorithm).
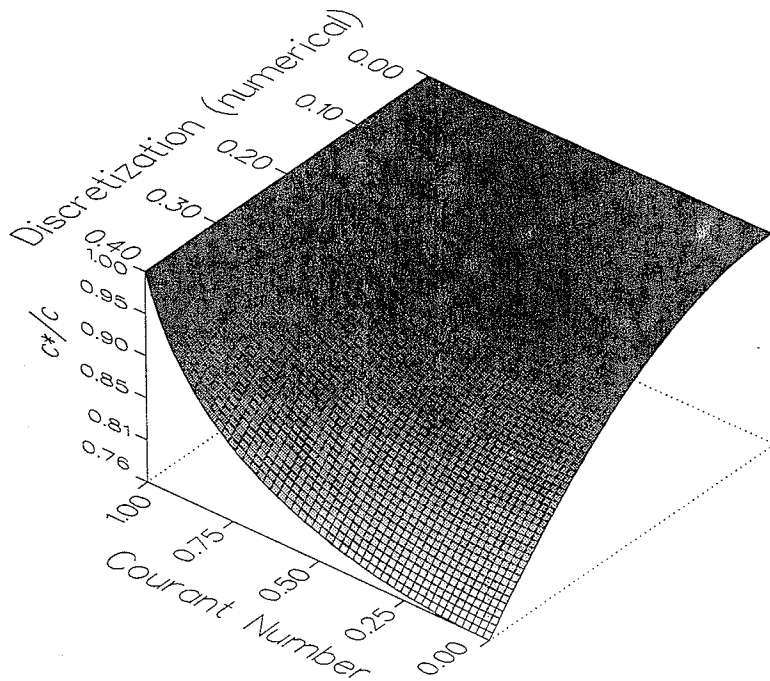
Figure 6.10: c*/c as a function of the Courant number, k and the numerical discretization ratio Δl/λ* (Nodal-Quadrature Algorithm).

6.2.2: Finite-Difference Discretization

Starting from the three-dimensional expanded form of the vector wave equation, it can be demonstrated that its analytic form reduces to three uncoupled scalar wave equations in E_x, E_y, and E_z. Considering a one dimensional system (no variation in y or z coordinates) yields,

$$\frac{\partial^2 E_u}{\partial x^2} = \varepsilon\mu\frac{\partial^2 E_u}{\partial t^2} + \sigma\mu\frac{\partial E_u}{\partial t} \ , \ u=x,y \text{ or } z \tag{6.39}$$

Consider the discretization of (6.39) on a uniform grid of spacing Δx (see Figure 6.11). Applying second-order-accurate central-differencing to both the spatial and temporal derivatives in (6.39) yields,

$$E_{n_2}^{t+1} = \left\{ k^2 E_{n_1}^t + \left(2 - 2k^2\right)E_{n_2}^t + k^2 E_{n_3}^t \right\} - E_{n_2}^{t-1} \tag{6.40}$$

The above expression is identical to the nodal-quadrature finite element algorithm (6.36), and therefore, the same stability criterion and dispersion relation apply.
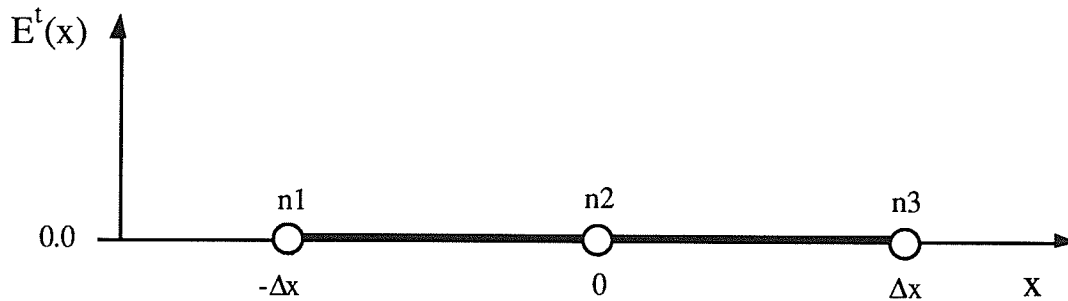
Figure 6.11: Uniform one-dimensional computation grid.

6.2.3: Extension to Three Dimensions

The equivalence of the finite-difference and finite-element discretizations of the one-dimensional wave equation described above has also been investigated for the discretization of the three-dimensional modified vector wave equation. The algorithm

which results from the application of the integral-lumped procedure described in section 6.1 over a mesh of regular cubic elements (with mesh spacings Δx, Δy, and Δz) is,

$$\frac{E^t(x+\Delta x,y,z) - 2E^t(x,y,z) + E^t(x-\Delta x,y,z)}{\Delta x^2} + \frac{E^t(x,y+\Delta y,z) - 2E^t(x,y,z) + E^t(x,y-\Delta y,z)}{\Delta y^2}$$

$$+ \frac{E^t(x,y,z+\Delta z) - 2E^t(x,y,z) + E^t(x,y,z-\Delta z)}{\Delta z^2} = \frac{1}{c^2} \frac{E^{t+\Delta t}(x,y,z) - 2E^t(x,y,z) + E^{t-\Delta t}(x,y,z)}{\Delta t^2}$$

This algorithm is identical to that obtained from the second-order central-difference approximation of the modified vector wave equation.

6.2.4: Equivalence of Finite-Difference and Finite-Element Algorithms

In the previous section it has been demonstrated that two unique numerical discretization techniques (finite-element using the weighted residual approach on linear elements with a nodal quadrature formula, and a second-order central-difference approximation) yield identical algorithms. Therefore, the nodal-quadrature finite-element algorithm and the finite-difference algorithm provide exactly the same accuracy. The claims made in [Mads88] regarding the poor behavior of time-domain finite-element algorithms are not applicable to all formulations. In [Mads88], a non-rigorous lumping procedure was used to obtain an explicitly time-stepped algorithm. This procedure caused the excessive dispersive errors and thus the inferiority of their finite-element algorithm when compared to results obtained from a finite-difference algorithm.

6.3: Summary

In this chapter a time-domain finite-element algorithm is presented which is based on a formulation originally introduced by Lynch and Paulsen [Lync90]. In the first part of this chapter, the time-domain finite-element algorithm is introduced with emphasis placed on aspects of the algorithm which differ from that presented in [Lync90], including the application of a scattered field formulation and local absorbing boundary conditions Numerical examples are provided to validate the program. In the second part of this chapter, the equivalence of the finite-element formulation (if applied on a regular mesh) and a finite-difference formulation is discussed. A dispersion analysis of the integral lumped and exactly integrated finite-element algorithms was presented to illustrate the differences in the two approaches. The results of this analysis indicate the possibility of using different numerical integration schemes to obtain optimal dispersive behavior.

Chapter 7: Application of Cellular Automata to Computational Electromagnetics

7.1: Introduction

Physical phenomena are typically described by partial differential equations which are continuous in space, time, and the variables used to describe the system. In Chapter 2, the overview of differential equation based numerical techniques provided a unified view of the various finite-difference, finite-element and transmission line matrix methods that have appeared in the literature. Although many differences in the final algorithms appear, the starting point for all of them (and all of the traditional computational approaches applied to model electromagnetic phenomena [Mill88]) is Maxwell's equations, a set of partial differential equations. Jackson has similarly summarized the basic approach to all of computational physics as [Jack90]:

Observation of Physical Phenomena

        Stylization into Differential Equations

            Discretization of Differential Equations
               (using finite-differences, method of weighted residuals, etc ...)

                    Computation (usually by implementation on a digital computer)

In the majority of cases the last step, computation, is not directly considered in the development of the numerical model. The assumption is made that the implementation (programming and hardware) will be performed on a general-purpose computer. This is due, in part, to the availability, flexibility, and low-cost of general purpose computers. In situations that require excessive computational resources, rather than wait for faster and larger general purpose computers to be built, it is worth-while to question the original approach given above, to computational physics. Recently, the application and development of parallel architectures and algorithms to computational electromagnetics has been investigated. These approaches can provide computationally efficient solutions to complex problems, however, the cost of high-performance parallel architectures is prohibitive. As well, the starting point for these approaches is the same, the description of physical phenomena by differential equations. A differential-equation assumes infinite information within a finite region of space. A digital computer is a discrete machine capable of manipulating a finite amount of information. This discrepancy between the original model used to describe the physical phenomena and the machine which performs the computation has been noted by several authors. The following quotations are representative:

> P. B. Johns: " ... *for problems that will ultimately need the use of a computer, formulation of calculus equations may be an unnecessary and even undesirable step. The time has come when we must open our minds to the fact that continuous mathematics is only one modelling technique ... "* (from [John79])

> T. Toffoli: " ... *The moment one gives up symbolic manipulation as a major motive for using differential equations, one starts wondering whether one should still keep them as the starting point for numerical modelling. In fact, they lead to concrete numerical computation (e.g., as run on a general purpose computer) that is at least three levels removed from the physical world that they try to represent. That is, first (a) we stylize physics into differential equations, then (b) we force these equations into the mold of discrete space and time and truncate the resulting power series, so as to arrive at finite-difference equations, and finally, in order to commit the latter to algorithms, (c) we project real-valued variables onto finite computer words ("round-off"). At the end of the chain we find the computer - again a physical system; isn't there a less roundabout way to make nature model itself? ... "* (from [Toff84a])

In this chapter, the application of cellular automata to computational electromagnetics is considered. Cellular automata are realizable in the form of low-cost high-performance digital hardware which (given suitable cellular automata rules) can be exploited for the modelling of physical phenomena.

The invention of cellular automata is attributed to VonNeumann (with advice from S. Ulam) [Neum30]. Von Neumann was interested in investigating self-replicating systems, with the intention of discovering some of the basic properties of living organisms. Recently, the field of *artificial life* has continued these investigations with cellular automata playing a central role [Lang86]. The following characterization of cellular automata has been presented by Wolfram (see [Wolf84a] and the Outline at the beginning of [Wolf86a]):

1) they consist of a discrete lattice of cells (which are arranged in a regular array),

2) they evolve in discrete time steps,

3) each cell takes on a finite set of possible values (usually only two possible values are used and the system is therefore described by binary variables),

4) each cell evolves according to the same deterministic rule, and

5) the rules are local in space and time.

Cellular automata are distinct from the traditional numerical techniques (finite-difference or finite-element methods), because in the latter values at each site are continuous real numbers, while in the former the values are members of a small set. In addition, the finite-difference and finite-element algorithms are derived from a partial-differential-equation as a discrete version of it. The cellular automata rules are usually idealized microscopic systems which upon coarse-graining yield the appropriate macroscopic dynamics.

Vichniac has described three approaches to the application of cellular automata to the simulation of physical phenomena [Vich84a]. The first approach (which is considered in this chapter) considers cellular automata as a computational tool. The essential concepts can be found in [Vich84a] and [Toff84a]. Toffoli questions the traditional partial differential equation description of physical phenomena (when computer simulation is ultimately required) and presents cellular automata as an alternative representation for modelling (see the above quotation). The lattice gas automata (to be introduced in the following section) have been considered as computational tools for the modelling of fluid dynamics [Dool90]. In the second approach to the simulation of physical phenomena, cellular automata are considered as discrete dynamical systems. In the early 1980's, through experimentation with various one-dimensional cellular automata, Wolfram demonstrated that these simple systems are capable of complex dynamical behavior [Wolf84b]. Cellular automata have been considered as a tool for understanding the origin of self-organization and complexity that

can appear in physical systems [Wolf83]. Wolfram was able to demonstrate that simple one-dimensional cellular automata are capable of producing behavior analogous to that found with non-linear dynamical systems. Analogues of limit points, limit cycles, and strange attractors can be found within the dynamics of one-dimensional cellular automata [Wolf84b]. The third approach to the application of cellular automata to the simulation of physical phenomena is as original models of physics. This approach can be considered as an attempt to validate the following statement made by Feynman:

> R. P. Feynman: " ... *It has always bothered me that, according to the laws as we understand them today, it takes a computing machine an infinite number of logical operations to figure out what goes on in no matter how tiny a region of space, and no matter how tiny a region of time. How can all that be going on in that tiny space ? Why should it take an infinite amount of logic to figure out what one tiny piece of space/time is going to do ? So I have often made the hypothesis that ultimately physics will not require a mathematical statement, that in the end the machinery will be revealed, and the laws will turn out to be simple, like the checker board with all its apparent complexities. ... "*   (from [Feyn65])

The above line of thought has been investigated by Fredkin, who proposes that there exists a single reversible universal cellular automata rule which is capable of modelling all of microscopic physics exactly [Fred90]. Research regarding the fundamental relationship between physics and computation has also made use of cellular automata [Marg84], [Toff91a], [Marg92].

The use of cellular automata for modelling electromagnetic phenomena has been previously considered. In [Born89], background information regarding cellular automata and strategies for the development of possible rules are presented. Optimal parallel architectures for the simulation of cellular systems (a generalization of cellular automata) are discussed in [Thie93]. However computational experiments or details regarding the application to modelling electromagnetic phenomena are not provided. In two dimensions, electromagnetic phenomena can be described by the linear scalar wave equation (vector wave equation in three-dimensions) with the application of appropriate boundary conditions and sources. The lattice gas automata yield linear wave behavior for small perturbations to an equilibrium distribution [Dool90]. This approach has also been considered by Toffoli and Margolus using their TM-GAS rule [Toff87]. Appropriate qualitative behavior for the reflection and refraction of plane waves has been obtained [Toff87]. Rothman has considered the application of the lattice gas automata to the modelling of Seismic P-waves [Roth87]. The approach used in this chapter is similar to that of Rothman and is discussed further in section 7.3.

7.2: Review of Lattice Gas Automata

The behavior of a fluid can be modelled by the Navier-Stokes equation, which in two dimensions is expressed as,

$$\frac{\partial}{\partial t} \rho\mathbf{u} + \rho(\mathbf{u}\cdot\nabla)\mathbf{u} = -\nabla p + \eta\nabla^2\mathbf{u} + (\zeta + \frac{\eta}{2})\nabla(\nabla\cdot\mathbf{u}) \tag{7.1}$$

and the continuity equation,

$$\frac{\partial\rho}{\partial t} + \nabla\cdot(\rho\mathbf{u}) = 0 \tag{7.2}$$

where ρ is the density, $\mathbf{u}$ is the flow velocity, p is the pressure, and η and ζ are the shear and bulk viscosity, respectively. For isothermal flow and small flow velocity $\mathbf{u}$, the pressure and density can be related by,

$$p = c_s^2\rho \tag{7.3}$$

where c_s is the propagation velocity for sound waves. For equilibrium distributions with $\mathbf{u}\to 0$ and small variations ρ_{small} in a uniform background density ρ_o (i.e., $\rho = \rho_o + \rho_{small}$), the non-linear and viscous terms in (7.1) can be neglected, and equations (7.1)-(7.3) yield the linear wave equation for ρ_{small},

$$\nabla^2\rho_{small} = \frac{1}{c_s^2}\frac{\partial^2\rho_{small}}{\partial t^2} \tag{7.4}$$

These small perturbations in an otherwise uniform distribution correspond physically to sound waves. The above wave equation can also be expressed in terms of a corresponding small perturbation in the pressure or the velocity. A system capable of modelling the behavior of a fluid is therefore also capable of modelling two-dimensional electromagnetic phenomena, since it encompasses linear wave behavior.

Cellular automata have been applied to model a wide variety of physical phenomena [Toff87]. Studies involving the application of the lattice gas automata to fluid dynamics have received the most attention in terms of producing quantitative

results. The HPP lattice gas automaton was introduced in 1976 as a conceptual model for the microscopic behavior of a fluid (the name HPP is derived from the initials of its inventors) [Hard76] and can be considered as an idealized representation of a true physical fluid. The HPP lattice gas automaton algorithm follows the interaction of particles on a lattice, as shown in Fig. 7.1. The lattice spacing is Δl in each direction. Each cell has four links, with each link representing a possible velocity state in which a particle can exist. Particles obey a Boolean exclusion principle - only one particle is allowed to reside in a particular velocity state within a particular cell. The lattice gas algorithm operates in two synchronized steps. In the first step the particles interact within cells following specific collision rules. In the subsequent step the resultant velocity states are transferred to adjacent cells. An example of the operation of the algorithm over a single time step Δt is illustrated in Fig. 7.1 where a single cell is outlined. The arrows indicate the velocity states in which the particles exist. Figs. 7.1(a) and (b) show the state of the particles before and after collision, respectively. In Fig. 7.1(c) the particles are transferred to adjacent cells. With the HPP model only two body collisions occur and only if the particles exist in opposing velocity states. This results in two particles existing in states at right angles to the initial pair. The outlined cell of Fig. 7.1 illustrates a two-body collision. For all other possible situations, including a single particle, two particles at right angles, three particles, or four particles, no transformation of velocity states takes place. With these rules, conservation of momentum and energy are satisfied. The transition from one state to the next is unique, and can be implemented with a look-up table. The lattice gas automata are exactly computable (not affected by finite-precision arithmetic) and reversible.
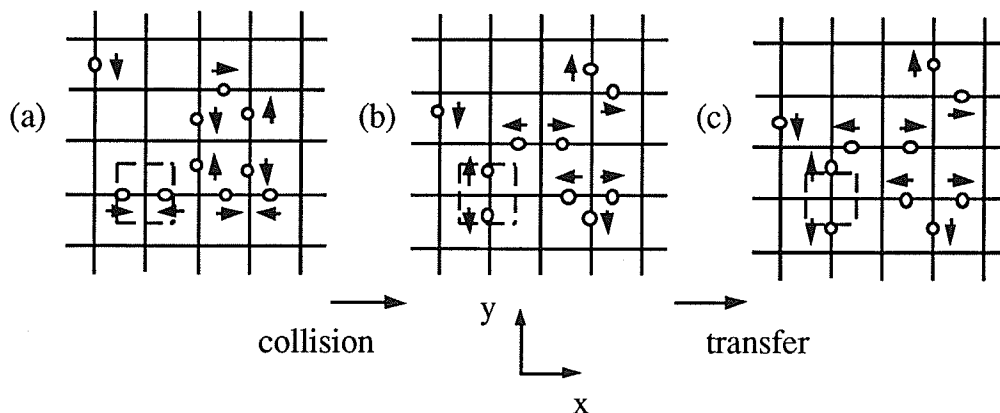
Figure 7.1: Operation of the HPP lattice gas automaton over a single time step Δt. In Figure 7.1(a), the particles are travelling toward the centre of the cells. Figure 7.1(b) shows the state of the lattice after the collisions have taken place, and in Figure 7.1(c), the particles have been transferred to adjacent cells.
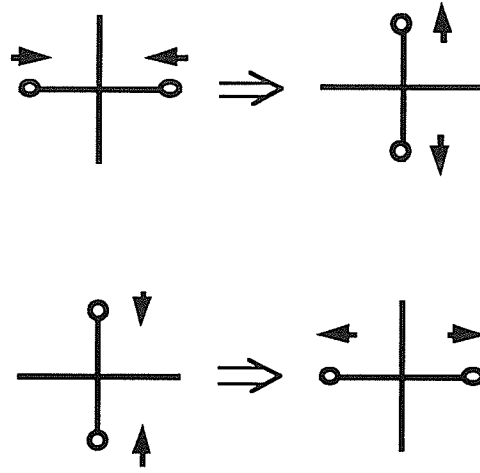
Figure 7.2: Two-particle collisions in the HPP lattice gas automaton.

For the HPP automaton, the state of each cell can be described by four Boolean variables, and the number of states for each cell is 2^4. The microscopic state of a particular cell located in space at (x,y) can be expressed in terms of a Boolean variable, $N_i(x,y)$, where i indexes the four possible velocity states (i.e., i=1 to 4). The value of $N_i(x,y)$ is 1 if a particle at the cell location (x,y) exists in velocity state i, and 0 otherwise. The velocity states c_i of a cell within the HPP model are defined as,

$$c_1 = +\hat{y} \qquad c_2 = +\hat{x} \qquad c_3 = -\hat{y} \qquad c_4 = -\hat{x} \qquad (7.5)$$

At a particular cell, the density ρ_{cell} and fluid velocity u_{cell} can be defined as,

$$\rho_{cell} = \sum_{i=1}^{4} N_i \qquad (7.6a)$$

$$u_{cell} = \sum_{i=1}^{4} N_i c_i \qquad (7.6b)$$

The macroscopic quantities of the fluid are defined by local averaging of the particle distribution. For example, the macroscopic density ρ at a location (x,y), is determined from,

$$\rho(x,y) = \sum_R \rho_{cell}(x_R, y_R) \tag{7.7}$$

where $\rho_{cell}(x_R, y_R)$ is determined from (7.6a), and R is a neighborhood surrounding (x,y). In Figure 7.3, the calculation of an arbitrary field variable F from the microscopic cell states f_{cell} in a circular neighborhood is illustrated. If a sufficiently large neighborhood is used, it is possible to obtain a *continuum* approximation ([Toff84a], [Toff91a-section 2]).
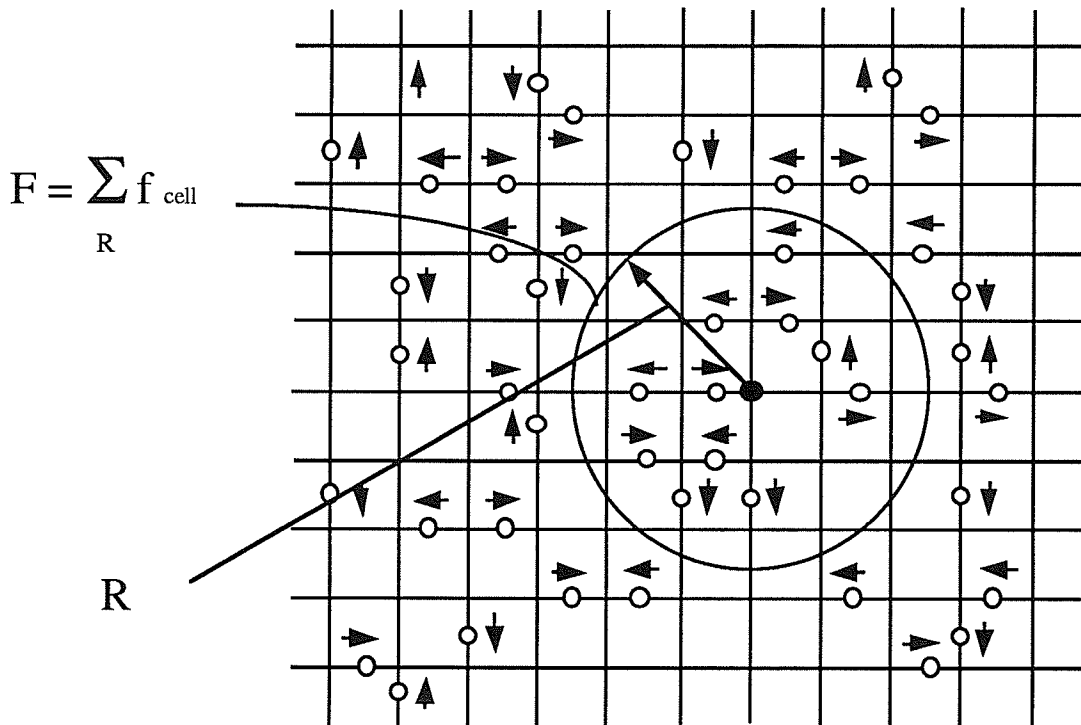
Figure 7.3: Calculation of an arbitrary field variable F from cell states over a circular neighborhood.

In [Hard76], the derivation of a simple model of fluid dynamics from the HPP model is presented. Differences between the behavior of the HPP model and the Navier-Stokes equation have been noted, and have led to the development of lattice gas models which are capable of more accurate modelling of fluid dynamics [Fris86]. For the purpose of the present investigation (obtaining linear wave behavior), the HPP model is adequate. The derivation of the Navier-Stokes equation from lattice gas models has been presented in [Fris86], [Wolf86b], [Fris87]. Detailed discussions of the deficiencies of the HPP lattice gas model with respect to modelling the Navier-Stokes equation are found in [Fris86], [Wolf86b], [Fris87].

From this brief introduction to the HPP lattice gas automaton, a reader familiar with the transmission line matrix method [John71], [Hoef89] will have noticed several similarities. The lattice gas automata follows the evolution of particles on a spatial lattice, while the transmission line matrix algorithm follows the evolution of voltage pulses on a transmission line grid. The operation of the lattice gas automata in terms of collision and transfer events is similar to the scattering and transfer events of a transmission line matrix algorithm. In subsequent sections, implementation of boundary conditions and association of fields with the elemental particles of the lattice gas automata will be presented which are similar to the techniques employed with the transmission line matrix method. Previous experience with the transmission line matrix method has been helpful in the development of the lattice gas automata simulation program. Despite the similarities, the fundamental formulation of the lattice gas automata and the transmission line matrix method are distinct. The voltage pulses of the transmission line matrix algorithm are real variables, and when cast on a digital computer take on a finite (but very large) set of values. The variables of the lattice gas automata represent the occupancy of the states of the lattice and are binary. Each variable denotes the presence or absence of a particle ("1" if a particle is present, "0" if it is not). Essentially, the difference noted above is defining characteristic 3) discussed in the introduction - cellular automata are fully discrete computational models [Toff84a], [Vich84a]. In addition, the traditional techniques (transmission line matrix, finite difference, etc. ...) only yield the behavior that is characteristic of the partial differential equations they are numerically approximating. The lattice gas approach has underlying simplistic rules which models the behavior of the same partial differential equations but also has the potential to produce much more complex and physically interesting behavior. The emergence of interesting behavior from systems of simple construction is a primary motivation for cellular automata research [Wolf86a], [Lang86], [Toff87].

7.3: Application to Two-Dimensional Electromagnetic Field Problems

In this section, modifications to the HPP lattice gas automaton are presented that allow application to two-dimensional electromagnetic field problems. In the previous section it was noted that the lattice gas automaton yields the linear wave equation for small perturbations within an equilibrium distribution. The basic approach applied is to equate the density distribution in the lattice gas with an electric field distribution. Unlike a fluid, a model of electromagnetic phenomena must incorporate polarization. In order to

accomplish this, and implement both Neumann and Dirichlet boundary conditions, the approach of Rothman [Roth87] is used where dual lattices are employed. One lattice carries *positive* particles, the other carries *negative* particles (see Figure 7.4). The particles on the positive and negative lattices do not interact (with the exception of along perfect electrical conducting boundaries), each set of particles follow the collision rules independently. Particles on the positive and negative lattices are referred to as e_+ and e_- particles, respectively. The particles represent the microscopic contribution to the electric and magnetic fields. The fields associated with e_+ and e_- particles are provided in Table 7.1. Using the definitions provided in Table 7.1, the collision and transfer events can be shown to satisfy continuity in the electromagnetic field quantities at the microscopic cell level.

Table 7.1: Fields Components Associated with Particles

particle	direction of propagation	electric field	magnetic field
e_+	$+x$	$+E_z$	$-H_y$
e_+	$-x$	$+E_z$	$+H_y$
e_+	$+y$	$+E_z$	$+H_x$
e_+	$-y$	$+E_z$	$-H_x$
e_-	$+x$	$-E_z$	$+H_y$
e_-	$-x$	$-E_z$	$-H_y$
e_-	$+y$	$-E_z$	$-H_x$
e_-	$-y$	$-E_z$	$+H_x$

The microscopic z directed electric field distribution E_z, at a cell located at (x,y) is obtained by subtracting the number of negative particles from the number of positive particles,

$$E_{z,cell}(x,y) = \sum_{i=1}^{4} \left(N_i^+(x,y) - N_i^-(x,y) \right) \qquad (7.8a)$$

The macroscopic z directed electric field distribution E_z, at a particular spatial location (x,y), is obtained by local averaging of the microscopic electric field distribution,

$$E_z(x,y) = \sum_R \sum_{i=1}^{4} \left(N_i^+(x_R, y_R) - N_i^-(x_R, y_R) \right) \qquad (7.8b)$$

where $N_i^+(x_R, y_R)$ and $N_i^-(x_R, y_R)$ are Boolean variables describing the state of a cell located at (x_R, y_R) within the positive and negative lattice, respectively. The x and y components of the magnetic field can be defined in a similar manner.

————————— lattice for e+ particles

— — — — — lattice for e- particles
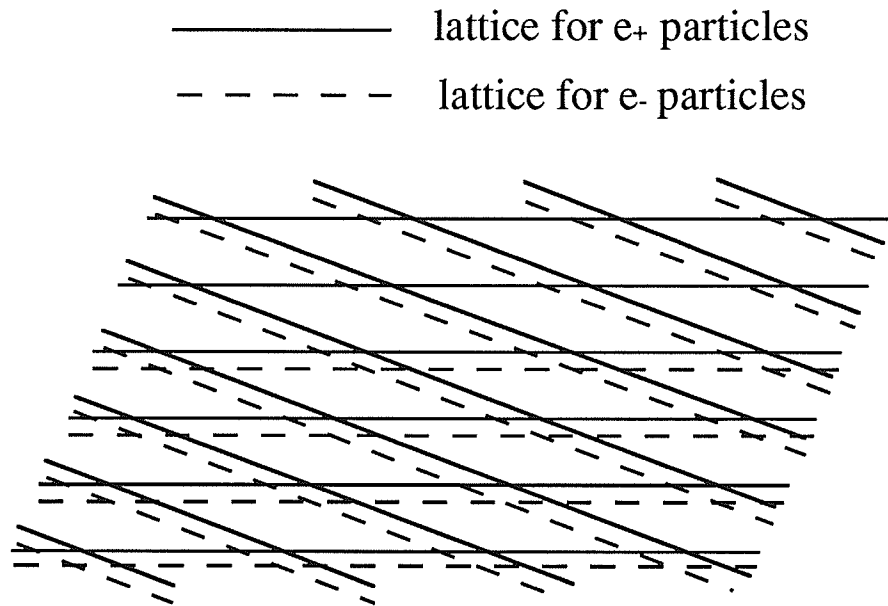
Figure 7.4: Dual lattice approach used for the analysis of two-dimensional electromagnetic field problems.

To obtain linear wave behavior, the lattice gas automata requires a uniform background density of particles. This is accomplished by randomly filling a specific fraction of states in the lattice with particles (the background distribution is the same for both the positive and negative lattices). A source is implemented by superimposing a distribution of particles on the background density.
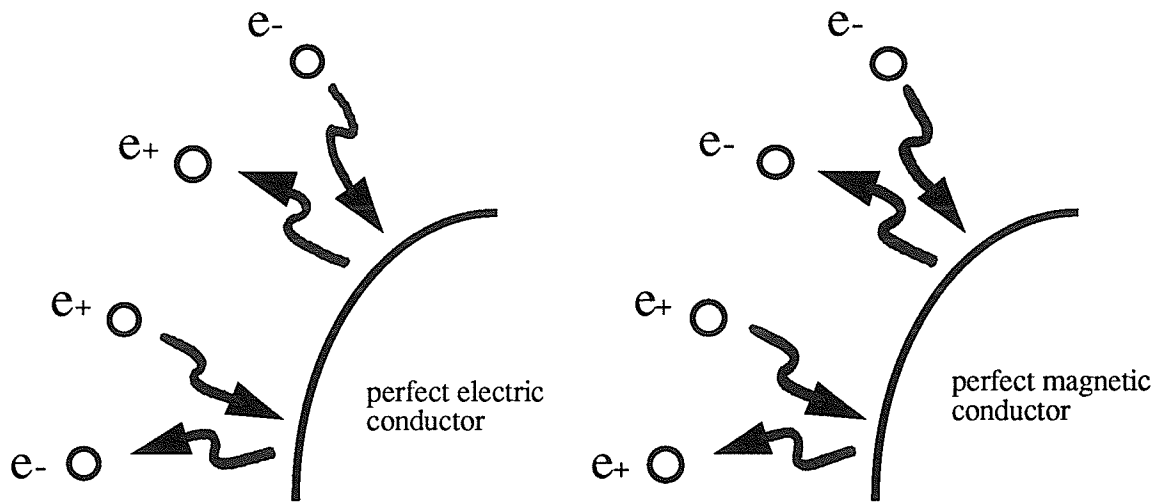
Figure 7.5: Implementation of perfect electrical conducting and perfect magnetic conducting boundary conditions.

Boundary conditions have been implemented in order to properly truncate the HPP lattice and implement scattering obstacles. These boundary conditions include perfect electric conducting boundaries, perfect magnetic conducting boundaries, and an initial attempt at an absorbing boundary condition. The implementation of the perfect electrical conducting and perfect magnetic conducting boundary conditions is illustrated in Figure 7.5. A perfect electric conducting boundary condition is modelled by forcing the tangential electric field along the boundary to be zero. If an e_+ particle is incident upon the boundary, an e_- particle is reflected back at the following time step. If an e_- particle is incident upon the boundary, an e_+ particle is reflected back at the following time step. A perfect magnetic conducting boundary condition is modelled by forcing the tangential magnetic field along the boundary to be zero. Particles incident on a perfect magnetic conductor are reflected back onto the same lattice (*i.e.,* an e_+ particle is reflected back onto the positive lattice and an e_- particle is reflected back onto the negative lattice). An absorbing boundary condition has also been implemented. The algorithm injects particles back into the lattice at an appropriate rate to maintain the initial background density. Although the accuracy of this absorbing boundary condition is quite poor, it demonstrates the applicability of the concept to the lattice gas automata.

7.4: Results From Numerical Experiments

In this section results obtained from lattice gas numerical experiments are provided for a few simple problems. The results validate: the basic ability of the lattice gas automata to model linear wave behavior, the dual lattice approach, and the implementation of boundary conditions.

7.4.1: Cylindrical Wave Propagation

The propagation of a cylindrical wave is first considered to qualitatively illustrate basic wave propagation characteristics of the cellular automata model. The simulation space is defined as $0<x<600\Delta l$ and $0<y<600\Delta l$, with a uniform background particle density of 0.5 (50% of all possible states are filled with particles, for both the positive and negative lattices). At the centre of the lattice, an additional uniform cylindrical distribution of particles is superimposed on the positive lattice, as an initial source condition. In Figure 7.6(a), (b), and (c) the electric field distribution within the lattice is provided at 60, 140, and $220\Delta t$, respectively. The field distribution at a particular spatial location $(m\Delta l, n\Delta l)$ is obtained by performing operation (7.8b) over a circular region with radius $30\Delta l$, centered at $(m\Delta l, n\Delta l)$. The results of Figure 7.6 indicate appropriate qualitative behavior with the initial disturbance propagating as a cylindrical wave. The wave front propagates isotropically at a velocity $c=\Delta l/(\sqrt{2}\Delta t)$ as predicted in [Hard76], [Wolf86b], [Fris87]. If no perturbations are present, the observed field quantity will be zero since the positive and negative background levels cancel.

7.4.2: Plane Wave Propagation

In the second example considered, a Gaussian-pulsed plane wave is propagated through the lattice. The simulation space is provided in Figure 7.7(a) and is defined as $0<x<600\Delta l$ and $0<y<2400\Delta l$. PMC boundary conditions are applied parallel to the y axis at the top and bottom of the lattice, and PEC boundary conditions are applied parallel to the x axis at the left and right lattice boundaries. Observation points are located along the centre of the lattice $(x=300\Delta l)$ at $y=1020$, 1420, and $1820\Delta l$. A uniform background density of 0.5 (50% of all possible states are randomly filled) is applied to both the

positive and negative lattices. The plane wave is excited by superimposing a Gaussian distribution (centered at y=620Δl) of particles on top of the existing background distribution, at t=0. The superimposed Gaussian source distribution is defined as,

$$Me^{-(y-y_0)^2/w^2} \tag{7.9}$$

where M is the magnitude, y_0 is the location of the excitation, and w is the pulse width. The source distribution with respect to the y axis is constant. For this example M=0.25 (indicating that a maximum of 25% of the unoccupied states above the background level in the positive lattice are filled on average at y_0=620Δl), and the pulse width, w is 120Δl. A circular window of radius 30Δl is used to determine the macroscopic field E_z. In the experiment, the PEC boundary conditions are located a sufficient distance from the source and observation locations such that the simulation effectively takes place in an infinite lattice. The simulation is evolved for 2000Δt. In Fig. 7.7(b), the transient response at each observation location is provided. An appropriate delay is observed between the response at each output location, indicating a propagation velocity of c=Δl/(√(2)Δt). The transient signals appear to be corrupted with a large high frequency noise. The noise is a result of the background random distribution and depends on the chosen sampling window. The noise does not significantly effect results after a discrete Fourier transform is applied.

Figure 7.7(c) also contains the frequency response from a TLM simulation of the same problem. The transmission line matrix results are scaled by the appropriate value such that the frequency values correspond with the lattice gas results. The results indicate reasonable agreement between the lattice gas automata and transmission line matrix results for the lower spectrum of frequencies. For higher frequencies, differences between the transmission-line matrix and lattice gas results exist. These results may indicate a problem with respect to the dynamic range of the lattice gas model.

7.4.3: Reflection From a Perfect Electrical Conducting Wall

The third numerical experiment tests the perfectly electric conducting boundary condition. Within a 400 by 1800Δl lattice, a Gaussian-pulsed plane wave source (M=0.2, and w=80Δl) is excited at y=632Δl. The x=1.5Δl and x=398.5Δl lattice boundaries parallel to the direction of propagation are terminated with perfect magnetic conducting boundaries conditions. The y=1.5Δl and y=1798.5Δl lattice boundaries are terminated

with perfect electric conducting boundary conditions. An observation point is located at x=200 and y=312Δl . The transient response of the problem is provided in Figure 7.8(b) and displays the expected polarity change in the electric field as the wave reflects off the PEC boundary. The discrete Fourier transform of the transient response is provided in Figure 7.8(c) along with corresponding transmission line matrix results. The results indicate the appropriate behavior of a standing wave pattern with decreasing amplitude due to the frequency spectrum of the Gaussian source. The locations and values of the maxima and nulls are within reasonable agreement with the TLM results.

In addition to the two examples considered above, the analysis of plane wave scattering from a perfectly conducting rectangular cylinder, and a numerical evaluation of the linearity of the HPP lattice gas automaton have been presented in [Simo94d].
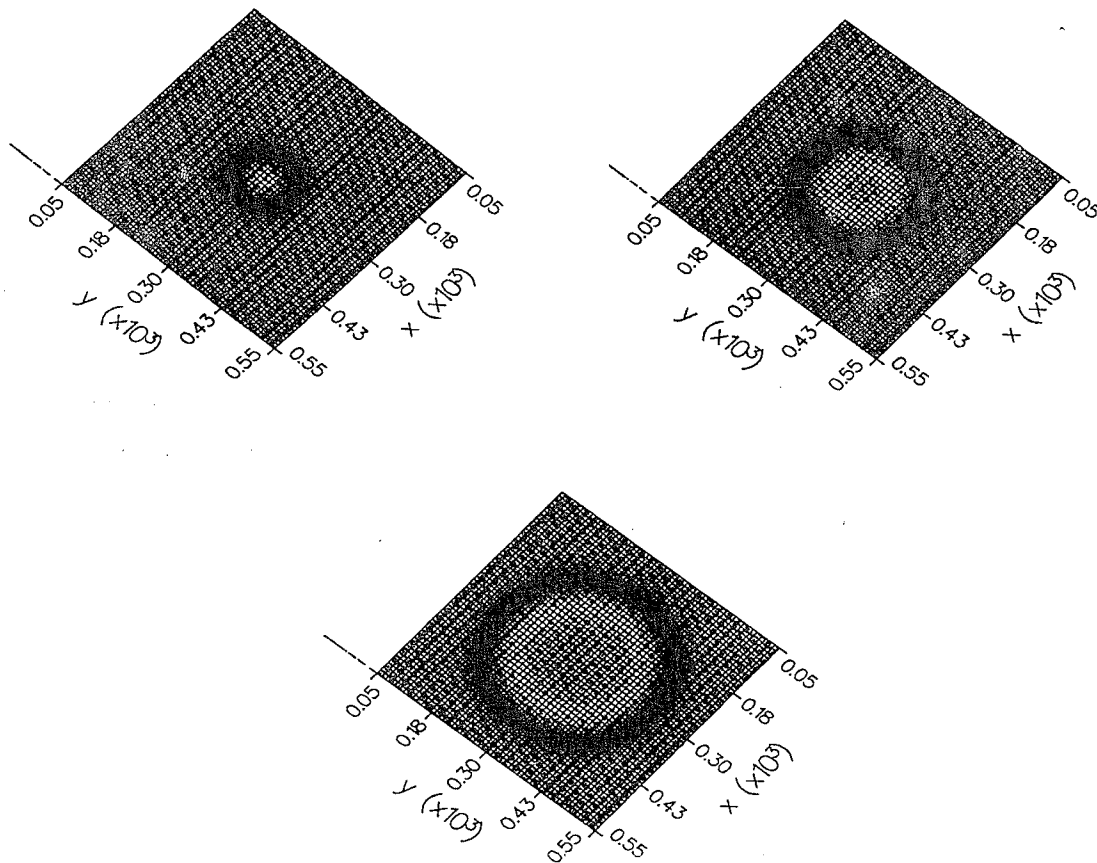
Figure 7.6: Propagation of a cylindrical wave within the two-dimensional lattice gas automaton at (a) 60Δt (b) 140Δt, and (c) 220Δt, within a 600 by 600Δl lattice.

(a)

(b)

(c)
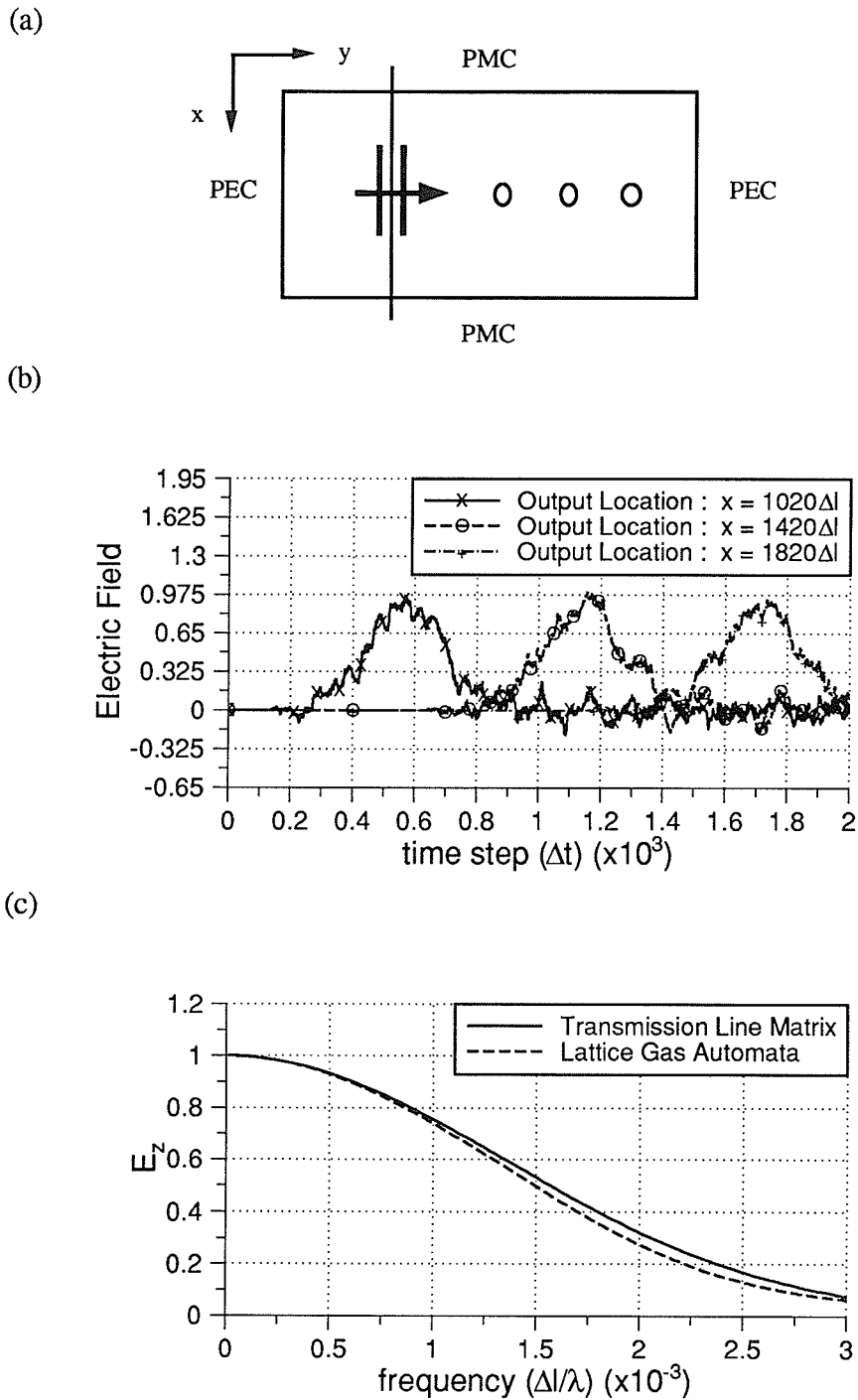
Figure 7.7: Gaussian pulsed plane wave propagation: (a) lattice diagram, (b) transient response at the three output locations, and (c) comparison of frequency domain results at the final observation location of the lattice gas automata simulation with results from an equivalent transmission line matrix simulation.

196

(a)

(b)

(c)
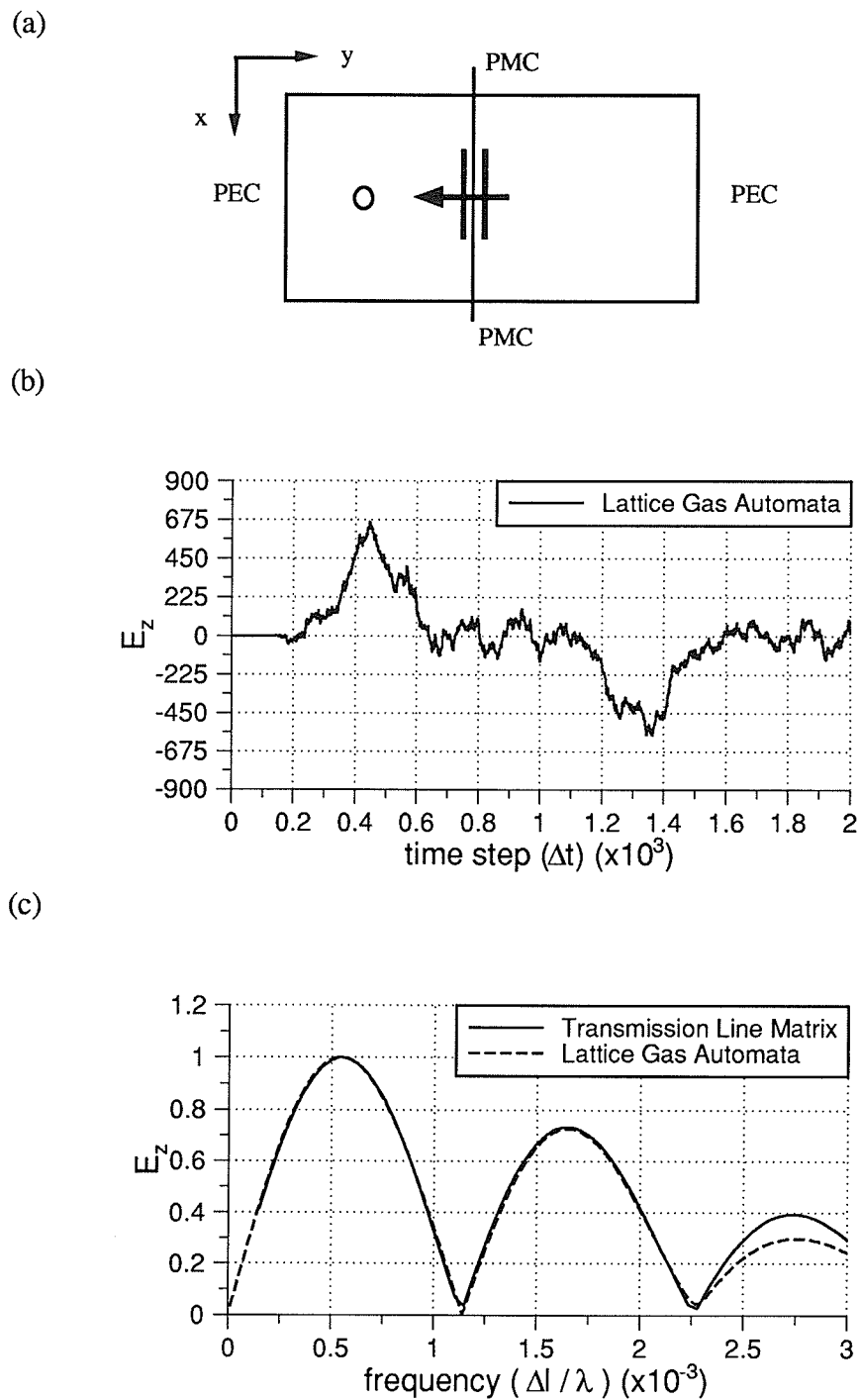
Figure 7.8: Test of the perfect electric conducting boundary condition (a) lattice diagram, (b) transient response at the output location, and (c) comparison of frequency domain results from the lattice gas automata and results from a transmission line matrix simulation.

7.5: Cellular Automata Machines

The computation time required for the evaluation of the examples considered in the previous section is on the order of hours using traditional computational hardware (SUN Sparcstation 10). The time required for the equivalent transmission line matrix or finite-difference time-domain simulations is on the order of 10's of seconds. A difference of approximately three *orders of magnitude* favours the traditional methods - a severe disadvantage of the lattice gas automata approach. These computation times indicate that if general purpose computers (such as a typical workstation or PC) are the only facilities available, the lattice gas automata approach is not a feasible one for modelling electromagnetic phenomena. However, special purpose computing environments exist, specifically designed for the efficient evaluation of cellular automata. The cost of these special purpose machines is on the same order of magnitude as a typical engineering workstation. Several generations of these special purpose computers (referred to as cellular automata machines) have been developed by Toffoli and Margolus (see [Toff84b] for a description of CAM-5, [Toff87] for a description of CAM-6, and [Marg90], [Toff91b] for a description of the latest machine, the CAM-8). Favourable comparisons of the performance of cellular automata machines to supercomputers for the evaluation of cellular automata have been obtained [Marg86]. Using the CAM-8, the dual lattice model presented in section 3 can be evaluated at a rate of 400 million cell updates per second [Marg93]. Evaluation of the examples provided in section 4 would require simulation times on the order of seconds. The use of these special purpose machines may allow the cellular automata approach to be competitive with the existing numerical approaches - in terms of the computation time per dollar of computational equipment.

Although cellular automata machines are special purpose computers which are only useful for exploring cellular automata behavior, the cost effectiveness of this approach and the benefit of using special purpose computers has been described by Toffoli,

> T. Toffoli: " ... *The fact remains that if I put one-million dollars' worth of cellular automaton VLSI circuits in a black box, and ask somebody to simulate its behavior with one-million dollars' worth of general-purpose computer, their simulation will be perhaps 10^{12} (one million million) times slower. The challenge is, of course, unfair, because a general-purpose computer is optimized to do other things, but that is exactly the point ! ... "*   (from [Toff84b])

7.6: Discussion

In this chapter, the application of cellular automata to the modelling of electromagnetic phenomena has been considered. The results obtained from the modified HPP lattice gas automaton indicate correct qualitative behavior and reasonably accurate quantitative results. With special purpose computational hardware, the lattice gas approach may provide an efficient tool for the analysis of electromagnetic phenomena.

Several questions regarding the accuracy of the lattice gas automata for modelling linear wave behavior come to mind. The convergence of the lattice gas automata (i.e., *how many cells are required ?*, and *averages over how large of a neighborhood are required ?*) is an important topics for consideration. The convergence to a macroscopic solution with a desired degree of accuracy in a lattice gas automata is statistical, distinct from the traditional methods applied in computational electromagnetics. For instance, in the application of the finite-difference method the order of accuracy of the difference approximations can be increased, or the density of the mesh can be increased to improve convergence. The lattice gas automata requires statistical convergence - averaging over a large number of particles and a lattice of sufficient size such that the appropriate behavior emerges. For linear wave behavior to be supported by the lattice gas automata, only small perturbations of particle densities within an equilibrium distribution of particles are permitted. Additional questions to be considered include: *how large can the initial perturbation be before undesired non-linear behavior is introduced ?* and *how many particles are required to be able to obtain a sufficient computational dynamic range ?*

The general approach to the analysis of a specific problem using the lattice gas approach will be essentially the same as that employed with the time-domain differential equation based methods investigated in this thesis . The entire spatial domain of the problem requires discretization, and therefore absorbing boundary conditions will be required for open region problems. As well, for the successful application of cellular automata to modelling practical problems, algorithmic *add-ons* such as boundary conditions, sources, lattice-zoning, and the calculation of field distributions (with perhaps transformation to the frequency domain or far field region) are required. All of the algorithmic *add-ons* required by the traditional numerical approaches will also be required in the application of cellular automata. The ease with which these algorithmic add-ons can be implemented into a lattice gas automata model remains to be investigated.

As well, the modelling of material regions with arbitrary permittivity, permeability, and conductivity; and the extension to three-dimensions will also be required.

Chapter 8: Conclusions and Future Directions

8.1: Conclusions

In this thesis the development and application of general purpose techniques for the simulation of electromagnetic field problems have been investigated. The goal of this research is to investigate general purpose numerical methods capable of analyzing a wide variety of macroscopic electromagnetic phenomena. With respect to this goal, the following contributions have been presented in this thesis,

- A review of differential-equation based numerical methods has been presented which allows a concise description and comparison of the relative advantages and disadvantages of various methods.

- Three new TLM models have been developed for modelling the two-dimensional wave equation. These models demonstrate the relevance of different grid structures and orders of spatial accuracy to the TLM method.

- A general purpose electromagnetic simulation program has been developed which is based on the three-dimensional symmetric-condensed TLM model [John87b]. The simulation program has been successfully applied to the analysis of three classes of electromagnetic scattering and radiation problems (half space geometries, radar-cross-section analysis, and microstrip geometries), and therefore validates the concept of a general purpose electromagnetic simulation program.

- The framework of a general purpose electromagnetic simulation program has been presented which is based on the scattered field formulation (with local absorbing boundary conditions) of a time-domain finite-element algorithm originally introduced by Lynch and Paulsen [Lync90]. The equivalence of this time-domain finite-element algorithm with a second-order central-finite-difference algorithm is demonstrated.

- The potential application of cellular automata to computational electromagnetics has been demonstrated.

8.2: Future Directions

Upon consideration of the above contributions, the following topics are proposed for future investigation:

- To exploit the computational advantages of the new two-dimensional TLM models for the solution of practical problems, the extension of these models to three-dimensional problems is highly recommended for further investigation.

- To further enhance the capabilities of the TLM simulation program, the implementation of techniques for modelling fine geometrical detail such as thin-wire modelling and variable meshing techniques is desirable.

- To allow the application of the time-domain finite-element simulation program to practical problems, this code should be interfaced to a flexible mesh generator.

- Further investigation of the theoretical finite-element / finite-difference equivalence to determine optimal integration schemes.

- Various aspects of the application of cellular automata to computational electromagnetics can be investigated. These include the implementation of the existing models onto special-purpose computational hardware, and the investigation of various practical aspects such as the modelling of material properties and the extension to three-dimensional scattering and radiation problems.

Appendix A: Derivation of the Two-Dimensional TLM Algorithm Using a Characteristic-Based Field Decomposition

Consider the derivation of the original two-dimensional transmission line matrix model [John71] by a characteristic-based field decomposition following the theory presented in [LoVe92], [LoVe93]. Maxwell's equations as expressed in conservation law form are provided in Chapter 2. In two-dimensions, (2.6) is reduces to,

$$\partial_t \mathbf{u} + A_E \partial_x \mathbf{u} + A_G \partial_z \mathbf{u} = 0 \tag{A.1}$$

where $\partial_\alpha = \partial/\partial\alpha$, and

$$A_E = \begin{bmatrix} 0 & 0 & e \\ 0 & 0 & 0 \\ m & 0 & 0 \end{bmatrix}$$

$$A_G = \begin{bmatrix} 0 & -e & 0 \\ -m & 0 & 0 \\ 0 & 0 & 0 \end{bmatrix}$$

$e=1/\varepsilon$, $m=1/\mu$ and $\mathbf{u}$ is the solution vector,

$$\mathbf{u} = \begin{bmatrix} E_y \\ H_x \\ H_z \end{bmatrix}$$

A.1: Numerical Approximation

Following [LoVe92], consider the discretization of (A.1) in two dimensions by assuming the geometrical space (x,z) is discretized into rectangular cells (see Figure A.1). Within each cell, it is assumed that propagation in the two orthogonal directions (x and z), involves no variation with respect to the other orthogonal direction, and (A.1) is therefore approximated by the two equations,

$$\partial_t \mathbf{u} + A_E \partial_x \mathbf{u} = 0 \qquad\qquad \text{(A.2a)}$$

and

$$\partial_t \mathbf{u} + A_G \partial_z \mathbf{u} = 0 \qquad\qquad \text{(A.2b)}$$
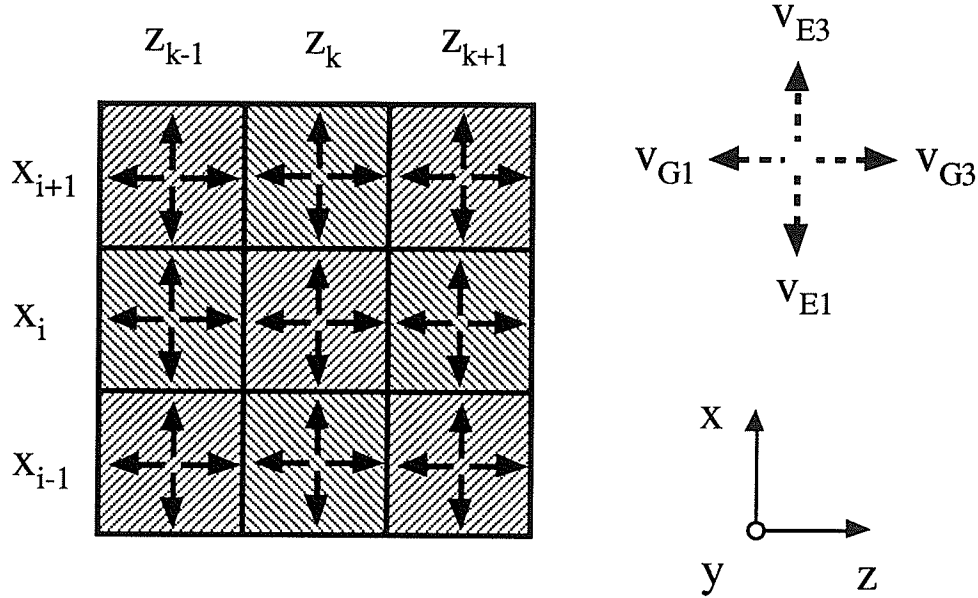
Figure A.1: Discretization of the spatial domain into rectangular cells. Characteristic directions are shown within each cell.

To uncouple (A.2), the matricies A_E and A_G are diagonalized and new variables are defined. Using the eigenvalues $\lambda = \{-\sqrt{(\mu\varepsilon)}, 0, \sqrt{(\mu\varepsilon)}\}$, and the right and left eigenvalue matricies,

$$R_E = \begin{bmatrix} 1 & 0 & 1 \\ 0 & \sqrt{2} & 0 \\ -Y & 0 & Y \end{bmatrix} \quad L_E = \frac{1}{2}\begin{bmatrix} 1 & 0 & -Z \\ 0 & \sqrt{2} & 0 \\ 1 & 0 & Z \end{bmatrix} \quad R_G = \begin{bmatrix} 1 & 0 & 1 \\ Y & 0 & -Y \\ 0 & \sqrt{2} & 0 \end{bmatrix} \quad L_G = \frac{1}{2}\begin{bmatrix} 1 & Z & 0 \\ 0 & 0 & \sqrt{2} \\ 1 & -Z & 0 \end{bmatrix} \quad \text{(A.3)}$$

(which satisfy LR=RL=I), the similarity transformation of A_E and A_G is defined as,

$$L_E A_E R_E = L_G A_G R_G = \text{diag}(\lambda) = \Lambda \qquad\qquad \text{(A.4)}$$

New variables, refered to as Riemann Invariant (RI) variables are defined as [Sod85],

$$v_E = L_E u = \frac{1}{2} \begin{bmatrix} E_y - ZH_z \\ \sqrt{2}H_x \\ E_y + ZH_z \end{bmatrix} = \begin{bmatrix} v_{E1} \\ v_{E2} \\ v_{E3} \end{bmatrix} \qquad \text{(A.5a)}$$

$$v_G = L_G u = \frac{1}{2} \begin{bmatrix} E_y + ZH_x \\ \sqrt{2}H_z \\ E_y - ZH_x \end{bmatrix} = \begin{bmatrix} v_{G1} \\ v_{G2} \\ v_{G3} \end{bmatrix} \qquad \text{(A.5b)}$$

Premultiplying (A.2a) by L_E and substituting $u = Iu = R_E L_E u$ yields,

$$\partial_t L_E u + \partial_x L_E A_E R_E L_E u = 0 \quad \text{or,}$$

$$\partial_t v_E + \partial_x \Lambda v_E = 0 \qquad \text{(A.6a)}$$

and similarly (A.2b) becomes,

$$\partial_t v_G + \partial_z \Lambda v_G = 0 \qquad \text{(A.6b)}$$

The solutions to these uncoupled partial differential equations are,

$$v_{Ei}(x,t) = f_{Ei}(x - \lambda_i t) \quad \text{and} \quad v_{Gi}(z,t) = f_{Gi}(z - \lambda_i t) \qquad \text{for } i = 1,2,3 \qquad \text{(A.7)}$$

The Reimann Invariant variables v_{Ei} and v_{Gi} are constant along the lines defined by $x - \lambda_i t = \text{const.}$ and $z - \lambda_i t = \text{const.}$ These lines are refered to as characteristic directions.

Examining v_{Ei} in more detail, v_{E1} and v_{E3} are constant along the $x + ct = \text{const.}$ and $x - ct = \text{const.}$ directions, respectively, and can therefore be considered as solutions which propagate in the $-x$ and $+x$ directions, respectively. v_{E2} is constant along the horizontal line $x = \text{const.}$ and therefore the H_x component of the field does not vary in the x direction. This illustrates the fundamental approximation of this approach. For RIs which propagate in the $\pm x$ direction, only the variation in the transverse field components (H_z, E_y) is considered. Along the $\pm x$ direction variation in the normal component of the fields (H_x) is ignored. A similar examination of v_{Gi} can be performed.

The propagating RIs can be expressed as,

$$\mathbf{v} = \begin{bmatrix} v_{E1} \\ v_{E3} \\ v_{G1} \\ v_{G3} \end{bmatrix} = \frac{1}{2} \begin{bmatrix} E_y - ZH_z \\ E_y + ZH_z \\ E_y + ZH_x \\ E_y - ZH_x \end{bmatrix} = \frac{1}{2} \begin{bmatrix} 1 & 0 & -Z \\ 1 & 0 & Z \\ 1 & Z & 0 \\ 1 & -Z & 0 \end{bmatrix} \begin{bmatrix} E_y \\ H_x \\ H_z \end{bmatrix} = \mathbf{Au} \qquad (A.8)$$

A.2: Transfer of Riemman Invariant Variables Across Cell Interfaces

The mapping (A.8) permits determination of the RI values, $\mathbf{v}$ from specification of the field components $\mathbf{u}$. To illustrate the development of the remainder of the algorithm, consider specification of a initial field distribution $\mathbf{u}(x,z,t=0)$. Following (A.8), this distribution intializes the RIs $\mathbf{v}(x_i,z_k,t=0)$. Following the discussion above, the RIs are propagated out from the centres of the cells until the interface between cells is reached. Following the principle of the existence of unique field values at these interfaces, and assuming identical cells, it can be shown that the RIs simply pass through the interfaces without any alteration. The $\pm x$ propagating RIs just prior to reaching the interface shown in Figure A.2 (at time $t=(\Delta t/2)^-$) are,

$$v_{E1}(x_{i+1},z_k,(\Delta t/2)^-) = \frac{1}{2}(E_y - ZH_z) \qquad v_{E3}(x_i,z_k,(\Delta t/2)^-) = \frac{1}{2}E_y + ZH_z) \qquad (A.9)$$

and just after interacting at the interface (at time $t=(\Delta t/2)^+$) the RIs are,

$$v_{E1}(x_i,z_k,(\Delta t/2)^+) = \frac{1}{2}E_y - ZH_z) \qquad v_{E3}(x_{i+1},z_k,(\Delta t/2)^+) = \frac{1}{2}E_y + ZH_z) \qquad (A.10)$$

The field components at the cell interface at time $(\Delta t/2)^-$ and $(\Delta t/2)^+$ are given by,

$$E_y(x_{i+1/2},z_k,(\Delta t/2)^-) = v_{E1}(x_{i+1},z_k,(\Delta t/2)^-) + v_{E3}(x_i,z_k,(\Delta t/2)^-)$$

$$H_z(x_{i+1/2},z_k,(\Delta t/2)^-) = Y(v_{E3}(x_i,z_k,(\Delta t/2)^-) - v_{E1}(x_{i+1},z_k,(\Delta t/2)^-))$$

and

$$E_y(x_{i+1/2},z_k,(\Delta t/2)^+) = v_{E1}(x_i,z_k,(\Delta t/2)^+) + v_{E3}(x_{i+1},z_k,(\Delta t/2)^+)$$

$$H_z(x_{i+1/2},z_k,(\Delta t/2)^+) = Y(v_{E3}(x_{i+1},z_k,(\Delta t/2)^+) - v_{E1}(x_i,z_k,(\Delta t/2)^+))$$

respectively. Continuity of the field the components in space and time requires,
$E_y(x,z,t^-)=E_y(x,z,t^+)$ and $H_z(x,z,t^-)=H_z(x,z,t^+)$. Enforcing this requirement on the definitions given above leads to the requirement of continuity of the RIs across cell interfaces. The RIs are propagated without alteration across cell interfaces, and therefore,

$$v_{E1}(x_i,z_k,(\Delta t/2)^+) = v_{E1}(x_{i+1},z_k,(\Delta t/2)^-)$$

$$v_{E3}(x_{i+1},z_k,(\Delta t/2)^+) = v_{E3}(x_i,z_k,(\Delta t/2)^-)$$
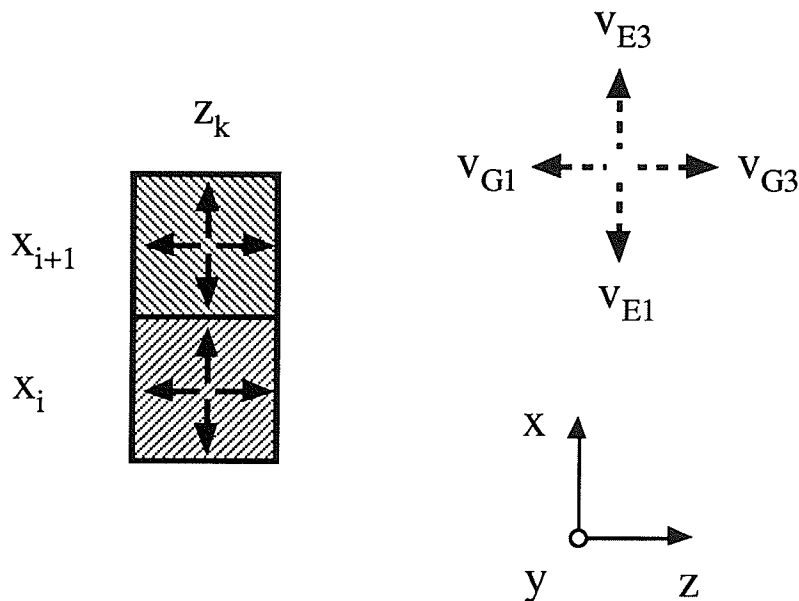
Figure A.2: Two RIs at the interface between adjacent computational cells.

A.3: Interaction of Riemman Invariant Variables At Cell Centres

       To complete the development of the algorithm, specification of the interaction of RIs when they meet at the cell centres is required. Consider the state of the cells at a time $(t+\Delta t)^-$ (just before the RIs reach the cell centres) and time $(t+\Delta t)^+$ (just after the RIs pass the cell centres). Again, the principle of continuity of field components in space and time is applied. Using (A.8), the field components just before and after interaction at the cell centres can be expressed as,

$$\mathbf{v}(x,z,(t+\Delta t)^-) = A\,\mathbf{u}(x,z,t+\Delta t) \quad \text{and} \quad \mathbf{v}(x,z,(t+\Delta t)^+) = A\,\mathbf{u}(x,z,t+\Delta t) \qquad \text{(A.11)}$$

From the above expressions it is tempting to write, $\mathbf{v}(x,z,(t+\Delta t)^+)=\mathbf{v}(x,z,(t+\Delta t)^-)$, however in general this is not true because (A.8) is an overdetermined system. Different $\mathbf{v}$ are capable of satisfying (A.8) for a unique field distribution $\mathbf{u}$. To determine the interaction at the centre of cells, i.e., the transformation $\mathbf{v}(x,z,(t+\Delta t)^- \rightarrow \mathbf{v}(x,z,(t+\Delta t)^+)$, $\mathbf{u}(x,z,t+\Delta t)$ is first defined from $\mathbf{v}(x,z,(t+\Delta t)^-)$ and then $\mathbf{v}(x,z,(t+\Delta t)^+)$ is determined from $\mathbf{u}(x,z,t+\Delta t)$ using the Moore-Penrose generalized inverse of A, defined as,

$$A^{\dagger} = (A^T A)^{-1} A^T = \begin{bmatrix} 1/2 & 1/2 & 1/2 & 1/2 \\ 0 & 0 & Y & -Y \\ -Y & Y & 0 & 0 \end{bmatrix} \qquad \text{(A.12)}$$

The transformation $\mathbf{v}(x,z,(t+\Delta t)^- \rightarrow \mathbf{v}(x,z,(t+\Delta t)^+$ can now be expressed as,

$$\mathbf{v}(x,z,(t+\Delta t)^+) = A A^{\dagger}\,\mathbf{v}(x,z,(t+\Delta t)^-) \qquad \text{(A.13)}$$

Any matrix, B that is in the null space of $A^{\dagger}$, can be added to the transformation matrix $AA^{\dagger}$. Therefore the most general form of the transformation matrix S, can be expressed as,

$$S_{\alpha} = A A^{\dagger} + B = \frac{1}{2} \begin{bmatrix} 3/2 & -1/2 & 1/2 & 1/2 \\ -1/2 & 3/2 & 1/2 & 1/2 \\ 1/2 & 1/2 & 3/2 & -1/2 \\ 1/2 & 1/2 & -1/2 & 3/2 \end{bmatrix} + \alpha \begin{bmatrix} -1 & -1 & 1 & 1 \\ -1 & -1 & 1 & 1 \\ 1 & 1 & -1 & -1 \\ 1 & 1 & -1 & -1 \end{bmatrix} \qquad \text{(A.14)}$$

Following [LoVe92], selection of $\alpha=1/4$ yields a conservative scheme for which,

$$S_{1/4} = \begin{bmatrix} 1/2 & -1/2 & 1/2 & 1/2 \\ -1/2 & 1/2 & 1/2 & 1/2 \\ 1/2 & 1/2 & 1/2 & -1/2 \\ 1/2 & 1/2 & -1/2 & 1/2 \end{bmatrix} \qquad \text{(A.15)}$$

The above matrix describing the transformation $\mathbf{v}(x,z,(t+\Delta t)^- \rightarrow \mathbf{v}(x,z,(t+\Delta t)$ is identical to the scattering matrix for the original two-dimensional transmission line matrix model introduced by Johns in 1971 (provided the correct mapping from the variables $\mathbf{v}$ to the original voltage pulse as defined by Johns is performed - the difference is notational) [John71]. Also, the transfer of RIs accross cell interfaces (described in section A.2 is

identical to the original transfer event [John71] (again with the appropriate transformation). The three-dimensional symmetric-condensed transmission line matrix algorithm [John87b] has been derived in a similar manner [LoVe93].

References

[Akht75a] S. Akhtarzad and P. B. Johns, "Generalized Elements for the TLM Method of Numerical Analysis," *Proc. Inst. Elec. Eng.*, vol 122, no. 12, pp. 1349-1352, December 1975.

[Akht75b] S. Akhtarzad and P. B. Johns, "Solution of Maxwell's Equations in Three Space Dimensions and Time by the TLM Method of Numerical Analysis," *Proc. Inst. Elec. Eng.*, vol 122, no. 12, pp. 1344-1348, December 1975.

[Alan84] E. Alanen and I. V. Lindell, "Impedance of vertical electric and magnetic dipole above a dissipative ground," *Radio Science*, vol. 19, no. 6, pp. 1469-1474, Nov-Dec 1984.

[Alle87] R. Allen, A. Mallik and P. B. Johns, "Numerical Results for the Symmetric Condensed TLM Node," *IEEE Transactions on Microwave Theory and Techniques*, vol. 35, no. 4, pp. 378-382, April 1987.

[Arle69] P. L. Arlett, A. K. Bahrani and O. C. Zienkiewicz, "Application of finite elements to the solution of Helmholtz's equation," *Proc. Inst. Elec. Eng.*, vol 115, no. 12, pp. 1762-1766, December 1968.

[Arva91] E. Arvas, A. Rahhal-Arabi, A. Sadigh and S. M. Rao, "Scattering from Multiple Conducting and Dielectric Bodies of Arbitrary Shape," *IEEE Antennas and Propagation Magazine*, vol. 33, no. 2, pp. 29-36, April 1991.

[Bala89] C. A. Balanis, **Advanced Engineering Electromagnetics**, John Wiley and Sons, 1989.

[Bano66] A. Banos, **Dipole Rediation in the Presence of a Conducting Half Space**, Permagon Press, 1966.

[Bark92] S. Barkeshli, H. A. Sabbagh, D. J. Radecki and M. Melton, "A Novel Implicit Time-Domain Boundary-Integral/Finite-Element Algorithm for Computing Transient Electromagnetic Field Coupling to a Metallic Enclosure," *IEEE Transactions on Antennas and Propagation*, vol. 40, no. 10, pp. 1155-1164, October 1992.

[Bayl80] A. Bayliss and E. Turkel, "Radiation Boundary Conditions for Wave-Like Equations," *Communications on Pure and Applied Mathematics*, vol. 33, pp. 707-725, 1980.

[Blas88] J. G. Blaschak and G. A. Kriegsmann, "A Comparative Study of Absorbing Boundary Conditions," *Journal of Computational Physics*, vol. 77, pp. 109-139, July 1988.

[Born89]   J. M. Bornholdt and K. D. Tatalias, "The Application of Lattice Gas Techniques to Electromagnetic Problems," *IEEE Trans. Magnetics*, vol. 25, no. 4, pp. 2916-2918, July 1989.

[Boys92]   W. E. Boyse, D. R. Lynch, K. D. Paulsen and G. N. Minerbo, "Nodal-Based Finite-Element Modeling of Maxwell's Equations," *IEEE Transactions on Antennas and Propagation*, vol. 40, no. 6, June 1992.

[Brea86]   J. K. Breakall, M. J. Barth and K. S. Kunz, "A Comparison of Method of Moments and Finite Differences for the Detection of a Buried Object in a Lossy Medium," *National Radio Science Meeting*, 1986.

[Brew80]   C. R. Brewitt-Taylor and P. B. Johns, "On the Construction an Numerical Solution of Transmission-Line and Lumped Network Models of Maxwell's Equations," *International Journal for Numerical Methods in Engineering*, vol. 15, pp. 13-30, 1980.

[Brid93]   Private communication with Professor G. Bridges, University of Manitoba, 1993.

[Brit89]   C. L. Britt, "Solution of Electromagnetic Scattering Problems Using Time Domain Techniques," *IEEE Transactions on Antennas and Propagation*, vol. 37, pp. 1181-1192, September 1989.

[Burk81]   G. J. Burke, Miller, Brittingham, Lager, Lytte, and Okada, "Computer Modelling of Antennas Near the Ground," *Electromagnetics*, vol. 1, pp. 29-49, 1981.

[Burk84]   G. J. Burke and E. K. Miller, "Modelling Antennas Near to and Penetrating a Lossy Interface," *IEEE Transactions on Antennas and Propagation*, vol. 32, no. 10, pp. 1040-1049, October 1984.

[Cang87]   A. C. Cangellaris, C. C. Lin and K. K. Mei, "Point-Matched Time Domain Finite Element Methods for Electromagnetic Radiation and Scattering," *IEEE Transactions on Antennas and Propagation*, vol. 35, no. 10, pp. 1160-1173, October 1987.

[Cang91]   A. C. Cangellaris and D. B. Wright, "Analysis of Numerical Error Caused by the Stair-Stepped Approximation of a Conducting Boundary in FDTD Simulations of Electromagnetic Phenomena," *IEEE Transactions on Antennas and Propagation*, vol. 39, no. 10, pp. 1518-1525, October 1991.

[Care84]   G. F. Carey and J. T. Oden, **Finite Elements: Computational Aspects**, vol. III, Englewood Cliffs, Prentice-Hall, 1984.

[Celu93]   M. Celuch-Marcysiak and W. K. Gwarek, Comments on: [Chen91b] "A New Finite-Difference Time-Domain Formulation and its Equivalence with the TLM Symmetrical Condensed Node," *IEEE Transactions on Microwave Theory and Techniques*, vol. 41, no. 1, pp. 168-172, January 1993.

[Cham93] W. A. Chamma, "Study on the Applications of the Finite-Difference Time-Domain Method for Solutions of Electromagnetic Problems," PhD Thesis, University of Manitoba, 1993.

[Char81] M. V. K. Chari, Z. J. Csendes, P. Silvester, A. Konrad and M. A. Palmo, "Three-Dimensional Magnetostatic Field Analysis of Electrical Machinery by the Finite-Element Method," *IEEE Transactions on Power Apparatus and Systems*, vol. 100, no. 8, pp. 4007-4015, August 1981.

[Chen91a] Z. Chen, M. M. Ney and W. J. R. Hoefer, "A New Boundary Description in Two-Dimensional TLM Models of Microwave Circuits," *IEEE Transactions on Microwave Theory and Techniques*, vol. 39, pp. 377-382, March 1991.

[Chen91b] Z. Chen, M. M. Ney and W. J. R. Hoefer, "A New Finite-Difference Time-Domain Formulation and its Equivalence with the TLM Symmetric Condensed Node," *IEEE Transactions on Microwave Theory and Techniques*, vol. 39, pp. 2160-2169, 1991. (see also [Celu93])

[Conn76] J. J. Connor and C. A. Brebbia, **Finite Element Techniques for Fluid Flow**, Newnes-Butterworths, 1976.

[Cote88] M. G. Cote, M. B. Woodworth and A. D. Yaghjian, "Scattering from the Perfectly Conducting Cube," *IEEE Transactions on Antennas and Propagation*, vol. 36, no. 9, pp. 1321-1329, September 1988.

[D'Ang89] J. D. D'Angelo and I. D. Mayergoyz, "On the Use of Local Absorbing Boundary Conditions for RF Scattering Problems," *IEEE Transactions on Magnetics*, vol. 25, no. 4, pp. 3040-3042, July 1989.

[D'Ang90] J. D. D'Angelo and I. D. Mayergoyz, "Finite Element Methods for the Solution of RF Radiation and Scattering Problems," *Electromagnetics*, vol. 10, pp. 177-199, 1990.

[Davi89] J. B. Davies, "The Finite Element Method," in: **Numerical Techniques for Microwave and Millimeter Wave Passive Structures**, Edited by T. Itoh, New York: Wiley, 1989.

[Deli91] G. Y. Delisle, K. L. Wu and J. Litva, "Coupled finite element and boundary element method in electromagnetics," *Computer Physics Communications*, vol. 68, pp. 255-278, 1991.

[Deve92] T. Deveze, L. Beaulieu and W. Tabbara, "A Fourth Order Scheme for the FDTD Algorithm Applied to Maxwell's Equations," 1993 IEEE AP-S Symposium, Chicago Illinois, pp. 346-349, 1992.

[Dool90] G. D. Doolen, U. Frisch, B. Hasslacher, S. Orszag and S. Wolfram (eds), **Lattice Gas Methods for Partial Differential Equations**, Santa Fe Institute, 1990.

[Duba90] J. L. Dubard, D. Pompei, J. Le Roux and A. Papiernik, "Characterization of Microstrip Antennas Using the TLM Simulation Associated with a Prony-Pisarenko Method," *International Journal of Numerical Modeling*, vol. 3, pp. 269-285, 1990.

[Duff93] A. P. Duffy, P. Naylor, T. M. Benson and C. Christopoulos, "Numerical Simulation of Electromagnetic Coupling and Comparison with Experimental Results," *IEEE Transacions on Electromagnetic Compatibility*, vol. EMC-35, pp. 46-54, 1993.

[Enge82] M. S. Engelman, R. L. Sani and P. M. Gresho, "The Implementation of Normal and/or Tangential Boundary Conditions in Finite Element Codes for Incompressible Fluid Flow," *International Journal for Numerical Methods in Fluids,* vol. 2, pp. 225-238, 1982.

[Engq77] B. Engquist and A. Majda, "Absorbing Boundary Conditions for the Numerical Simulation of Waves," *Mathematics of Computation*, vol. 31, pp. 629-651, 1977.

[Eswa90] Eswarappa, G. I. Costache and W. J. R. Hoefer, "Transmission Line Matrix Modeling of Dispersive Wide-Band Absorbing Boundaries with Time-Domain Diakoptics for S-Parameter Extraction," *IEEE Transactions on Microwave Theory and Techniques*, vol. 38, no. 4, pp. 379-386, April 1990.

[Fang89] J. Fang and K. K. Mei, "A Higher Order Finite Difference Scheme for the Solution of Maxwell's Equations in the Time Domain," *Proceedings of the 1989 URSI Radio Science Meeting*, San Jose, California, 1989.

[Fels69] L. B. Felson and N. Marcuvitz, **Radiation and Scattering of Waves**, Prentice-Hall, New York, 1969.

[Feyn65] R. P. Feynman, **The Character of Physical Law**, MIT Press, 1965.

[Feyn82] R. P. Feynman, "Simulating Physics with Computers," *International Journal of Theoretical Physics*, vol. 21, no. 6/7, pp. 467-488, 1982.

[Fred90] E. Fredkin, "Digital Mechanics: An Informational Process Based on Reversible Universal Cellular Automata," *Physica D*, vol. 45, pp. 254-270, 1990.

[Fris86] U. Frisch, B. Hasslacher and Y. Pomeau, "Lattice-Gas Automata for the Navier-Stokes Equations," *Physical Review Letters*, vol. 56, no. 14, pp. 1505-1508, 1986 (this paper is also reprinted in [Dool90]).

[Fris87] U. Frisch, D. d'Humieres, B. Hasslacher, P. Lallemand, Y. Pomeau and J-P. Rivet, "Lattice Gas Hydrodynamics in Two and Three Dimensions," *Complex Systems*, vol. 1, pp. 649-707, 1987 (this paper is also reprinted in [Dool90]).

[Furs90] C. M. Furse, S. P. Mathur and O. P. Gandhi, "Improvements to the Finite-Difference Time-Domain Method for Calculating the Radar Cross Section of a Perfectly Conducting Target," *IEEE Transactions on Microwave Theory and Techniques*, vol. 38, no. 9, pp. 919-927, 1990.

[Germ90a] F. J. German, G. K. Gothard and L. S. Riggs, "RCS of Three-Dimensional Scatterers using the Symmetrical Condensed TLM Method," *Electronics Letters*, vol. 26, no. 10, pp. 673-674, 1990.

[Germ90b] F. J. German and R. W. Johnson, "Full Wave Three-Dimensional Simulation of Maxwell's Equations for the Electrical Characterization of High-Speed

Interconnects," *IEEE Transactions on Components, Hybrids, and Manufacturing Technology*, vol. 13, no. 2, pp. 341-346, June 1990.

[Germ90c] F. J. German, G. K. Gothard and L. S. Riggs, "Modelling of Materials with Electric and Magnetic Losses with the Symmetrical Condensed TLM Method," *Electronics Letters*, vol. 26, no. 16, pp. 1307-1308, 1990.

[Givo91] D. Givoli, "Non-reflecting Boundary Conditions," *Journal of Computational Physics*, pp. 1-29, 1991.

[Goor92] P. M. Goorjian, A. Taflove, R. M. Joseph and S. C. Hagness, "Computational Modelling of Femtosecond Optical Solitons from Maxwell's Equations," *IEEE Journal of Quantum Electronics* , vol. 28, pp. 2416-2422, October 1992.

[Gray76] W. G. Gray and G. F. Pinder, "On the Relationship Between the Finite Element and Finite Difference Methods," *International Journal for Numerical Methods in Engineering*, vol. 10, pp. 893-923, 1976.

[Hard76] J. Hardy, O. de Pazzis and Y. Pomeau, "Molecular dynamics of a classical lattice gas: Transport properties and time correlation functions," *Physical Review A*, vol. 13, no. 5, pp. 1949-1961, May 1976.

[Harr61] R. F. Harrington, **Time-Harmonic Electromagnetic Fields**, McGraw-Hill Book Company, New York, 1961.

[Harr69] R. F. Harrington, **Field Computation by Moment Methods**, Macmillan, 1969.

[Hela90] A. Helaly, L. Shafai and A. Sebak, "Low-frequency response of a buried object in a lossy ground," *Canadian Journal of Physics*, vol. 68, pp. 111, 1990.

[Hers91] N. Herscovici and D. M. Pozar, "Full-Wave Analysis of Aperture Coupled Microstrip Lines," *IEEE MTT Symposium*, pp. 139-142, 1991.

[Himd89] M. Himdi, J. P. Daniel and C. Terret, "Resonant Behavior of Slot-Coupled Microstrip Antennas," *Proceedings ISAP `89*, Japan, 1989.

[Hoef85] W. J. R. Hoefer, "The Transmission-Line Matrix Method - Theory and Applications," *IEEE Transactions on Microwave Theory and Techniques*, vol. 33, no. 10, pp. 882-893, October 1985.

[Hoef89] W. J. R. Hoefer, "The Transmission-Line Matrix (TLM) Method," in: **Numerical Techniques for Microwave and Millimeter Wave Passive Structures**, Edited by T. Itoh, New York: Wiley, 1989.

[Hoef91] W. J. R. Hoefer, "Huygens and the Computer - A Powerful Alliance in Numerical Electromagnetics," *Proceedings of the IEEE*, vol. 79, no. 11, pp. 1459-1471, October 1991.

[Holl91] R. H. Holland, V. P. Cable and L. C. Wilson, "Finite-Volume Time-Domain (FVTD) Techniques for EM Scattering," *IEEE Transactions on Electromagnetic Compatibility*, vol. 33, no. 4, pp. 281-294, Nov 1991.

[Itti91] A. Ittipiboon, R. Oostlander, Y. M. M. Antar and M. Cuhaci, "A Modal Expansion Method of Analysis and Measurement on Aperture-Coupled Microstrip Antenna," *IEEE Transactions on Antennas and Propagation*, vol. 39, no. 11, November 1991.

[Itti93] Private communication with Dr. A. Ittipiboon of the Communications Research Centre, Ottawa, Ontario, 1993.

[Jack90] E. A. Jackson, **Perspectives of Nonlinear Dynamics**, volume 2, Cambridge University Press, pp. 496, 1990.

[Jin92a] J. -M. Jin, J. L. Volakis and V. V. Liepa, "Ficticious absorber for truncating finite element meshes in scattering," *IEE Proceedings, Pt. H*, vol. 139, no. 5, pp. 472-476, October 1992.

[Jin92b] H. Jin and R. Vahldieck, "The Frequency-Domain Transmission Line Matrix Method - A New Concept," *IEEE Transactions on Microwave Theory and Techniques*, vol. 40, no. 12, pp. 2207-2218, December 1992.

[John71] P. B. Johns and R. L. Beurle, "Numerical Solution of Two-Dimensional Scattering Problems using a Transmission-Line Matrix," *Proceedings of the IEE*, vol. 118, pp. 1203-1208, 1971.

[John74a] P. B. Johns, "The Solution of Inhomogeneous Waveguide Problems Using a Transmission-Line Matrix," *IEEE Transactions on Microwave Theory and Techniques*, vol. 22, no. 3, pp. 209-215, March 1974.

[John74b] P. B. Johns, "A new mathematical model to describe the physics of propagation," *Radio Electron. Eng.* vol. 44, no. 12, pp. 657-666, December 1974.

[John79] P. B. Johns, "The Art of Modelling," *Electronics and Power*, vol. 25, no. 8, pp. 565-569, 1979.

[John86] P. B. Johns, "Use of condensed and symmetrical TLM nodes in computer-aided electromagnetic design," *IEE Proceedings*, vol. 133, Pt. H, no. 5, pp. 368-374, October 1986.

[John87a] P. B. Johns, "On the Relationship Between TLM and Finite-Difference Methods for Maxwell's Equations," *IEEE Transactions on Microwave Theory and Techniques*, vol. 35, no. 1, pp. 60-61, 1987.

[John87b] P. B. Johns, "A Symmetric Condensed Node for the TLM Method," *IEEE Transactions on Microwave Theory and Techniques.*, vol. 35, no. 4, pp. 370-377, April 1987.

[Jurg92] T. G. Jurgens, A. Taflove, K. Umashankar and T. Moore, "Finite-Difference Time-Domain Modeling of Curved Surfaces," *IEEE Transactions on Antennas and Propagation*, vol. 40, no. 4, pp. 357-366, April 1992.

[Kish86] A. A. Kishk and L. Shafai, "Different Formulations for Numerical Solution of Single or Multibodies of Revolution with Mixed Boundary Conditions," *IEEE Transactions on Antennas and Propagation*, vol. 34, no. 5, pp. 666-673, May 1976.

[Konr89] A. Konrad, "A Method for Rendering 3D Finite Element Vector Field Solutions Non-Divergent," *IEEE Transactions on Magnetics*, vol. 25, no. 4, pp. 2822-2824, July 1989.

[Kron43] G. Kron, "Equivalent Circuits to Represent the Electromagnetic Field Equations," *Physical Review*, vol. 64, pp. 126-128, 1943.

[Kron44] G. Kron, "Equivalent Circuit of the Field Equations of Maxwell - I," *Proc. Inst. Radio Engrs.*, vol. 32, pp. 289-299, 1944.

[Kron45] G. Kron, "Numerical Solution of Ordinary and Partial Differential Equations by Means of Equivalent Circuits," *Journal Applied Physics*, vol. 16, pp. 172-186, 1945.

[Kunz93] K. S. Kunz and R. J. Luebbers, **The Finite Difference Time Domain Method for Electromagnetics**, CRC Press, Boca Raton FL, 1993.

[Lang86] C. G. Langton, "Studying Artificial Life with Cellular Automata," *Physica D*, vol. 22, pp. 120-149, 1986.

[Lapi82] L. Lapidus and G. F. Pinder, **Numerical Solution of Partial Differential Equations in Science and Engineering**, John Wiley and Sons, 1982.

[Lee92] J-F. Lee, R. Palandech and R. Mittra, "Modelling Three-Dimensional Discontinuities in Waveguides Using Nonorthogonal FDTD Algorithm," *IEEE Transactions on Microwave Theory and Techniques*, vol. 40, no. 2, pp. 346-352, February 1992.

[Lee94] J-F. Lee, "WETD-A Finite Element Time-Domain Approach for Solving Maxwell's Equations," *IEEE Microwave and Guided Wave Letters*, vol. 4, no. 1, pp. 11-13, January 1994.

[Ling91] R. T. Ling, "A time-dependent method for the numerical solution of wave equations in electromagnetic scattering problems," *Computer Physics Communications*, vol. 68, pp. 213-223, 1991.

[Litv93] J. Litva, C. Wu, K-L Wu and J. Chen, "Some Considerations for Using the Finite Difference Time Domain Technique to Analyze Microwave Integrated Circuits", *IEEE Microwave and Guided Wave Letters*, vol. 3, no. 12, pp. 438-440, December 1993.

[Liu91a] C. Liu and L. C. Shen, "Response of Electromagnetic-Pulse Logging Sonde in Axially Symmetrical Formation," *IEEE Transactions on Geoscience and Remote Sensing*, vol. 29, no. 2, pp. 214-221, March 1991.

[Liu91b] C. Liu and L. C. Shen, "Numerical Simulation of Subsurface Radar for Detecting Buried Pipes," *IEEE Transactions on Geoscience and Remote Sensing*, vol. 29, no. 5, pp. 795-798, September 1991.

[LoVe91] J. LoVetri, "Algorithmic Techniques," Part II of: Ph.D. Thesis, University of Ottawa, 1991.

[LoVe92] J. LoVetri and N. R. S. Simons, "Derivation of TLM Type Methods from Characteristic Field Decompositions," *Proceedings of ANTEM'92*, pp. 185-190, Winnipeg, Manitoba, 1992.

[LoVe93] J. LoVetri and N. R. S. Simons, "A Class of Symmetrical Condensed Node TLM Methods Derived Directly from Maxwell's Equations," *IEEE Transactions on Microwave Theory and Techniques*, vol. MTT-41, no. 8, pp. 1419-1428, August 1993.

[Lync90] D. R. Lynch and K. D. Paulsen, "Time-Domain Integration of the Maxwell Equations on Finite Elements," *IEEE Transactions on Antennas and Propagation*, vol. AP-38, no. 12, pp. 1933-1942, December 1990.

[Lync91] D. R. Lynch and K. D. Paulsen, "Origin of Vector Parasites in Numerical Maxwell Solutions," *IEEE Transactions on Microwave Theory and Techniques*, vol. MTT-39, no. 3, pp. 383-394, March 1991.

[Mads88] N. K. Madsen and R. W. Ziolkowski, "Numerical Solution of Maxwell's Equations in the Time Domain Using Irregular Nonorthogonal Grids," *Wave Motion*, vol. 10, pp. 583-596, 1988.

[Mads90] N. K. Madsen and R. W. Ziolkowski, "A Three-Dimensional Modified Finite Volume Technique for Maxwell's Equations," *Electromagnetics*, vol. 10, pp. 147-161, 1990.

[Maha92] K. Mahadevan, H. A. Auda, and A. W. Glisson, "Scattering from a Thin Perfectly-Conducting Square Plate," *IEEE Antennas and Propagation Magazine*, vol. 34, no. 1, pp. 26-32, February 1992.

[Marg84] N. Margolus, "Physics-Like Models of Computation," *Physica D*, vol. 10, pp. 81-95, 1984.

[Marg86] N. Margolus, T. Toffoli and G. Vichniac, "Cellular-Automata Supercomputers for Fluid-Dynamics Modelling," *Physical Review Letters*, vol. 56, no. 16, pp. 1694-1696, 1986.

[Marg90] N. Margolus and T. Toffoli, "Cellular Automata Machines," in **Lattice Gas Methods for Partial Differential Equations**, ed: Doolen *et al*, Santa Fe Institute, 1990.

[Marg92] N. Margolus, "A Bridge of Bits," in **Workshop on Physics and Computation, PhysComp'92**, D. Matzke (workshop organizer), IEEE Computer Society Press, Los Alomitos CA, 1992.

[Marg93] N. Margolus and T. Toffoli, *private communication*, 1993.

[Mari85] G. E. Mariki and C. Yeh, "Dynamic TLM Analysis of Microstriplines on Anisotropic Substrate," *IEEE Transactions on Microwave Theory and Techniques*, vol. MTT-33, pp. 789-799, September 1985.

[Marp87] S. L. Marple, **Digital Spectral Analysis: With Applications**, Prentice-Hall, 1987.

[Maut79] J. R. Mautz and R. F. Harrington, "Electromagnetic Scattering from a Homogeneous Material Body of Revolution," *Arch. Elektron. Ubertragungstechn.*, vol. 33, pp. 71-80, 1979.

[Maye91] I. D. Mayergoyz and J. D'Angelo, "New Finite-Element Formulation for 3-D Scattering Problems," *IEEE Transactions in Magnetics*, vol. MAG-27, no. 5, pp. 3967-3970, September 1991.

[McCa89] B. J. McCartin and J. F. Dicello, "Three Dimensional Finite Difference Frequency Domain Scattering Computation Using the Control Region Approximation," *IEEE Transactions in Magnetics*, vol. MAG-25, no. 4, pp. 3092-3094, July 1989.

[McDo72] B. H. McDonald and A. Wexler, "Finite element solution of unbounded field problems," *IEEE Transactions on Microwave Theory and Techniques*, vol. MTT-20, pp. 841-847, December 1972.

[Mei74] K. K. Mei, "Unimoment method of solving antenna and scattering problems," *IEEE Transactions on Antennas and Propagation*, vol. AP-22, pp. 760-766, November 1974.

[Mei84] K. K. Mei, A. Cangellaris and D. J. Angelakos, "Conformal time domain finite difference method," *Radio Science*, vol. 19, no. 5, pp. 1145-1147, 1984.

[Mere80] D. E. Merewether, R. Fisher and F. W. Smith, "On Implementing a Numeric Huygen's Source Scheme in a Finite Difference Program to Illuminate Scattering Bodies," *IEEE Transactions on Nuclear Science*, vol. NS-27, no. 6, pp. 1829-1833, December 1980.

[Mill88] E. K. Miller, "A Selective Survey of Computational Electromagnetics," *IEEE Transactions on Antennas and Propagation*, vol. AP-36, no. 9, pp. 1281-1305, September 1988.

[Mill92] E. K. Miller, L. Medgyesi-Mitschang and E. H. Newman (ed), **Computational Electromagnetics: Frequency-Domain Method of Moments**, IEEE Press, New York, 1992.

[Mitt89a] R. Mittra and R. K. Gordon, "Radar Scattering from Bodies of Revolution Using an Efficient Partial Differential Equation Algorithm," *IEEE Transactions on Antennas and Propagation*. vol. AP-37, no. 5, pp. 538-545, May 1989.

[Mitt89b] R. Mittra, O. Ramahi, A. Khebir, R. Gordon and A. Kouki, "A Review of Absorbing Boundary Conditions for Two and Three-Dimensional Electromagnetic Scattering Problems," *IEEE Transactions on Magnetics*, vol. MAG-25, no. 4 pp. 3034-3039, July 1989.

[Moha91] A. H. Mohammadian, V. Shankar and W. F. Hall, "Computation of electromagnetic scattering and radiation using a time-domain finite-volume discretization procedure," *Computer Physics Communications*, vol. 69, pp. 175-196, 1991.

[Mohe90] H. Moheb and L. Shafai, "Modal Analysis Method for Bodies of Arbitrary Cross-Section for Numerical Computation," *IEE Proceedings*, vol. 137, Pt. H, no. 5, pp. 255-262, 1990.

[Mohe91] H. Moheb and L. Shafai, "Numerical Solution of Integral Equations for Dielectric Objects of Prismatic Shapes," *IEEE Transactions on Antennas and Propagation*, vol. 39, no. 6, pp. 758-766, 1991.

[Moor88] T. G. Moore, J. G. Blaschak, A. Taflove and G. A. Kriegsmann, "Theory and Application of Radiation Boundary Operators," *IEEE Transactions on Antennas and Propagation*, vol. 36, no. 12, pp. 1797-1812, December 1988.

[More92] J. A. Morente, J. A. Porti and M. Khalladi, "Absorbing Boundary Conditions for the TLM Method," *IEEE Transactions on Microwave Theory and Techniques*, vol. MTT-40, no. 11, pp. 2095-2099, 1992.

[Mors53] P. M. Morse and H. Feshbach, **Methods of Theoretical Physics**, McGraw-Hill Book Company, 1953.

[Mosi85] J. R. Mosig and F. E. Gardiol, "Rayonnement d'une antenne microruban de forme arbitraire," *Annales des Telecommunication*, vol. 40, no. 3-4, pp. 181-189, 1985.

[Mosi90] J. R. Mosig, "Numerical Analysis of Microstrip Patch Antennas," in **Handbook of Microstrip Antennas**, Ed: J. R. James and P. S. Hall, Peter Peregrinus, 1990.

[Mull82] R. Mullen and T. Belytschko, "Dispersion Analysis of Finite Element Semidiscretizations of the Two-Dimensional Wave Equation," *International Journal for Numerical Methods in Engineering*, vol. 18, pp. 11-29, 1982.

[Mur85] G. Mur and A. T. de Hoop, "A Finite-Element Method for Computing Three-Dimensional Electromagnetic Fields in Inhomogeneous Media," *IEEE Transactions on Magnetics*, vol. MAG-21, no. 6, pp. 2188-2191, November 1985.

[Mur88] G. Mur, "Optimum Choice of Finite Elements for Computing Three-Dimensional Electromagnetic Fields in Inhomogeneous Media," *IEEE Transactions on Magnetics*, vol. MAG-24, no. 1, pp. 330-333, January 1988.

[Neum30] J. Von Neumann, **Theory of Self-Reproducing Automata**, edited by A. W. Burks, University of Illinois, 1966.

[Niel91] J. S. Nielson and W. J. R. Hoefer, "A Complete Dispersion Analysis of the Condensed Node TLM Mesh," *IEEE Transactions on Magnetics*, vol. MAG-27, no. 5, pp. 3982-3985, September 1991.

[O'Bri50] G. O. O'Brien, M. A. Hyman and S. Kaplan, "A Study of the Numerical Solution of Partial Differential Equations," *J. Math. and Phys.*, vol. 29, pp. 223, 1950.

[Parh80] P. Parhami and R. Mittra, "Wire Antennas Over a Lossy Half Space," *IEEE Transactions on Antennas and Propagation*, vol. AP-28, pp. 397-403, 1980.

[Paul88] K. D. Paulsen, D. R. Lynch and J. W. Strohbehn, "Three-Dimensional Finite, Boundary, and Hybrid Element Solutions of the Maxwell Equations for Lossy Dielectric Media," *IEEE Transactions on Microwave Theory and Techniques*, vol. MTT-36, no. 4, pp. 682-693, April 1988.

[Paul91a] K. D. Paulsen and D. R. Lynch, "Elimination of Vector Parasites in Finite Element Maxwell Solutions," *IEEE Transactions on Microwave Theory and Techniques*, vol. MTT-39, no. 3, pp. 395-404, March 1991.

[Paul91b] D. L. Paul, E. M. Daniel and C. J. Railton, "Fast Finite Difference Time Domain Method for the Analysis of Planar Microstrip Circuits", *Proceedings of the 21st European Microwave Conference,* Stuttgart, pp. 303-308, 1991.

[Paul92] K. D. Paulsen, W. E. Boyse and D. R. Lynch, "Continuous Potential Maxwell Solutions on Nodal-Based Finite Elements," *IEEE Transactions on Antennas and Propagation,* vol. AP-40, no. 10, pp. 1192-1200, October 1992.

[Pete88] A. F. Peterson, "Absorbing Boundary Conditions for the Vector Wave Equation," *Microwave and Optical Technology Letters*, vol. 1, no. 2, pp. 62-64, 1988.

[Pete89] A. F. Peterson, "A Comparison of Integral, Differential and Hybrid Methods for TE-Wave Scattering from Inhomogeneous Dielectric Cylinders," *Journal of Electromagnetic Waves and Applications*, vol. 3, no. 2, pp. 87-106, 1989.

[Petr94] P. G. Petropoulos, "Stability and Phase Error Analysis of FD-TD in Dispersive Dielectrics", *IEEE Transactions on Antennas and Propagation,* vol. AP-42, no. 1, pp. 62-69, January 1994.

[Pind77] G. F. Pinder and W. G. Gray, **Finite Element Simulation in Surface and Subsurface Hydrology**, Academic Press, 1977.

[Poza90] D. M. Pozar, "Analysis and Design Considerations for Printed Phased-Array Antennas," in **Handbook of Microstrip Antennas**, Ed: J. R. James and P. S. Hall, Peter Peregrinus, 1990.

[Rahm84] B. M. A. Rahman and J. B. Davies, "Penalty Function Improvement of Waveguide Solution by Finite Elements," *IEEE Transactions on Microwave Theory and Techniques*, vol. MTT-32, no. 8, pp. 922-928, August 1984.

[Rail92] C. J. Railton and E. M. Daniel, "Comparison of the effect of discretization on absorbing boundary algorithms in the finite difference time domain method," *Electronics Letters*, vol. 28, no. 20, pp. 1891-1893, 1992.

[Rail93] C. J. Railton, E. M. Daniel, D-L Paul and J. P. McGeehan, "Optimized Absorbing Boundary Conditions for the Analysis of Planar Circuits Using the Finite Difference Time Domain Method", *IEEE Transactions on Microwave Theory and Techniques",* vol. MTT-41, no. 2, pp. 290-297, February 1993.

[Rao82] S. M. Rao, D. R. Wilton, and A. W. Glisson, "Electromagnetic Scattering by Surfaces of Arbitrary Shape," *IEEE Transactions on Antennas and Propagation*, vol. AP-30, no. 3, pp. 409-418, May 1982.

[Rein89] A. Reineix and B. Jecko, "Analysis of Microstrip Patch Antennas using Finite Difference Time Domain Method," *IEEE Transactions on Antennas and Propagation*, vol. AP-37, no. 11, pp. 1361-1369, November 1989.

[Rich66] J. H. Richmond, "Scattering by a Dielectric Cylinder of Arbitrary Cross Section Shape," *IEEE Transactions on Antennas and Propagation*, vol. AP-14, no. 6, pp. 334-341, May 1966.

[Rile93] R. J. Riley, "Locally Non-Uniform Finite-Difference Time-Domain with Application to Stealth, Crosstalk, and Narrow Apertures," Sandia National Laboratories, Sandia Report SAND93-0735, 1993.

[Roth87] D. H. Rothman, "Modelling Seismic P-Waves with Cellular Automata," *Geophysical Research Letters*, vol. 14, no. 1, pp. 17-20, January 1987.

[Sagu89] P. Saguet, "The 3D Transmission-Line Matrix Method: Theory and Comparison of the Processes," *International Journal of Numerical Modelling*, vol. 2, no. 4, pp. 191-201, 1989.

[Sark89] T. K. Sarkar, E. Arvas and S. Ponnapalli, "Electromagnetic Scattering from Dielectric Bodies," *IEEE Transactions on Antennas and Propagation*, vol. AP-37, no. 5, pp. 673-676, May 1989.

[Sark90] T. K. Sarkar, S. M. Rao and A. R. Djordjevic, "Electromagnetic Scattering and Radiation from Finite Microstrip Structures," *IEEE Transactions on Microwave Theory and Techniques*, vol. MTT-38, no. 11, pp. 1568-1575, November 1990.

[Scha84] D. H. Schaubert, D. R. Wilton and A. W. Glisson, "A Tetrahedral Modelling for Electromagnetic Scattering by Arbitrarily Shaped Inhomogeneous Dielectric Bodies," *IEEE Transactions on Antennas and Propagation*, vol. AP-32, no. 1, pp. 77-85, January 1984.

[Shla93] K. L. Shlager, J. G. Maloney, S. L. Ray and A. F. Peterson, "Relative Accuracy of Several Finite-Difference Time-Domain Mathods in Two and Three Dimensions," *IEEE Transactions on Antennas and Propagation*, vol. AP-41, no. 12, pp. 1732-1737, December 1993.

[Shaf90] L. Shafai and A. A. Kishk, "Analysis of Circular Microstrip Antennas," in **Handbook of Microstrip Antennas**, Ed: J. R. James and P. S. Hall, Peter Peregrinus, 1990.

[Shan89] V. Shankar, W. F. Hall and A. H. Mohammadian, "A Time-Domain Differential Solver for Electromagnetic Scattering Problems," *Proceedings of the IEEE*, vol. 77, no. 5, pp. 709-721, May 1989.

[Shan90] V. Shankar, A. H. Mohammadian and W. F. Hall, "A Time-Domain Finite-Volume Treatment for the Maxwell Equations," *Electromagnetics*, vol. 10, pp. 127-145, 1990.

[Shee90] D. M. Sheen, S. M. Ali, M. D. Abouzahra and J. A. Kong, "Application of the Three-Dimensional Finite-Difference Time-Domain Method to the Analysis of Planar Microstrip Circuits," *IEEE Transactions on Microwave Theory and Techniques*, vol. MTT-38, no. 7, pp. 849-857, 1990.

[Shib88] T. Shibata, T. Hayashi and T. Kimura, "Analysis of Microwave Circuits Using Three-Dimensional Full-Wave Electomagnetic Field Analysis in the Time Domain," *IEEE Transactions on Microwave Theory and Techniques*, vol. MTT-36, no. 6, pp. 1064-1070, June 1988.

[Simo90] N. R. S. Simons, "Application of the TLM Method to Open Region Field Problems," M. Sc. Thesis, University of Manitoba, 1990.

[Simo91a] N. R. S. Simons and E. Bridges, "Equivalence of Propagation Characteristics for the Transmission-Line Matrix an Finite-Difference Time-Domain Methods in Two Dimensions," *IEEE Transactions on Microwave Theory and Techniques*, vol. MTT-39, pp. 243-267, 1991.

[Simo91b] N. R. S. Simons and A. A. Sebak, "New transmission-line matrix node for two-dimensional electromagnetic field problems," *Canadian Journal of Physics*, vol. 69, no. 11, pp. 1388-1398, 1991.

[Simo91c] N. R. S. Simons, "Survey of Antenna Modelling Techniques," Technical Report prepared for NovAtel Communications Ltd., May 1991.

[Simo91d] N. R. S. Simons, A. A. Sebak, E. Bridges and Y. M. M. Antar, "Transmission-Line Matrix (TLM) Method for Scattering Problems," *Computer Physics Communications*, vol. 68, pp. 197-212, 1991.

[Simo92] N. R. S. Simons and E. Bridges, "Application of the TLM Method to Two-Dimensional Scattering Problems," *International Journal of Numerical Modelling*, vol. 5, pp. 93-110, 1992.

[Simo93] N. R. S. Simons and A. A. Sebak, "Spatially Weighted Numerical Models for the Two-Dimensional Wave Equations: FD Algorithm and Synthesis of the Equivalent TLM Model," *International Journal of Numerical Modelling*, vol. 6, pp. 47-65, 1993.

[Simo94a] N. R. S. Simons and A. A. Sebak, "A Fourth-Order in Space and Secons-Order Accurate in Time TLM Model," accepted for publication in *IEEE Transactions on Microwave Theory and Techniques*, 1994.

[Simo94b] N. R. S. Simons, G. E. Bridges, and A. A. Sebak, "Analysis of Half-Space Problems Using the Transmission Line Matrix Method," accepted for publication in *IEEE Transactions on Geoscience and Remote Sensing*, 1994.

[Simo94c] N. R. S. Simons and A.A. Sebak, "Application of the Transmission Line Matrix Method to the Analysis of Scattering by Three-Dimensional Objects", accepted for publication in *IEE Proceedings Microwaves, Antennas and Propagation*, 1994.

[Simo94d] N. R. S. Simons, G. E. Bridges, B. W. Podaima and A. Sebak, "Cellular Automata: A New Approach for Simulating Electromagnetic Phenomena", Technical Report #TR-94-101, Department of Electrical and Computer Engineering, University of Manitoba, 1994.

[Simo94e] N. R. S. Simons, G. E. Bridges and A.A. Sebak, "Reversibility, Information-Preservation, and the Presence of Instabilities in Time-Domain Numerical Methods", presented at *ANTEM'94*, Ottawa, Ontario 1994.

[Sod85] G. A. Sod, **Numerical Methods in Fluid Dynamics: Initial and Initial Boundary-Value Problems**, Cambridge University Press, Cambridge, 1985.

[Somm64] A. Sommerfeld, **Partial Differential Equations in Physics**, vol. 6, Academic Press, New York, 1964.

[Span49] K. Spangenberg, G. Walters and F. Schott, "Electrical Network Analyzers for the Solution of Electromagnetic Field Problems Part I Theory, Design, Construction," *Proceedings of the Institute of Radio Engrs.*, vol. 37, pp. 724-729, 1949.

[Ston89] W. R. Stone (ed), **Radar Cross Sections of Complex Objects**, IEEE Press, New York, 1989.

[Stra41] J. A. Stratton, **Electromagnetic Theory**, McGraw-Hill Book Company, 1941.

[Stra73] G. Strang and G. J. Fix, **An Analysis of the Finite Element Method**, Prentice-Hall, Inc. Englewood Cliffs, 1973.

[Sull86] P. L. Sullivan and D. H. Schaubert, "Analysis of an Aperture Coupled Microstrip Antenna", *IEEE Transactions on Antennas and Propagation* vol. AP-34, no. 8, pp. 977-984, August 1986.

[Sumb91] E. Sumbar, F. E. Vermeulen and F. S. Chute, "Implementation of Radiation Boundary Conditions in the Finite Element Analysis of Wave Propagation," *IEEE Transactions on Microwave Theory and Techniques*, vol. MTT-39, no. 2, pp. 267-273, 1991.

[Tafl83] A. Taflove and K. Umashankar, "Radar Cross Section of General Three-Dimensional Scatterers," *IEEE Transactions on Electromagnetic Compatibility*, vol. EMC-25, no. 4, pp. 433-440, November 1983.

[Tafl89] A. Taflove and K. R. Umashankar, "Review of FD-TD Numerical Modelling of Electromagnetic Wave Scattering and Radar Cross Section," *Proceedings of the IEEE*, vol. 77, no. 5, pp. 682-699, May 1989.

[Take92a] K. Taketomi and Y. Miyazaki, "Analysis of Scattering by Buried Objects Using FD-TD Method and Spectrum Separate Calculation Method", *Proceedings of International Symposium on Antennas and Propagation*, Sapporo Japan, 1992.

[Take92b] K. Takeuchi, W. Chujo and M. Fujise, "Fundamental Characteristics of a Slot-Coupled Microstrip Antenna using High Permittivity Feed Substrate," *22nd European Microwave Conference Digest*, pp. 769-774, 1992.

[Thie92] E. Thiele, "Parallel Implementation of Cellular Systems for Numerical Modelling," *International Journal of Numerical Modelling*, vol. 5, pp. 203-218, 1992.

[Toff84a] T. Toffoli, "Cellular Automata as an Alternative to (Rather than an Approximation of) Differential Equations in Modelling Physics," *Physica D*, vol. 10, pp. 117-127, 1984.

[Toff84b] T. Toffoli, "CAM: A High-Performance Cellular-Automata Machine," *Physica D*, vol. 10, pp. 195-204, 1984.

[Toff87] T. Toffoli and N. Margolus, **Cellular Automata Machines: A New Environment for Modelling**, Cambridge: MIT Press, 1987.

[Toff91a] T. Toffoli, "How Cheap Can Mechanics' First Principles Be ?" in: **Complexity, Entropy and the Physics of Information** ed: W. H. Zurek, Santa Fe Institute, 1991.

[Toff91b] T. Toffoli and N. Margolus, "Programmable Matter: Concepts and Realization," *Physica D*, vol. 47, pp. 263-272, 1991.

[Tref82] L. N. Trefethen, "Group Velocity In Finite Difference Schemes," *SIAM Review*, no. 24, pp. 113-136, 1982.

[Umas82] K. Umashankar and A. Taflove, "A Novel Method to Analyze Electromagnetic Scattering of Complex Objects," *IEEE Transactions on Electromagnetic Compatibility*, vol. EMC-24, no. 4, pp. 397-405, November 1982.

[Vich82] R. Vichnevetsky and J. B. Bowles, **Fourier Analysis of Numerical Approximations of Hyperbolic Equations**, SIAM Philadelphia, 1982.

[Vich84a] G. Y. Vichniac, "Simulating Physics with Cellular Automata," *Physica D*, vol. 10, pp. 96-116, 1984.

[Vich84b] G. Y. Vichniac, "Instability in Discrete Algorithms and Exact Reversibility," *SIAM Journal on Algebraic and Discrete Methods*, vol. 5, no. 4, pp. 596-602, December 1984.

[Wait69] J. R. Wait, "Characteristics of Antennas Over Lossy Earth," Chapter 23 in: Antenna Theory (Part II) Ed: R. E. Collin and F. J. Zucker, 1969.

[Whin44] J. R. Whinnery and S. Ramo, "A New Approach to the Solution of High-Frequency Field Problems," Proc. Inst. Radio Engrs., vol. 32, pp. 284-288, 1944.

[Wolf83] S. Wolfram, "Statistical mechanics of cellular automata," *Reviews of Modern Physics*, vol. 55, no. 3, pp. 601-644, July 1983.

[Wolf84a] S. Wolfram, "Preface to a special issue on Cellular Automata," *Physica D*, vol. 10, pp. vii-xii, 1984.

[Wolf84b] S. Wolfram, "Universality and Complexity in Cellular Automata," *Physica D*, vol. 10, pp. 1-35, 1984 (this paper is also reprinted in [Wolf86a]).

[Wolf86a] S. Wolfram (ed), **Theory and Applications of Cellular Automata**, World Scientific, Singapore, 1986.

[Wolf86b] S. Wolfram, "Cellular Automata Fluids 1: Basic Theory," *Journal of Statistical Physics*, vol. 45, no. 3/4, pp. 471-526, 1986 (this paper is also reprinted in [Dool90]).

[Wolf92] I. Wolff, "Finite Difference Time Domain Simulation of Electromagnetic Fields and Microwave Circuits," *International Journal of Numerical Modelling*, vol. 5, no. 3, pp. 163-182, 1992.

[Wolf93] Interview of Steven Wolfram, *Dr. Dobb's Journal*, pp. 105-108, February 1993.

[Wu90] S-C. Wu, H-Y Yang, N. G. Alexopoulos and I. Wolff, "A Rigorous Dispersive Characterization of Microwave Cross and T Junctions", *IEEE Transactions on Microwave Theory and Techniques*, vol. MTT-38, no. 12, pp. 1837-1844, December 1990.

[Yee66] K. S. Yee, "Numerical Solution of Initial Boundary Value Problems Involving Maxwell's Equations in Isotropic Media," *IEEE Transactions on Antennas and Propagation*, vol. AP-14, no. 3, pp. 302-307, May 1966.

[Yuan90]   X. Yuan, "Three-Dimensional Electromagnetic Scattering from Inhomogeneous Objects by the Hybrid Moment and Finite Element Method," *IEEE Transactions on Microwave Theory and Techniques*, vol. MTT-38, no. 8, pp. 1053-1058, August 1990.

[Yuan91] X. Yuan, D. R. Lynch and K. Paulsen, "Importance of Normal Field Continuity in Inhomogeneous Scattering Calculations," *IEEE Transactions on Microwave Theory and Techniques*, vol. MTT-39, no. 4, pp. 638-642, April 1991.

[Zhan88a] X. Zhang, J. Fang, K. K. Mei and Y. Liu, "Calculations of the Dispersive Characteristics of Microstrips by the Time-Domain Finite Difference Method," *IEEE Transactions on Microwave Theory and Techniques*, vol. MTT-36, no. 2, February 1988.

[Zhan88b] X. Zhang and K. K. Mei, "Time-Domain Finite Difference Approach to the Calculation of the Frequency-Dependent Characteristics of Microstrip Discontinuities," *IEEE Transactions on Microwave Theory and Techniques*, vol. MTT-36, no. 12, pp. 1775-1787, December 1988.

[Zien83] O. C. Zienkiewicz, "Finite Elements in the Time Domain," Chapter 13 in **State-of-the-Art Surveys on Finite Element Technology**, Ed: A. K. Noor and W. D. Pilkey, 1983.

[Zien91] O. C. Zienkiewicz and R. L. Taylor, **The Finite Element Method**, volumes 1 and 2, (fourth edition), McGraw-Hill Book Company, 1991.

[Ziol83] R. W. Ziolkowski, N. K. Madsen and R. C. Carpenter, "Three-Dimensional Computer Modelling of Electromagnetic Fields: A Global Lookback Lattice Truncation Scheme," *Journal of Computational Physics*, vol. 50, pp. 360-408, 1983.